Fermi National Accelerator Laboratory

FERMILAB-Pub-93/179-E
DØ 1808
DØ

The DØ Detector

S. Abachi et al
The DØ Collaboration

Fermi National Accelerator Laboratory
P.O. Box 500, Batavia, Illinois 60510

July 1993

Submitted to *Nuclear Instruments and Methods*

Disclaimer

The DØ Detector

S. Abachi[8], M. Abolins[17], B.S. Acharya[28], I. Adam[7], S. Ahn[8], H. Aihara[14], G. Alvarez[12], G.A. Alves[6], N. Amos[16], W. Anderson[13], Yu. Antipov[23], S.H. Aronson[3], R. Astur[26], R.E. Avery[20], A. Baden[15], J. Balderston[11], B. Baldin[23], J. Bantly[4], E. Barasch[26], J.F. Bartlett[8], K. Bazizi[5], T. Behnke[26], V. Bezzubov[23], P.C. Bhat[8], G. Blazey[24], S. Blessing[20], A. Boehnlein[30], F. Borcherding[8], J. Borders[24], N. Bozko[23], A. Brandt[8], R. Brock[17], A. Bross[8], D. Buchholz[20], V. Burtovoy[23], J.M. Butler[8], O. Callot[26], D. Chakraborty[26], S. Chekulaev[23], J. Chen[2], L.-P. Chen[14], W. Chen[26], B.C. Choudhary[5], J. H. Christenson[8], D. Claes[26], A.R. Clark[14], W.G. Cobau[15], J. Cochran[26], W.E. Cooper[8], C. Cretsinger[24], D. Cullen-Vidal[4], M. Cummings[11], D. Cutts[4], O.I. Dahl[14], B. Daniels[3], K. De[29], M. Demarteau[8], K. Denisenko[8], N. Denisenko[8], D. Denisov[23] S. Denisov[23], W. Dharmaratna[10], H.T. Diehl[8], M. Diesburg[8], R. Dixon[8], P. Draper[29], Y. Ducros[25], S. Durston-Johnson[24], D. Eartly[8], P.H. Eberhard[14], D. Edmunds[17], A. Efimov[23], J. Ellison[5], V.D. Elvira[8], R. Engelmann[26], O. Eroshin[23], V. Evdokimov[23], S. Fahey[17], G. Fanourakis[24], M. Fatyga[3], J. Featherly[3], S. Feher[26], D. Fein[2], T. Ferbel[24], D. Finley[8], G. Finocchiaro[26], H.E. Fisk[8], E. Flattum[17], G.E. Forden[2], M. Fortner[19], P. Franzini[7], S. Fuess[8], E. Gallas[30], C.S. Gao[8], T.L. Geld[16] K. Genser[8], C.E. Gerber[8], B. Gibbard[3], V. Glebov[27], J.F. Glicenstein[25], B. Gobbi[20], M. Goforth[10], M.L. Good[26], F. Goozen[14], H. Gordon[3], N. Graf[3], P.D. Grannis[26], D.R. Green[8], J. Green[19], H. Greenlee[8], N. Grossman[17], P. Grudberg[14], J.A. Guida[26], J.M. Guida[3], W. Guryn[3], N.J. Hadley[15], H. Haggerty[8], S. Hagopian[10], V. Hagopian[10], R.E. Hall[5], S. Hansen[8], J. Hauptman[13], D. Hedin[19], A.P. Heinson[5], U. Heintz[7], T. Heuring[26], R. Hirosky[24], K. Hodel[24], J.S. Hoftun[4], J.R. Hubbard[25], T. Huehn[5], R. Huson[30], S. Igarashi[8], A.S. Ito[8], E. James[2], J. Jiang[26], K. Johns[2], C.R. Johnson[31], M. Johnson[8], A. Jonckheere[8], M. Jones[11], H. Jöstlein[8], C.K. Jung[26], S. Kahn[3], S. Kanekal[7], A. Kernan[5], L. Kerth[14], A. Kirunin[23], A. Klatchko[10], B. Klima[8], B. Klochkov[23], C. Klopfenstein[26], V. Klyukhin[23], V. Kochetkov[23], J.M. Kohli[21], W. Kononenko[22], J. Kotcher[27], I. Kotov[23], J. Kourlas[18], A. Kozelov[23], E. Kozlovsky[23], G. Krafczyk[8], K. Krempetz[8], M.R. Krishnaswamy[28], P. Kroon[3], S. Krzywdzinski[8], S. Kunori[15], S. Lami[26], G. Landsberg[26], R.E. Lanou[4], P. Laurens[17], J. Lee-Franzini[26], J. Li[29], R. Li[8], Q.Z. Li-Demarteau[8], J.G.R. Lima[6], S.L. Linn[10], J. Linnemann[17], R. Lipton[8], Y.-C. Liu[20], D. Lloyd-Owen[26], F. Lobkowicz[24], S.C. Loken[14], S. Lokos[26], L. Lueking[8], A.K.A. Maciel[6], R.J. Madaras[14], R. Madden[10], E. Malamud[8], Ph. Mangeot[25], I. Manning[8], B. Mansoulié[25], V. Manzella[26], H.-S. Mao[8], M. Marcin[16], L. Markosky[2], T. Marshall[12], H.J. Martin[12], M.I. Martin[8], P.S. Martin[8], M. Marx[26], B. May[2], A. Mayorov[23], R. McCarthy[26], J. McKinley[17], D. Mendoza[1], X.-C. Meng[8],

K.W. Merritt[8], A. Milder[2], A. Mincer[18], N.K. Mondal[28], M. Montag[3], P. Mooney[17], M. Mudan[18], G.T. Mulholland[8], C. Murphy[12], C.T. Murphy[8], F. Nang[4], M. Narain[8], V.S. Narasimham[28], H.A. Neal[16], P. Nemethy[18], D. Nešić[4], K.K. Ng[26], D. Norman[15], L. Oesch[16], V. Oguri[6], E. Oltman[14], N. Oshima[8], D. Owen[17], M. Pang[13], A. Para[8], C.H. Park[8], R. Partridge[4], M. Paterno[26], A. Peryshkin[8], M. Peters[11], B. Pi[17], H. Piekarz[10], Yu. Pischalnikov[23], D. Pizzuto[26], A. Pluquet[25], V. Podstavkov[23], B.G. Pope[17], H.B. Prosper[8], S. Protopopescu[3], Y.-K. Que[8], P.Z. Quintas[8], G. Rahal-Callot[26], R. Raja[8], S. Rajagopalan[26], M.V.S. Rao[28], L. Rasmussen[26], A.L. Read[8], T. Regan[27], S. Repond[19], V. Riadovikov[23], M. Rijssenbeek[26], N.A. Roe[14], P. Rubinov[26], J. Rutherfoord[2], A. Santoro[6], L. Sawyer[29], R.D. Schamberger[26], J. Sculli[18], W. Selove[22], M. Shea[8], A. Shkurenkov[23], M. Shupe[2], J.B. Singh[21], V. Sirotenko[19], W. Smart[8], A. Smith[2], D. Smith[5], R.P. Smith[8], G.R. Snow[16], S. Snyder[26], M. Sosebee[29], M. Souza[6], A.L. Spadafora[14] S. Stampke[17], R. Stephens[9], M.L. Stevenson[14], D. Stewart[16], F. Stocker[27], D. Stoyanova[23], H. Stredde[8], K. Streets[15], M. Strovink[14], A. Suhanov[23], A. Taketani[8], M. Tartaglia[8], J.D. Taylor[14], J. Teiger[25], G. Theodosiou[22], J. Thompson[26], S. Tisserant[17], T.G. Trippe[14], P.M. Tuts[7], R. Van Berg[22], M. Vaz[6], P.R. Vishwanath[28], A. Volkov[23], A. Vorobiev[23], H.D. Wahl[10], D.-C. Wang[8], L.-Z. Wang[8], H. Weerts[17], W.A. Wenzel[14], A. White[29], J.T. White[30], J. Wightman[30], S. Willis[19], S.J. Wimpenny[5], Z. Wolf[9] J. Womersley[27], D.R. Wood[8], Y. Xia [17], D. Xiao[10], P. Xie[8], H. Xu[4], R. Yamada[8], P. Yamin[3], C. Yanagisawa[26], J. Yang[18], M.-J. Yang[8], C. Yoshikawa[11], S. Youssef[10], J. Yu[26], R. Zeller[31], S. Zhang[16], Y.H. Zhou[8], Q. Zhu[18], Y.-S. Zhu[8], D. Zieminska[12], A. Zieminski[12], A. Zinchenko[13], A. Zylberstejn[25]

The DØ Collaboration

[1]Universidad de los Andes, Bogota Colombia
[2]University of Arizona
[3]Brookhaven National Laboratory
[4]Brown University
[5]University of California, Riverside
[6]LAFEX, Centro Brasileiro de Pesquisas Físicas, Rio de Janeiro, Brazil
[7]Columbia University
[8]Fermi National Accelerator Laboratory
[9]University of Florida
[10]Florida State University
[11]University of Hawaii
[12]Indiana University
[13]Iowa State University

[14]Lawrence Berkeley Laboratory
[15]University of Maryland
[16]University of Michigan
[17]Michigan State University
[18]New York University
[19]Northern Illinois University
[20]Northwestern University
[21]University of Panjab, Chandigarh, India
[22]University of Pennsylvania
[23]Institute for High Energy Physics, Protvino, Russia
[24]University of Rochester
[25] DAPNIA-CE Saclay,France
[26]State University of New York - Stony Brook
[27]Superconducting Supercollider Laboratory
[28]Tata Institute of Fundamental Research, Bombay India
[29]University of Texas - Arlington
[30]Texas A&M University
[31]ZRL, Bristol Rhode Island

Abstract

The DØ Detector is a large general purpose detector for the study of short-distance phenomena in high energy antiproton-proton collisions, now in operation at the Fermilab Tevatron Collider. The detector focusses upon the detection of electrons, muons, jets and missing transverse momentum. We describe the design and performance of the major elements of the detector, including the tracking chambers, transition radiation detector, liquid argon calorimetry and muon detection. The associated electronics, triggering systems and data acquisition systems are presented. The global mechanical, high voltage, and experiment monitoring and control systems which support the detector are described. We also discuss the design and implementation of software and software support systems that are specific to DØ.

1. Introduction

The DØ Detector has been constructed to study proton-antiproton collisions at $\sqrt{s}$ =2 TeV in the Fermilab Tevatron Collider. The experiment was first provisionally approved in 1983 and the full conceptual design report[1] was prepared a year later. The prime physics focus of the DØ Experiment is the study of high mass states and large p_T phenomena. These include the search for the top quark, precision study of the W and Z bosons to give sensitive tests of the Standard Electroweak Model, various studies of perturbative QCD and the production of b-quark hadrons, and searches for new phenomena beyond the standard model.

This paper gives a description of the elements of the DØ Detector and the systems for collecting data from it. Earlier reports[2] [3] [4] [5] [6] [7] [8] have summarized the main features and design goals of the experiment.

The DØ detector was optimized with the following three general goals in mind:

- Excellent identification and measurement of electrons and muons.
- Good measurement of parton jets at large p_T through highly segmented calorimetry with good energy resolution.
- A well-controlled measure of missing transverse energy ($\not\!\!E_T$) as a means of signalling the presence of neutrinos and other non-interacting particles.

These principles derive from the observation that new objects or phenomena typically have appreciable branching ratios into states including leptons and jets, while the dominating QCD backgrounds have quite small leptonic branching fractions. The focus on parton jets is more important for deciphering the underlying physics processes than emphasis on the individual final particles emitted after hadronization.

The detector design which emerged had as its central design features:

- Stable, unit gain, hermetic, finely segmented, thick and radiation-hard calorimetry, based on detection of ionization in liquid argon. The inner radius of the calorimetry was chosen to be small to accomodate the desired depth and not compromise the surrounding muon detector.
- Muon detection with thick magnetized iron absorbers to provide sufficient momentum measurement and to minimize backgrounds from hadron punchthrough.
- A compact non-magnetic tracking volume within r = 75 cm with adequate spatial resolution and particular emphasis on suppression of backgrounds to electrons.

A cutaway isometric view of the detector is shown in Fig. 1. The nested shells of the tracking and transition radiation detectors, calorimetry and muon detectors are shown. The support platform on which the core detector elements were assembled serves as the transporter for the detector to and from the DØ intersection region. Much of the front-end electronics for the detectors also rests on the platform. The elevation view of the detec-

tor shown in Fig. 2 shows the same detector system shells and, in addition, the support platform in which detector electronics, cable connections, and services for power, gas and cryogens are located. Fig. 2 also shows the Tevatron beam pipe centered within the detector and the lower energy Main Ring beam pipe used for preacceleration of protons which passes above the detector center. The cables from the detector elements pass over an articulating bridge to the Moving Counting House (MCH), providing sufficient separation of detector and MCH to keep the latter in a radiation-safe environment outside the Tevatron shield wall. Digitized information produced in the MCH is collected, zero-suppressed, and passed over high-speed data highways to one of many data acquisition processor nodes located in the control room area. Here, event building and event filtering functions are performed before passing an acceptable event to the host computer for on-line monitoring and recording on magnetic media. Events of sufficient interest are sent over the network to an 'Express Line' disk storage for immediate reconstruction.

Subsequent portions of this paper discuss the goals, detector designs, electronics systems, and test performance data for the Central Detectors (Section 2), Calorimeters (Section 3), and Muon Detection (Section 4). The various stages of triggering and data acquisition are described in Section 5. The main subsystems which support the detector and electronics systems are summarized in Section 6. The basic structure of the main software components of the experiment are outlined in Section 7. We adopt a right-handed coordinate system, in which the z-axis is along the proton direction and the y-axis is upward. The angles ϕ and θ are respectively the azimuthal and polar angles ($\theta = 0$ along the proton beam direction). The r-coordinate denotes the perpendicular distance from the beam axes. The pseudo-rapidity, $\eta \equiv -ln\big(tan(\theta/2)\big)$, approximates the true rapidity $y = 1/2\ ln\big((E + p_z)/(E - p_z)\big)$, for finite angles in the limit that $(m/E) \rightarrow 0$.

2. Central Detectors

2.1 Central Detector Layout

The DØ tracking and transition radiation detectors comprise the Central Detector (CD). The separate systems are (i) the Vertex Drift Chamber (VTX), (ii) the Transition Radiation Detector (TRD), (iii) the Central Drift Chamber (CDC) and (iv) two Forward Drift Chambers (FDC). The VTX, TRD, and CDC cover the large angle region and are arranged in three cylinders concentric with the beams. The FDCs are oriented perpendicular to the beams. Figure 3 shows the layout of these detectors. The full set of CD detectors fits within the inner cylindrical aperture of the calorimeters in a volume bounded by r=78 cm and z=$\pm$135 cm.

The design and optimization of the DØ tracking detectors was influenced by the absence of a central magnetic field. Without the need to measure momenta of charged particles, the prime considerations for tracking were good two-track resolving power, high efficiency, and good ionization energy measurement so as to distinguish single electrons from close-spaced conversion pairs. The TRD was included in order to gain an additional factor of about 50 for rejection of isolated pions beyond that given by the calorimeter alone. The scale for track spatial resolutions is set by the need for primary z-vertex determination and by calorimeter shower matching, to be about 1 mm. Good track-fitting efficiency and recognition of $\pi(K) \rightarrow \mu$ decay kinks benefit from as good resolution as can be attained. Some physics issues, such as the desire to tag separated vertices arising from b-quark jets from top decays, also stress the need for good position resolution.

The transition between the large-angle tracking chambers with wires parallel to the beams and the small-angle tracking with wires perpendicular to the beam was matched to the corresponding transition between central and end calorimeters.

The CD detectors were designed to match the Collider bunch-time interval of 3.5 μs. This time allows relatively long drift cells. Good two-track resolving power is obtained by employing a flash analog-to-digital (FADC) conversion system for signal digitization in which the charge is sampled at $\sim$10 ns intervals. This gives an effective detector granularity of 100 - 350 μm, but with relatively few channels (about 4200 wires and 6080 total channels). In order to obtain robust measurement of the z-coordinate in the large angle chambers, different methods are used for obtaining that coordinate in the VTX, TRD, and CDC. They include charge division (VTX), helical cathode pads (TRD) and delay lines (CDC). The FDC also employs delay lines for measuring coordinates parallel to the wires.

More discussion of the design criteria for the CD detectors is described in the DØ Design Report[1] . Tests of prototype chambers[9] [10] [11] [12] demonstrated that the design goals for DØ could be achieved and are summarized in Section 2.7.

2.2 Vertex (VTX) Chamber

The VTX chamber[12] is the innermost tracking detector in DØ. It has an inner radius of 3.7 cm (just outside the beryllium beam pipe) and an outer active radius of r=16.2 cm. As shown in Fig. 4, there are three mechanically-independent concentric layers of cells in the VTX chamber, each supported by thin G-10 bulkheads mounted on carbon fiber support tubes. Titanium tie rods connect each bulkhead to the next inner carbon fiber tube to support the wire tensions. In each cell, eight sense wires provide measurement of the $r-\phi$ coordinate. As indicated in Fig. 5, the innermost layer (VTX0) has 16 cells in azimuth; the outer two layers (VTX1 and VTX2) have 32 cells. Adjacent sense wires are staggered by $\pm$ 100μm to resolve left-right ambiguities; the cells of the three layers are offset in ϕ to further aid pattern recognition and to facilitate calibration.

The sense wires are 25 μm NiCoTin[13] at 80 g tension. They have a resistivity of 1.8 kΩ/m and provide a measurement of the z-coordinate from readouts at both ends. The electrostatic properties of the cell are determined by the grounded planes of grid-wire on either side of the sense wires planes and the outer cathode field wires which shape the electric field in the cell. Coarse field shaping is provided by aluminum traces on carbon fiber support tubes just beyond the fine field shaping wires. Field and grid wires are made of 152 μm gold plated aluminum at a tension of 360g. Further discussion of the electrostatics of the VTX chamber can be found elsewhere[11].

To obtain good spatial resolution and track pair resolving power, the gas chosen for operation of the VTX is CO_2(95%)-ethane(5%) at one atmosphere with a small admixture of H_2O. At our operating conditions, this gas is unsaturated; good knowledge of the electric field is necessary to obtain accurate velocities across the cell. Figure 6 shows the distance-time correlation for the VTX chamber as measured in a test beam (the scatter of distance values is attributed to the imprecision of the beam particle position determination). The average drift velocity under normal DØ operating conditions ($\langle\vec{E}\rangle \approx$ 1kV/cm) is about 7.3μm/ns. Gas gain at the sense wires is approximately 4 $\times$ 10^4. Studies have shown that the addition of 0.5% H_2O helps stabilize the chamber operation in a high radiation environment[14].

2.3 Transition Radiation Detector (TRD)

The TRD occupies the space between the VTX and the CDC and provides independant electron identification in addition to that given by the calorimeters. Transition radiation X-rays are produced when highly-relativistic particles ($\gamma > 10^3$) traverse boundaries between media with different dielectric constants[15]. The DØ TRD consists of three separate units, each containing a radiator and an X-ray detection chamber. Extensive studies and prototype tests were made to optimize the TRD performance and to simplify the construction techniques[16] [17] [18].

The energy spectrum of the X-rays is determined by the thickness of the radiator foils and the gaps between the foils. The radiator section of each TRD unit consists of 393 foils of 18 μm thick polypropylene in a volume filled with nitrogen gas. The mean gap between foils is 150 μm; the fluctuations in the gap thickness are comparable to the mean gap thickness. The gaps between foils are made by embossing a pattern in the polypropylene sheets. This is achieved by laying the sheets over a polyethylene 2×2 cm mesh and heating the foil to 85°C for five minutes. The foil is cooled under suction; the imprint of the mesh maintains the spaces between adjacent foils. The radiator foil is wound directly from the embossing facility onto its inner cylindrical support. For the DØ configuration, the transition-radiation X-rays have an energy distribution which peaks at 8 keV and is mainly contained below 30 keV[18] .

The detection of X-rays is accomplished in a two-stage time-expansion radial-drift PWC mounted just after the radiator. The X-rays convert mainly in the first stage of the chamber, and the resulting charge drifts radially outward to the sense cells, where the avalanche occurs. Figure 7 illustrates the construction of the TRD chamber with its conversion and amplification stages. The interaction length of the X-rays is energy dependent, but the conversion usually occurs in the first few millimeters of the conversion gap. In addition to the charge deposited by the transition-radiation X-rays, ionization is produced by all charged particles traversing the conversion and amplification gaps. The X-ray conversions and ionization delta-rays produce clusters of charge, which arrive at the sense wires over the full 0.6 μsec drift-time interval. Figure 8 shows the arrival-time distribution of the charge generated in the detection chamber due to transition-radiation X-rays and ionization from a single 5 GeV electron. Both the magnitude and the time of arrival of the clusters of charge are useful in distinguishing electrons from hadrons. Figure 9 shows the average ionization observed for electrons and for pions in the 5 GeV test beam as a function of arrival time. The peak at short times is due to ionization left in the amplification stage; the excess energy for electrons at long times is due to the conversion of transition-radiation X-rays near the start of the conversion stage. The total energy deposited by 5 GeV electrons exceeds that deposited by pions of the same energy because of the transition-radiation X-rays and the relativistic rise of the specific ionization.

The outer support cylinder of each of the TRD units is a 1.1 cm thick plastic honeycomb with fiber-glass skins. Kevlar end-rings support the cathode structures. The radiator section is enclosed in a carbon-fiber tube with end flanges made of Rohacell with carbon-fiber skins. The radiator and detector volumes are separated by a pair of 23 μm windows. Dry CO_2 gas flows through the gap between these two windows to keep the nitrogen in the radiator from leaking into the detector volume and polluting the recirculating chamber gas, a mixture of $Xe(91\%)/CH_4(7\%)/C_2H_6(2\%)$. These windows must be thin to minimize the attenuation of the low-energy transition- radiation X-rays. The outer window is aluminized and serves as a high-voltage cathode for the drift field in the conversion stage of the detection chamber. The windows are kept accurately cylindrical by maintaining small

pressure differences between the radiator, gap, and detector volumes.

The 15 mm conversion stage and the 8 mm amplification stage of the X-ray detector are separated by a cathode grid of 70 μm gold-plated tungsten wires. The outer cathode of the amplification stage is made of helical copper strips deposited on Kapton foil. The anodes of the amplification stage are 30 μm gold-plated tungsten wires (parallel to the chamber axis), separated by 100 μm gold-plated copper/beryllium potential wires. Each TRD chamber has 256 anode readout channels. The outer chamber has 512 anode wires to keep the basic electrostatic cell approximately 'square', but the wires are ganged together two-by-two into 256 readout channels. There are also 256 helical cathode strips in each chamber, with pitch angles between 24° and 47°. The thickness of the full TRD at θ=90° is 8.1% of a radiation length and 3.6% of an interaction length.

2.4 Central Drift Chamber (CDC)

The Central Drift Chamber[9] provides coverage for tracks at large angles, after the TRD and just prior to their entrance into the Central Calorimeter. The CDC is a cylindrical shell of length 184 cm and radii between 49.5 and 74.5 cm. Figure 10 shows an end view of the CDC. It consists of four concentric rings of 32 azimuthal cells per ring. Each cell contains seven 30 μm gold-plated tungsten sense wires, read out at one end, and two delay lines located just before (after) the first (last) sense wires, each read out at both ends. Adjacent wires within the cell are staggered in ϕ by $\pm$ 200 μm to remove the left-right ambiguity at the cell level. In addition, alternate cells in radius are offset by one half cell to further aid in pattern recognition. The maximum drift distance is $\sim$ 7 cm.

The chamber construction[19] is modular; 32 separate identical modules are assembled into a single cylinder as indicated in Fig. 10. Each module is made from a set of Rohacell structural members ('shelves') covered with epoxy-coated Kevlar cloth and wrapped with a double layer of 50 μm Kapton. Grooves are cut into each shelf at the azimuth corresponding to the sense wire locations to accomodate a teflon tube containing a delay line. Resistive strips are screen-printed on the cathode surfaces to provide the field shaping for the cells. The separate modules are positioned within a single support cylinder. The inner surface is a composite carbon fiber/Rohacell tube to minimize conversions. The outer cylinder is 0.95 cm aluminum and serves as the main support for the full CD. A precision-machined end plate contains oval openings into which the plugs containing the sense and potential wires are fastened. In its final configuration, the CDC wire tension load is wholly transferred to this end plate and the wire alignment is controlled by the end plate.

The delay lines embedded in the inner and outer shelves of each cell propagate signals induced from the nearest neighboring anode wire; measurement of the difference of arrival times at the two ends permits location of the track along the z-coordinate. Surrounding the first and last anode wires, an additional grounded potential wire is added to the usual

pair of potential wires between anodes (see Fig. 10) to minimize the signal induced upon the delay line from inner sense wires. The inductive delay lines are constructed by winding a coil on a carbon fiber epoxy core. Propagation velocities are $\approx$ 2.35 mm/ns; the ratio of delay time to rise time is about 32:1.

The CDC is operated with $Ar(92.5\%)CH_4(4\%)CO_2(3\%)$ gas with 0.5% H_2O. Irradiation of a sample cell of the CDC using a Co^{60} source has shown that the chamber is stable for collected charges on the anode wires of up to 0.35 C/cm. With a drift field of 620 V/cm (in the region where dv_{drift}/dE is negative), the drift velocity is about 34 μm/ns. The voltages on the outer sense wires are raised with respect to the inner sense wires to induce larger delay line signals. The gas gains are 2×10^4 for the inner sense wires (6×10^4 for the outer anodes) for the standard voltage settings of 1.45 kV (1.58kV). The grounded potential wires are provided with current monitoring so that abnormal conditions can generate a voltage trip. Individual cell high voltages can be remotely turned off using a set of relays mounted in the detector platform.

A single layer scintillating fiber detector for spatial calibration was installed between the CDC and surrounding Central Calorimeter covering about 1/32 of the full azimuth. The 128 individual fibers are 1 mm in diameter and are aligned parallel to the beams; optical readout is made with a multi-anode photomultiplier tube. Individual particle traversals are recorded with about 30% efficiency; the struck fiber can be used in conjunction with the measured CDC drift time to improve knowledge of the drift time *vs.* distance relation and to regain the calibration constants rapidly upon change of operating conditions.

2.5 Forward Drift Chambers (FDC)

The Forward Drift Chambers[9] [20] extend the coverage for charged particle tracking down to $\theta \approx 5^\circ$ with respect to both emerging beams. As shown in Fig. 3, these chambers are located at either end of the concentric barrels of the VTX, TRD, and CDC and just before the entrance wall of the end calorimeters. They extend to somewhat smaller radii than the large angle chambers ($r \leq 61$ cm) to allow passage of the cables from the interior chambers.

Each FDC package consists of three separate chambers: the Φ module whose sense wires are radial and measure the ϕ coordinate, sandwiched between a pair of Θ modules whose sense wires measure (approximately) the θ coordinate. Figure 11 indicates the sense wire orientations for each of these modules. The Φ module is a single chamber containing 36 sectors over the full azimuth, each with 16 anode wires along the z-coordinate traversed by particles. Each Θ module consists of four mechanically separate quadrants, each containing six rectangular cells at increasing radii. Each cell contains eight anode wires in z; the sense wires in the three inner cells are at one edge of the cell so that the electrons drift in just one direction (removing the left-right ambiguity). Each Θ cell is equipped with one delay line

of identical construction to the CDC in order to give local measurement of the orthogonal coordinate. All adjacent anode wires (in z) of both Φ and Θ modules are staggered by ± 200 μm to help resolve ambiguities. The upstream and downstream Θ modules are rotated by 45° in ϕ with respect to each other. The maximum drift distance is 5.3 cm.

The Φ chamber electrostatic environment is determined by a single grounded guard wire between anodes. The cell walls are etched 25 μm aluminum strips on 125 μm G-10 to form the field shaping electrodes. The front and back surfaces are Kevlar coated Nomex honeycomb with copper traces on Kapton. The Θ module electrostatic cell employs two grounded guard wires between adjacent anodes, similar to the CDC construction. The front and back surfaces of the Θ cells are Kevlar-coated Rohacell with copper traces on Kapton giving the field shaping electrodes. The side walls are 200 μm aluminum foil on Nomex honecomb.

The FDC chambers are operated with the same gas as the CDC, with similar values of the drift field and gas gain. The maximum drift time at the outer portion of the Φ chamber is 1.5 μs.

2.6 Central Detector Electronics

The electronics for reading out signals from the Central Detectors are almost the same for all CD devices. There are three stages of signal processing: the preamplifiers mounted directly on the chambers themselves, the shapers located in the detector platform, and the flash ADC digitizers located in the MCH. Subsequent digital signal handling is considered part of the data acquisition system.

The sense wire, TRD cathode strip and CDC/FDC delay line preamplifiers are based upon the Fujitsu MB43458 quad common base amplifier[21] available in a surface mount package. The full CD requirement for the DØ tracking and TRD detectors is 6080 channels. The preamplier gain is 0.3 mV/fC. Rise and fall times are 5 ns and 34 ns respectively. Input noise is 2300 electrons for a detector input capacitance of 10 pF. Eight hybridized channels are mounted in a 28-pin DIP package. Provision is made for test pulse charge injection to the preamplifer inputs for calibration purposes.

The preamp output signals are carried via coaxial cables of length about 15 m to the shaping circuits[22] . The shaper contains a video amplifier, a two-zero three-pole shaping circuit, and a cable driver. The gain and shaping components are mounted on separate header boards so that the detailed shaping needs for each detector and for cable matching can be accomodated.

The shaper output signals are transported over 45 m on 75 Ω coaxial cables to the MCH where digitization occurs. Figure 12 shows the block diagram for the CD digitization electronics, which consists of three main sections. Design of this system was refined on the basis of early studies using prototype tracking chamber models and a flexible waveform

digitization readout system[10] . The input signals enter an analog buffer amplifer circuit[23] in which voltage offset and gain corrections are made using stored digital information for each channel. The gain correction is such that large signals are amplified by a factor of about 8.5 less than small signals, thus expanding the dynamic range of the device by a factor of about 3, or from 8 to an effective 9.5 bits. Studies[10] [24] on prototype chambers showed that this extended response makes considerable improvement in the dE/dx capability of the system.

The gain corrected signals are input to the flash ADC section, based on the SONY eight bit FADC part CX20116, operated at 106 MHz. Typical FADC outputs are shown in Fig. 13. The digitized data from the FADC are stored in a FIFO circuit, pending decision to proceed with processing from the trigger system.

Since the full cell chamber drift times occupy up to 256 FADC samplings and triggered events can occur at approximately 200 Hz, the resulting data load would be of order 325 Mbyte/s if no data compression were applied. This load would exceed the capability of the data acquisition data highways, and thus zero suppression is required. It is performed in the final section of the digitization process, based on a custom made Application Specific Integrated Circuit (ASIC) designed at Fermilab[25] and manufactured by Intel, Inc. The Zero Suppression (ZSP) circuit operates at 26.5 MHz on 4 byte words and hence is able to process data in real time. It examines the sequence of digitized charges and adjacent FADC bucket charge differences . Digitizings are saved between the leading edge and trailing edge of a signal; leading and trailing edges are defined by one of several algorithms based on digitized charges or charge differences over threshold.[26] Thresholds are determined by real-time settable registers. Figure 14 shows a schematic version of a pulse train from the FADC and illustrates the quantities (signal amplitudes B_i and adjacent bin differences D_i) used for defining a sequence of interesting FADC digitiztions.

The three sections of the FADC/ZSP circuit are packaged on a single VME 9U card. Each card contains 16 channels.

2.7 Central Detector Performance

All DØ tracking detectors have been operated in both particle beams and cosmic rays; descriptions and more detail on performance can be found elsewhere[9] [10] [11] [12] [20] . Correction of these detectors for gas content and atmospheric conditions in the full experiment has been assisted by the use of special monitoring 'canary' chambers external to the detector. Separate canaries are operated on the full gas system for the VTX, TRD, and CDC/FDC[27] .

Figure 15 shows the efficiency for finding hits in the VTX chamber as a function of high voltage. The more rapid rise to full efficiency is accomplished with lower thresholds applied in the FADC hit-finding algorithms; the penalty is an increase of the number of

multiple hits found. Figure 16 shows the hit-finding efficiency *vs.* high voltage for the FDC.

Spatial resolutions for the tracking chambers are shown in Figs. 17, 18, 19, taken from test beam studies with the final detectors. For the VTX chamber[12] , resolutions were based on the deviation of a particular hit from the expected value based on its neighbors. Corrections for drift velocity variation across the cell have been made in the VTX analysis. The CDC and FDC resolutions are obtained from the deviation of a particular hit from the full track in the chamber. In Figs. 18 and 19 for the CDC and FDC, the point for which resolution is measured was included in the fit; if excluded, the resolutions degrade by about 10%. Resolutions of (typically) 50 μm are seen for the VTX chamber; the resolutions in the CDC and FDC vary between 150-200 μm.

Pulse pair resolutions are important in the non-magnetic environment of DØ. Figures 20 and 21 show the efficiency for resolving two hits as a function of their time separation. These data result from off-line superposition of single track test beam data. For the VTX, 90% efficiency for 2-hit resolution is achieved for 0.63 mm separation; for the FDC (or CDC), 90% efficiency is reached for a $\simeq$2 mm separations[28] .

The delay lines used in both CDC and FDC have been studied using cosmic ray data. The coordinate along the delay line is determined from the time differences at the two ends. Propagation velocities were determined in a special calibration fixture and corrected using test beam data. Single delay line position resolution for the FDC is measured to be $\sigma_z \simeq 4$ mm. The CDC delay lines have been shown[19] to have $\sigma_z \simeq 2$ mm when fitting to the 8 delay lines along a track. The z-resolution from charge division in the VTX was measured in a prototype chamber[11] to be better than 1% of the wire length or $\approx$ 1 cm.

It is important for the DØ tracking chambers to distinguish an unresolved overlay of two tracks (e.g. from γ-conversions) from a single track. Figure 22 shows the ionization distributions for one and two track traversals of a single cell (2 track events are made by offline overlay of single track events). In Fig. 22, the ionization signal is taken to be the sum of the smallest 70% of the hits participating in the track; this procedure reduces the effects of delta-ray production[27] . Studies using the FDC[20] show an energy loss resolution of 13.3% for single tracks. Studies using the CDC and VTX show rejection factors for two overlapped tracks in the range of 75-100 for 98% efficiency for retaining single tracks.

The ability of the TRD to discriminate electrons from hadrons has been studied in some detail in test beams[16] [18] and the results compared to a detailed Monte Carlo calculation[29] . Measures of the difference between electron and hadron include the total collected charge on anode wires, the number of charge clusters, and the position of clusters determined through the time of arrival at the anodes. Figure 23 shows the observed energy distribution, summed over all three TRD layers, for pions and electrons. Use of total energy alone allows a rejection factor of about 10 for pions while retaining 90% of the electrons. The distribution of the likelihood function,

$$\mathcal{L} = \sum_{i=1}^{3} \ln\left((P_e(E_i)/P_\pi(E_i)\right)$$

is shown in Fig. 24; the probablities for a given energy in layer i are based upon the observed total energy and number and position of clusters. Figure 25 shows the pion rejection factor as a function of electron inefficiency for particle incidence angles of 90° (normal) and 50°. Pion rejections of approximately 50 are found for 90% efficiency for electrons in this analysis using the likelihood function. The rejection factors are better at non-normal incidence, in part because of the increased path length and in part due to space charge distortions at normal incidence induced by pile-up of all ionization along a particular track.

3. Calorimeters

3.1 Calorimeter Design Issues

The calorimeter design[1] [30] is crucial for the optimization of the DØ detector. Since there is no central magnetic field, the calorimetry must provide the energy measurement for electrons, photons and jets. In addition, the calorimeters play important roles in the identification of electrons, photons, jets and muons, and in establishing the transverse energy balance in an event. Early in the design phase, the decision was taken to employ liquid argon as the active medium to sample the ionization produced in electromagnetic or hadronic showers. This choice was supported by the unit gain of liquid argon, the relative simplicity of calibration, the flexibility offered in segmenting the calorimeter into transverse and longitudinal cells, the good radiation hardness, and the relatively low unit cost for readout electronics. Factors weighing against the choice of liquid argon included the complication of cryogenic systems; the need for relatively massive containment vessels (cryostats) which give regions of uninstrumented material; and the inaccessibility of the calorimeter modules during operation.

Since provision must be made for some degree of access to the Central Detectors within the calorimeter cavity, more than one vessel is necessary. We chose the solution shown schematically in Fig. 26 in which a central calorimeter (CC) covers roughly $|\Delta\eta| \leq 1$ and a pair of end calorimeters, (ECN (north) and ECS (south)), extends the coverage out to $|\eta| \approx 4$. The boundary between CC and EC was chosen to be approximately perpendicular to the beam direction; this choice was shown to introduce less degradation in missing transverse energy ($\not\!\!E_T$) than one in which the EC's nest within the CC shell with a boundary approximately parallel to the beams.

The dimensions of the calorimeters were set by the constraints imposed by the size of the experimental hall, the need for adequate depth to ensure good containment of shower energy, the requirements of magnetic measurement of muon momenta outside the calorimeter, and the need for sufficient tracking coverage in front of the calorimetry. The resulting design has three distinct types of modules in both CC and EC: an electromagnetic section (EM) with relatively thin uranium absorber plates, a fine-hadronic section with thicker uranium plates and a coarse-hadronic section with thick copper or stainless steel plates. Inclusion of the coarse sections allow sampling of the end of hadronic showers while keeping the density high (and hence outer radius small). Except at the smallest angles in the EC, several (16 or 32) modules of each type are arranged in a ring. The modular design provides units of workable size without creating undue complications from degraded response near module boundaries. At $\eta = 0$, the CC has a total of 7.2 nuclear absorption lengths (λ_A); at the smallest angle of the EC, the total is $10.3\lambda_A$.

The a typical calorimeter unit cell is shown in Fig. 27. The electric field is established by grounding the metal absorber plate and connecting the resistive surfaces of the signal boards to a positive high voltage (typically 2.0 - 2.5 kV). The electron drift time across

the 2.3 mm gap is $\approx$ 450ns. The gap thickness was chosen to be large enough to observe minimum ionizing particle signals and to avoid fabrication difficulties.

Different absorber plate materials were used in different locations. The EM modules for both CC and EC used nearly pure depleted uranium[31] ; the thicknesses were 3 mm and 4 mm respectively (production difficulties with the larger EC plates necessitated the thicker plates). The fine hadronic module sections have 6 mm thick uranium-niobium (2%) alloy[31] . The coarse hadronic module sections contain relatively thick (46.5 mm) plates of either copper (CC) or stainless steel (EC). Electrical connections to all absorber plates were made by percussive welding of thick niobium wires to the edges of the plates. This technique proved to be simple and very reliable. The density of these (ground) connections is about 1 for every 2 - 4 signal connections.

To avoid breakdown across the gap, absorber electrodes must have relatively smooth surfaces. The surface treatment of the uranium plates evolved as manufacturing experience was gained. Although oxidation in air was not generally a problem, care had to be taken to avoid oxidation of the uranium through the reaction $U + 2H_2O \rightarrow UO_2 + 2H_2$ which is strongly suppressed by the presence of oxygen[32] . For the earlier production of the CC uranium, surfaces were cleaned by mechanical abrasion. Subsequently, EC plates were cleaned using jets of high pressure hot water. Most surfaces remained free of excessive oxidation, although some unexplained centimeter-scale patches of oxide appeared on a small number of plates. These were removed when possible since the oxide is sufficiently conducting to give unwanted current draw in a module.

Signal boards for all but the EM and small-angle hadronic modules in the EC were constructed by laminating two separate 0.5 mm thick G-10[33] sheets. Each signal board had one surface coated with high resistivity (typically 40 M$\Omega/\square$) carbon-loaded epoxy[34] . One of the inner surfaces was left with bare G-10 on the uncoated side; the other sheet, originally copper-clad, was milled into the pattern desired for the segmented readout. Several such pads at approximately the same η and ϕ are ganged together in depth to form a readout cell. Details of signal ganging to make the readout cells vary from module to module.

The two smallest angle modules in each EC have the added problem that even small gaps between neighboring azimuthal sectors would give undesired dead regions. Thus, the signal boards for these monolithic modules were made from multilayer printed circuit boards. The outer surfaces were coated with the same resistive epoxy as for the other signal boards. Etched pads on an interior surface give the desired segmentation. Signal traces on another interior surface bring the signals to the outer periphery. The pad and trace layers are connected by plated-through holes. The signals from these multilayer boards in the electromagnetic (ECEM) and the small angle hadronic (ECIH) modules were ganged together along the depth of the modules using solder-tail header connectors and kapton printed circuit lines. In the ECIH module, the ganged signals were brought to the rear plate of the module using twist and flat ribbon cable.

In all other modules, ganging connections were made using insulation displacement connectors (IDCs) and solid wires. This technique proved to be very reliable: there are no observed IDC failures with approximately 500,000 connections in the installed modules.

The pattern and sizes of readout cells were determined from several considerations. The transverse sizes of the cells were chosen to be comparable to the transverse sizes of showers: ~1-2 cm for EM showers and ~ 10 cm for hadronic showers. The variables more directly useful for physics are $\Delta\eta$ and $\Delta\phi$; the scale is set by the typical size of parton jets, $\Delta R = \sqrt{\Delta\eta^2 + \Delta\phi^2} \sim 0.5$. Segmentation finer than this is useful in probing the shape of jets. Longitudinal subdivision within the EM, fine hadronic and coarse hadronic sections is useful since the longitudinal shower profiles help distinguish electrons and hadrons. Variations in cell capacitance cause changes in the pulse rise time but the sampling of signals occur at fixed time intervals synchronized to the accelerator bunch crossing time ($\Delta t = 3.5\mu$s). This implies that each readout cell, with associated cabling, should have a capacitance that does not exceed 5 nF.

The final design was chosen to have a 'pseudo-projective' set of readout towers, with each tower subdivided in depth. The term pseudo-projective refers to the fact that the *centers* of cells of increasing shower depth lie on rays projecting from the center of the interaction region, but the cell boundaries are aligned perpendicular to the absorber plates. Figure 28 shows a portion of the DØ calorimeter segmentation pattern. There are 4 separate depth layers for the EM modules in CC and EC. The first two layers are typically 2 radiation lengths (X_0) thick and are included to help measure the longitudinal shower development near the beginning of showers where photons and π^0s differ statistically. The third layer spans the region of maximum EM shower energy deposits and the fourth completes the EM coverage of approximately 20 X_0. The fine hadronic modules are typically segmented into 3 or 4 layers; coarse hadronic modules are ganged into one or three layers. Typical transverse sizes of towers in both EM and hadronic modules are $\Delta\eta = 0.1$ and $\Delta\phi = 2\pi/64 \approx 0.1$. The third section of EM modules is twice as finely segmented in both η and ϕ to allow more precise location of EM shower centroids. Inter-module gangings are provided in the early stages of the front-end electronics (prior to digitization) in order to join segments of cells which cross EC and CC module boundaries.

3.2 Central Calorimeter

The central calorimeter (CC) shown in Fig. 29 comprises three concentric cylindrical shells. There are 32 EM modules in the inner ring, 16 fine hadronic (FH) modules in the surrounding ring, and 16 coarse hadronic (CH) modules in the outer ring. The end view of the CC in Fig. 29 shows that the EM, FH and CH module boundaries are rotated so that no projective ray encounters more than one intermodule gap.

Figure 30 shows a schematic view of a CC module. Each is made by loosely stacking

the alternating absorber plates and signal boards within a stainless steel welded box structure consisting of perforated side skins, somewhat thicker front and back walls, and thick machined end plates. Delrin spacers inserted through holes in the signal boards extend 2.3 mm on one side and 1.5 mm on the other side of the boards. Adjacent spacers have opposite long and short segments so that the boards have some freedom to flex in response to mechanical and thermal stresses. The absorber plates are prevented from movement along the long axis of the modules by keys on the side skins.

The end plates serve as the support members for the modules in the ring structure. Large fasteners are bolted on, linking adjacent endplates into the cylindrical rings. Support for the CC is transmitted to the underlying detector platform through four feet which pass through the cryostat vessel to a supporting cradle. Flexible support stanchions transfer the load from the inner cold vessel to the outer room temperature vacuum vessel.[35] .

The CCEM modules have four longitudinal gangings of signals of approximately 2.0, 2.0, 6.8, and 9.8 X_0, with transverse segmentation as described above. The ganged signals from the pads making up a particular readout cell are collected on special readout boards located just behind the signal boards of a given depth and are transmitted along the length of the module to connectors at the end plates. The total number of signals for the 32 modules is about 10,400, spanning 24 $\Delta\eta = 0.1$ towers along the 260 cm length. A full module comprises 20.5 X_0 and 0.76 λ_A and weighs 0.6 metric tons.

The CCFH modules have three longitudinal gangings of approximately 1.3, 1.0 and 0.9 λ_A. The CCCH modules contain just one depth segment of 3.2 λ_A. The signal collection scheme is similar to that for the CCEM modules. The CCFH (CCCH) modules weigh 8.3 (7.2) metric tons; the full rings provide about 3500 (770) signals. The total weight of the CC modules and their support structure is 305 metric tons, with an additional 26 metric tons contributed by liquid argon.

3.3 End Calorimeters

The two mirror-image end calorimeters (ECN and ECS) contain four module types as shown in Fig. 26 and Fig. 28. To avoid the dead spaces in a multi-module design, there is just one EM module and one inner hadronic (IH) module, shown schematically in Fig. 31. Outside the EM and IH, there are concentric rings of 16 middle and outer (MH and OH) modules. As seen in Fig. 32, the azimuthal boundaries of the MH and OH modules are offset to prevent cracks through which particles could penetrate the calorimeter.

The ECEM modules[36] [37] contain four readout sections (0.3, 2.6, 7.9, and 9.3 X_0) with outer radii varying between 84 and 104 cm and inner radius of 5.7 cm. The material of the cryostat wall brings the total absorber for the first section up to about 2 X_0. The alternating absorber plates and signal boards of the ECEM modules were stacked on both sides of a thick stainless steel support member whose thickness in radiation lengths

is equivalent to a uranium plate. Each circular absorber plane consisted of three separate uranium plates. As indicated in Fig. 33, a collection of tie-rods and spacers position the assembly of absorber plates and signal boards from the surface of a 'central support plate'; the weight of the absorber plates is supported from the central support plate by a central support tube. Each ECEM module weighs 5 metric tons and provides 7488 signals.

The two ECIH modules are cylindrical, with inner and outer radii of 3.92 and 86.4 cm. The fine hadronic portion consists of four readout sections, each containing sixteen 6 mm semicircular uranium plates (1.1 λ_A each). Alternate plates have their boundary rotated by 90° to avoid through-going cracks. The coarse hadronic portion has a single readout section containing thirteen 46.5 mm stainless steel plates (4.1 λ_A). The full ECIH module weighs 28.4 metric tons and provides 5216 signals.

Each of the ECMH modules has 4 fine-hadronic (uranium) sections of about 0.9 λ_A each and a single coarse-hadronic (stainless steel) section of 4.4 λ_A. Signal boards are similar to those used in the CC. Signals are brought to the azimuthal boundaries where they are ganged by short jumper cables to make the pseudo-projective cells. Each ganged signal is transported to a connector located at the rear of the module. ECMH module weights are 4.3 metric tons; there are 1856 signals in an MH ring.

The ECOH modules employ stainless steel plates inclined at an angle of about 60° with respect to the beam axis as shown in Fig. 28. Module weights are 5.5 metric tons; a full ring has 960 signals.

The ECOH module ring forms a support platform for the remaining EC modules. Inconel 718 and 304 stainless steel studs are inserted into ears on the stainless steel plates near the front and rear of OH modules to fasten together adjoining modules. The ring of ECMH modules resting within the OH ring supports both the ECIH and ECEM module. The OH ring load is transferred via a beam and strap assembly to four bosses and through the cryostat on flexible stanchions as for the CC calorimeter described above. The overall EC calorimeter weighs about 238 metric tons.

3.4 Intercryostat Detectors and Massless Gaps

As shown in Fig. 28 , the region $0.8 \leq |\eta| \leq 1.4$ contains a large amount of uninstrumented material in the form of cryostat walls, stiffening rings, and module endplates. The material profile along a particle path varies rapidly with rapidity through this region. To correct for energy deposited in the uninstrumented walls, we have built two scintillation counter arrays called intercryostat detectors (ICD) that are mounted on the front surface of the ECs (see Fig. 28). Each ICD consists of 384 scintillator tiles of size $\Delta\eta = \Delta\phi = 0.1$ exactly matching the liquid argon calorimeter cells. In addition, separate single-cell structures called massless gaps also shown in Fig. 28 are installed in both CC and EC calorimeters. One ring with standard segmentation was mounted on the end plates

of the CCFH modules (320 channels); additional rings were mounted on the front plates of both ECMH and ECOH modules (192 channels). Together, the ICD and massless gaps provide a good approximation to the standard DØ sampling of EM showers.

The ICD tiles are constructed from Bicron BC-414 scintillator[38] into which three or four 3 mm grooves are milled. Two millimeter diameter bundles of 200 μm polystyrene wavelength-shifting scintillating fibers are epoxied into these grooves to collect the light and carry it through a 180° bend to phototubes mounted just behind the tile. Figure 34(a) shows the arrangement of fibers in a scintillator tile. Tests have shown that the collected light is uniform across the face of a tile to within about 10%. The tiles are packaged into light-tight boxes containing three tiles at fixed ϕ as shown in Fig. 34(b).

The ICD readout uses 1.3 cm diameter phototubes[39] . All tubes were subjected to extensive testing and burn-in to reduce subsequent failures and to provide matched triplets to be installed in a given box with a common high voltage supply. The overall combination of scintillator, wavelength shifter and phototube gave approximately 20 photoelectrons per minimum ionizing particle for the crucial larger η boxes. Since the typical number of particles crossing a given tile in a typical high-p_T 2-jet event is of order 25, the signals from the ICD are quite large. Relative calibration of the ICD response is maintained using optical fibers which distribute light from a UV laser to each separate tile.

3.5 Cryogenic System

Three separate double-walled stainless steel cryostats enclose and support the DØ calorimeters as shown in Fig. 28. The outer diameter of these vessels is 518 cm; CC and EC cryostats are approximately 306 and 263 cm long, respectively. Forty layers of superinsulation fill the vacuum space between inner and outer shells. The torospherical ends of each cryostat can be cut off (and subsequently rewelded) to give access to the interior volume for module assembly. Each cryostat has four 20-cm diameter ports for the passage of signal cables. In addition, each vessel has two smaller ports for the penetration of the high voltage, temperature and purity monitoring cables. Four feet support each cryostat and its modules upon an external cradle. These feet[35] are specially constructed from low thermal conductivity laminations and are also capable of flexing to accomodate the displacements induced during calorimeter cool-down.

The main ring beam passes through the three cryostats near the outer radius of the vessels; the Tevatron beams pass through the EC vessels on the centerline. Bellows are incorporated in these penetrations to accomodate the thermal and differential pressure motion of the ends of the vessels to which they are welded.

The front heads of the EC cryostats are specially designed to provide both strength and minimum material in front of the EM module. A small radius convex (thin) spherical section is joined to a large radius (thick) concave annulus at a stiffening ring located

between ECEM and ECMH modules. The EC cryostats have inner cylindrical surfaces attached to the rest of the vessel through a flexible stainless steel bellows; this permits the needed flexibility of motion needed near the beam pipe. Special rotating cryogenic supply tubes were designed to allow retraction of the ECs to give access to the tracking detectors.

Each calorimeter has three finned-tubing cooling coils which are located near the top of its cryostat. Independent liquid-nitrogen flow control is provided for the topmost coil, intended for steady-state operation; the two symmetrically located lower coils are used only for calorimeter cooldown. Temperature monitors are mounted at many locations on modules and cryostat walls. A maximum 50 K difference between any two monitors is imposed during cool-down. Cooling to liquid argon temperature (78 K) occurs in approximately 10 days. Once cool, argon is introduced in part by means of liquid transfer from a 20,000 gallon argon storage tank at approximately the same elevation as the calorimeters and in part by condensation of gaseous argon using the cooling coils. Rapid transfer of the full load of liquid between storage dewar and cryostats is possible (in about 8 hours) using modest gas pressures. Such empty and fill operations occur after each move of the detector between collision hall and assembly hall. The system has been designed to warm up in about six weeks.

An inventory of 20,000 gallons of liquid argon is maintained in the cryostats and in the storage dewar. Argon purchases specify an O_2 contamination of less than 0.6ppm. Each cryostat and storage dewar is equipped with four argon-purity monitoring detectors[40] . Each such device contains a radioactive β source, triggered so as to give full traversal of a standard argon gap by the β-particle. In addition, there is a cell equipped with an α source. The dependence of α and β signals on applied voltage is a sensitive indicator of the equivalent oxygen content of the argon[41] . Independent measures of oxygen and nitrogen contaminations are obtained using standard gas monitors. We have observed that the response of test cells, as well as of the calorimeters, drops less than 0.5% over the course of many months of operation.

3.6 Calorimeter Readout Electronics

Signals from the calorimeter modules are brought to the four cryostat feedthrough ports by specially fabricated Tefzel[42] insulated 30 Ω coax cables. These cables are connected to multilayer printed-circuit feedthrough boards located above the liquid level in each feedthrough port. Eight T-shaped, 27-layer feedthrough boards penetrate each port and provide a re-ordering of signals between the module-oriented input side and the $\eta - \phi$ order appropriate to analysis on the output side.

Short cables connect the output from the feedthrough boards to charge-sensitive hybrid preamplifiers[43] [44] [45] [46] mounted in four enclosures on the surface of each cryostat, near the ports. The schematic diagram for the calorimeter preamplifiers is shown in

Fig. 35. A single 2SK147 Toshiba j-FET with $g_m \sim 0.05\Omega^{-1}$ is used at the input. The equivalent noise density is $e_n = 0.46\ nV/\sqrt{Hz}$. Preamplifiers with two different gains were made (equivalent full scale gains of about 100 and 200 GeV) to provide full dynamic range response. Variation in the gains of the preamps was controlled to within about 0.5%.

Output signals from the preamplifiers are transported on twisted pair cable some 30 m to baseline subtractor (BLS) shaping and sampling hybrid circuits[43][44][45] [46] ; input signals are integrated (430 ns) and differentiated (33 μs). Figure 36 shows the schematic diagram of the BLS. Signals from portions of logical cells that straddle the CC-EC boundary are merged at the BLS input. At the input to the BLS, a portion of the signal is extracted with $\simeq$ 100 ns rise time and added into trigger towers of $\Delta\eta = \Delta\phi = 0.2$ for use in event selection. The main signals are sampled just before a beam-crossing and 2.2 μs after; the difference is provided as a *dc* voltage proportional to the collected charge. Two storage capacitors for each channel allow double buffering at the analog level. Fast baseline restoration occurs in a few μs so as to minimize the effects of event pile-up. Figure 37 shows the equivalent signal after BLS sampling and difference.

Depending on signal size, the BLS outputs can be amplified by 1 or by 8 so as to reduce the dynamic range requirements of the subsequent digitization. A bit is set to record the chosen amplification; there is special provision for forcing a specific amplification (or both) for calibration purposes. The BLS outputs are multiplexed 16-fold onto the crate backplane, and each channel is sent in serial time slices over 50 m twisted pair cables from the detector platform to the MCH.

The 24-channel 12-bit ADC circuits[43][44][45] [46] in the MCH, together with the $\times 1$ or $\times 8$ amplifier allows an overall dynamic range of 2^{15}. Each time-slice of each channel is digitized in about 10 μs, yielding a total digitization time of 160 μs for 384 signals. Gain parameters are set so that about 3.75 MeV of deposited energy correponds to one least count. Minimum ionizing particles deposit between 8 (EM1) and 90 (FH1) MeV in the layers of the calorimeters. Channels which have an absolute difference of signal and pedestal below an adjustable threshhold can be suppressed from the readout buffer.

Both single-channel random noise (electronics and uranium radioactivity) and multi-channel coherent noise have been measured in beam tests and in the DØ Hall. The single channel noise can be characterized as $2000 + 3100 \times C(nF)$ electrons. For many channels, the total random noise varies with $\sqrt{N}$, where N is the number of channels included; the total coherent noise varies typically as N. A useful measure of coherent noise is the number of channels that can be summed before the coherent noise exceeds the random noise. In the DØ environment this number is typically >5000 channels[47] .

Calibration of the various components of the electronics is accomplished by a precision pulser[48] which injects charge through a large accurately known resistor at the front end of each preamplifier. The pulse distribution system has been carefully designed to deliver equal pulses at each input. A range of attenuator settings can be programmed to allow calibration over the full dynamic range of the system. Precision and stability of the

calibration system have been demonstrated to be better than 0.25%.

3.7 Calorimeter Performance

The DØ calorimeters have been tested in a variety of ways. Prototype studies in test beams[49] [50] [51] [52] have verified performance goals and led to the optimization of the design. Subsequent beam tests involved combinations of the CCEM/CCFH and ECMH modules[53] [54] [55] [56] as well as the ECEM/ECIH modules[36] [37] [57] [58] [59] [60] [61] . The full CC calorimeter was tested using cosmic rays before the detector moved to the beam line[62] . Details of these measurements can be found in the references.

The response of the ECIH module as a function of high voltage for 100 GeV pions and electrons is shown in Fig. 38. For comparison, the response of the test cell to β particles is also shown. The three distributions are similar and the slope of the plateau is small, characteristic of oxygen contamination below 1.0 ppm. Small differences between electrons and the β cell are seen due to effects of induced voltages on the module uranium surfaces. Electron and pion responses can differ due to the presence of heaviliy ionizing components in hadron showers.

Extensive studies of the performance of modules were made using pions and electrons with energies between 10 and 150 GeV[63] . Figure 39 shows the response to 100 GeV pions in the ECEM/ECIH. The low energy excess seen in the distribution is due to upstream interactions in the beam and cryostat materials and can be eliminated by requiring that $\leq$ 0.4 GeV be observed in the first EM layer. Electron distributions are essentially Gaussian. The response to both electrons and pions is linear with beam energy to within 0.5%. The longitudinal profile of the energy deposited by pions is shown in Fig. 40.

Energy resolution for electrons and pions obtained after subtraction of pedestals, and after corrections for gain variations and beam particle momentum (of the order of 1%), are shown in Figs. 41 and 42. The relative resolution as a function of energy for the ECEM and ECMH modules can be parametrized as

$$(\sigma_E/E)^2 = C^2 + S^2/E + N^2/E^2,$$

where the constants C, S, and N represent the calibration errors, sampling fluctuations and noise contributions respectively. We obtain $C = 0.003 \pm 0.002$ and $S = 0.157 \pm 0.005\sqrt{GeV}$ for electrons in ECEM and $C = 0.032 \pm 0.004$ and $S = 0.41 \pm 0.04\sqrt{GeV}$ for pions in ECMH. The noise contribution is dominantly due to uranium radioactivity, and is consistent with our previous discussion of random and coherent noise.

The calorimeter position resolution is important for identification of backgrounds to electrons from the near-overlap of photons and charged particles. Figure 43 shows the position resolution for 100 GeV electrons determined from comparison of the test beam track and the energy-weighted position of the shower determined solely from ECEM layer 3. This resolution varies between 0.8 and 1.2mm over the full range of impact positions; the position resolution varies approximately as $E^{-\frac{1}{2}}$.

A good measure of the sensitivity of the calorimeters is their response to muons. Figure 44 shows the energy seen in the CCFH layer 1 in a tower centered a cosmic ray track. The noise contribution indicated is deduced from the signal observed in an equivalent road perpendicular to the track. A three standard deviation suppression on the noise signal is applied to the data.

The resolution and linearity obtainable in the calorimeter is closely related to the ratio of response of electrons and pions[64] . Figure 45 shows this ratio for the ECEM/ECIH data. Corrections have been been applied for effects due to out-of-time event pileup, early showering, and energy deposition outside the $\Delta\eta \times \Delta\phi$ region used to sum the energies. The e/π response ratio falls from about 1.11 at 10 GeV to about 1.04 at 150 GeV.

Correction procedures have been developed to account for energy lost within uninstrumented material in module walls and cryostats. Figure 46 (a) shows a scatter plot of total energy (EM + hadronic) *vs.* position across the boundary between two adjacent CCEM modules near $\eta = 0$. The dip at x=0 corresponds to the intermodule crack. Using the full energy correlation matrix[65] and the observed energy deposits in the neighboring modules, a predicted correction[66] for the energy deposits in the dead material can be made. Figure 46(b) shows the distribution after applying this correction. A similar technique has been developed[67] [68] for using ICD, massless gaps, and regular calorimeter deposits to correct for the losses in the thick CC and EC cryostat walls in the range $0.8 \leq |\eta| \leq 1.4$. Energy depositions with and without the ICD/massless gap corrections are shown in Fig. 47.

4. Muon Detection

4.1 Muon System Design

The DØ muon detection system consists of five separate solid-iron toroidal magnets, together with sets of proportional drift tube chambers (PDT's) to measure track coordinates down to approximately 3°. The purpose of this system is the identification of muons produced in $\bar{p}$-p collisions and determination of their trajectories and momenta. Since muons are measured after most of the debris of electromagnetic and hadronic particle showers is absorbed in the calorimeters, muons can be identified in the middle of hadron jets with much greater purity than electrons.

Since the bend in the toroids ($\vec{B} \sim B_0\hat{\phi}$) is approximately in the $r-z$ plane and the Tevatron interaction region is long ($\sigma_z \approx 30$ cm), it is necessary to measure muon directions both before and after the bend. A closely-spaced set of measurements of the muon track is provided before the toroid and yields the entrance point; two sets of measurements separated by 1 to 3 m after the toroid yield the exit direction. The incident trajectory is determined from a combination of the primary interaction point, the track seen in the central tracking and the first muon chamber track vector. Muons can also be seen in the calorimeter. A comparison of incident and exit muon directions provides the bend angle in the toroid, and hence the momentum. Multiple Coulomb scattering in the iron toroids limits the relative momentum resolution to $\geq 18\%$ up to the limit imposed by the bend coordinate resolution in the PDT's. With final precise alignment of the muon chambers, three standard deviation determination of the sign is expected for $p_T \leq 200$ GeV/c at $\eta = 0$ and $p_T \leq 30$ GeV/c at $|\eta| = 3.3$.

The central toroid (CF) covers the region $|\eta| \leq 1$ and two end toroids (EFs) cover $1 < |\eta| \leq 2.5$. The small-angle muon system (SAMUS) differs somewhat from the larger angle system; the SAMUS toroids fit in the central hole of the EF toroids and cover $2.5 < |\eta| \leq 3.6$. Figure 48 shows the elevation view of the DØ detector with the five toroids and their associated PDT layers indicated. The muon system is quite thick as shown in Fig. 49 and affords a clean environment for identification and momentum measurement of high p_T muons[69] . Figure 50 shows the geometrical acceptance of the muon chamber system. Some loss of acceptance occurs near $|\eta| = 0.75$ due to the CF/EF transition. Apart from gaps caused by various support elements and the need to provide access corridors to the detectors, the coverage for muons is hermetic. The minimum momentum required for a muon to emerge from the iron toroids varies from about 3.5 GeV/c at $\eta = 0$ to about 5 GeV/c at larger η.

The wide angle muon system (WAMUS) provides measurements for all muons traversing the CF and most of those which cross the EF toroids. The WAMUS system consists of 164 distinct proportional drift tube chambers with sizes up to 2.5×5.8 m^2. The WAMUS chamber wires are oriented along the primary $\vec{B}$-field direction to give accurate measurement of the bend coordinate. Each end of the SAMUS system contains three stations with

three planes per station. Figure 51 shows the disposition of these chambers.

4.2 Muon Toroids

The CF toroid[70] [71] , shown in perspective in Fig. 52, is a square annulus 109 cm thick and weighs 1973 metric tons; it is centered on the Tevatron beam lines. The inner and outer surfaces of CF are 317.5 and 427 cm from the beams respectively. In order to give access to the inner portions of the detector, the CF is built in three separate pieces. A middle (bottom) section is a 150 cm wide beam fixed to the detector platform which also provides the support for the enclosed calorimeters and tracking detectors. The CF is completed by two C-shaped shells which can be moved perpendicular to the beams to allow access to interior detectors. The mating surfaces at top and bottom include 4.8 and 3 mm stainless steel spacers respectively, which reduce remanent field and facilitate separation of the sections. Twenty coils of 10 turns each carry currents of 2500 A and excite internal fields of 1.9 T. Since the coils are not symmetrically placed on the CF (there are no coils on the central beam), the fringe fields are moderately strong and exceed 0.01T near the central beam. Leakage represents 3.7% of the total CF flux.

The two EF toroids are located at $447 \leq |z| \leq 600$ cm. Their outer surfaces are at a perpendicular distance of 417 cm. The EF's have a 183 cm square inner hole centered on the Tevatron beams. The main ring beam passes through a 25 cm diameter hole in the EFs. Eight coils of eight turns each carry 2500 A (in series with the CF) and excite fields of up to about 2 T. Each EF toroid weighs 800 metric tons.

Within the inner hole of each EF toroid there is a separate SAMUS toroid. The SAMUS toroids, weighing 32 metric tons each, have outer surfaces at 170 cm from the beam axis and 102 cm square inner hole. Two coils of 25 turns each carry currents of 1000 A. Figure 53 shows a magnetic field contour plot for EF and SAMUS; the field vectors in the two magnets are aligned in the same directions. The EF/SAMUS combinations can be retracted along the beam line by approximately 1 m in order to provide access to the detectors around the interaction point.

A pair of special tungsten-lead collimators were constructed to fill the space between the SAMUS toroid and the Tevatron beam pipe. These collimators intercept beam halo and collision products at small angles and thereby reduce the rate of hits in the small angle muon system. Multiplicities of clusters observed in the A, B and C stations of SAMUS are typically about 9, 5, and 11 per event.

4.3 Wide Angle Muon Chambers

The WAMUS chambers[72] are deployed in three layers: the "A" layer before the iron toroids and the "B" and "C" layers after the magnets. The distance between B and C layers is ≥ 1 m, so that a good measurement of the direction of the muon after the magnet can be made. There are 4 PDT planes in a A layer chamber and 3 PDT planes in the B and C layer chambers. The cell structure for the PDTs is the same for all WAMUS

chambers; the 164 individual WAMUS chambers differ mainly in the number of cells in depth (3 or 4) and width (between 14 and 24), and in their length (between 191 and 579 cm).

The WAMUS PDTs are formed from aluminum extrusion unit cells as shown in Fig. 54. The extrusions are cut to the appropriate lengths and press fit into an identical neighbor. Figure 54 shows a relative transverse offset between the planes of chambers that allows breaking of the left-right drift-time ambiguity. Cathode-pad strips are inserted into the top and bottom of each unit cell and the anode wire is held near the center of the cell, as shown in Fig. 55. The maximum drift distance is 5 cm. The 50 μm gold-plated tungsten anode wires are held at 300 g tension by a special plug mounted in an aluminum cap extrusion covering the ends of the chamber. The holes containing the wires are drilled with a precision of $\pm 130\mu$m. Wire sag over 610 cm is 0.6mm. The aluminum extrusion itself is operated at ground potential with the cathode pads and anode wires held at +2.3 kV and +4.56 kV respectively. The total number of WAMUS PDT cells is 11,386.

The coordinate (ξ) along the wire direction is measured by a combination of cathode pad signals and timing information from the anode wires. Wires from adjacent cells are jumpered at one end, and signals are taken for the pair from the other ends in order to simplify access to chamber electronics. A coarse indication of the ξ coordinate can be obtained by measuring the time difference for a particular anode signal from the two ends of the paired wire. Two hits per wire-pair are accommodated to allow for δ rays. The Δt measurement determines ξ with a precision varying from 10 to 20 cm along the wire.

Fine resolution in ξ is obtained using information from the cathode pad signals. The upper and lower cathode planes shown in Fig. 55 are made from two independent electrodes as shown in Fig. 56, forming the inner and outer portions of a repeating diamond pattern whose repeat distance is 61 cm. The two inner pads of a given cell are added and read independently of the sum of the outer pads. Subsequent calculation of the ratio of sum and difference of inner and outer signals gives a measure of the ξ coordinate, modulo the approximately 30 cm half-wavelength of the pattern. The pointer for the correct cathode pad solution is given by the Δt measurement. The diamond patterns for adjacent planes of PDT are shifted in ξ by about 1/6 of the repeat distance to minimize the ambiguities encountered near the diamond pattern extrema. The ξ resolution achieved in a given chamber is approximately $\pm$ 3 mm.

Cathode pads were fabricated from copper-clad Glasteel (polyester and epoxy copolymer sheets with chopped glass fibers)[73] . The copper cladding was routed into the desired diamond pattern by a computer controlled milling machine. After cutting to the appropriate lengths, the pad surfaces facing the active portion of the cell were covered with 50 μm thick Kapton tape to ensure electrical isolation from the chamber extrusion.

The chambers are operated using the trinary gas mixture $Ar(90\%)/CF_4(5\%)/CO_2(5\%)$ for which the drift velocity about of order 6.5 cm/μs, but varies across the cell with changing $\vec{E}$[74] [75] . Tests of this gas have shown a nearly linear time-distance relation.

Typical leak rates of completed chambers was about 0.005 standard cubic feet per hour.

4.4 Small Angle Muon Chambers

The layout of the SAMUS system was shown in Fig. 51. The A station precedes the SAMUS toroid; the B and C stations are between the toroid and the beginning of the low-beta quadrupole for the DØ insertion. The SAMUS stations cover 312 × 312 cm^2 square areas perpendicular to the exit beams. An interior 61 (86) cm square hole permits passage of the beam pipe in the A and B (or C) stations. Each station consists of three doublets of 29 mm internal diameter cylindrical proportional drift tube chambers[76] . These doublets are oriented in x, y and u directions (u is at 45° with respect to x, y). Individual PDT's in a doublet form a close packed array with adjacent tubes offset by one half a tube diameter. There is a total of 5308 tubes in the SAMUS system.

The SAMUS PDT's are constructed from 3 cm external diameter stainless steel tubes with individual end plugs for provision of gas and electrical connections as shown in Fig. 57. The anode wire is 50 μm gold plated tungsten and is tensioned with 208 g. The sagitta for these wires is 0.24 mm over a length of 3.1 m. The system is operated with $CF_4(90\%)/CH_4(10\%)$ gas whose average drift velocity is 9.7 cm/μs. The resulting maximum drift time is 150 ns. The time of arrival is approximately linear with drift distance. Survey of the tubes within a station was made to a precision of 0.3 mm.

The SAMUS A and B stations are mounted from the EF toroids on the same support structures as the WAMUS EF A and B chambers. The C station is supported on the free-standing truss which holds the small angle portion of the WAMUS C layer chambers.

4.5 Muon Readout Electronics

Because of the large area over which the muon chambers are dispersed, much of the signal processing electronics for the PDTs is located on the chamber modules. Signal shaping, time-to-voltage conversions, latching of struck cells, chamber monitoring and multiplexing of signals for efficient transport to the digitizers are all performed locally. Digitizers and trigger electronics reside in the MCH.

Each of the WAMUS chambers has its set of electronics boards housed in a specially constructed enclosure on the side of the chamber body. These include separate 'Motherboards' (fast signal shaping) for each 6 cells of each plane of the chamber, one 'Cornerboard' per chamber (multiplexing and signal-drivers to the digitizers and triggers), and one 'Monitor' board per chamber (hardware-status monitoring).

The Motherboard contains a set of hybrid circuits which provide signal shaping and time-information encoding. For each cell, the sum of upper and lower cathode-pad signals from the inner and outer portion of the diamond pattern is brought to a hybrid circuit charge-sensitive preamplifier (CSP). This hybrid is very similar to that used for the calorimeter preamplifier. Each CSP is followed by a baseline subtractor circuit (BLS),

again like those for the calorimeter; the BLS performs a before and after sampling of the signal and stores the difference on one of two output capacitors. Signals from the anode wires arrive at the ends of a pair of wires jumpered at their far ends; these are amplified and discriminated in a pair of hybrid circuits (2WAD). The 2WAD outputs are supplied to two Time to Voltage hybrids and two Time-Difference ('Delta-time') to Voltage hybrids which provide analog information on time and time difference for up to two hits on the wire pair. The final element on the Motherboard is the Pad Latch which records the PDT cells that have had their cathode pads struck, based on the information present in the pad BLS hybrids.

Each chamber contains a Cornerboard which collects the signals from the Motherboard. The Pad Latch information is multiplexed by a factor of 4 and sent across the long cables from the chambers to the MCH. In addition, the latch bits are ORed on the Cornerboard to provide summary information on muon activity and majority logic indicating 1, 2, 3, or 4 hits in the chamber. The analog information from the pad BLSs and the time and Delta-time circuits is multiplexed and transmitted in 96 time slices to digitizers in the MCH. Provision is made in the Cornerboards for future inclusion of signals from an array of scintillation counters to be mounted on the outer portion of the detector. The Cornerboard also contains the test pulser for front-end electronics calibration.

The Monitor board associated with each chamber is connected to the general experiment monitoring services by the token ring described in Section 6.7. It provides the local interface to the operating characteristics of the chamber, including temperature, gas flow, voltages, and currents. The Monitor board is also used to set thresholds for latching pad cells and for test pulser amplitudes.

For each SAMUS PDT anode signal, the front-end electronics provide a card with the amplifier, discriminator, time-to-voltage converter, and a latch indicating a struck tube. Under the supervision of a SAMUS Control board, these signals are multiplexed and sent to the MCH in a similar fashion to the WAMUS information. The Monitor board for SAMUS is identical to that for WAMUS. The latch bit information is the basis for formation of small angle muon triggers.

Digitization of the muon chamber cathode pad signals and voltage-encoded time information is performed in the MCH using 12-bit ADC circuits which are variants of those used for the calorimeter digitization. There are 50,920 analog elements in the muon system.

4.6 Muon Chamber Performance

Tests of the muon chambers have proceeded through several phases. Early studies[69] measured the penetration probabilities for particles through magnetized steel within roads around incident muons and hadrons and helped establish the thicknesses of the toroids. Subsequent studies were conducted using WAMUS PDT chambers in test beams[77] and cosmic rays[78] [79] . Early tests employed gas mixtures of Ar(90%)/CO_2(10%) with drift

velocity 4.6 cm/μs. Subsequent operation with the faster gas Ar(90%)/CO_2(5%) /CF_4(5%) whose drift velocity is about 6.5 cm/μs has shown qualitatively similar performance characteristics.

Response of the PDT pad latches to cosmic rays as a function of anode potential is shown in Fig. 58; an operating range of 100 - 200 V is observed for each of several potentials applied to the cathode pads. The corresponding pad signal amplitudes are shown in Fig. 59.

In a test stand employing a set of proportional wire chambers with resolution $\pm$0.3 mm to define cosmic ray tracks in a WAMUS PDT, the track coordinate could be determined independently from the PDT time measurement. Figure 60 shows scatter plots of drift time and position for tracks incident at 0° (normal) and 45°. Although the drift time relation is approximately linear, detailed fits showed non-linearities of about $\pm$1mm due to the variations in electric field within the cell. Figure 61 shows the comparison of PDT coordinate (determined from the linear approximation) and the predicted location based on the PWC information. After unfolding the PWC resolution, this linear approximation gave the PDT drift-coordinate resolution of about $\pm$0.53 mm. Employing the fitted non-linear function to the distance-time curve of Fig. 60 reduced the PDT resolution to $\pm$0.3 mm, which is close to the diffusion limit. Figure 62 shows the variation in PDT resolution with angle of incidence. Studies of the chamber efficiency as a function of position within the unit cell showed nearly full efficiency except in the 2 mm window at the cell extrusion wall.

Cosmic ray studies were also conducted to measure the ξ coordinate resolution along the PDT wires. Because of attenuation and dispersion effects, the Δt measurement taken from the time of arrival of pulses at the ends of adjacent wires has a resolution which is dependent on the ξ coordinate. The Δt measurement error was found to be $\pm$9 cm near the ends of the wires furthest from the amplifier/discriminators and $\pm$23 cm nearest the electronics. This is sufficient to resolve the ambiguity of the repeating diamond pattern. The ratio of difference and sum of outer and inner cathode pads is shown in Fig. 63. Figure 64 shows the distribution of deviations in the ξ coordinate as determined from the cathode pad ratios using the PWC. The fitted resolution for the ξ coordinate along the 5.5 m long wire is $\pm$ 1.6 mm.

The SAMUS chambers were tested[76] in a 40 GeV/c muon beam. The time-distance relation was measured using beam proportional wire chambers. The resolution was determined by directing a test muon beam along three contiguous SAMUS tubes and measuring the deviation of the middle tube drift distance from the average of the first and last distance. Figure 65 shows the time to distance relation and coordinate resolution *vs.* drift distance. Averaged over tube radius, the resolution of a single drift tube is 0.35 mm, as shown in Fig. 66. The operating anode potential of the SAMUS drift tubes is 4.00 kV.

Studies of the gas properties for the muon chambers have been made[74] [75] [79] . For the gases including CF_4, the drift velocity variation was shown to be about 3% for 10%

change in electric field. The drift velocity is sensitive to CF_4 content; this gas content is specified with a precision of $\pm 0.1\%$.

5. Trigger and Data Acquisition

The DØ trigger and data acquisition systems are used to select and record interesting physics and calibration events. The trigger has three levels of increasingly sophisticated event characterization. The Level 0 scintillator-based trigger indicates the occurrence of an inelastic collision. At a luminosity of $\mathcal{L}= 5 \times 10^{30}\text{cm}^{-2}\text{s}^{-1}$ the Level 0 rate is about 150 KHz. Level 1 is a collection of hardware trigger elements arranged in a flexible software-driven architecture which allows easy modification. Many Level 1 triggers operate within the 3.5μs time interval between beam crossings and thus contribute no deadtime. Others, however require several bunch crossing times to complete and are referred to as the Level 1.5 triggers. The rate of successful Level 1 triggers is about 200 Hz; after action by the Level 1.5 triggers, the rate is reduced to under 100 Hz. Candidates from Level 1 (and 1.5) are passed on the standard DØ data acquisition pathways to a farm of microprocessors which serve as event builders as well as the Level 2 trigger systems. Sophisticated algorithms reside in the Level 2 processors which reduce the rate to about 2 Hz before passing them on to the Host computer for event monitoring and recording on permanent storage media. A block diagram of the trigger and data acquisition system is shown in Fig. 67.

5.1 Level 0 Trigger

The Level 0 trigger registers the presence of inelastic collisions and serves as the luminosity monitor for the experiment. It uses two hodoscopes of scintillation counters mounted on the front surfaces of the end calorimeters. These hodoscopes have a checker-board-like pattern of scintillators inscribed within a 45 cm radius circle giving partial coverage for the rapidity range $1.9 < \eta < 4.3$ and nearly full coverage for $2.3 < \eta < 3.9$. The rapidity coverage is set by the requirement that a coincidence of both Level 0 detectors be $\geq 99\%$ efficient in detecting non-diffractive inelastic collisions.

Figure 68 shows the layout of the Level 0 counters. Two planes rotated by 90° are mounted on each endcap calorimeter 140 cm from the center of the detector. Each hodoscope has 20 short (7×7 cm^2 squares) scintillation elements with single photomultiplier readout and 8 long (7×65 cm^2 rectangles) elements with photomultiplier readout on each end. To obtain good timing characteristics, 1.6 cm thick Bicron BC-408 PVT scintillator and 5 cm diameter Phillips XP-2282 photomultiplier tubes are used. Light pulses from a UV laser are distributed to each photomultiplier tube via fiber optics for use in calibration and monitoring the detector.

In addition to identifying inelastic collisions, the Level 0 trigger provides information on the z-coordinate of the primary collision vertex. The large spread of the Tevatron vertex distribution ($\sigma = 30$ cm) has the potential for introducing substantial error in the E_T values used in the trigger. To provide E_T corrections, a vertex position resolution of 8 cm is needed at Level 1 and 3 cm at Level 2. The z-coordinate is determined from the difference in arrival time for particles hitting the two Level 0 detectors. The Level 0

counters provide excellent time resolution since the active scintillator elements are either small or viewed by photomultiplier tubes on both ends so that time averaging can be used. The time resolution of each Level 0 counter was measured in a cosmic ray test stand; Fig. 69 shows time resolutions of typically 100-150 ps, which is well matched to the required vertex position accuracy.

At high luminosity, there is appreciable probability for multiple interactions; at $\mathcal{L} = 5 \times 10^{30}$ cm^{-2}s^{-1} there are on average 0.75 interactions per crossing. In the case of multiple interactions in one crossing, the Level 0 time difference information is ambiguous and a flag is set to identify these events to the subsequent trigger levels.

A block diagram of the Level 0 electronics is shown in Fig. 70. PMT signals are amplified and split into two readout paths. One path makes an analog sum of the small counter signals for each hodoscope and uses a GaAs-based digital TDC to make a fast measurement of the vertex position for Level 1 ET corrections.[80] A cut $|z_{vtx}| < 100$ cm is made to separate beam-beam interactions from beam-gas and beam-halo events. The second path digitizes the time and integrated charge for each counter. A more accurate slower measure of the vertex position is made by applying full calibration and charge slewing corrections to the data and using the mean time for each hodoscope to determine the vertex position. The rms deviation of the time difference is also computed and used to flag events with multiple interactions. All Level 0 calculations are performed in hardware and are available for use in the Level 1 and Level 2 trigger decisions.

The Tevatron luminosity is obtained by measuring the rate for non-diffractive inelastic collisions. Events of this type are selected by requiring a Level 0 coincidence with $|z_{vtx}| <$ 100 cm. Scalers count various quantities: live crossings, coincidences satisfying the vertex cut, and single hits in groups of similar counters with and without valid coincidences. These scalers allow the luminosity to be measured independently for each beam bunch and provide feedback to accelerator operations.

5.2 Level 1 Framework

Operation of the Tevatron collider with six bunches of protons and antiprotons gives 3.5 μs between crossings. Any rejection of events which can be accomplished in this time incurs no deadtime penalty. The hardware calorimeter trigger and a part of the muon trigger satisfy this constraint, but the remaining portion of the muon trigger takes several bunch crossing times to complete and is logically incorporated as a veto on event transmission. A trigger based upon TRD energy deposits which has been designed but not yet implemented would also operate in this extended time interval. The overall control of these Level 1 trigger components and the interface to the next higher level trigger resides in the Level 1 Framework[81] [82] and is shown in Fig. 67.

The Framework gathers digital information from each of the specific Level 1 trigger devices and chooses whether a particular event is to be kept for further examination. In addition, it coordinates various vetos which can inhibit triggers, provides the prescaling of

triggers too copious to pass on without rate reduction, correlates the trigger and readout functions, manages the communication tasks with the front-end electronics and with the Trigger Control Computer (TCC), and provides a large number of scalers which allow accounting of trigger rates and dead-times.

The selection of triggers is performed with a 2-dimensional AND-OR Network. 256 latched bits called AND-OR Input Terms form one set of inputs to the AND-OR network; these bits bear specific pieces of detector information (*e.g.*, 2 calorimeter clusters over 5 GeV). The 32 orthogonal AND-OR lines are the outputs from the AND-OR Network and correspond to 32 Specific Level 1 Triggers. Each of these Specific Triggers is defined by a pattern indicating, for every AND-OR Input Term, whether that term is required to be asserted, required to be negated, or is to be ignored. Satisfaction of one or more Specific Triggers while free from front-end busy restrictions and other vetos results in a request for readout by the data acquisition hardware. If Level 1.5 confirmation of a Specific Trigger is required, the Framework forms the Level 1.5 decision and communicates the results to the data acquisition hardware. The Level 1 Framework assembles a block of information summarizing all the conditions leading to a positive Level 1 decision (and Level 1.5 confirmation if required) for transmission to the succeeding levels of analysis.

Interactions with the Level 1 trigger system occur through the TCC. The configurations of the active Specific Triggers are downloaded from the Host computer to the TCC. The large tables of information used for programming and verification of the hardware memories in specific Level 1 trigger systems are downloaded to the TCC and stored on its local disk. Scalers and registers can be accessed through the TCC in order to perform trigger system programming, diagnostics, and monitoring. The TCC software is based on the DEC VAXELN multitasking real-time system software. The TCC software uses a low-level hardware database which establishes aliases and descriptions of specific hardware elements allowing easy reference, and a high-level object-oriented database in which trigger configurations are defined and recorded. The trigger system is monitored continuously to verify that its configuration files remain valid; failures cause alarms to be set in the general DØ Alarm monitoring system. The Level 1 Trigger Data Block is passed along to the data logging stream so that subsequent processors can recompute the input information and thus confirm the Level 1 decision.

5.3 Level 1 Calorimeter Trigger

A schematic diagram of the logic of the Level 1 calorimeter trigger[81] [82] is shown in Fig. 71. The system operates on the analog trigger pickoffs from the calorimeter BLS circuits, summed into $\Delta\eta = \Delta\phi = 0.2$ trigger towers out to $|\eta| = 4.0$. Separate trigger inputs are provided for the EM and hadronic sections (1280 of each) of the calorimeters.

Each input signal voltage is analog-weighted by the sine of the trigger tower polar angle to give the transverse energy appropriate for an interaction vertex at $z = 0$. This weighted signal is then digitized in a fast 8-bit flash ADC (20 ns from input to output) and

clocked into latches, allowing pipeline synchronization of all calorimeter information. The latches can also be supplied by test information allowing diagnostic studies of all subsequent trigger functions. This pipelined architecture is compatible with future Tevatron upgrades incorporating shorter bunch times (and thus requiring a larger number of crossings for decision making).

The 8-bit digital information from the flash ADC provides part of the address for several lookup memories. The Level 0 trigger provides an additional 3 address bits indicating the interaction z-vertex. The lookup memories provide both EM and hadronic transverse energies for each trigger tower above a fixed cut based on both electronics noise and physics considerations, and corrected for the z-vertex position, if known. The sum of EM and hadronic transverse energies for each trigger tower is formed and stored in a 9-bit register as an input for future, more powerful, hardware triggers. This sum is used to form the x- and y-components of transverse energy using lookup memories. Lookup memories also return the EM and hadronic transverse energies for each trigger tower, without the cut and z-correction. The global sums of the six energy variables returned from the lookup memories for each trigger tower are computed over the full set of trigger towers by pipelined Adder Trees. The Adder Trees are arranged such that geographically contiguous regions of the calorimeter are kept together. This permits the creation of intermediate energy clusters over larger regions of the detector, which may be used by future, more sophisticated, cluster handling hardware.

The full event missing transverse energy, $\not\!\!E_T$, is formed from the x- and y-component global transverse energies. The global total transverse energies, both corrected and uncorrected, are formed from the corrected and uncorrected global EM and hadronic transverse energies respectively. These seven energy variables (global corrected EM E_T, global corrected hadronic E_T, global corrected total E_T, missing E_T, global uncorrected EM E_T, global uncorrected hadronic E_T, and global uncorrected total E_T) are each compared with up to 32 programmable thresholds. Each such comparison provides a Level 1 Framework AND-OR Input Term.

In addition to the sums described above, each individual EM trigger tower transverse energy is compared to 4 programmable reference values. The corresponding hadronic trigger tower transverse energy is likewise compared to 4 different programmable reference values. For each trigger tower, a bit is set for each of the EM reference values exceeded, if not vetoed by the corresponding hadronic trigger tower energy exceeding its reference value. The total transverse energy (sum of EM and hadronic transverse energies) for each trigger tower is also compared to a set of 4 programmable reference values, producing 4 more bits. These 12 reference values are separately programmable for each individual trigger tower. For each of these 4 EM E_T and 4 total E_T reference value sets, the global count of the number of trigger towers with transverse energies exceeding their reference values is computed by summation over the full set of trigger towers in the pipelined Counter Trees. The global counts for each reference set are then compared with up to 32 programmable

count thresholds; these comparisons provide Level 1 Framework AND-OR Input Terms.

5.4 Level 1 Muon Triggers

A block diagram of the muon trigger system[83] is shown in Fig. 72. The basic information provided by the wide and small angle muon chambers to the muon trigger system is a single latch bit for each of the approximately 16,700 drift cells of the muon system. This information gives the bend coordinate of hit drift cells with a granularity of 10 cm in WAMUS and 3 cm in SAMUS. These bits are received in the MCH by 200 Module Address Cards (MAC's) which reside in 24 VME digitizing crates using custom backplanes. Each muon digitizing crate has a 68020 microprocessor used for downloading data and event building. The MAC cards and subsequent Level 1 and Level 1.5 muon trigger electronics are kept physically distinct for the 5 separate eta regions of the muon detector (CF, EF-North, EF-South, SAMUS-North, and SAMUS-South).

The MAC cards perform zero-suppression and generate bit patterns corresponding to hit centroids for the Level 1 and Level 1.5 muon trigger electronics. A centroid is defined as the most likely half-cell (5 cm in WAMUS and 1.5 cm in SAMUS) traversed by a track, projected to the midplane of a chamber. Centroid PAL logic is programmed using pairs of drift cells and can find the correct centroid even in the presence of geometrical inefficiencies or delta rays. The MAC cards produce a bit pattern corresponding to a logical OR of the centroids for use by the Level 1 muon trigger (called the CCT or Coarse Centroid Trigger). In WAMUS (SAMUS) this OR is performed on a group of 3 (4) centroids. The MAC cards also produce a full list of centroids to be sent to the Level 1.5 muon trigger (called the OTC or Octant Trigger Card).

The WAMUS CCT cards further OR the centroid bit pattern by a factor of four to give a hodoscopic pattern 6 cells wide (60 cm). Each CCT can accept inputs from up to 13 MAC cards. In the CF region this corresponds to 3, 5, and 5 inputs from the A, B, and C layers. The B and C layer MAC bit patterns are input to two PALs which jointly produce a 12 bit output pattern corresponding to 12 possible roads for A layer bits. Comparison with the actual 12 bit A layer pattern determines good Level 1 trigger muons. Other eta regions such as SAMUS and overlap regions in which tracks begin in SAMUS chambers and continue into sections of the WAMUS chambers also use CCT cards for Level 1 triggering. For example, in the SAMUS region, CCT's first find x, y and u space-point triplets in each of the three layers. Bits from good triplets are then used to search for independent x, y and u roads of 12 cm width. Finally, bits from the valid roads are used to find triple coincidences corresponding to good A layer space points.

The output of all CCTs for a given eta region is sent to a second CCT-like card which counts muon candidates in that region. Two bits of muon multiplicity information per region are sent to the Trigger Monitor Card (TRGMON) described below. CCT decisions are available within the 3.5 μs bunch crossing time. The results from individual CCT cards are latched and read out using the CCT LATCH card in the OTC VME crates.

After a trigger framework decision on any Level 1 muon trigger, the MAC full centroid lists are strobed into the OTC cards for Level 1.5 confirmation with a sharper p_T threshold. Each OTC accepts inputs from 3 layers of MAC's. The OTC compares all combinations of A, B, and C layer centroids to determine if they correspond to tracks above a p_T threshold (typically 3 to 7 GeV/c). The A, B, and C layer centroids are used as addresses to a pair of SRAMs whose patterns correspond to tracks above a given p_T threshold. A 4×4 array of these SRAMs allows the lookups for the 16 combinations of 1 A, 4 B and 4 C centroids to be carried out in parallel. Processing times for the Level 1.5 trigger in WAMUS regions are typically less than 2 μs.

The SAMUS Level 1.5 trigger faces a large combinatoric problem due to the large flux of small-angle beam-jet particles. In the SAMUS region, OTCs are used to first find separate roads in x and y for the three layers and good x, y, u space-point triplets in the B layer. Centroids from these OTCs are sent to a second level of OTC's which link the B layer centroids from x and y roads with the B layer centroids of good x, y, u triplets. Combined processing times for both stages of SAMUS OTC's can exceed 100 μs; each OTC contains a programmable timeout which aborts trigger processing in the case of very long processing times.

Further processing is done for each good OTC trigger combination using the latched input centroids as address inputs for a second set of memories. These memories produce two 24-bit user defined trigger words which are placed in FIFO's for readout by the OTC Manager (OTCMGR) card. Presently these trigger words are simply the centroids for good triggers. After each OTC's processing is complete, its output FIFO is read by the OTCMGR. This information is available for further processing both on the OTCMGR and at Level 2. A status word for each defined OTC is read out as well. The OTCMGR uses the centroid information contained in the trigger words to apply a second p_T threshold to the event, giving the flexibility of two different transverse momentum thresholds. The OTCMGR for each eta region processes all the trigger words for that region and sends three user-defined bits to the TRGMON corresponding to transverse momentum, multiplicity, and geographic information. Upon receipt of good Level 1 or Level 1.5 trigger from the framework, all trigger words in the OTCMGR are read out by the VME Buffer/Driver (VBD) in each OTC crate.

The TRGMON (Trigger Monitor) card receives two bits of Level 1 muon multiplicity and three bits of Level 1.5 information from each eta region. These Level 1 and Level 1.5 eta region bits are mapped into 16 Level 1 and 16 Level 1.5 physics bits (*e.g.* two muons anywhere in $|\eta| \leq 3.4$) via downloadable RAM on the TRGMON. These 32 bits are sent to the AND-OR network of the trigger framework for full trigger formation.

5.5 Level 1 TRD Trigger

The Transition Radiation Detector collects an excess of charge from converted X-rays produced by particles passing through a stack of thin foils. The zero-suppress (ZSP) cir-

cuit following a flash ADC for each anode wire in the TRD contains a stream of signals within successive 10 ns buckets. The ZSP circuit sums these signals over time and makes them available for a refined Level 1.5 TRD trigger, designed but not yet implemented. The purpose of this trigger is to certify electron candidates found in the Level 1 Calorimeter trigger. The TRD sums are joined in the Level 1.5 trigger[84] by a 5-bit representation of the interaction z-coordinate as determined from the Level 0 trigger and two 6-bit representations of the η and ϕ coordinates from the Level 1 EM calorimeter trigger towers. The calorimeter tower $\eta - \phi$ coordinates are strobed into FIFOs in the order of decreasing likelihood for being an electron. Each $\Delta\phi = 0.2$ calorimeter tower is matched to 8 TRD anode wires.

5.6 Data Acquisition Architecture

The DØ data acquisition system and the Level 2 trigger hardware are closely intertwined and are discussed together in this section. The system[85] [86] [87] [88] [89] [90] is based upon a farm of 50 parallel nodes connected to the detector electronics and triggers by a set of eight 32-bit wide high speed data cables. The nodes consist of a VAXstation processor coupled via a VME bus adaptor to multiport memory (for receiving data), an output memory board and an option for an attached coprocessor. The function of the Level 2 system is to collect the digitized data from all relevant detector elements and trigger blocks for events that successfully pass the Level 1 triggers and to apply those software algorithms on the data needed to reduce the rate from the approximately 100 Hz input to about 2 Hz output to the host computer and data logger. All the data for a specific event is sent over parallel paths to memory modules in a specific, selected node (one of the 50). The event data is collected and formatted in final form in the node, and the Level 2 filter algorithms are executed. An overall block diagram of the Level 2 system is shown in Fig. 73.

Fully digitized data appears in the output buffers of the approximately 80 VME crates containing the calorimeter and muon chamber ADC's and the tracking and TRD chamber FADCs about 1 msec after receipt of a valid Level 1 or 1.5 trigger. In addition, the Level 0 and Level 1 triggers themselves prepare registers containing information characterizing the trigger decision. Each crate of primary digitized data contains a 512 KByte memory module with two data buffers. Each VME Buffer Driver board[91] (VBD) contains list processors for controlled data transfer from VME locations in the crate onto an output data cable highway. Internal crate transfers occur at up to 30 Mbyte/s. The VBD outputs for each particular sector of the detector are connected sequentially to a high speed data cable. The data cable consists of 32 twisted pair lines for data and 13 pairs for control and parity; the clock rate on the data cable is 100 ns for a data transfer rate of 40 MByte/s/cable. Eight such data cables are provided for the eight detector sectors: VTX, TRD, CDC, FDC, the two halves of the calorimeter (north and south), muon chambers, and Levels 0 and 1 triggers. The data cable segment lengths are restricted to less than 12 m; since most DØ

data cables must circulate over a longer path than this, repeaters are provided to de-skew the signals. Readout control for the VBD and arbitration is achieved with a token passing scheme. When a token is received, the VBD external port processor compares the token bits with the crate buffers; if a match occurs, pending buffers are transferred to the data cable. Token passes are clocked at 1 MHz.

The real time operation of the data acquisition system is under the control of the Level 2 Supervisor processor. A Sequencer processor controls the operation of the data cables through a set of Sequencer control boards (one for each data cable). For each valid hardware trigger, the Level 1 system interrupts the Supervisor with the 32-bit pattern of Specific Triggers for that event, together with a 16-bit event number. The Superviser sends a 32-bit disabled-trigger pattern to the Level 1 Trigger Control Computer that changes with time, depending on the state of the run or the availability of Level 2 nodes for specific trigger bits. On receipt of a Level 1 trigger, the Supervisor assigns a Level 2 node and then interrupts the Sequencer processor. The Sequencer hardware in turn fashions readout tokens for a specific list of crates appropriate to the specific trigger pattern, and includes low order bits of the event number to insure readout integrity. Token circulation and data readout on each data cable are managed in parallel by separate Sequencer boards. Provision is made for readout of any combination of data cables collecting data from any desired set of crates. Debugging and calibration operations are handled flexibly in this way.

The eight data cables also circulate to each of the 50 Level 2 processor nodes. Whereas the VME digitization crates and the Level 1 triggers are in the MCH, the nodes are located in the fixed counting area. The data cable connections between MCH and the counting area are made through an optical isolator circuit to maintain isolation of grounds between detector and fixed counting areas. Each Level 2 node, shown schematically in Fig. 74, consists of memory modules which receive data from the data cable, a VAXstation 4000-60 processor, an optional special function co-processor and an output VBD which buffers data for transfer to the host computer. Central to each node is the multi-port memory[91] (MPM) accessed by the processor, the input data paths, the optional coprocessor, and the output VBD. Four MPM modules, each having two channels of 2 Mbyte multiported memory, serve incoming data from each of the eight data cables arriving at an aggregate rate of 320 Mbyte/s. The MPM memory appears as contiguous I/O space memory to the processor. The incoming data is mapped directly into the desired raw data ZEBRA structures as described in Section 7.2. No copy operations are required on the data in the Level 2 nodes and no reformatting is necessary for subsequent offline analysis.

During the setup of a data acquisition cycle, the supervisor polls the processor nodes to find one available to be the target for the detector data. Particular event types may be steered to specific nodes for special calibration purposes. Special coprocessors can be attached to the special function port of the MPM's to allow certain simple repetitive computations to be performed on the data rapidly, in parallel with the VAX processor analysis.

Each node normally contains an identical copy of the filter software which operates under the VAXELN system, although special calibration or test nodes may be loaded with different code. Development of the software algorithms and control code is developed in high level languages (FORTRAN, C, and EPASCAL) and downloaded over Ethernet into the nodes. A special 'Surveyor' processor monitors the operation of the data flow, the processor node operations, and the Sequencer and Supervisor nodes. The Surveyor collects statistics for on-line monitoring of the full system and provides diagnostics which are available for real-time displays and alarms. Once the Level 2 filter code has selected an event for subsequent data logging and analysis, the event and added information from the Level 2 analysis are sent directly from the MPM's through a VBD to the host computer. Transfer of the event from a Level 2 node to the host is managed in a similar way to the readout from the digitizing crates into the Level 2: a control processor ('Sanitizer') circulates a token to the Level 2 output VBDs. A VBD with data dumps its event on the output data cable where it is received by a MPM module in a crate connected to the host system via a VME/XMI bus adaptor.

5.7 Level 2 Filter

Software event-filtering in the 50 Level 2 nodes is expected to reduce the approximately 100 Hz of input rate to 2 Hz to be logged for offline analysis. Modelling[92] shows that to keep the deadtime due to Level 2 processing below 2%, average processing time should be $\leq$ 70% of the average time between events sent to a particular node, or 350 ms. The present processing time is less than 200 ms, which comfortably meets this budget.

The VAXELN filtering process in each node is built around a series of filter tools. Each tool has a specific function related to identification of a type of particle or event characteristic. Among the tools are those for jets, muons, calorimeter EM clusters, track association with calorimeter clusters, ΣE_T, and missing E_T. Other tools recognize specific noise or background conditions. The tools are associated in particular combinations and orders into 'scripts'; a specific script is associated with each of the 32 Level 1 trigger bits. The script can spawn several Level 2 filters from a given Level 1 trigger bit; for example, a single electron trigger from Level 1 might be given different Level 2 bits depending upon the E_T threshold or other features present in the event (*e.g.* energy isolation or the presence of missing E_T). There are 128 Level 2 filter bits available in all.

Tools are typically developed offline in a VMS environment where they can be subjected to a variety of tests and verifications using data or Monte Carlo events. Incorporation of a new tool or assembly of a set of scripts into the package for the Level 2 nodes is achieved with a facility called L2STATE[93] . The L2STATE output consists of a set of FORTRAN files comprising the tools, configuration files that specify the arrangements of the Level 2 (and Level 1) filter tools, the specific parameters for use in the tools (*e.g.* thresholds) and lists of required resources. The COOR task of the on-line host computer program (*c.f.* Section 5.8) assembles this output and coordinates the downloading of code, configuration

files and resource lists to the relevant lower level hardware processors.

The Level 2 nodes are coordinated through the Host Computer. Provision is made for run-time distributions of parameters to the nodes, for collecting statistics on the processing history for the nodes, and collection of error statistics and alarms.

Filter tools are typically developed using FORTRAN. Incorporation of these tools into the ELN environment imposes certain constraints. Standard FORTRAN-77 will run in ELN, but I/O and system-calling services require special handling. There is no provision for virtual memory in the Level 2 operating system, so all code and constants must fit in the available 8 Mbyte memory. Operation of multinode systems has occurred for most of the DØ beam and cosmic ray tests[94] as well as for the generation of Monte Carlo events in the farm system.[95] .

Preparation of triggers and modelling the timing and rate-rejection properties is done using a pair of linked utilities called L1SIM and L2SIM. Respectively, these programs operate on simulated detector data, using simulated Level 1 trigger elements and the AND-OR network, or the actual configuration files and filter scripts for Level 2. A standard set of physics and background events, generated by ISAJET and converted to simulated hits in all detectors by DØGEANT (see Section 7.3) is used for these simulations. The outputs of these calculations are used to optimize both the Level 1 trigger specifications and the Level 2 scripts within the overall constraints of the rates and rejection factors.

5.8 Host Computer and On-Line Software

The host cluster consists of VAX 6620, VAX 6410 and VAX 8810 processors and a set of shared disks connected by the high speed Digital Equipment CI cluster protocol, together with 12 VAXstations connected by an Ethernet/FDDI network. The 6620 is the primary data collection engine receiving events from the Level 2 output data-cable. It logs these events to a staging disk and dispatches a sample to the various workstations for online monitoring purposes. Recording occurs at rates of up to approximately three 500 KByte events per second. The 6410 is the primary machine responsible for spooling events from the staging disk to 8 mm tape. It also performs downloading operations. The 8810 is devoted primarily to hardware monitoring, but also participates in downloading operations.

The Host cluster also serves as the primary human interface to the detector systems. In this role it is responsible for high level control of the data-taking system, downloading of all settable parameters, specifying hardware monitoring activities, and the recording and displaying of data produced by the detector. These data include $\bar{p}$-p interactions, calibrations, monitoring information and alarms.

The event data-taking system is designed to support flexibly defined partitions of the detector, allowing for many users to collect individually tailored data streams. Each such user has his or her own runs, triggers, event filtering or processing nodes, recording streams

and event monitoring tasks.

Figure 75 shows the hardware configuration of the Host cluster and Fig. 76 shows key processes of the software system. These processes are distributed across various members of the cluster. Communication between processes is accomplished by a package called Inter-Task Communication (ITC) developed by DØ. ITC works transparently between processes within a single node or across nodes of the cluster. Data samples are sent to monitoring, display or calibration processes running within the cluster over a DØ developed network extension of the standard Global Shared Common (GSC) system supplied by the Fermilab Computing Division. Events are inserted into GSC through a subprocess of the data logging task which receives the events from the Level 2 filter nodes. Events are selected from the extended GSC by consumer tasks, based on those filter bits satisfied during the filtering processes.

Event monitoring tasks are based on a program framework called EXAMINE. EXAMINE is one of the frameworks supported by the Program Builder (Section 7.2), and thus the application packages that operate within it are portable to the other standard DØ frameworks described in Section 7.2. Interaction with EXAMINE is through the COMPACK menus facility described in Section 7.2. Utilities within EXAMINE present the user with lists of currently available triggers and inform the user of ends of runs. Under normal data-taking conditions, there is an EXAMINE running for each of the major detector subsystems as well as global analysis and global display versions.

The COOR task is responsible for the overall coordination of the data taking system and runs as a detached server process. Client tasks connect to COOR to request specific configurations of the detector, or to request operational changes. In turn, COOR has connections to various data-taking subsystems through which it sends download and control messages. The targets for these messages include various parts of the Level 1 and Level 1.5 trigger system, the data gathering and event filtering components of the Level 2 system, the front-end digitizing crates, pulsers, various timing and gating logic, and the data logging system. The paths for these messages include FDDI, Ethernet and IBM Token-Ring networks.

A typical use of the various elements of the host cluster and related processors for the electronic calibration of the calorimeter electronics is shown in Fig. 77. Under operator control, the Host computer sends configuration files to Level 2 nodes and Level 1 triggers to start processing special electronics calibration data. It issues commands over the control data path to pulsers situated in the various calorimeter preamplifier enclosures. Pulse pattern sequences are generated which flow along the normal data collection paths through digitization, Level 2 nodes, and into the shared data space in the Host. Computations involving the pulser data are done either using filter scripts in the Level 2 nodes or in tasks operating on one of the elements of the Host cluster. The associated input data may be recorded, but in most cases only the resultant pedestals, gains, bad channels *etc.* are retained.

6. Detector Services

DØ has chosen wherever possible to unify its support systems across the detector subsystem boundaries. In this chapter, we briefly describe some of the mechanical, electrical and monitoring systems which serve the detector as a whole.

6.1 Support Platform

The detector support platform[96] is a box-beam welded structure consisting of four beams assembled into a "tic-tac-toe" pattern. The beams parallel to the accelerator beamline are 13.4m long; the transverse beams are 11.6m long. The box cross-sections are 1.3m high by 0.8m wide. Track plates are mounted on the tops of the beams to allow motion of the muon toroids (the CF shells retract perpendicular to the beams and the EF magnets move parallel to the beams). The central beam portion of the CF toroids is fixed to the platform (see Fig. 52) directly under the Tevatron beamline and serves as the support for the calorimeters. The end calorimeters retract along this beam to give access to the innermost tracking detectors.

The space within the platform is used to house electronics, gas, power, cryogenic and cable utilities for the detector. Access to this interior space is given by holes in the central sections of the box-beams parallel to beamline. The five non-corner cells of the "tic-tac-toe" pattern contain electronics racks which house the high voltage fanouts and current monitors and the shaping circuits for tracking, TRD and calorimeter detectors. The corner cells are reserved for the incoming and outgoing detector services: ac power, drift chamber gas connections, calorimeter cryogens, and the merge point for cable communication to the radiation safe areas.

The platform is the transporter for the detector travel between the collision hall and assembly area. Twenty 500-ton Hillman rollers are mounted under the transverse box beams to allow movement on hardened steel tracks in the building floor. Vertical lift for the platform is provided by 500-ton hydraulic cylinders mounted on each of the rollers. Independent operation of these lift cylinders allows the detector to be levelled at beam height. The platform is moved on the rollers by two pairs of hydraulic push/pull cylinders attached on one end to the ends of the transverse box beams. The other end is fitted to a pin which is dropped into holes in the track plates. The hydraulic rams contract to pull the detector over the 24 inch interval between holes.

6.2 Cable Plant

DØ contains approximately 5.5×10^6 meters of cable pairs for distribution of signals, high voltage, monitoring, and controls. The cable connections to the DØ detector must penetrate the 12-foot thick concrete block shield wall which separates the collision hall from

the radiation-free assembly hall where the digital electronics and control areas are located. The main cable path segments are (a) detector preamplifier to shaper/multiplexer; (b) shaper to digitizers; and (c) digitizers to event builder/Level 2 trigger.

Preamplifiers are located as near the physical detector elements as possible. Each detector element signal (approximately 120,000) is carried by its dedicated cable to the shaper electronics. Articulated cable trays are provided for the preamplifier to shaper cables from detectors which can be moved. The shaper crates are typically located in the detector platform (muon chambers are the exception where shaping is done locally at the chambers). The Central Detector signals are transported on 73 Ω 28 AWG coaxial cables assembled into 18 wide ribbon pairs, terminated in 40-pin cable connectors. Calorimeter signals are transported on 110Ω twist and flat (TnF) 25-pair wide ribbons.

The shaper outputs, multiplexed in the case of calorimeter and muon detectors, are gathered at the 'cable corner' of the platform and carried over a cable bridge through the shield wall and to the Moving Counting House (MCH) which houses the digitizers. The cable bridge is an open channel, lined with copper sheet. It has a total length of about 8m and is approximately 235 cm across and 50 cm deep. The bridge is attached at one end to the cable corner of the platform and on the other end to the MCH. It is hinged in the middle and can be folded vertically to allow relative motion between MCH and platform. With the detector in the collision hall, the bridge is fully extended and filled with bags of glass beads to fill the remaining interstices, and covered with a copper lid to complete the shielding against noise pickup. In this position, the cables pass through a penetration through the stacked block shield wall. On leaving the bridge, cables are directed upward through a cable tower fixed to the side of the MCH. Bundles of cables in the bridge and tower are organized such that at each of the three levels of the MCH appropriate cable streams are peeled off to deliver signals to the relevant electronics circuits. The cable tower also houses the ultraviolet laser which feeds calibration light to the Level 0 and ICD detectors along fiber optic cables. Central Detector shaper to MCH cables are ribbons of coax pairs similar to those used from preamplifier to shaper. Calorimeter multiplexed signal and muon latch signals are transported on ribbon TnF cables. Calorimeter trigger and muon chamber time and pad analog signals use the 110 Ω ribbon coax cables.

High voltage for all detectors is distributed from power supplies to active elements on 8-conductor cable with a single outer ground sheath. Special 8 pin connectors and plugs are provided to allow disconnection of the high voltage path. Connectors are specified to give less than 10 nA current when ±10kV is applied to odd and even pins. The full DØ detector is supplied from approximately 1000 HV supplies described in Section 6.4. Successive HV fanouts to individual detector elements are located in both the MCH and the detector platform. In the case of the calorimeter, where current draw information is desired for individual HV interleaves, special current monitoring fanouts are provided.

All cables in the DØ detector were provided with a bar code for specific identification and were entered into the cable database. The database contains information about the

manufacturer, connector and cable types, slot/crate/rack address for both ends, as well as information about the detector channel served by the cable with the appropriate channel address name and number. This database enables easy access to the collection of cables, connectors, crate, slots *etc.* implicated in any specified detector channel.

6.3 Moving Counting House

The MCH is a three story enclosure housing the Level 0 and 1 trigger electronics, high voltage power supplies, and digitization electronics for all detectors. It supports the load of the cable bridge and moves on wheels along the side of the assembly hall. Two parking positions are provided with doorways from the fixed counting areas; one serves the MCH when the detector is in the Assembly Hall and the other is used for the detector in the Collision Hall. The MCH is electrically isolated from the building ground and is electrically connected to the detector through the cable grounds. Cables enter each level of the MCH from the cable tower into space beneath a removable tile computer floor. Each floor of the MCH contains 25 electronics racks accessible from front and rear. Almost all crates are VME standard. The lowest floor nearest the detector houses the Level 0 and 1 trigger framework, calorimeter trigger, and HV power supplies for all detectors. The middle floor contains the master detector clock and the flash ADC electronics for the tracking and TRD detectors., together with the MCH end of the Level 2 control and data cables. The top floor is devoted to the calorimeter and muon digitizers and the muon trigger elements.

6.4 High Voltage Power

In order to provide compact high voltage power, standardize monitoring and computer control and simplify maintenence, DØ has developed a new computer controlled VME-based HV power supply[97] [98] [99] . The supply is a 6U×60 mm wide unit containing eight individual outputs. Six of these supplies are housed in each crate, together with a crate monitoring module and the 68000-based HV control module. Three module types were produced. Two are negative and positive polarity supplies operating between 10V and 5.6kV (in 1.36V increments) at $\leq$1.0 mA. The third is a positive supply operating between 10V and 2.0kV (in increments of 0.49V) at $\leq$3.0 mA. Each supply unit contains a control board which supports the VME-bus interface, digital controls, and ADC/DAC functions. Eight self-contained plug-in units (pods) mounted on the control board contain the dc-to-dc converter circuits which supply the high voltage. Any mixture of HV pods can be installed on a single control board. Figure 78 gives a block diagram for the HV control board; Fig. 79 shows the dc-to-dc converter supply schematic. Each power supply unit is provided with a front panel SHV connector and with a potentiometer for correction of the resistor tolerances.

The control board contains separate 16-bit DAC's used for high voltage setting and 12-bit DAC's for over-current trip setting, and a single 15-bit multiplexed ADC for readback monitoring of voltage, current, low voltage levels, temperature, and limit settings for current and voltage. HV trips are initiated by over-current or over-voltage using comparators on the control board. Provision is made for grouping supply channels together for common ramp and common trip in the event of any single member channel trip. Hardware trips can also be generated by external fault conditions (fire alarms, gas leaks *etc.*). Upon receipt of a trip, a latch is set to prevent turning on the supply without operator reset; the voltage DAC is also reset to 0 volts. Front panel potentiometers provide an override limit to the maximum voltage available.

Each crate contains a control module with a 68020 subordinate processor which is responsible for recording the recent history of the supplies in that crate, thus facilitating information polling by higher level processors. The subordinate processor also controls the individual supply conditions. A collection of crates are controlled by a master 68020 processor which governs the group trips and ramps. External communication with the crate level processors is achieved over two distinct paths. A PC-based host can be connected to the system via a BIT3 interface or Token Ring; this system is used for expert debugging and monitoring at the local (crate or rack) level. A VAX-based software system connects to the HV power supplies through the standard DØ control path described below. It allows multiple user interaction with the high voltage system and provides the high level monitor and control required by the non-expert experimenter. Facilities exist with either system for logging supply conditions, producing histograms, strip charts, and parameter pages summarizing the system status.

Correction functions can be downloaded to the supplies to improve hardware inaccuracies. Measurements show that with these corrections, the set voltages are within 0.5V of the nominal desired value. Current readback offsets are less than 32 nA. Output voltage temperature coefficients are 300 ppm/°C.

6.5 Clock

Many separate processes for the operation of the DØ detector require a precise train of timing pulses, synchronized with the accelerator clock. The DØ clock system provides such pulses with a flexible control system to allow user formulation of the clock pulse train desired for particular use.

The clock system hardware[100] consists of three module types: the Phase Coherent Clock (PCC), Sequencer, and Selector Fanout. The PCC receives signals from the Tevatron timing and RF sequences, and provides synchronized signals at the first harmonic RF frequency of 106 MHz. In the event that the accelerator is not operational, the necessary RF and Tevatron synchronization pulses can be generated internally in the PCC.

The Sequencer modules generate up to 23 independent timelines of 1113 elements each, corresponding to the 1113 RF buckets in one full turn of the Tevatron. The Selector Fanout module receives the signals from the Sequencer and distributes them to the various detector subsystems.

Multiple clients can be served by the DØ Clock Interface[101] for establishing one or more of the 11 particular time sequences available for general users. The Clock Interface manages the various reserved timelines and prevents interactions between the separate client processes. Commands are available which allow opening, initialization and closing timeline requests, programming the specific pulse sequences desired, referencing the sequence to a specific Tevatron time, establishing error handling response and requesting state change notification messages for the user. The Selector Fanout modules can also be programmed to receive timelines via the COM_TKR program on the host VAX system.

6.6 Alignment

Maintaining good knowledge of the locations of the DØ subdetectors relative to each other and to the Tevatron beams is essential. The DØ alignment problem is compounded by the fact that the detector is to good approximation hermetic, so that inner detectors are hidden from external view, and by the fact that major pieces (CF, EF's, EC's) are moved for access and thus can return to different locations. In addition, the detector is heavy and thus the floors of Assembly and Collision halls themselves are deformable.

The detector has been fitted with several sensors serving different purposes.[102] The liquid level system uses closed vessels of water connected by tubes; the water level is sensed by capacitive proximity sensors. These devices[103] are mounted on the detector platform and tunnel magnets to provide vertical reference over the full experiment to within about 100 μm. A tilt sensor system based on an electrolytic bubble tilt meter[104] measures angular motions of the toroid elements to within about $\pm$ 20μrad. These measurements monitor tilts induced by magnetic forces and movements of detector pieces. Proximity sensors[105] determine the distance to iron elements using eddy current detectors and allows positioning of the detector or moveable subdetectors to a precision of about 25 μm.

The history of changes in position and tilt sensors are referenced to the values obtained at the time of the baseline optical survey. The optical survey yields a few millimeter accuracy for absolute location of the large muon chambers in the outer shell of the detector. The inner tracking detector survey is somewhat more accurate. Final location of active detector elements relative to the beam axis and to each other is determined by minimizing the fitted position residuals from particles produced in $\overline{p}$-p collisions.

6.7 Experiment Monitoring and Control

There are two independent pathways for communication and data flow between the DØ detector and the host computer cluster. The collection of event information from the detector digitizer buffers is of prime importance and is transferred over the high speed data cable highways discussed in Section 5.6. Event data acquisition is essentially a uni-directional process with the minimum of controls. The bi-directional polling of detector hardware elements and front-end software processes, the collection of alarms, and the downloading of the numerical specifications for digitizer and data-acquisition crate operations uses a completely independent control pathway.

Hardware

Figure 77 shows the block diagram of the hardware monitoring system together with the event data path and host system.[106] [107] [108] The on-line host computer system described in Section 5.8 provides the high level control and user interfaces. An Ethernet LAN connects the host VAX processors via one of several gateway processors to an IEEE 802.5, 4 MHz token-ring LAN. The gateways are microVAX processors which are connected to both the Ethernet and token-ring LAN's and which execute DØ-developed software under the VAXELN operating system. The token-ring LAN services the front-end processors such as the Motorola 68020 processors located in the VME-based electronic crates in the MCH and in the high-voltage control systems and the IBM-compatible processors in the gas-flow control systems. No processors are installed in the front-end analog signal processing crates or on the detector platform to prevent noise generation.

The 68020 processors control and collect information from remote readout modules called Rack Monitor Interfaces (RMI's) which are connected by a MIL-1553B serial link and are distributed throughout the detector elements, support platform electronics, and MCH racks. The RMI's collect information such as voltages, currents, temperatures, or water flows from all crates in the experiment. Each RMI contains a 646-channel differential ADC, 8 channels of DAC output, and 32 bits of digital input and output. The MIL-1553 bus serving the RMI's has no continuous clock and thus is quiet except at data transmission time. Although provision was made to inhibit RMI data exchange during event acquisition times, this has not proved necessary.

The 68020 processors are also connected to the digital electronics crates in the MCH by means of a Vertical Interconnect card in a master processor crate which drives a single, 64-pair cable in a daisy chain of a few meters length to several slave crates. The Vertical Interconnect allows for the downloading of the several megabytes of constants required by the DØ trigger and digitizing electronics without putting every digital crate on the serial network. The Vertical Interconnect allows the memory from five 'slave' digitizing crates to be mapped to the master controller in a transparent way. Slave crates are allocated up to 2 Mbytes in the master VMEbus address space. Data transfer is controlled wholly by the master crate to prevent bus contention. The Vertical Interconnect system allows for

a variety of diagnostic and test modes of operation, as data can be downloaded into the primary digitizers for each detector and read back through the primary event acquisition system. This allows a system check of the full data acquisition system.

The control station processors provide the supervision of the RMI's and Vertical Interconnect to the digital crates. They acquire data at 15 Hz and buffer it for transmission through the control data path to the host system. Alarm scanning for hardware or software elements outside of preselected tolerances is done locally in the controller. Only those data requested by high level processes are transmitted. Operation of the hardware monitoring system can be done independently of the central host VAX computer by means of keyboards attached to the local control stations. The local stations utilize a local database in non-volatile RAM which is downloaded from the central database.

Control Software

The hardware monitoring system described in the preceeding section is controlled from the on-line host computer (see Fig. 75 and Fig. 76), but is separated from the main event collection and physics monitoring pathways. The processes in the host-level computers responsible for control, hardware monitoring, and downloading of run control and calibration data to the detector electronics communicate over the control path through a library of standard interface procedures called CDAQ (Control Data AcQuisition)[109] .

At the heart of the monitoring function is the relational hardware database called HDB[110] [111] [112] [113] , based on the RdB[114] product. HDB defines all of the essential attributes of the hardware (rack, crate, card addresses, cable connections, applicable voltage or current settings, *etc.*) and provides CDAQ with the information it needs to establish communications with a desired hardware device and to convey its description to the front-end node in appropriate format for direct access writes and reads. The HDB database is approximately 100 Mbytes in length. It contains information on all detector systems, support systems such as low voltage, high voltage power, cryogenics and argon purity monitoring, air handling systems, as well as software systems such as CDAQ itself. Various facilities for accessing the database have been provided, including interactive and batch interfaces.

The procedures in the CDAQ library hide the details of the actual data-acquisition protocols by translating from a simplified user's view of a device with multiple attributes to the required access path description via HDB queries. Requests in the form of multiple device/attribute pairs, which may reference several front-end nodes, are assembled into message packets called frames destined for individual front-end nodes. These requests are issued either in single-execution or periodic mode. The CDAQ interface manages the synchronization and assembly of replies from multiple front-end nodes, arbitrates contention for shared resources, and automates recovery of all allocated resources, both local and network-wide, when a request is deleted or the user's process terminates abnormally.

DØ has developed a number of application programs which give dynamic graphics

or text displays of the experiment hardware status. Many use routines from the CDAQ library to periodically gather information from selected devices which are monitored or otherwise accessible to the front-end computers. Typical examples of these programs are: (1) a general-purpose, parameter page program which displays readings of devices in numerical, strip-chart, or histogram format, (2) a high-voltage control program which provides complete management and display functions for the high-voltage hardware, and (3) a low-voltage program which provides a similar service for the many low-voltage power supplies in the MCH and on the detector platform.

Alarms Software

In a complex collection of systems such as the DØ Detector, there is a very large number of conditions which can damage the quality of the data being collected, or which threaten the detector systems themselves. These conditions can generally be sensed through some measurable parameter (temperature, power, voltage, current, humidity, *etc.*) going outside of permissible range resulting in the generation of an alarm. In an environment as strongly controlled by overlapping software systems as DØ, the continued functioning of the software tasks must itself be monitored. Since not all alarms can be examined immediately by the human operators, there is a need for long term alarm recording. Some attempt also needs to be made to ascertain the common root cause for a set of related alarms. The DØ Alarms package[115] , written mainly in PASCAL, has been created to handle these needs. Figure 80 shows the organization of the Alarms system software.

The DØ Alarm system operates with a central 'Alarm Server' task on the host VAX cluster which receives alarms from multiple sources and distributes alarms to multiple clients. It may receive messages from front-end processors which pass alarm information through the Token-Ring/Ethernet Gateways. Other processes on VAX nodes reachable via DECNET may also generate alarms. Any DECNET accessible node may also be a client.

The front-end processors monitor the hardware devices at 15 Hz and generate alarms when the devices go out of tolerance. Alarm messages contain the current device reading together with the local copy of descriptive information derived from the master HDB database. Critical software processes also send periodic 'heartbeats' to the central Alarm Server. The absence of a heartbeat, generally due to the disruption of the process, causes the Alarm Server to generate an alarm condition.

There are two types of alarm messages. The first is generated upon a state transition between an 'acceptable' and an 'unacceptable' condition. The central Alarm Server task maintains a list of devices in the 'unacceptable' condition which it can provide to client tasks. The second type of alarm message, more appropriately called a 'significant event', carries information for distribution to other processes and is not stored. For example, begin and end run notification are propagated in this way.

The central Alarm Server task collects alarms and heartbeats from all sources. These are distributed to client processes based upon filters which select classes of events. Standard client processes include a process to which to log events to a disk file, a process which notes high priority alarms and is capable of interrupting data acquisition, and a process for alarm display.

The interactive Alarm Display is built using the MOTIF windowing system. Customized displays can be created to produce multiple lists of alarms which satisfy different filters. In addition to the information contained within the alarm message, detailed information obtained from the HDB database can also be displayed for each alarm.

6.8 Test Beam System

Over the lifespan of a detector the size of DØ, there are many tests required for individual sub-detector systems as well as for larger collections of interconnected systems. A general facility was developed in a beamline of the Tevatron for this purpose. Many tests of tracking chambers, muon chambers and calorimeter modules have been performed in beams of pions and electrons ranging between 10 and 150 GeV/c. Recently, low energy particles were provided using tertiary beams[116] from targets located just upstream of the DØ facility in the beam transport system. Both electrons and hadrons were delivered to the detectors with momenta down to 1 GeV/c. A concrete shield behind the test facility allowed the use of tagged muons.

Several dedicated support systems were provided for the tests. Proportional wire chambers with 1 mm wire spacing recorded the trajectory of beam particles and allowed momentum determination with precision 1/4%. Two gas-filled Cerenkov counters gave discrimination of pions and electrons; the electron contamination of the pion sample selected was typically 10^{-4}. A precision table for supporting and positioning tracking chamber modules with remote translation and rotation was installed in the beam enclosure. A large liquid argon cryostat was built for testing a variety of calorimeter modules[57][117] . This cylindrical cryostat was supported on a moveable platform allowing translations in both horizontal and vertical directions and rotations about the vertical and the cryostat axes.

A trigger and data acquisition system was built which was virtually identical to that in the final experiment, except that fewer elements were needed. Thus although providing a trigger for the test beam is far simpler than in the collider, much valuable experience in operating the Level 1 and Level 2 trigger systems and hardware monitoring and downloading could be gained prior to installation of the detector in the collision hall. The host computer system was similar to the final system and the on-line control and data acquisition software was tested and evolved over the course of the test beam runs. A final benefit from the simulation of the DØ environment in the test beam facility was the training of the DØ physicists in operating the detector and interpreting the on-line monitoring data.

7. Software

A large body of software has been developed for acquiring data from the DØ detector, for monitoring and controlling the hardware, for off-line reconstruction, for Monte Carlo event simulation and for the related databases. In this section, we summarize the software and computational procedures developed with specific application for the DØ Experiment.

7.1 Structured Analysis/ Structured Design

It was recognized early in the design of DØ that it would be useful to adopt a more rigorous discipline for the development of software than had been common in past High Energy Physics experiments, since software would be produced by a large number of widely dispersed individuals with a moderately large turnover over the lifetime of the project. There was a need for clear design specification and documentation of the produced software. In addition, the broad dispersal of the effort placed a premium on clean delineation of the various sub-components of the project.

The methodology used for the software development was 'Structured Analysis/ Structured Design' (SA/SD)[118] [119] , developed for the commercial environment and previously adopted by the ALEPH Collaboration at LEP[120] . SA/SD stresses two phases in software development. The first is an analysis phase in which careful specification of the software is prepared using some well-defined graphical tools. The second is the detailed implementation phase.

A key element of SA/SD is the Dataflow Diagram (DFD) which focusses upon the flow of data through a software system and the transformations which are performed upon that data. The DFD's are arranged in hierarchies which describe succeedingly more restricted portions of the overall task. The stimuli and data transfers from one subprocess to another are essential elements. The definitions of the data being transferred are specified in accompanying Data Dictionaries. A particular example of a DFD is shown in Fig. 81.

Working from the documentation produced in the form of the DFD's in the analysis phase, code is then designed during the second SA/SD phase which implements specific diagrams. The State Transition Diagram is introduced to represent the dynamic activation of processes and to focus on the conditions which cause state transitions. An example State Transition Diagram is shown in Fig. 82. The Structure Chart represents the decomposition of tasks into functional modules which are the units of implementation. It approximates the traditional diagram of program logic and forms a primary component of the final software documentation. Review and criticism of the code design was conducted using these Structure Charts.

Our experience using SA/SD was good at the beginning of the project[121] . The initial work preparing and discussing Dataflow Diagrams and Structure Charts, though

imposing some overhead, did enhance some clarity of purpose and agreement on the basic structure of the DØ software system. The methodology also produced very useful software documentation early in the project. This documentation was not kept up to date over the long run, largely because no automated tools existed to support the editing, integration and verification of the various diagrams and associated dictionaries.

7.2 Utilities and Tools

Data Management

Data management in DØ is based on two products. The first is RdB[114], a relational database used in the real-time online environment. The second is ZEBRA[122] which is also incorporated into many of the generally available CERN packages. ZEBRA gives standardized, hierarchical storage banks for commonly used data, together with reference links to other related banks. It is used to manage data of many different types, including event data, detector descriptions (geometry, survey constants *etc.*), calibration constants, run control parameters, graphics control parameters and histograms. In the case of calibration constants and other data sets requiring complex access an additional layer is placed over ZEBRA. This layer is DBL3[123], developed by the L3 collaboration at CERN, which supplies a database set of utilities based on ZEBRA.

The event data are put into ZEBRA format even before on-line calculations are performed; this is done as part of the event building process in the Level-2 filter nodes. The event data forms a single tree structure and as reconstruction is done, extensive reference links among related bodies of data are established.

Various standard utilities are required to be supplied before any new ZEBRA bank is included in the library. They include documentation files, a parameter file giving the structural link, a bank booking routine, a function returning the pointer to the bank, a routine which returns the values of the bank data words, and a dump-printing routine.

Parameters controlling program behavior (such as values of cuts to be used in offline analyses) are kept in editable ASCII 'Run Control Parameter' files. A set of utilities have been developed which read these RCP[124] files, store the information in ZEBRA banks, get the specific RCP parameter, or add information to an RCP file. A particular use of the RCP files is the storage of detector geometry constants. Program use of geometry information is accomplished through the utilities for interacting with the associated ZEBRA files.

Code Management

DØ software is stored in a library maintained by a set of procedures based on the CMS (Code Management System) and MMS (Module Management System)[114]. Some

45 distinct subdirectories exist in the library, each associated with a specific software package such as the DØ Monte Carlo DØGEANT, the utilities for ZEBRA manipulations, *etc.*. Each such subdirectory is managed by a designated 'czar'. The CMS library keeps code sources, command procedures, documentation, and in cases when the code is not maintained by DØ, object libraries.

There is only one central copy of the CMS library which contains the update and release history of each of the subdirectories, so that retreat to the software status of an earlier epoch is possible. Code developers are encouraged to create local CMS libraries on their own clusters to facilitate local activity. At suitable intervals, updates are released by the library czar. Strict rules for reserving and replacing library modules are enforced, so that all software developers know the status of changes and inconsistencies can be avoided. Release of code generally occurs in two stages. First, a test release is made to all nodes; users are notified and encouraged to test the new code extensively. In this phase, test and prior official releases coexist in the library. After the test period, the test release is declared official and replaces the official release.

The source and object libraries are automatically distributed to DØ collaboration VAX computers so that identical environments exist at all institutions. Release to other than VAX computers requires intermediate steps to convert source codes.

Screen Management

Screen management and the interaction of users and DØ software is accomplished with a command input package called COMPACK[125] , written by DØ in VAX FORTRAN and utilizing the VAX Run Time Library. This set of routines supports the input of run-time options, program specifications, program control, or program parameters in a consistent way. COMPACK provides menu trees with well-defined formats and user interactions. Both line mode and full-screen modes are available.

Packages are provided within COMPACK for the creation of new menus and modifications of existing menus. Various utilities are incorporated allowing transparent handling of data, display and menu specification files, parameter specification, and fielding of system messages.

Graphics and Displays

The DØ event display facility uses the graphics system DI3000,[126] linked with a package written by DØ called PIXIE. The package gives the capability to make 2- or 3-dimensional views of detectors with superimposed hit or reconstructed track/ cluster information, or Lego plots of calorimetric energy deposits. A special package has been made to display the primary Monte Carlo events from ISAJET or other generators. The routines of this package are available for inclusion into any of the on-line or off-line DØ program frameworks. Special facilities are provided in PIXIE for temporary or permanent

zoom, hardcopy, or real-time editing of screen parameters.

Histogramming is done in DØ using the CERN package HBOOK4. Display of histograms is done with HPLOT5 (the CERN display package), PAW (CERN Physics Analysis Workstation package) or DISPLAY5 (a DØ modification of an LBL display package). DØ uses the Fermilab-maintained DI-3000 version of the PAW-HIGZ package.

Three dimensional displays of events are also made on Evans and Sutherland[127] color workstations permitting real time rotation, pan, and zoom operations.

Program Builder

A general facility has been developed for assembling DØ programs which simplifies and standardizes many routine functions. For example, reading events, creating standard output files, exercising certain standard analysis packages in the correct order, *etc.* is better kept hidden from the ordinary user so that these processes remain uniform and controlled. The tool for assembling the standard building blocks and enforcing discipline among users is the Program Builder (PBD). A standard framework is provided for each general functional group of programs; (*e.g.* Monte Carlo simulators, event reconstruction, on-line event monitoring, and offline event analysis.)

The Program Builder is driven by easily editable ASCII files. For each framework, there is a file listing the 'User Hooks', and files for every application package listing the corresponding interfaces to be called by those hooks. The hooks are typical stages in programs, such as job initialization, event processing, event display, event dump, job summary, *etc.*. In addition to the list of interfaces, such package files also list any special application object libraries and any RCP files they require.

A user can easily create a new package file by editing a previously existing package file. The same application package can be used in different frameworks. Thus, a package developed in the offline reconstruction may also be used in an online framework. The Program Builder is invoked by a simple command giving the framework and list of application packages as options. It then generates the Fortran code for the calls to interfaces by the user hooks, a link command file to make the executable, and a setup command file to run it. Complex application packages can be built from combinations of simpler application packages. Communication between applications can only occur through ZEBRA banks or utilities that access ZEBRA banks.

7.3 Event Monte Carlo

The Monte Carlo simulation of the DØ experiment has been of great importance throughout the planning and building phase of the project, and of course is essential for performing physics analyses. Early modelling gave crucial information affecting the

detailed design of the detector. For example, the design of the interface between central and end calorimeters was one of the most difficult to understand and the Monte Carlo simulations here were invaluable. In addition, preparation of the full reconstruction code for the analyses of events required a simulation of the *full* detector with all detailed physical processes of scattering and interactions included. This simulation, carried to the level of raw ADC hit simulation, was used to develop the event reconstruction code and to test its performance.

The DØ Monte Carlo[128] is based on the GEANT package developed at CERN[129]. This package provides tools for specifying volumes containing particular materials and the framework for transporting particles through these volumes with appropriate physical scattering and interaction processes included. Processes such as δ-ray production, multiple Coulomb scattering, full showering by electromagnetic and hadronic particles, decays, and Bremsstrahlung by electrons and muons are accurately simulated in GEANT. The energy deposits in any specific volume are recorded for subsequent collection and transformation to digitized signals.

The geometric simulation for the DØ Detector is quite detailed. The tracking chambers and muon chambers are simulated in full detail down to the level of the sense wires, cathode material, support structures *etc.*. Figure 83 shows the tracks from a representative $t\bar{t}$ event in which the various physical processes give rise to non-ideal straight-line tracks. The calorimeter modelling is less complete owing to the complexities of the showering process and the consequent CPU requirements: the full structure of supports and individual modules are present but the internal absorber plate/ liquid argon structure is replaced with a mixture of suitable effective atomic weight. Sampling fluctuations are added after showering for each track, and the appropriate hadron to electron response (as determined from DØ tests discussed in Section 3.7) is introduced. The appropriate $\Delta\eta \times \Delta\phi \times \Delta z$ segmentation of the readout cells is imposed and the compensated energies are added for each cell. For most applications, the electromagnetic showers are allowed to evolve until the particle energies fall to 200 MeV; beyond this point energies are estimated from simple parametrizations[130] resulting in a time savings of approximately a factor of 3. The energy deposits in the calorimeter cells are summed over all particles and noise is added.

For test beam studies, the simulation technique using calorimeter material mixtures has been compared with calculations using a full plate simulation, as well as with single electrons and pions data. Figure 84 shows a typical hadronic shower in the IH module of the end calorimeter as simulated in the plate level test beam Monte Carlo. Figure 85 shows the comparison of electron and pion energy resolutions obtained for both versions of Monte Carlo and data; both Monte Carlo techniques give adequate representation for the data. Figure 86 shows distribution of the fraction of energy deposited in the EM4 layer of the CC for 50 GeV electrons near 90°. The results from test beam data, and the Monte Carlo using the full plate representation and the mixture Monte Carlo with full showering and shower parametrization are shown. The plate Monte Carlo is a good representation

to the data; the parametrized mixture Monte Carlo is less good, but adequate for most purposes. Figure 87 shows the comparison of energy deposited in the ECIH hadron calorimeter layers for 100 GeV pions at $\eta = 1.95$. Both test beam data and the plate Monte Carlo distributions are shown and the agreement is good. Though not a perfect representation of all aspects of the data, the mixture version of the Monte Carlo for the calorimeters is useful because it allows a reduction in CPU time for single particle event generation by a factor of over four with respect to the full representation of the calorimeter at the plate level. For simulation of $\bar{t}$-t events in the full DØ detector, the mixture representation Monte Carlo requires about 23 VUP hours per event.

Another technique for speeding up the full Monte Carlo simulation of $\bar{p}$-p collisions which has been used successfully involves the creation of libraries[131] [132] [133] of showers in the calorimeters, generated from the full GEANT simulation. These showers are parametrized in terms of the particle momentum (7 ranges), location of the primary vertex along the beam line (6 ranges) and η (37 ranges) for both EM and hadronic showers. Interpolation of variables within the range is performed when a shower with approximately correct variables is chosen. The number of showers in the library is approximately 1.3×10^6. The shower library simulations have been extensively compared with the full (mixture level) event Monte Carlo simulations and represent the distributions and correlations quite well[133] . Simulation of events with shower libraries requires about 25 VUP-sec for $t\bar{t}$ events.

7.4 Offline Event Reconstruction and Processing

Development of the full DØ reconstruction program DØRECO has proceeded through the steps outlined above. Extensive SA/SD specifications were drawn up and discussed. ZEBRA structures were designed for data from each of the detectors, with increasing complexity of calculation and refinement. The code has been continuously developed by a large number of physicists working in many locations, with frequent updates and releases of the several libraries.

Certain rules were adopted from the beginning. All physics and calibration data were stored in ZEBRA banks. The various sub-packages of DØRECO communicate with each other only through ZEBRA blocks, and a strictly limited number of interface routines. Although most code development and the DØ Libraries are accomplished on VAX-VMS machines, all code has been developed in FORTRAN 77, augmented by a limited number of specific extensions. Special rules were adopted for machine dependent code. A tool called DØFLAVOR was developed which checked all code for adherence to DØ standards. A special editor, EVEDT[134] was employed which supported standard conventions for programming. EVEDT also implemented methods for accessing the source for any subroutine and ZEBRA bank documentation in the DØ library by simple request key operations.

A tool was developed for accessing ZEBRA bank documentation and content in memory during a debug session. The detector geometry and calibration constants are kept in RCP files. In applications programs, the FZ or RZ files made from these RCP files are accessed and maintained via the database program DBL3.

The detector specific code resulting in CD tracks, energy deposits in calorimeters, vector energy sums, and muon tracks was developed mostly by physicists closely connected with each detector. Once this code was completed in its first version, new groups were formed for the preparation of algorithms for physics signatures – electrons, photons, muons, jets and missing E_T. Membership in these groups was generally rather different from the original detector code development. The full DØRECO package contains about 150,000 lines of code, exclusive of utility libraries.

All DØ physics data is logged to double density 8mm video-quality magnetic tapes. The data samples expected for an approximately 12 month run are expected to be of order 20 million events and 10 Terabytes. In addition, those events judged to be of highest interest (approximately 10% of the full sample) based on Level 2 filter information are sent to the 'Express Line' over Ethernet for immediate reconstruction by one of six VAX 3100/76 workstations clustered with the Host computer. Event analysis of the full data set with DØRECO is made using the Fermilab Central Computing Facility farm of Silicon Graphics 4D/35 processors. A Silicon Graphics 4D/430 server provides program and calibration database storage. The production capability of this processor farm is about 100,000 events per day and is sufficient to keep processing up to date.

Two output data files from each run with DØRECO are provided: the STA file contains the raw data plus the complete results of reconstruction. The STA events are used for reprocessing events of particular interest and in preparing displays. Each STA event contains approximately 600 Kbytes. The DST file contains a compressed version of the event with the most important information intended to serve the bulk of subsequent analysis needs. The DST contains summaries of track and clusters as well as all parameters for electrons, photons, muons, jets, taus and missing E_T. The DST event size is approximately 20 Kbytes. Both versions utilize identical ZEBRA structures.

Control of the event reconstruction is provided through a software tool called the Production Manager. These programs supervise and control the flow of production jobs on each of the operations platforms. Multiple projects on multiple nodes are managed and provided with the necessary resources. Tools have been provided to submit and monitor jobs and to accumulate statistics on jobs. Each production job is fully specified in dedicated RCP files; submission of a job is done in consultation with a global resources RCP table.

The history of all files produced by the host computer and the offline production system is kept in a Production Database (PDB), based on RdB[114] . In addition to all types of event files, PDB keeps information on tapes, production programs, trigger tables and the relevant relationships. Dedicated servers trap information from the Host Computer and the Production Managers and insert it into the PDB. Tools have been developed to enable

queries and make lists of datasets conforming to specified conditions.

All files produced by the Production Manager are assigned generic names uniquely identifying the dataset, as well the production path. All DØ frameworks can accept these generic names for input files. Physics application programs are provided with requested datasets through the CERN distributed file and tape management facility, FATMEN[135] by referencing these generic names. These references are typically made across the boundaries between analysis and file serving/storage clusters.

The STA files are typically kept on tape, while the DST's are largely kept on disk of a special File Serving cluster consisting of VAX 4000/60 and 3100/76 workstations. This cluster provides approximately 300 Gbytes of disk storage and 16 8mm tape drives. Robotic tape mounts provide for 128 tapes on two of the tape server nodes. This cluster, housed in the main computing facility, is split into 9 Ethernet segments and is connected through a FDDI network to the remote physics analysis clusters.

In addition to serving files for analysis, the File Server cluster is used to run I/O intensive streaming and filtering jobs. Four overlapping data streams are defined on the basis of the Level 2 filter bits; they are Electrons, Muons, Mininum Bias , and Missing ET. These streams are provided for both STA and DST files and are intended to streamline any reprocessing made necessary by reconstruction program changes. In addition, events are filtered following reconstruction, based upon the full available offline information. The pool of filtered events consists of approximately 25% of the original sample for all physics groups except QCD jets. The QCD events are handled separately since most of these triggered events are of good quality. Instead of filtering these, special 'micro DST' files are written which achieve a factor three more compression than the regular DST's.

The offline reconstruction DØRECO was available well before the first DØ data from the collider. As a means of checking the code and allowing its evolution, a set of 100,000 events were prepared with the DØ Monte Carlo DØGEANT. These events were representative of what would be obtained with 33 nb^{-1} of data collection. They mainly contained the dominant QCD hard parton scattering processes with thresholds for jet triggering set to 50 GeV/c. In addition, some selected physics events of rarer provenance were added (together with triggers designed to select events with leptons and/or missing E_T). Analysis of this sample and associated known background samples served as the vehicle for developing DØRECO and its algorithms, as well as helping to guide the evolution of the various physics analysis techniques.

8. Acknowledgements

We express our gratitude to the superb support staffs at each of the DØ collaborating institutions. The technical staff within the Accelerator, Research and Computing Divisions and the Physics and Technical Support Sections at Fermilab have played vital roles in design, fabrication, test and operation of the detector. Financial support for the DØ Detector has been provided by the U.S. Department of Energy, the USSR State Committee for Atomic Energy, the Commissariat à L'Energie Atomique in France, the U.S. National Science Foundation, and the Department of Atomic Energy in India.

REFERENCES

1. Design Report, The DØ Experiment at the Fermilab $\bar{p}$-p Collider, November 1984.
2. S.H. Aronson *et al.*, Proceedings of Conference on Multiparticle Dynamics, Kiryat Anavim, p. 827 (1985).
3. P. Franzini, Perspectives in Electroweak Interactions, Proceedings of the XXth Rencontre de Moriond, Les Arcs, France , p. 185 (1985).
4. R. Yamada, Proceedings, Physics of Proton Antiproton Collisions, Tsukuba, Japan, p. 371 (1985).
5. M.A. Abolins, Proceedings of the First Aspen Winter Physics Conference, Annals of the New York Academy of Sciences, **461**, 63 (1986).
6. P.D. Grannis, Results and Perspectives in Particle Physics, Proceedings of Les Rencontres de Physique de la Vallée d'Aoste, La Thuile, Italy, p. 253 (1987).
7. A.P. White, Proceedings of the 8th Topical Workshop on Proton-Antiproton Collider Physics, Castiglione, Italy (1989).
8. R. Madaras, Proceedings of the Division of Particles and Fields Conference, Batavia IL, (November 1992).
9. A. Clark *et al.*, Nucl. Inst. and Methods in Phys. Res. **A279**, 243 (1989).
10. D. Buchholz *et al.*, Nucl. Instr. and Methods in Phys. Res. **A257**, 556 (1987).
11. A.R. Clark *et al.*, Nucl. Instr. and Methods in Phys. Res. **A261**, 420 (1987).
12. A.R. Clark *et al.*, Nucl. Instr. and Methods in Phys. Res., **A315**, 193, (1992).
13. NiCoTin is an alloy of Co, Cr, Ni, Fe, Mo in respective fractions of 38.8%, 19.3%, 15.6%, 13.3%, and 11.4%, manufactured by Microfil Industries SA, Switzerland.
14. J. Kadyk, Nucl. Instr. and Methods in Phys. Res., **A300**, 436 (1991).
15. V.L. Ginzberg and I.M. Frank JETP **16**, 15 (1946).
16. J.-F. Detoeuf *et al.*, Nucl. Instr. and Methods in Phys. Res. **A265**, 157 (1988).
17. J.-F. Detoeuf *et al.*, Nucl. Instr. and Methods in Phys. Res. **A279**, 310 (1989).
18. "Etude d'un Detecteur a Rayonnement de Transition pour l'Experience DØ au FNAL", Fabrice Feinstein, Ph.D Thesis, A l'Universite de Paris-Sud, Centre d'Orsay, December 1987 (unpublished).
19. "The Central Drift Chamber for the DØ Experiment: Design, Construction and Test", Ties Behnke, Ph.D Thesis, State University of New York at Stony Brook, August 1989 (unpublished).
20. "Results from a Beam Test of the DØ Forward Drift Chamber", R. Avery *et al.*, IEEE Trans. Nucl. Science (1992).
21. R. Yarema, IEEE Trans. Nucl. Science NS-33, 933 (1986).
22. B. Chase, "DØ Central Tracking Discrete Shaper", DØ Note #953 (Apr. 1990)

(unpublished).

23. G. Saewert and B. Chase, "Central Tracking Detector Flash A/D Converter Buffer Circuit Summary", DØ Note #669 (Jan. 1988) (unpublished).
24. D. Buchholz, D. Claes, B. Gobbi, S. Park, "FADC Simulation Studies", DØ Note #326 (Dec. 1985) (unpublished).
25. M.I. Martin, M.E. Johnson, M.J. Mayberry, and D.C. DeGroot, IEEE Trans. Nucl. Science NS-34, 258 (1987).
26. D. DeGroot, "DØ Central Tracking Zero Suppression Chip Description", DØ Note #1013 (Aug. 1990) (unpublished).
27. "The dE/dx Capabilities of the D0 Tracking System" S. Rajagopalan, Ph.D. Thesis, Northwestern University June 1992 (unpublished).
28. "The DØ Detector Forward Drift Chamber Performance and Physics Capability in the 1990 FNAL Testbeam Run" J. Bantly, Ph.D. Thesis, Northwestern University June 1992 (unpublished).
29. Y. Ducros *et al.*, Nucl. Instr. and Methods in Phys. Res. **A277**, 401 (1989).
30. W. Guryn, Proceedings of the Second Internatational Conf. on Calorimetry in High Energy Physics, Capri Italy, Oct 14 - 18 1991.
31. Manufacturing Sciences Corp., Oak Ridge TN.
32. M. M. Baker *et al.*, Trans. Farad. Soc. **62**, 2525 (1966).
33. NVF Company, P.O. Box 6096, Broadview IL 60153.
34. Abatron Inc., 33 Center Dr., Gilberts IL 60136.
35. R. D. Luther, G. T. Mulholland, and K. J. Krempetz Advances in Cryogenic Engineering, **35B**, 1819 (1989).
36. A.L. Spadafora, Proceedings of the 5th Pisa Meeting on Advanced Detectors, May 26-31, 1991 (Elba).
37. H. Aihara *et al.*Nucl. Instr. and Methods in Phys. Res. **A325**, 393 (1993).
38. Bicron Corp., 12345 Kinsman Rd., Newbury OH 44065.
39. The small-$|\eta|$ boxes, where the corrections are expected to be smaller, employed Russian built 10-stage PM60 phototubes. In the large-$|\eta|$ boxes where dead material corrections are expected be largest, we have used Hamamatsu R647 phototubes.
40. G.C. Blazey, Proceedings of the First Internatational Conf. on Calorimetry in High Energy Physics, Batavia, IL, Oct 29 - Nov 1, 1990, (ed. D. Anderson, M. Derrick, H.E. Fisk, A. Para, C. Sazama), p. 101.
41. W. Hoffmann *et al.*, Nucl. Instr. and Methods **135**, 151 (1976).
42. E.I. DuPont de Nemours Inc., Wilmington DE.
43. P. Franzini, Proceedings of the First Internatational Conf. on Calorimetry in High Energy Physics, Batavia, IL, Oct 29 - Nov 1, 1990, (ed. D. Anderson, M. Derrick,

H.E. Fisk, A. Para, C. Sazama), p. 359.

44. R. D. Schamberger, Proceedings of the Second International Conference on Advanced Technology and Particle Physics, Como Italy 11-15 June, 1990.
45. M. Demarteau, Proceedings of the First Internatational Conf. on Calorimetry in High Energy Physics, Batavia, IL, Oct 29 - Nov 1, 1990, (ed. D. Anderson, M. Derrick, H.E. Fisk, A. Para, C. Sazama), p. 91.
46. P.M. Tuts, Proceedings, Instrumentation For Colliding Beam Physics, Novosibirsk (1985), 183-188.
47. S. Feher, Proceedings of the Second Internatational Conf. on Calorimetry in High Energy Physics, Capri Italy, Oct 14 - 18 1991.
48. David L. Huffman, Proceedings of the IEEE Meeting, Nov. 1991 (Santa Fe NM).
49. B. Cox *et al.*, Proceedings of the 1985 DPF Meeting of the American Physical Society, Eugene, Oregon, p887 .
50. P.M. Tuts, Proceedings of the 1986 Conference on High Energy Physics, Berkeley CA, 1455 (1986) p.1455-1458.
51. S. Aronson *et al.*, Nucl. Instr.and Methods in Phys. Res. A269, 492 (1988).
52. Paolo Franzini, Nucl. Instrum. and Methods in Phys. Res., A263, 78 (1988).
53. Stephen J. Wimpenny, *et al.*, Nucl. Instr. and Methods in Phys. Res. A279, 107 (1989).
54. M. Abolins, *et al.*, Nucl. Instr.and Methods in Phys. Res. A280, 36 (1989).
55. Paul Draper, Proceedings of the European Physical Society, Madrid, September 1989, and Nucl. Inst. and Methods in Physics Res., B16, 506 (1990).
56. P. Franzini, Nucl. Instr. and Methods in Phys. Res. A289, 438, (1990).
57. S. Abachi *et al.*, Nucl. Instr. and Methods in Phys. Res., 53 (1993).
58. Anthony L. Spadafora, Proceedings of the First Internatational Conf. on Calorimetry in High Energy Physics, Batavia, IL, Oct 29 - Nov 1, 1990, (ed. D. Anderson, M. Derrick, H.E. Fisk, A. Para, C. Sazama), p. 77.
59. Hiroaki Aihara, Proceedings of the 1990 IEEE Nuclear Science Symposium (Arlington, VA) Oct 23-26, 1990.
60. N.A. Amos, Proceedings of the First Internatational Conf. on Calorimetry in High Energy Physics, Batavia, IL, Oct 29 - Nov 1, 1990, (ed. D. Anderson, M. Derrick, H.E. Fisk, A. Para, C. Sazama), p. 84.
61. N. A. Roe, Proceedings of the Second Internatational Conf. on Calorimetry in High Energy Physics, Capri Italy, Oct 14 - 18 1991.
62. Jonathon Kotcher, "Response of the DØ Calorimeter to Cosmic Ray Muons", Ph.D. thesis submitted to New York University, October 1992 (unpublished).
63. These studies have recently been extended down to 2 GeV.

64. R. Wigmans, Nucl. Inst. and Methods **A259**, 389, (1987); *ibid* **A265**, 53 (1986).
65. R. Engelmann *et al.*, Nucl. Instr. and Methods **216**, 45 (1983).
66. D. Kewley, G.C. Blazey, J. Chiu, T. Ferbel Nucl. Instr. and Methods in Phys. Res. A290, 346 (1990).
67. K. De, "A Monte Carlo Study of Hadronic Energy Corrections in the ICD", DØ Note #1017 (Aug. 1990) (unpublished).
68. R. Stephens, "Energy Corrections for the CC/EC Transition Region", DØ Note #1165 (Sept. 1991) (unpublished).
69. D. Green *et al.*, Nucl.Instr. and Methods **A244**, 356 (1986).
70. R. Yamada *et al.*, IEEE Transactions on Magnetics, **28**, 520 (1992).
71. R. Yamada *et al..*, "Field Calculation of DØ Toroids and Comparison with Measurement", Fermilab TM-1786 (1992).
72. C. Brown, *et al..*, Nucl. Instr. and Methods in Physics Research **A279**, 331 (1989).
73. Glasteel Inc., 1727 Buena Vista Ave, Duarte CA.
74. "Fast Non-Explosive Gases for Drift Chambers", D. Green *et al.*, Fermilab TM-1523, May 1988, (unpublished).
75. J.M. Butler *et al.*, Nucl. Instr. and Methods in Phys. Res. **A290**, 122 (1990).
76. Yu.M. Antipov *et al.*, Nucl. Instr. and Methods in Phys. Res. **A297**, 121 (1990).
77. Mao Huishun, "Muon Chamber Electrostatic Calculation and Comparison to Beam Test Results", DØ Note #1014 (Aug.1990) (unpublished).
78. T. Marshall, "Muon Chamber Performance in the Collision Hall and Background Studies", DØ Note #761 (Sept. 1989) (unpublished).
79. N. Oshima and S. Igarashi, "Response of the DØ Muon Chambers to Changes in Voltage, Incident Angle, Gas Composition and Oxygen Contamination", DØ Note #805 (Feb. 1989) (unpublished).
80. G.S. Gao and R. Partridge, IEEE Trans. Nucl. Sci. **38**, 286 (1991).
81. M. Abolins *et al.*, IEEE Trans. on Nucl. Sci **36**, 384 (1989).
82. M. Abolins *et al.* Nuclear Instruments and Methods in Physics Research, **A289**, 543 (1990).
83. M. Fortner *et al.*, IEEE Transactions on Nuclear Science **38**, 480 (1991).
84. M. Utes, M. Johnson and M. Martin, Proceedings of the IEEE Meeting, Nov. 1991 (Santa Fe NM)
85. D. Cutts, R. Zeller, R. D. Schamberger, R. Van Berg Proceedings of the 1984 Conference on Recent Developments In Computing, Processor and Software Research For High-energy Physics, Guanajuato Mexico) 403-411.
86. D. Cutts, *et al.*, Proceedings of the Conference on Computing In High Energy Physics

(Amsterdam) 287-291 (1985).

87. D. Cutts, *et al.*, Proceedings of the IEEE 1988 Nuclear Science Symposium, Orlando, FL, Nov 9-11, 1988.
88. D. Cutts, *et al.*, Proceedings of the International Conference on Computing in High Energy Physics, Oxford, England, Apr 10-14, 1989.
89. D. Cullen-Vidal *et al.*, Proceedings of the Conference on Computing in High Energy Physics, Tsukuba, Japan (March 1991).
90. D. Cutts *et al.*, Proceedings of the Conference on Computing in High Energy Physics, (Annecy, France) CERN Preprint 92-01, p. 262 (1992).
91. ZRL Inc., Bristol RI.
92. R. Angstadt *et al.*, Proceedings of the IEEE Meeting, Nov. 1991 (Santa Fe NM).
93. J. Hoftun, "Level 2 System Programmers Manual", DØ Note #909 (Dec. 1989) (unpublished).
94. J.S. Hoftun, *et al.*, IEEE Trans. Nucl. Sci. NS-34 (1987) 710-712.
95. D. Cutts and J. S. Hoftun Conference on Computer Simulation Techniques in High Energy Physics, Argonne, Ill., Aug 1987.
96. H. Stredde, "DØ Detector Platform", DØ Note #740, (Aug. 1988) (unpublished).
97. S. J. Wimpenny *et al.* Nucl. Instr. and Methods **A279**, 359 (1989).
98. M.-J. Yang *et al.*, Proceedings of the Second International Conference on Advanced Technology and Particle Physics, Como,Italy, July 11 -17, 1990, University of California at Riverside preprint UCR/DØ/90-10 (1990)
99. S.-C. Ahn, *et al.*, Proceedings of the IEEE Meeting, Nov. 1991 (Santa Fe NM).
100. C. Rotolo, "DØ Clock Selector Fanout Module Hardware description", DØ Note #926 (Jan. 1990) (unpublished); C. Rotolo, M. Fachin, "DØ Sequencer Hardware Description", DØ Note 927 (Jan. 1990) (unpublished); S.J. Chappa, C. Rotolo, "DØ Phase Coherent Clock", DØ Note #1214 (Oct. 1991) (unpublished).
101. L. Paterno and J. F. Bartlett, "User Manual for the DØ Clock Interface, DØ Note #1029 (Oct. 1991) (unpublished).
102. H. Jöstlein, Proceedings of the Second International Workshop on the Alignment of Accelerators, Hamburg Germany, September 1990.
103. Capacitec, P.O. Box 819, Ayer MA.
104. The Fredericks Co. P.O. Box 67, Huntington Valley PA.
105. Honeywell Corp. model 924AB4W-L2P.
106. R. Goodwin, *et al.*Nuclear Instruments and Methods in Physics Research **A247**, 107-111 (1986).
107. R. Goodwin, *et al.*, Proceedings of the International Conference on Accelerator and Large Experimental Physics Control Systems, p. 125, Vancouver, British Columbia,

Canada, October 1989.

108. M. F. Shea, *et al.*, Proceedings of the Europhysics Conference on Control Systems for Experimental Physics, Villars, Switzerland, September 1987.
109. J.F. Bartlett, S. Fuess, H. Prosper, "Users Reference Manual for DØ Control Data Acquisition Services", DØ Note #866 (Dec. 1989) (unpublished).
110. M.Frey and A. Waller, " DØ Hardware Database" DØ Note #821 (Dec. 1988) (unpublished).
111. M.Frey, " HdB Database User's Guide" DØ Note #822 (Dec. 1988) (unpublished).
112. M.Frey, " DØ Hardware Database – Fortran Version" DØ Note #823 (Dec. 1988) (unpublished).
113. M.Frey and A. Waller, "The Hardware Monitor Database Design Note", DØ Note #824 (Dec. 1988) (unpublished).
114. Digital Equipment Corp., Maynard MA 01754.
115. S. Fuess, "DØ Alarm System Programmer's Guide" DØ Note #1558 (Nov. 1992) (unpublished).
116. P. Bhat, "Proposed NW Beamline Upgrade for DØ Test Beam, Load 2", DØ Note #1104 (Mar. 1991) (unpublished).
117. C. Grozis, *et al.*, Advances in Cryogenic Engineering, **35**, 1811, (1990).
118. M. Page-Jones, The Practical Guide to Structured Systems Design, Yourdon Press (1980).
119. S. Mellor and P. Ward, Structured Development for Real Time Systems, Yourdon Press (1986).
120. G. Kellner, private communication and ALEPH notes 127 and 142.
121. J. Linnemann *et al.*, Comput. Phys. Commun. **45**, 245 (1987).
122. M. Goosens *et al.*, CERN Library Program No. Q100 (Nov. 1991)
123. B. Adeva *et al.*, Nucl. Instr. and Methods in Phys. Res., **A309**, 318 (1991)
124. H. Prosper, Proceedings of the First Internatational Conference on Calorimetry in High Energy Physics, Batavia, IL, Oct 29 - Nov 1, 1990, (ed. D. Anderson, M. Derrick, H.E. Fisk, A. Para, C. Sazama), p. 546.
125. J. Hoftun, " COMPACK, a Command Input Package for Interactive Programs", DØ Notes #542 and #543 (Apr. 1987) (unpublished).
126. DI3000 Users Guide, Visual Numerics, Inc., 14141 Southwest Freeway, Suite 3000, Sugarland TX, 77478.
127. Model PS390 3D display terminal, Evans and Sutherland, 540 Arapeen Drive, PO Box 58700, Salt Lake City UT 84158.
128. A.M. Jonckheere, Proceedings of the Argonne National Laboratory Detector Simulation Workshop, August 1987 and DØ Note 638.

129. F. Carminati *et al.*, " GEANT User's Guide", CERN Program Library (Dec. 1991).

130. S. Linn, "A Method for Fast Electromagnetic Shower Simulation in GEANT", DØ Note #874 (Aug. 1989) (unpublished).

131. W.J. Womersley, R. Raja, A.M. Jonckheere, "Shower Libraries for DØGEANT Monte Carlo", DØ Note #650 (Dec. 1987) (unpublished).

132. Rajendran Raja, Proceedings of the Workshop on Detector Simulation for the SSC, Argonne, IL, Aug 24-28, 1987.

133. N. A. Graf, Proceedings of the First Internatational Conf. on Calorimetry in High Energy Physics, Batavia, IL, Oct 29 - Nov 1, 1990, (ed. D. Anderson, M. Derrick, H.E. Fisk, A. Para, C. Sazama), p. 539.

134. O. Callot, "EVEDT, User Guide and Reference Manual", DØ Notes #564 (June 1987) and #728 (July 1988) (unpublished).

135. J.D. Shiers, FATMEN, CERN Program Library, 1992.

FIGURE CAPTIONS

1. Isometric view of the DØ Detector.
2. Elevation view of the DØ Detector. The scales are in meters.
3. Arrangement of the DØ tracking and transition radiation detectors.
4. Plan view of the ends of the Vertex chamber, showing the active chamber region, the support structure and the electronics and feedthrough bulkhead.
5. $r - \phi$ view of a quadrant of the VTX chamber showing the arrangement of the sense wires, grid wires and cathode field shaping electrodes.
6. Drift time *vs.* drift distance in the VTX chamber for CO_2(95%)-ethane(5%).
7. The TRD detector showing the end of the polypropylene foil radiator section, the two 23 μ windows separating radiator and chamber, the conversion gap for TR X-rays, followed by the grid wire plane and the proportional wire section, and the outer support structure.
8. A typical time distribution of charge arriving at the TRD sense wire for traversal of a single 5 GeV electron.
9. Average charge collected on the TRD anodes as a function of drift time for electrons and pions.
10. End view of three segments of the Central Drift Chamber.
11. View of the Forward Drift Chamber Θ and Φ modules.
12. Block diagram of the Central Detector signal digitization electronics.
13. FADC waveforms for test tracks in a CDC chamber cell. The top and bottom traces are for the delay lines (one end's signal is inverted in the display).
14. Sample waveform digitization from the FADC, showing the quantities used for determining pulse leading and trailing edge.
15. Hit finding efficiency as a function of high voltage for the VTX chamber. Data points for both low and high threshold settings are shown.
16. Hit finding efficiency as a function of high voltage for the FDC Θ and Φ chambers. The arrows indicate the operating points.
17. Position resolution vs. position for the sense wires of the VTX chamber.
18. Position resolution vs. position for the inner and outer sense wires of the CDC chamber.
19. Position resolution vs. position for the sense wires of the FDC Θ and Φ chambers.
20. Efficiency for resolving two hits in the VTX chamber as a function of their separation distance.
21. Efficiency for resolving two hits in the FDC chamber as a function of their separation distance.

22. 70% truncated mean of dE/dx for one and two tracks seen in the full CDC chamber.
23. Distribution of total energy observed on the 3 TRD layers for both electron and pion traversals.
24. Distribution of the likelihood value calculated for electrons and pion traversals of the three TRD layers.
25. Rejection factor for 5 GeV pions vs. electron inefficiency for track angles of 90° (normal incidence) and 50°. These data are obtained using the likelihood parameter.
26. Isometric view showing the Central and two End calorimeters.
27. Schematic view of the liquid argon gap and signal board unit cell.
28. Schematic view of a portion of the DØ calorimeters showing the transverse and longitudinal segmentation pattern. The shading pattern indicates the distinct cells for signal readout. The rays indicate the pseudorapidity intervals seen from the center of the detector.
29. (a) End view of the central calorimeter. (b) $r-z$ view of half of the central calorimeter.
30. Schematic view of the CC module construction.
31. view of ECEM. The readout boards form complete disks with no azimuthal cracks. The ECIH construction is similar.
32. End view of the end calorimeter showing the ECEM at small radii and the surrounding rings of ECMH and ECOH modules.
33. Layout of the ECEM signal pads for the four layers in depth. The upper portion of the ECEM indicates the uranium plate divisions and the location of the support bolts.
34. (a) The ICD tile design showing the placement of the readout optical fibers. (b) Schematic representation of the ICD boxes with three tiles, fiber, and phototube combinations.
35. Schematic of the calorimeter preamplifier
36. Schematic diagram of the BLS signal shaping and trigger pickoff circuit (above) and the BLS sample and hold circuit (below).
37. Equivalent signal shape after BLS filter, double sample and difference.
38. Signal response for electrons, pions and β test cell as a function of high voltage.
39. Response to 100 GeV pions, with EM1<0.38 GeV (shaded), and with no cut on EM1 (unshaded).
40. Longitudinal energy depositions for pions between 50 and 150 GeV. Test beam data is shown with the boxes, together with Monte Carlo simulations.
41. Fitted values of σ/E *vs.* energy for electrons in the ECEM module.
42. Fitted values of σ/E *vs.* energy for electrons and pions in the ECMH module.

43. Position resolution for electrons in the third layer of ECEM. The pad size is 2.5 cm.
44. Energy deposition by cosmic ray muons in the CCFH Layer 1. Noise contributions, shown with dark shading, are deduced from signals observed far from the cosmic track. The data are plotted with a 3-σ suppression.
45. Ratio of electron to pion response in the ECEM+ECIH modules after correction for transverse energy leakage. Test beam data and Monte Carlo simulations are shown.
46. Scatter plot of energy vs. position across the intermodule boundary between two CCEM modules for 25 GeV electrons. (a) Before correction for energy loss in uninstrumented material. (b) After correction.
47. Distribution of observed calorimeter energy for single 100 GeV pions, before and after applying corrections based on ICD and massless gaps at (a) $\eta = 1.15$ and (b) $\eta = 1.25$.
48. Elevation view of the DØ detector showing the five muon toroids and the approximate dispositions of the A, B, and C layers of proportional drift tubes.
49. Variation of the thickness of the DØ calorimeters and muon toroids as a function of polar angle.
50. Geometric acceptance of the muon system *vs.* η for all muons passing through two and three layers of muon PDT's.
51. Exploded view of the muon chamber layout.
52. Perspective view of the two halves CF toroid and the support beams in the detector platform.
53. Contours of magnetic induction for the EF/SAMUS combination for the case that the $\vec{B}$ in the two magnets are the same.
54. Extruded aluminum section from which the "B" and "C" layer PDT chambers are constructed. The "A" layer chamber extrusions are similar, but have 4 cells instead of 3.
55. A single cell of the PDT chambers showing the equipotential surfaces surrounding cathode pads and anode wire.
56. Layout of the two separate electrodes comprising the PDT cathodes. The signals on inner and outer segments of the diamond pattern are independently measured.
57. SAMUS drift tubes: (1) HV supply wire; (2) insulating tube; (3) 30 mm stainless steel outer tube; (4) silicon rubber; (5) epoxy; (6) groove; (7) anode wire; (8) copper pin; (9) end cap; (10), (11) solder; and (12) ground wire.
58. Rate of cosmic ray tracks seen as a function of the PDT anode potential for a set of different cathode pad potentials.
59. Pulse height observed on PDT cathode pads as a function of anode potential for 3 different values of cathode potential.

60. Scatter plot of muon PDT drift times *vs.* position as determined by a separate proportional wire chamber system, for angles of incidence of 0° and 45°.
61. Deviation of a muon PDT hit coordinate from the predicted position from the PWC telescope, for full length chambers and short test modules. The measurements are made using a PWC system which adds 0.29 mm in quadrature to the deviations which are not subtracted in these data.
62. Variation of muon PDT resolution as a function of the track angle of incidence.
63. Dependence of the ratio $(Q_a - Q_b)/(Q_a + Q_b)$ with the coordinate ξ along a PDT wire. The quantities Q_a and Q_b refer to signal charges on outer and inner portions of the diamond shaped cathodes.
64. Resolution in coordinate ξ along the wire from the cathode pad ratio signal.
65. Drift time to distance relation for the SAMUS drift tube.
66. Coordinate resolution of the SAMUS tubes *vs.* drift distance.
67. Block diagram of the trigger and data acquisition system.
68. (a) One plane of the Level 0 trigger hodoscopes. Active scintillator is shown shaded. (b) Two planes rotated by 90° constitute a complete Level 0 hodoscope.
69. Time resolution distribution for the Level 0 counters from cosmic ray tests.
70. Block diagram of the Level 0 electronics. QTAC is a Charge and Time to Amplitude Converter; CFD is a Constant Fraction Discriminator; LØCTRL is a VME Controller; and VI is the DØ Vertical Interconnect described in Section 6.7. The Slow z determination also produces a flag for multiple interactions (MI).
71. (a)Block diagram of the front end card of the Level 1 calorimeter trigger. (b) Detail of adder and counter trees used to give E_T, $\not\!\!E_T$and multiplicity outputs.
72. Block diagram of the main elements of the muon trigger system. The inputs from the muon chambers are latches derived from bits set by a cathode pad hit in a specific muon proportional drift tube.
73. Block Diagram of the Level 2 trigger and data acquisition system.
74. Schematic diagram of each of the Level 2 nodes and associated VME electronics. The VME crate contains the VME Bus Adapter (pVBA), a co-processor slot, four dual multiport memories (MPMs) and the VME Buffer Driver for output events (VBD2).
75. DØ Host System computer configuration.
76. DØ Host System Software Organization.
77. Schematic diagram showing the operation of the calibration procedure.
78. Block diagram of the HV control board.
79. Block diagram of the HV dc-to-dc supply circuit.
80. Dataflow Diagram for the Alarms system.
81. Dataflow Diagram for the DØ control path processes. The circular objects are sub-

processes and the objects between horizontal lines are data stores. Arrows indicate the directions of stimulii and data transfers.

82. Structure Chart for High Voltage control.

83. $r - z$ view of the tracks in the DØ tracking detectors and beginning of the central calorimeter from a single $t\bar{t}$ event.

84. Simulated hadronic shower for a 100 GeV pion in the End IH calorimeter module.

85. (a) Fractional energy resolution *vs.* energy for electrons in the ECEM for test beam data, mixture Monte Carlo and plate Monte Carlo. The curve is a fit to the data. (b) Fractional energy resolution *vs.* energy for pions in the EC for test beam data, with and without a veto on ECEM layer 1 energy of $E \leq 0.51$ GeV, and for the plate Monte Carlo. The curves are fits to the data distributions.

86. Energy distributions for 50 GeV electrons near 90° in the CCEM layer 4 for (a) test beam data; (b) the plate Monte Carlo; (c) the mixture Monte Carlo with full showering; and (d) the mixture Monte Carlo with shower parametrization below 200 MeV.

87. Energy deposition in the ECIH calorimeter layers for 100 GeV pions at $\eta = 1.95$ for test beam data and the plate Monte Carlo.

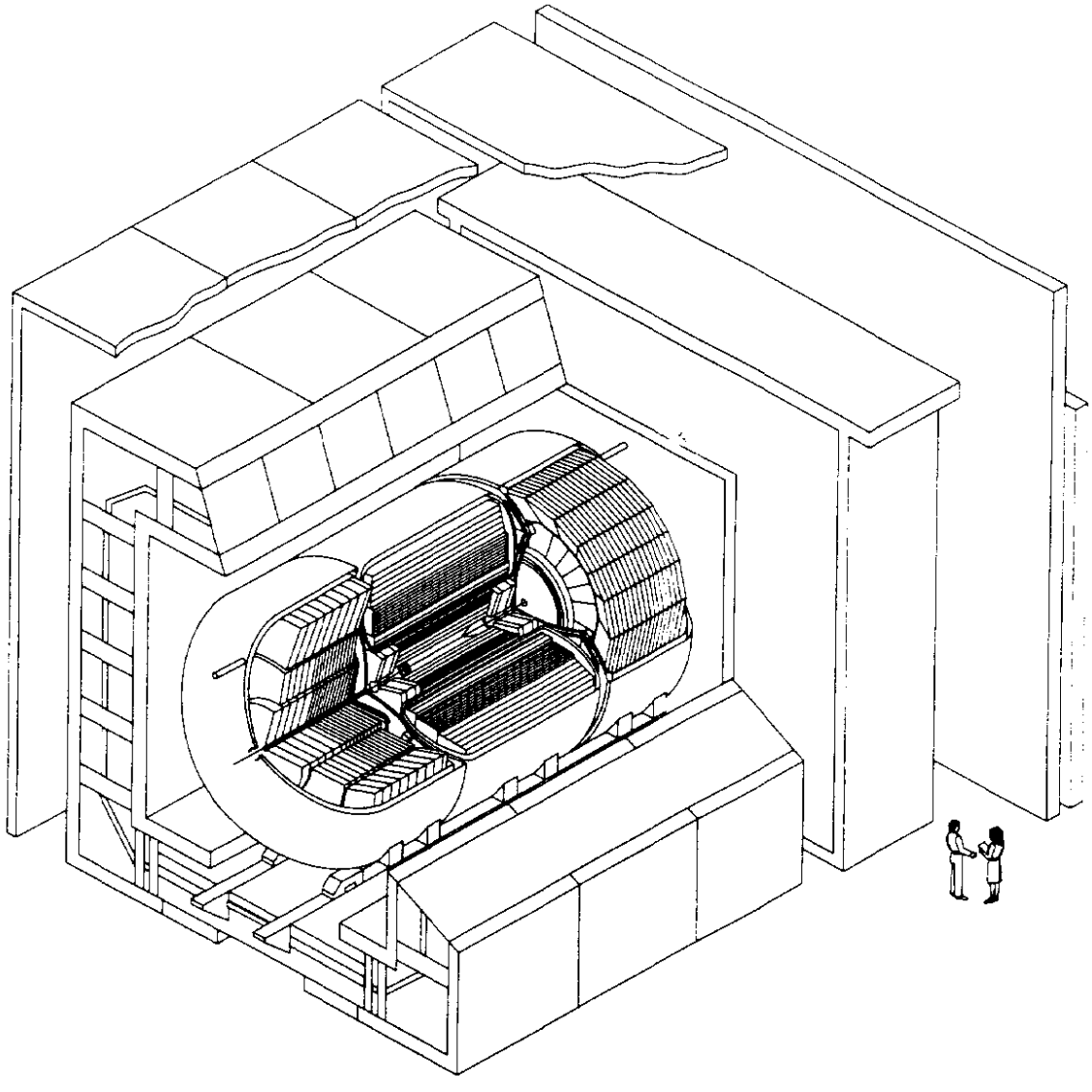

DØ Detector

Figure 1

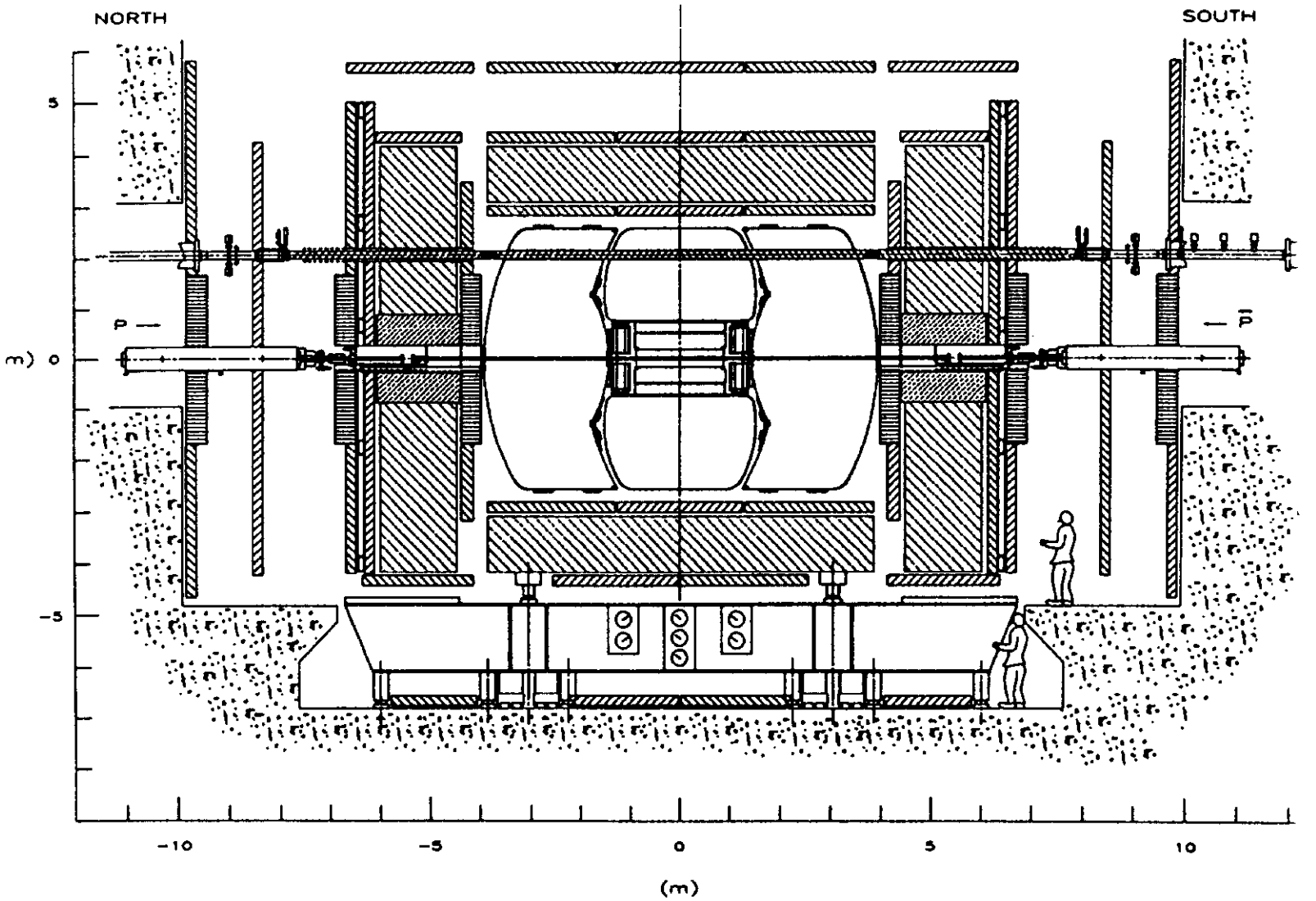

Figure 2

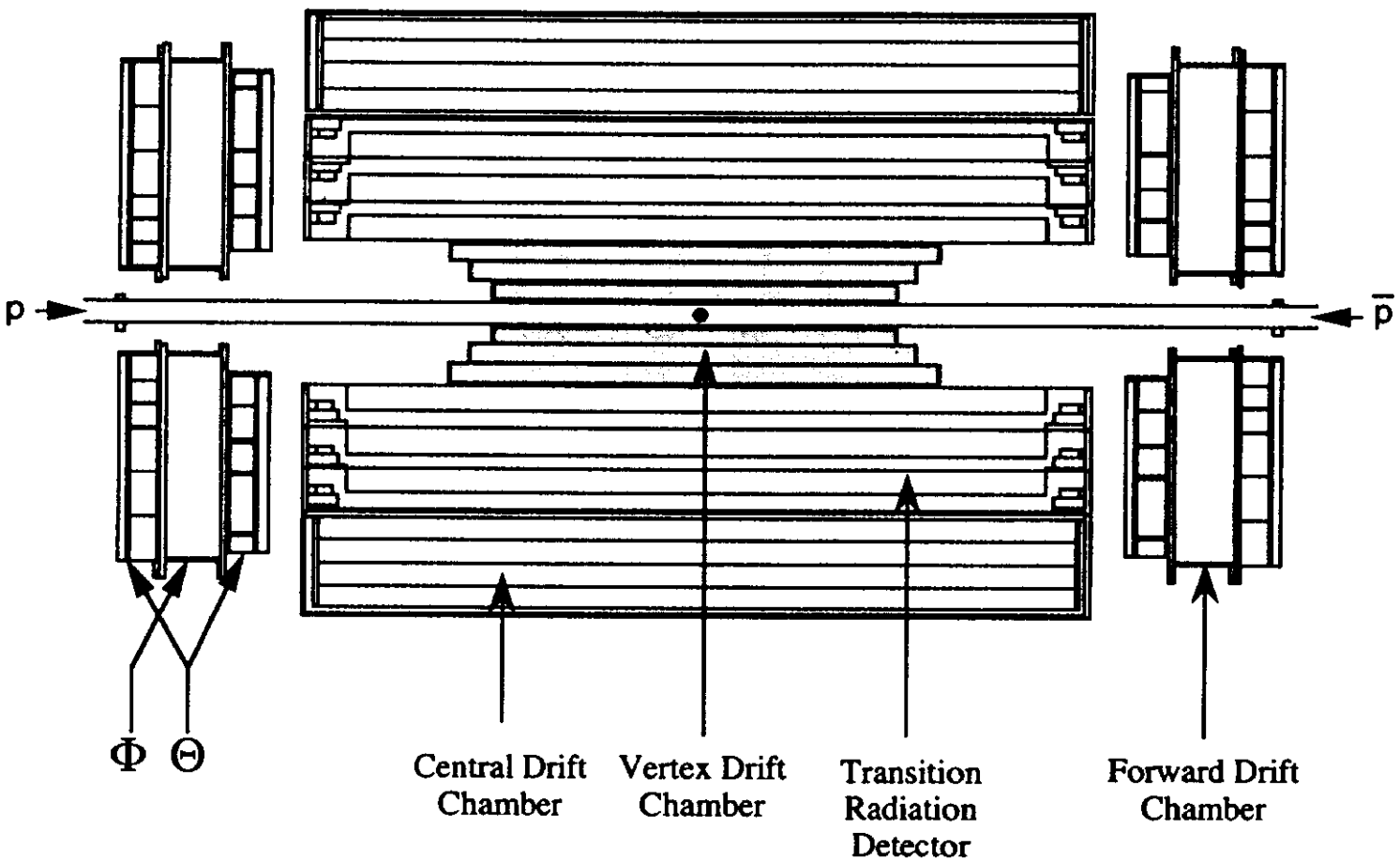
p
$\bar{p}$
Φ Θ
Central Drift Chamber
Vertex Drift Chamber
Transition Radiation Detector
Forward Drift Chamber

Figure 3

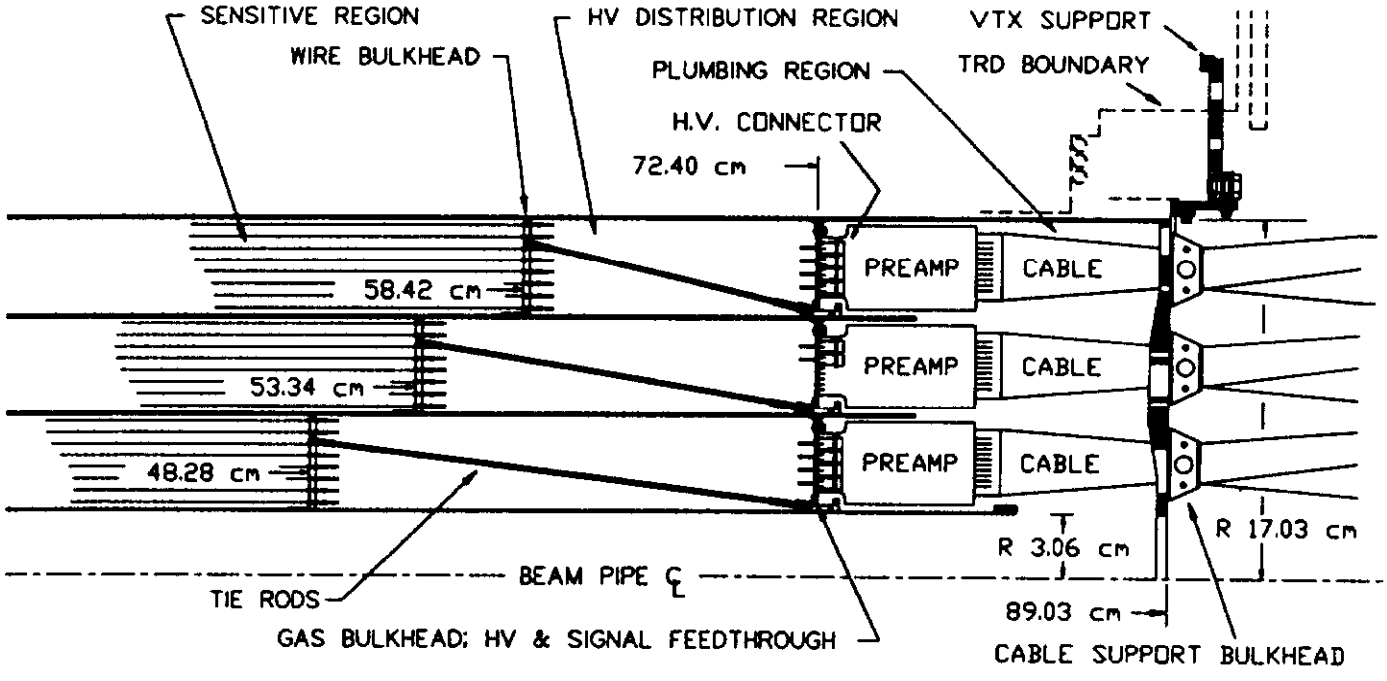
SENSITIVE REGION
WIRE BULKHEAD
HV DISTRIBUTION REGION
PLUMBING REGION
H.V. CONNECTOR
72.40 cm
VTX SUPPORT
TRD BOUNDARY
58.42 cm
53.34 cm
48.28 cm
PREAMP
CABLE
PREAMP
CABLE
PREAMP
CABLE
R 3.06 cm
R 17.03 cm
BEAM PIPE ℄
TIE RODS
89.03 cm
GAS BULKHEAD; HV & SIGNAL FEEDTHROUGH
CABLE SUPPORT BULKHEAD

Figure 4

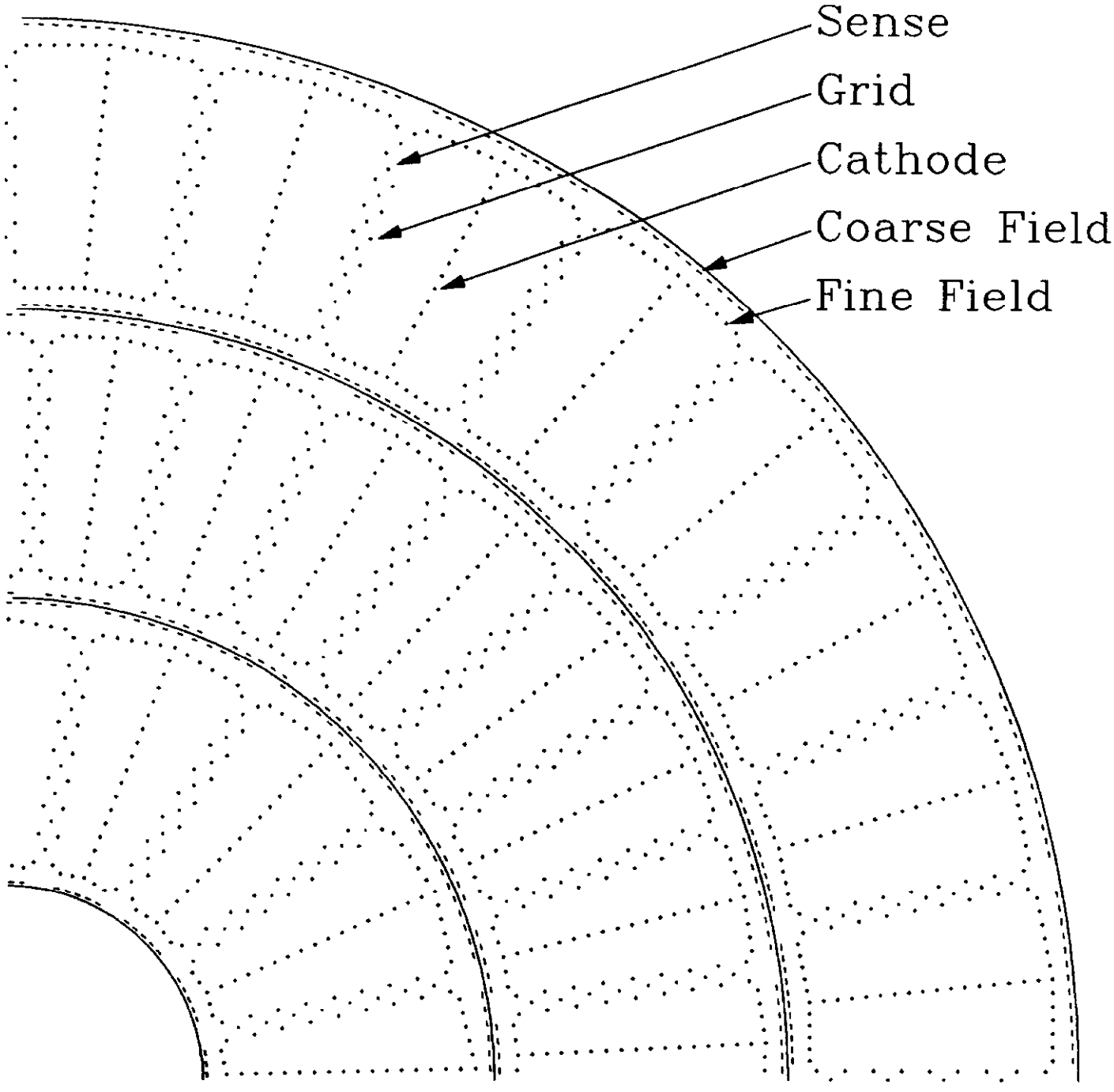

Figure 5

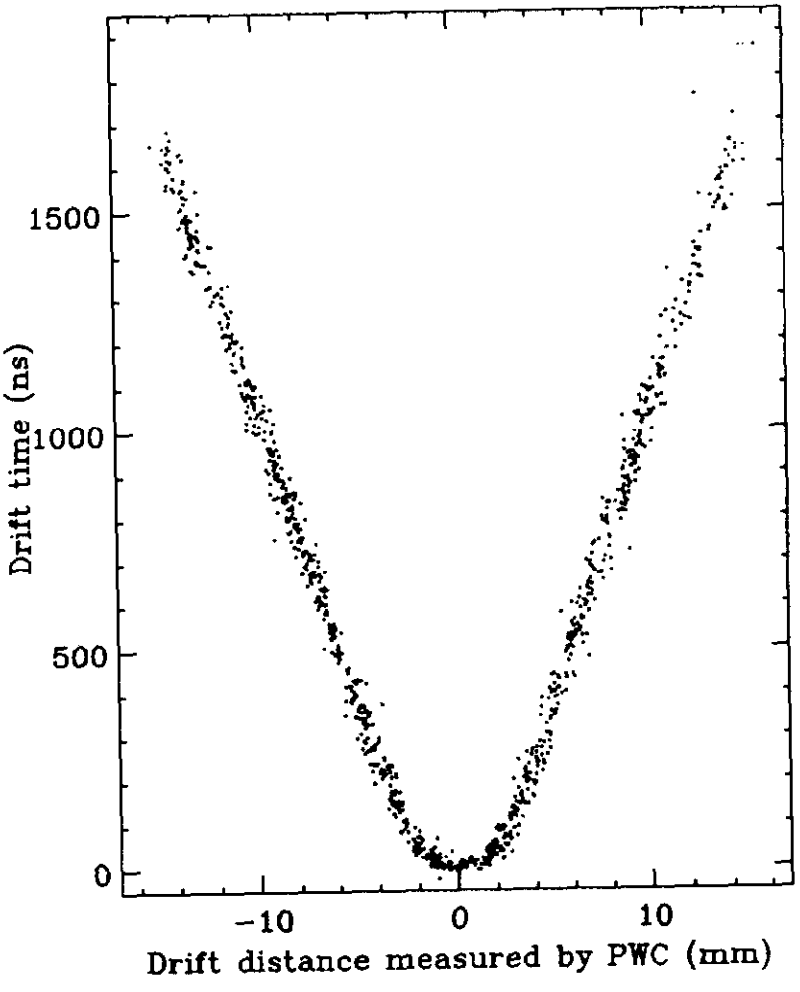
1500
1000
500
0
Drift time (ns)
−10
0
10
Drift distance measured by PWC (mm)

Figure 6

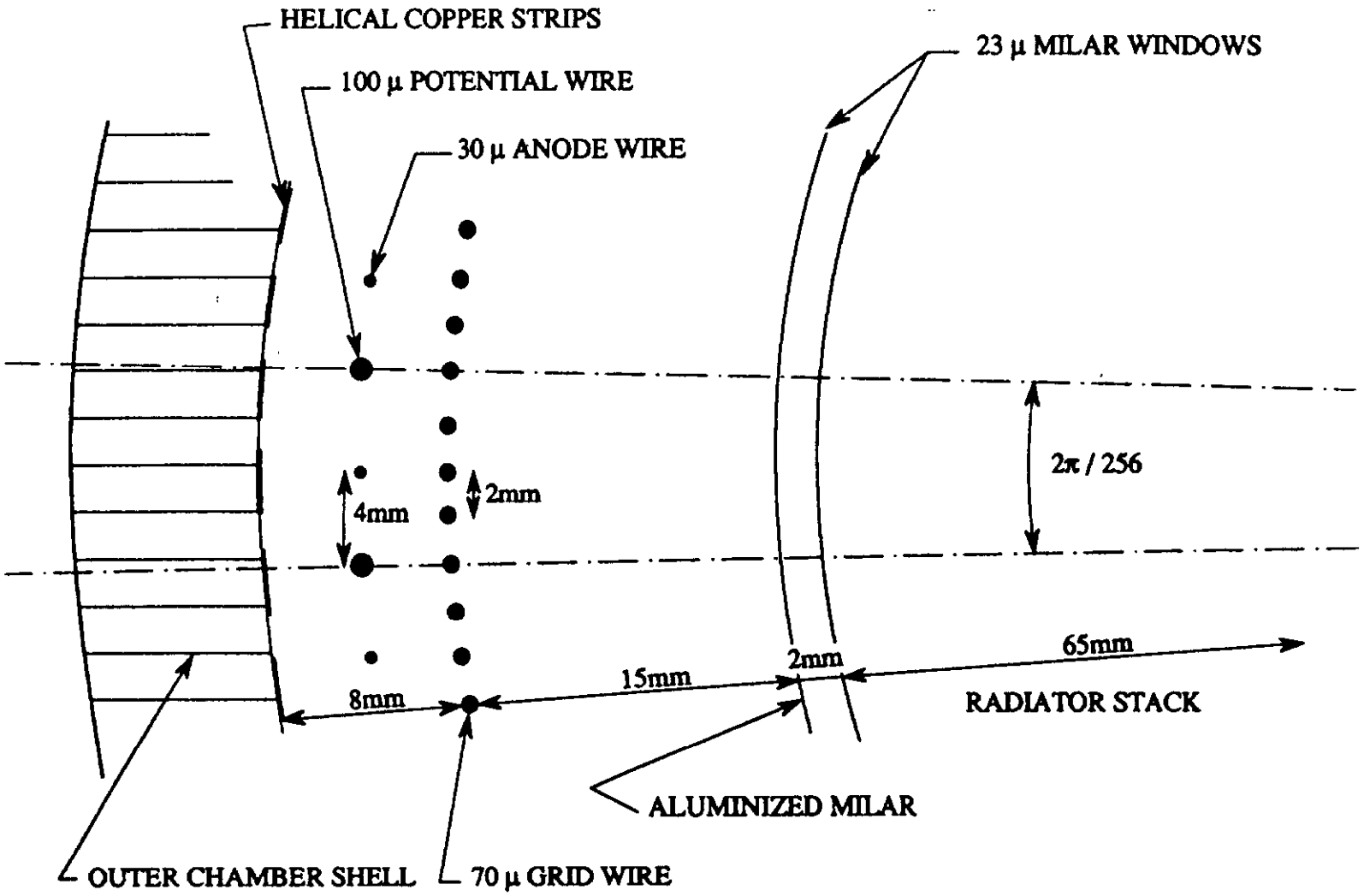
HELICAL COPPER STRIPS
100 μ POTENTIAL WIRE
30 μ ANODE WIRE
23 μ MILAR WINDOWS
2π / 256
4mm
2mm
8mm
15mm
2mm
65mm
RADIATOR STACK
ALUMINIZED MILAR
OUTER CHAMBER SHELL
70 μ GRID WIRE

Figure 7

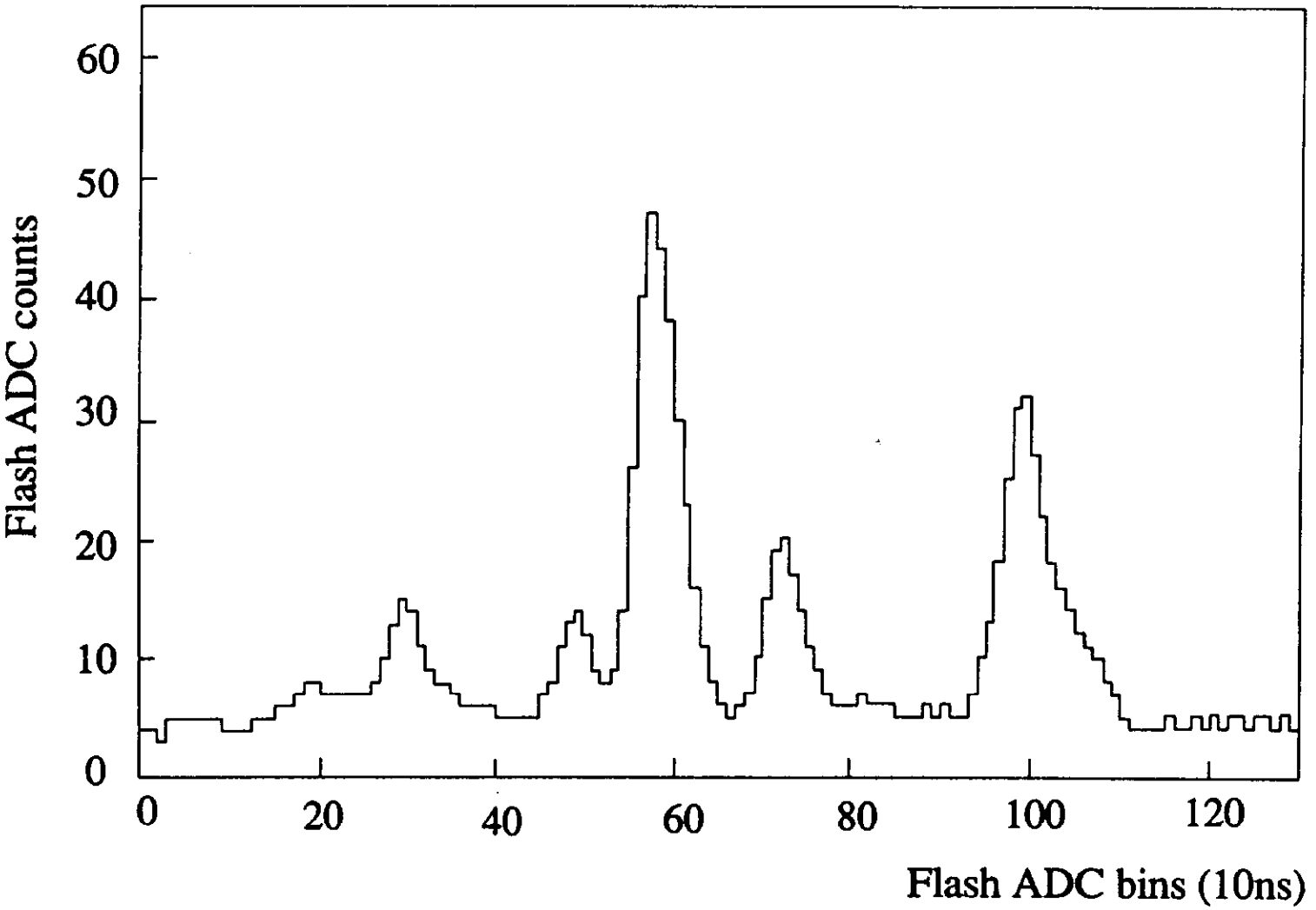
Flash ADC counts
60
50
40
30
20
10
0
0
20
40
60
80
100
120
Flash ADC bins (10ns)

Figure 8

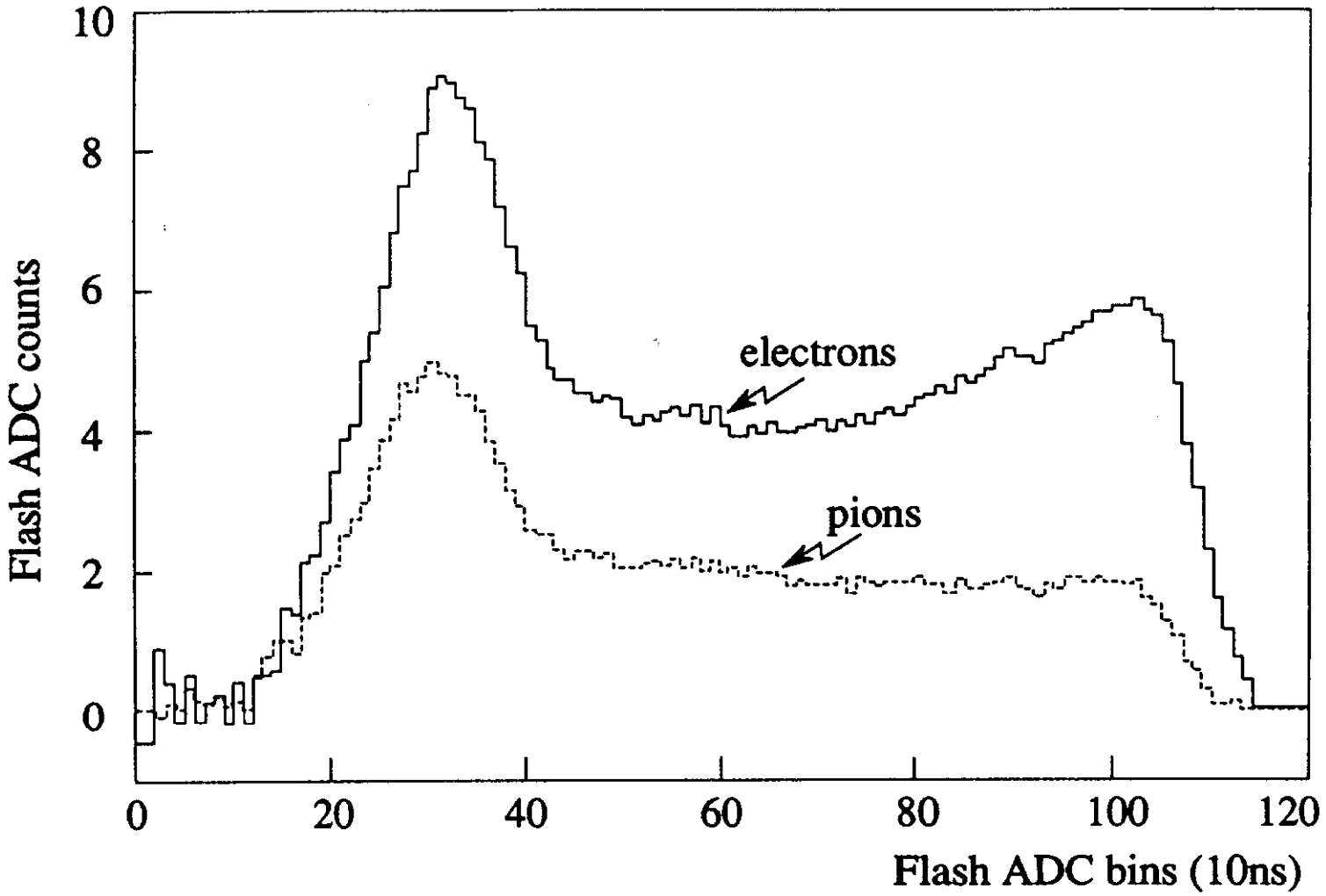
10
8
6
4
2
0
Flash ADC counts
electrons
pions
0
20
40
60
80
100
120
Flash ADC bins (10ns)

Figure 9

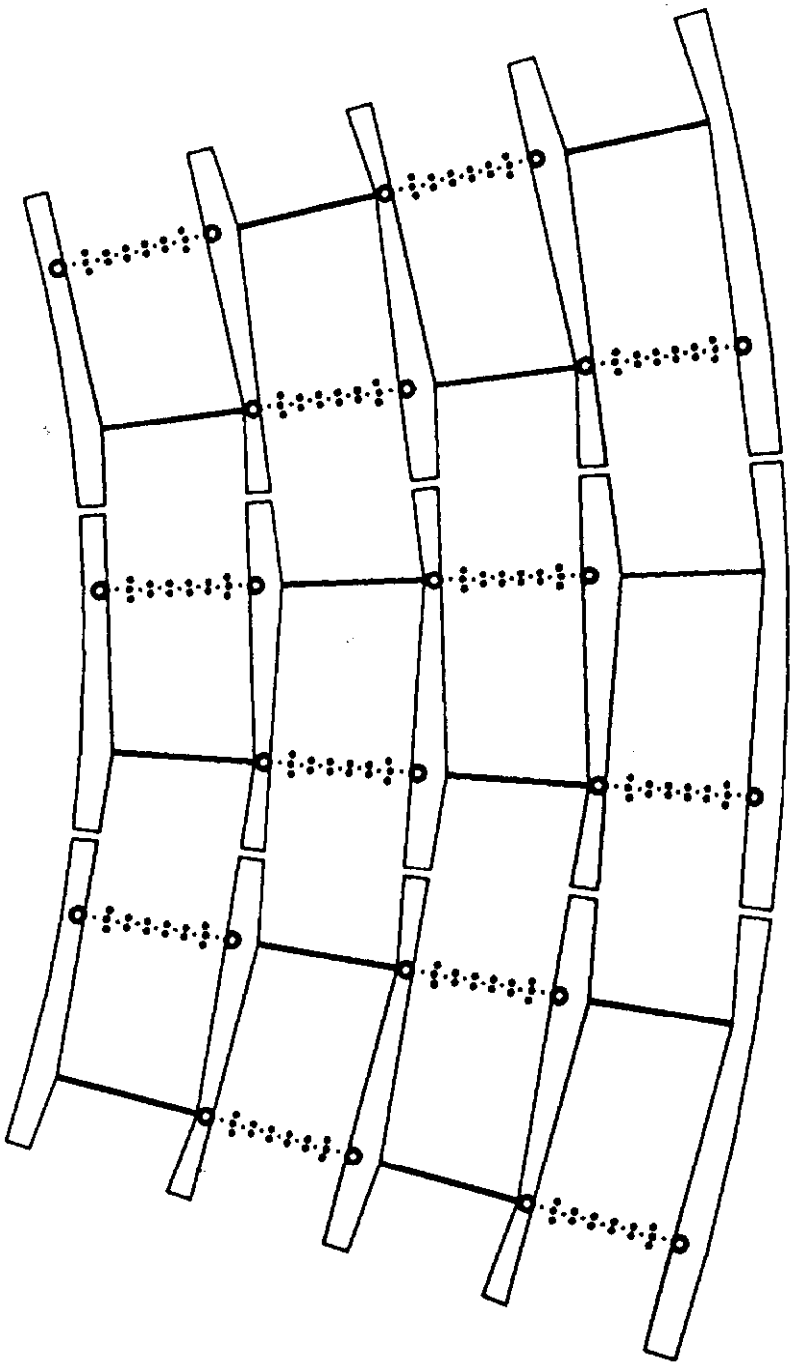

Figure 10

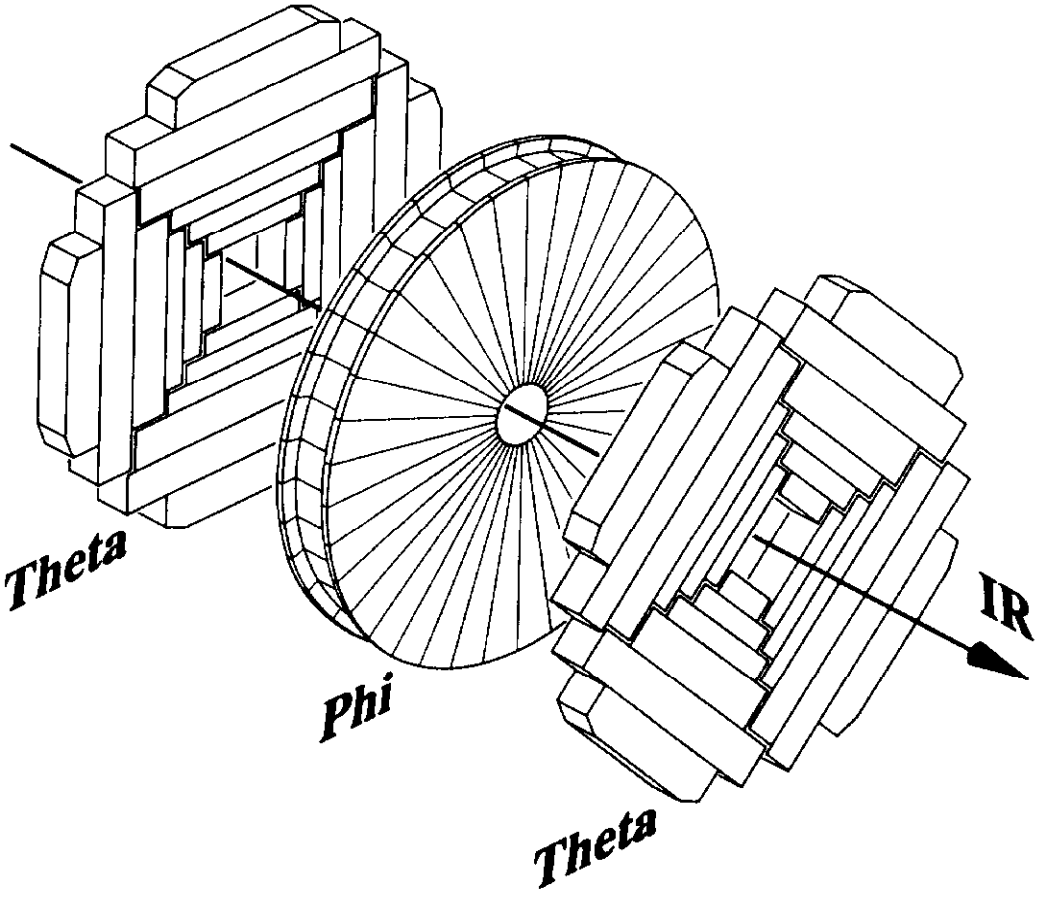

Figure 11

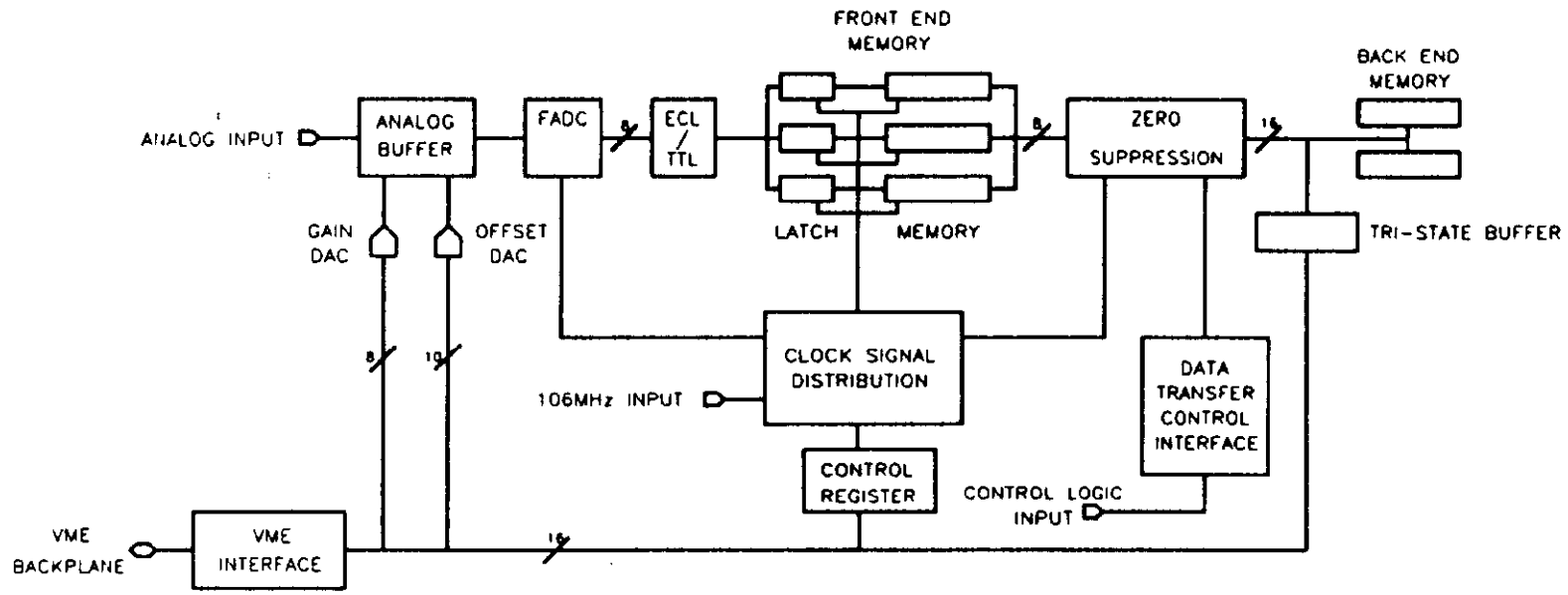

FADC MODULE – CHANNEL BLOCK DIAGRAM

Figure 12

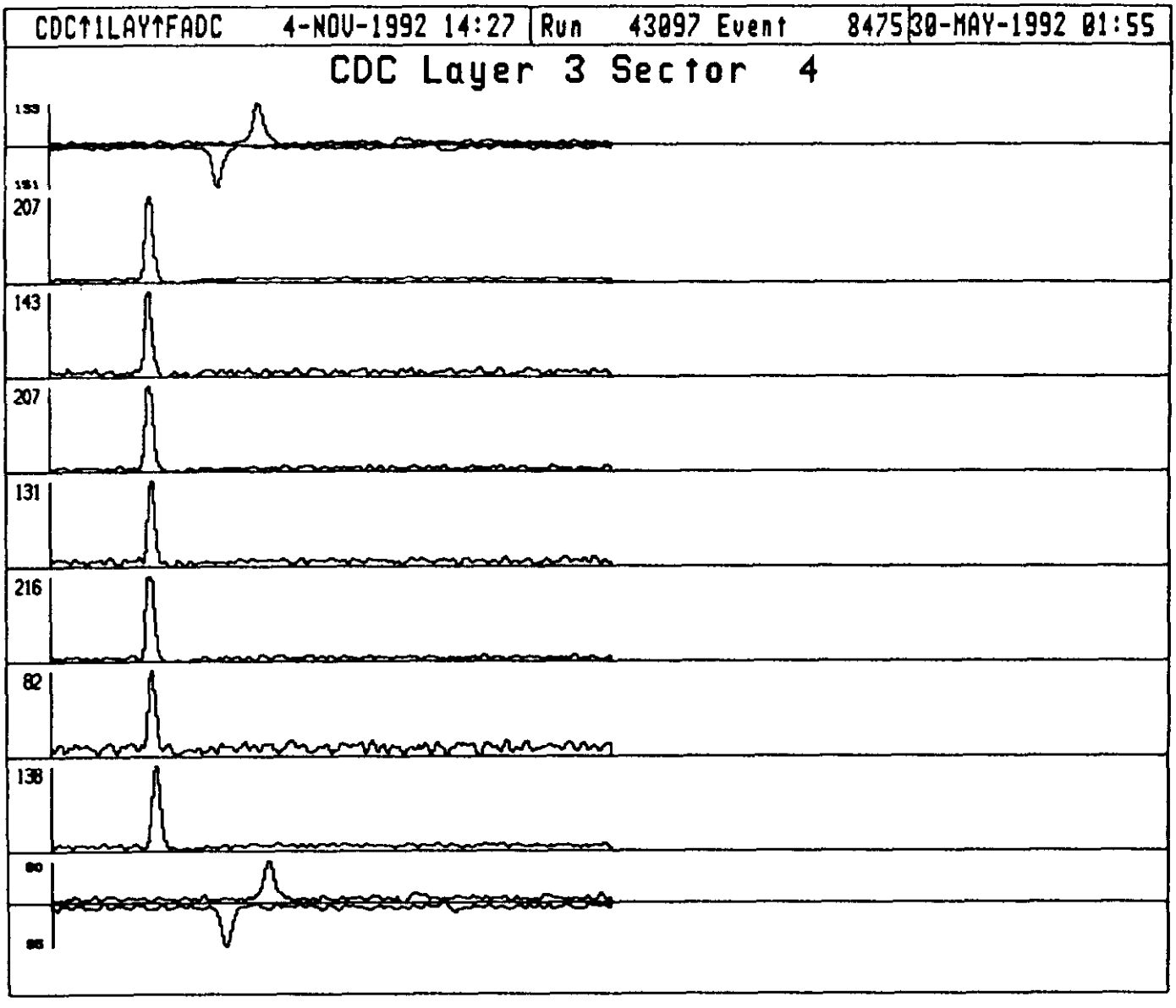
CDC1LAY1FADC
4-NOV-1992 14:27
Run 43097 Event 8475
30-MAY-1992 01:55
CDC Layer 3 Sector 4
207
143
207
131
216
82
138

Figure 13

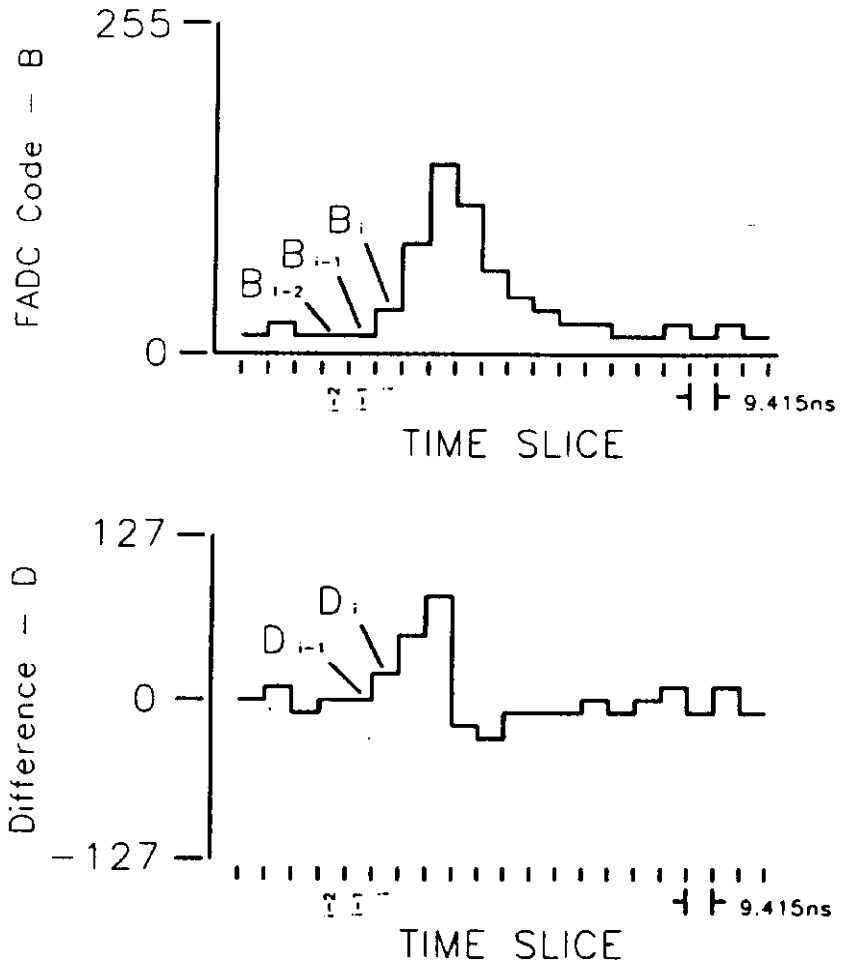

Zero Suppression Chip – Waveform Definitions

Figure 14

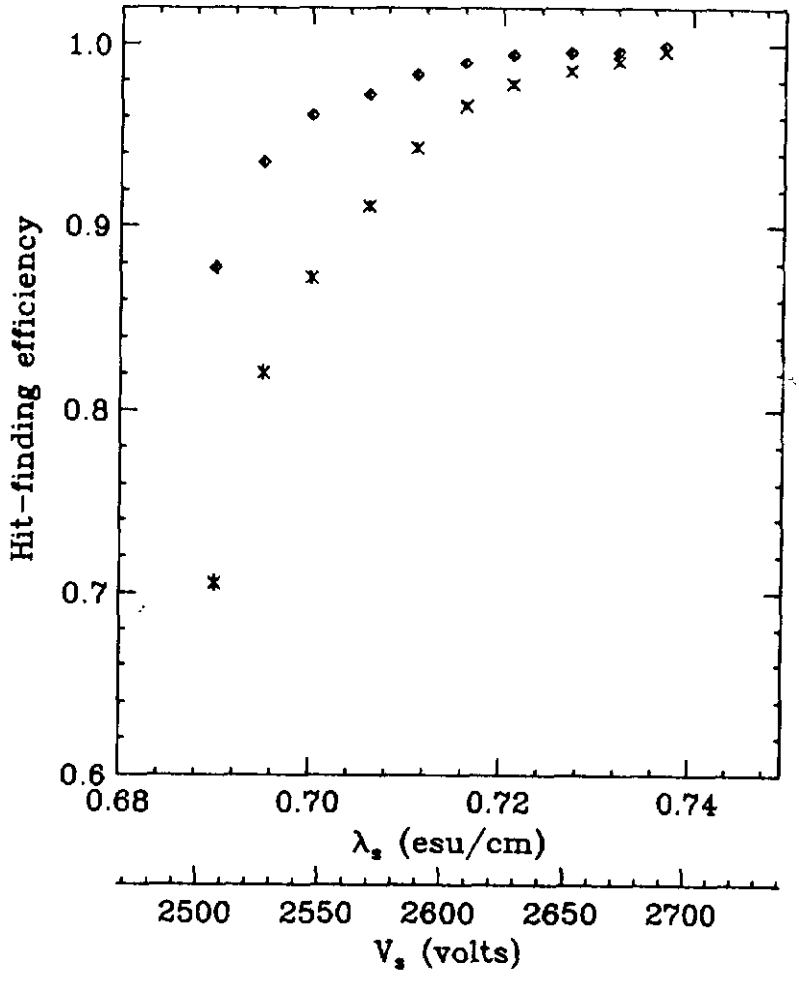
Hit-finding efficiency
1.0
0.9
0.8
0.7
0.6
0.68
0.70
0.72
0.74
λs (esu/cm)
2500
2550
2600
2650
2700
Vs (volts)

Figure 15

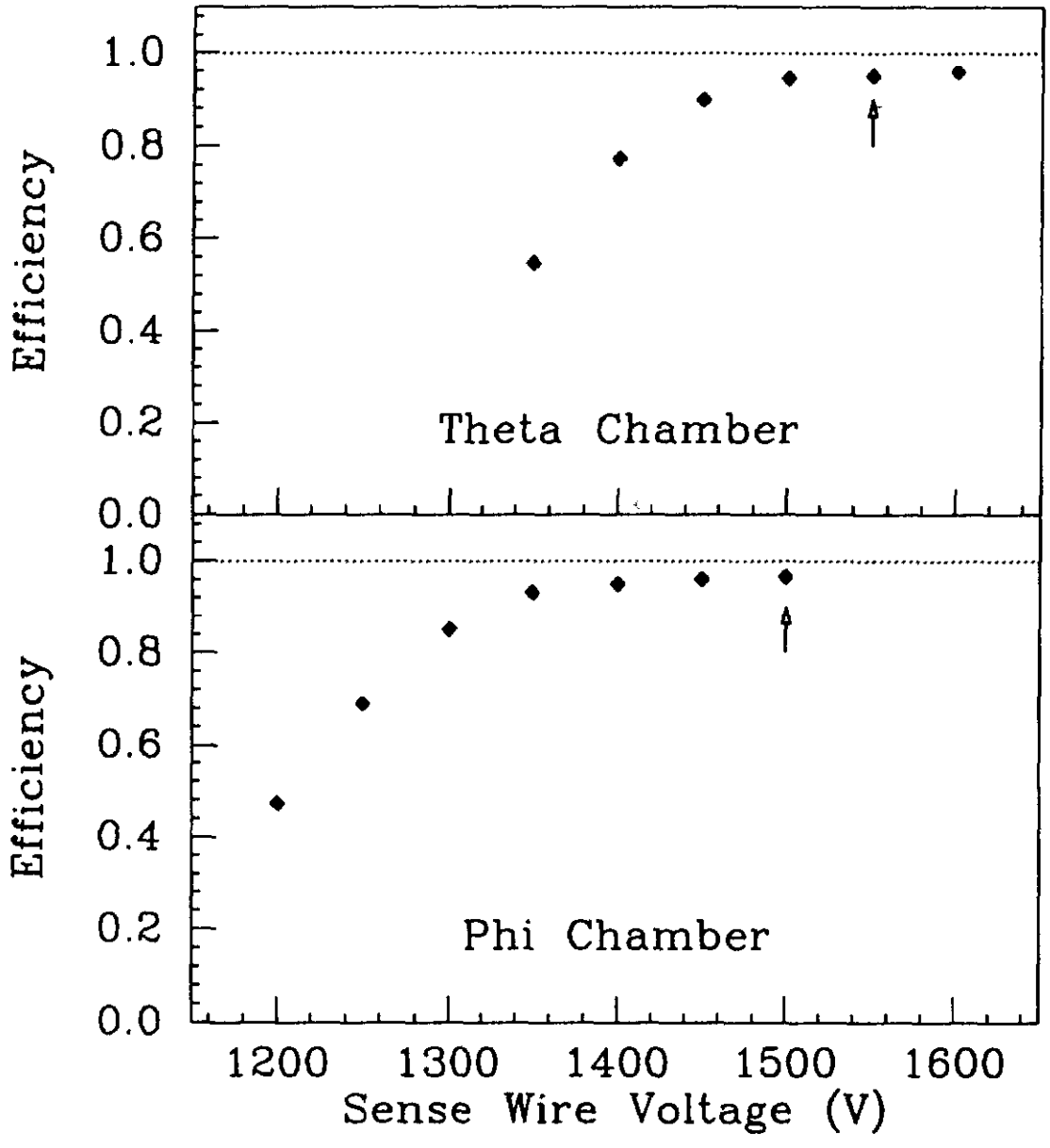
Efficiency
1.0
0.8
0.6
0.4
0.2
0.0
Theta Chamber
Efficiency
1.0
0.8
0.6
0.4
0.2
0.0
Phi Chamber
1200
1300
1400
1500
1600
Sense Wire Voltage (V)

Figure 16

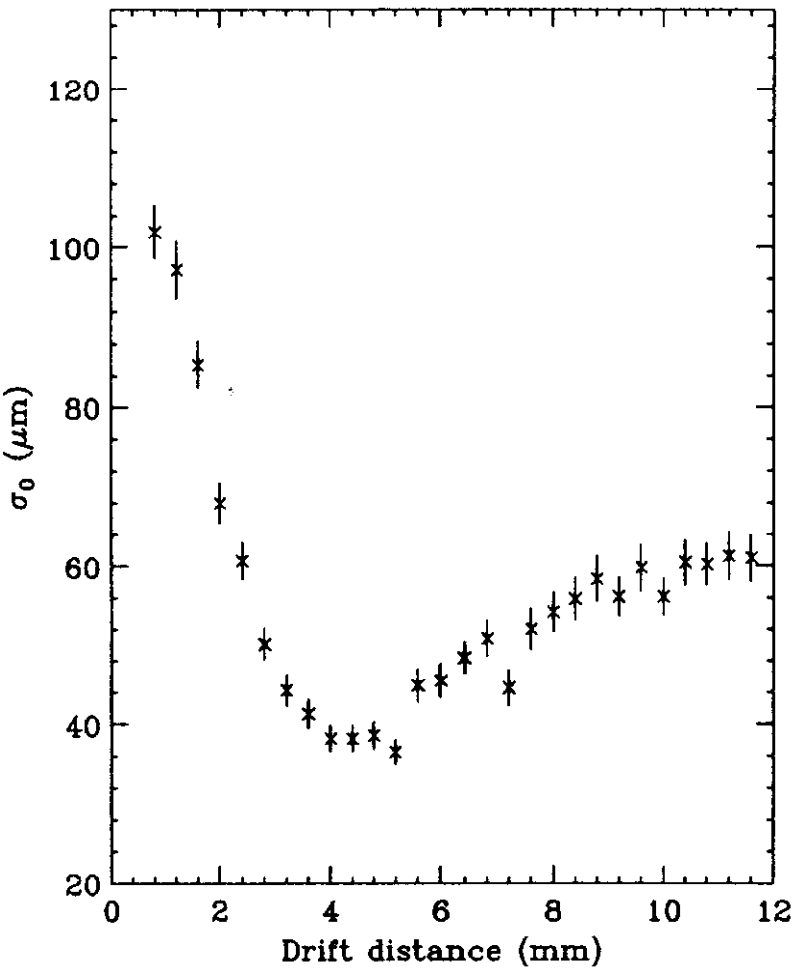

Figure 17

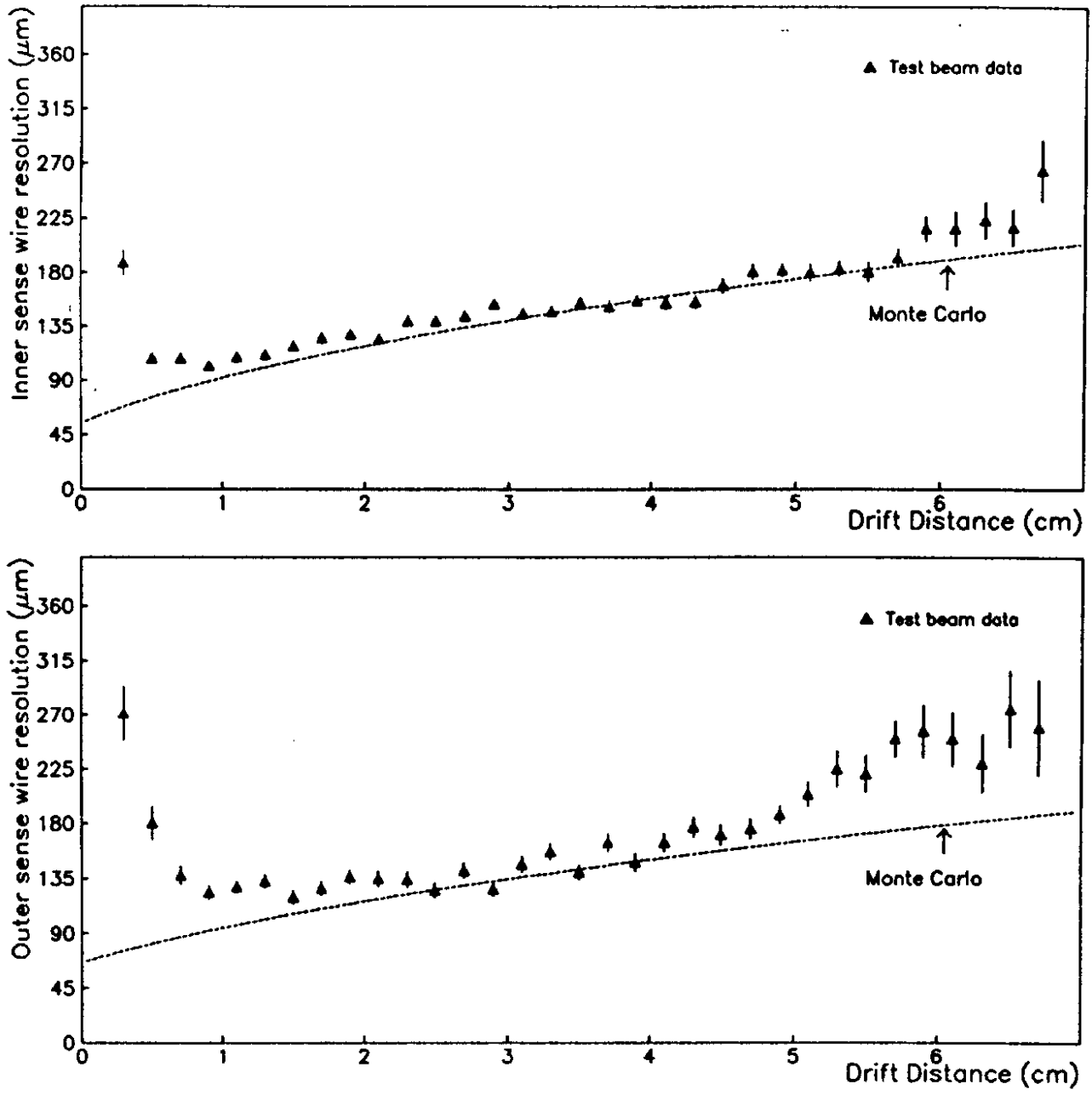
Inner sense wire resolution (μm)
360
315
270
225
180
135
90
45
0
0
1
2
3
4
5
6
Drift Distance (cm)
Test beam data
Monte Carlo
Outer sense wire resolution (μm)
360
315
270
225
180
135
90
45
0
0
1
2
3
4
5
6
Drift Distance (cm)
Test beam data
Monte Carlo

Figure 18

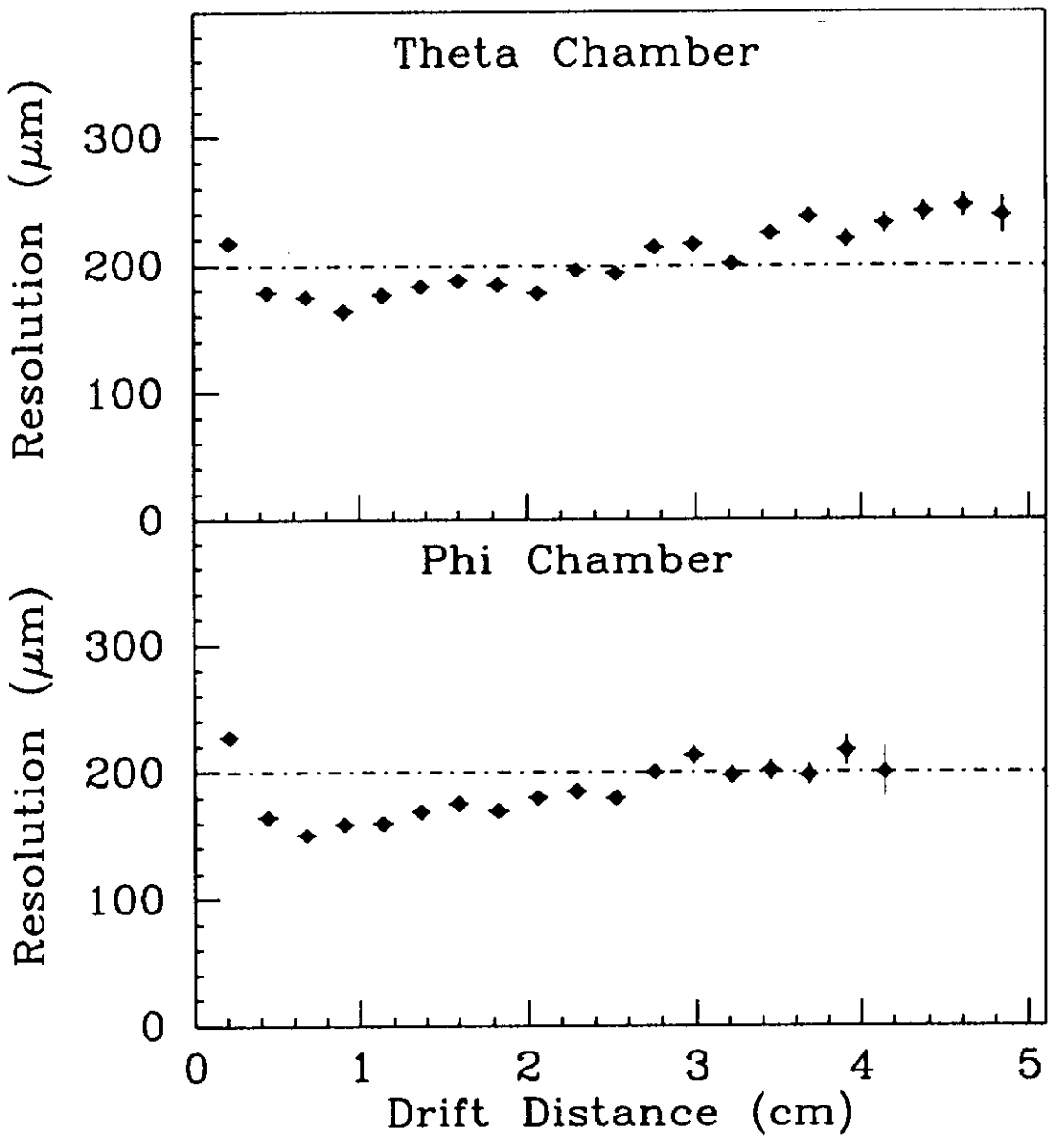
Theta Chamber
Phi Chamber
Resolution (μm)
Resolution (μm)
300
200
100
0
300
200
100
0
0
1
2
3
4
5
Drift Distance (cm)

Figure 19

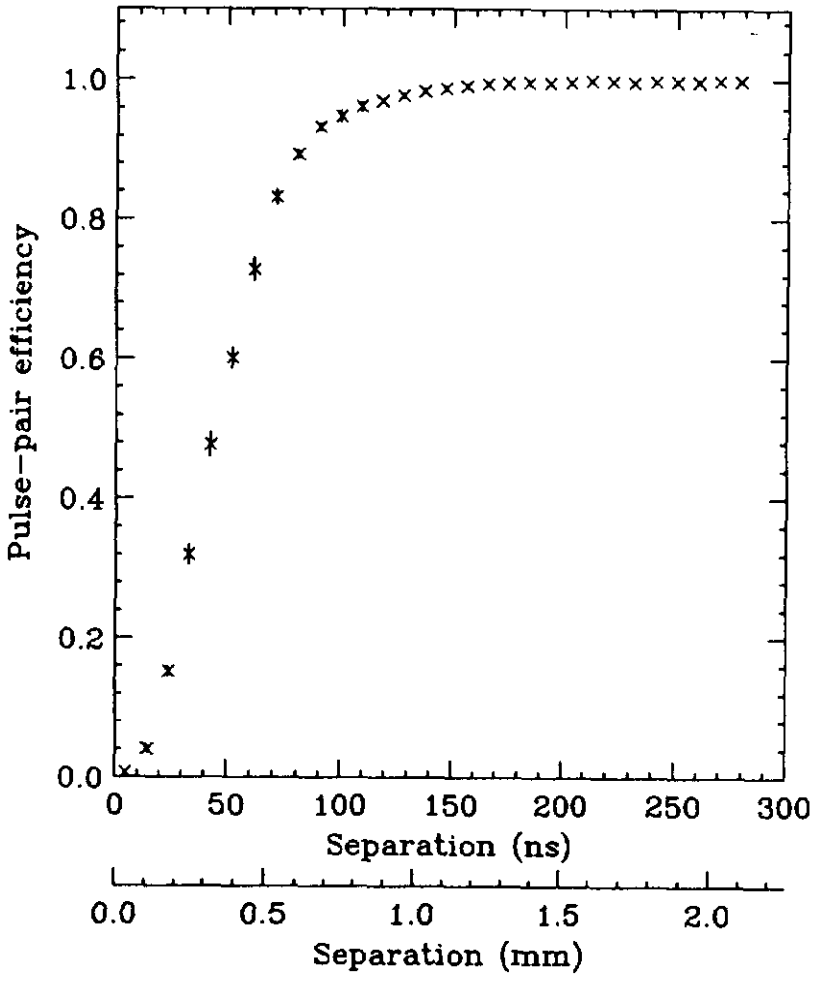
Pulse-pair efficiency
1.0
0.8
0.6
0.4
0.2
0.0
0
50
100
150
200
250
300
Separation (ns)
0.0
0.5
1.0
1.5
2.0
Separation (mm)

Figure 20

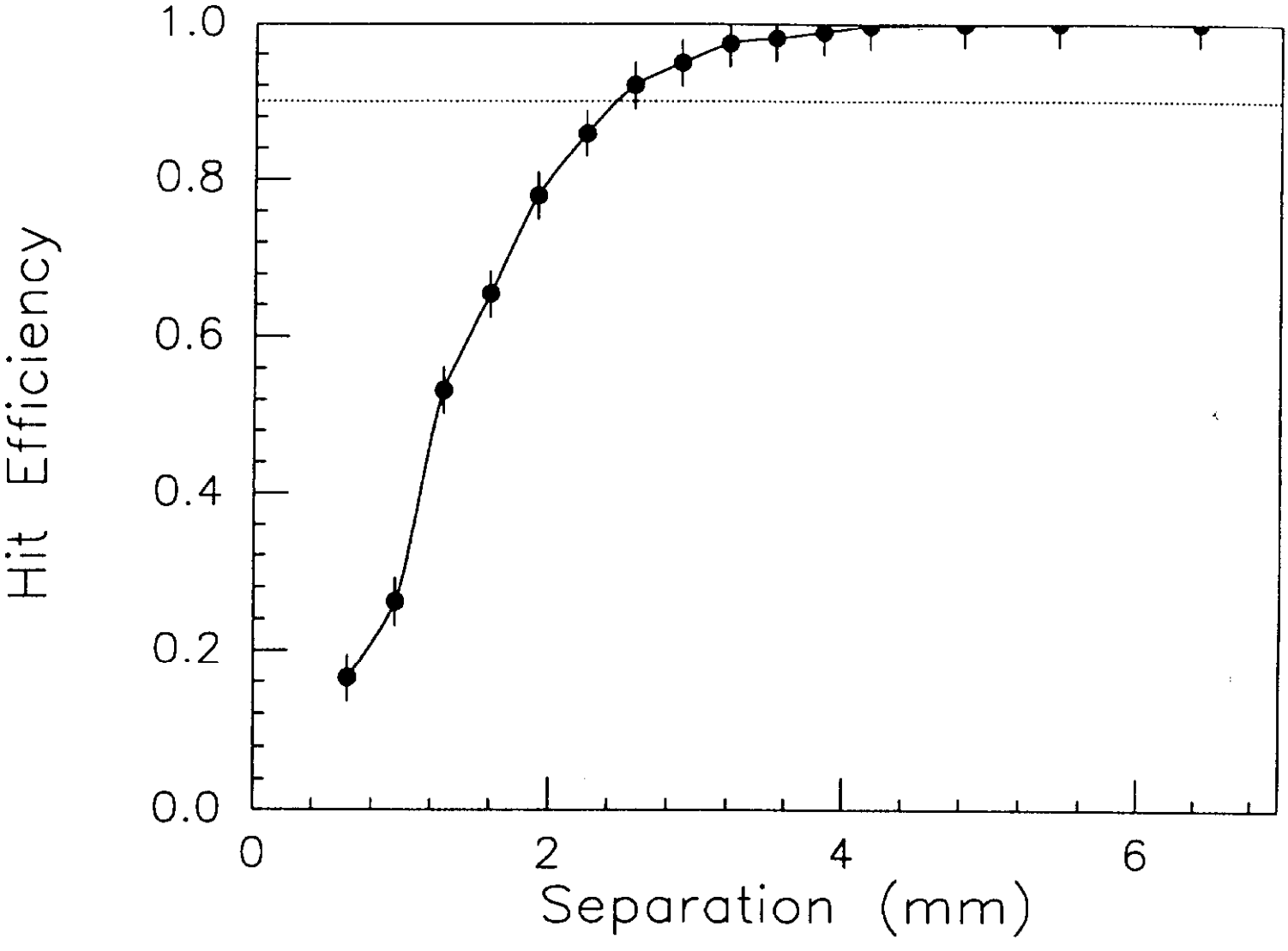

Figure 21

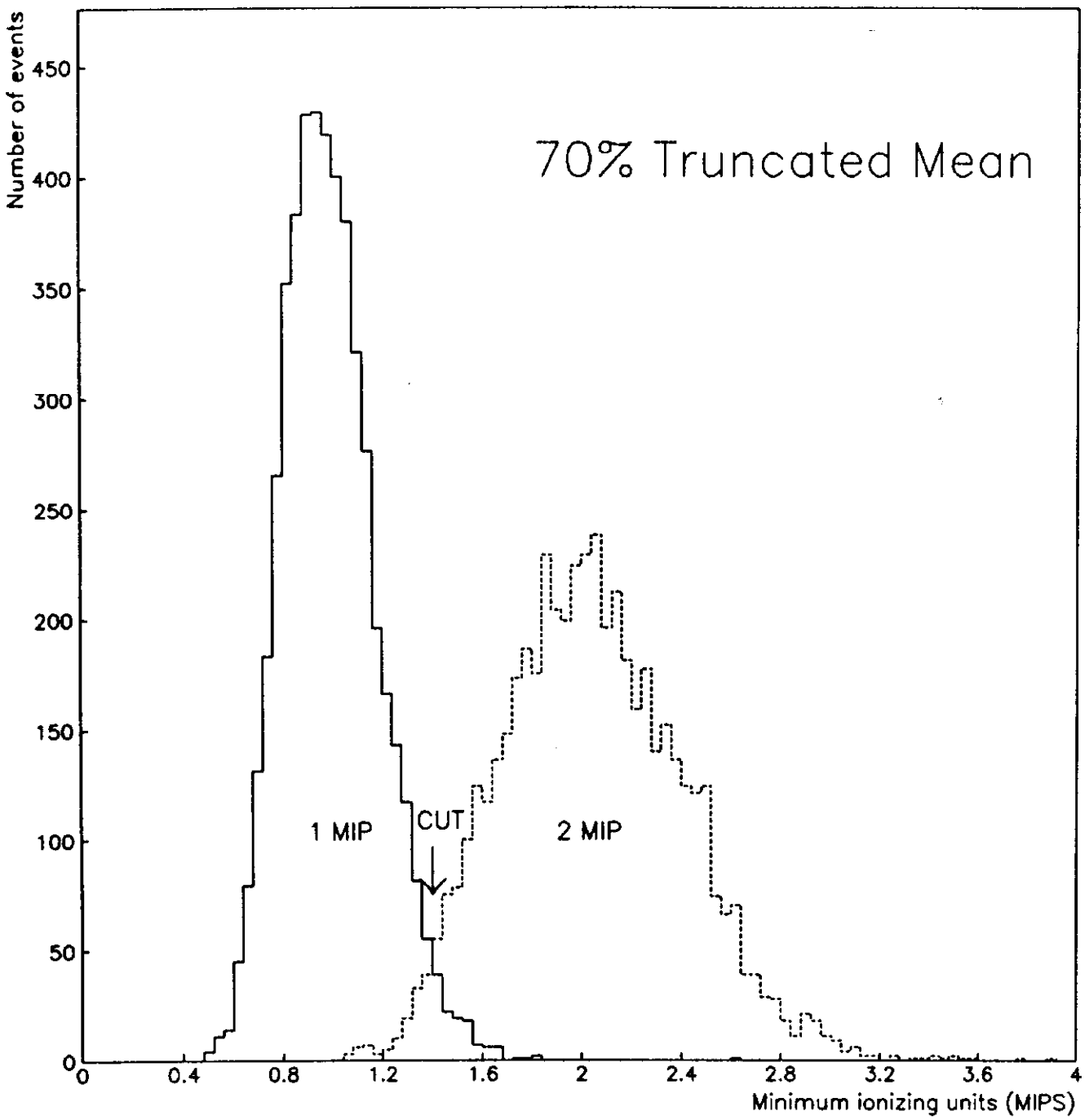
70% Truncated Mean
Number of events
Minimum ionizing units (MIPS)
1 MIP
CUT
2 MIP
0
50
100
150
200
250
300
350
400
450
0
0.4
0.8
1.2
1.6
2
2.4
2.8
3.2
3.6
4

Figure 22

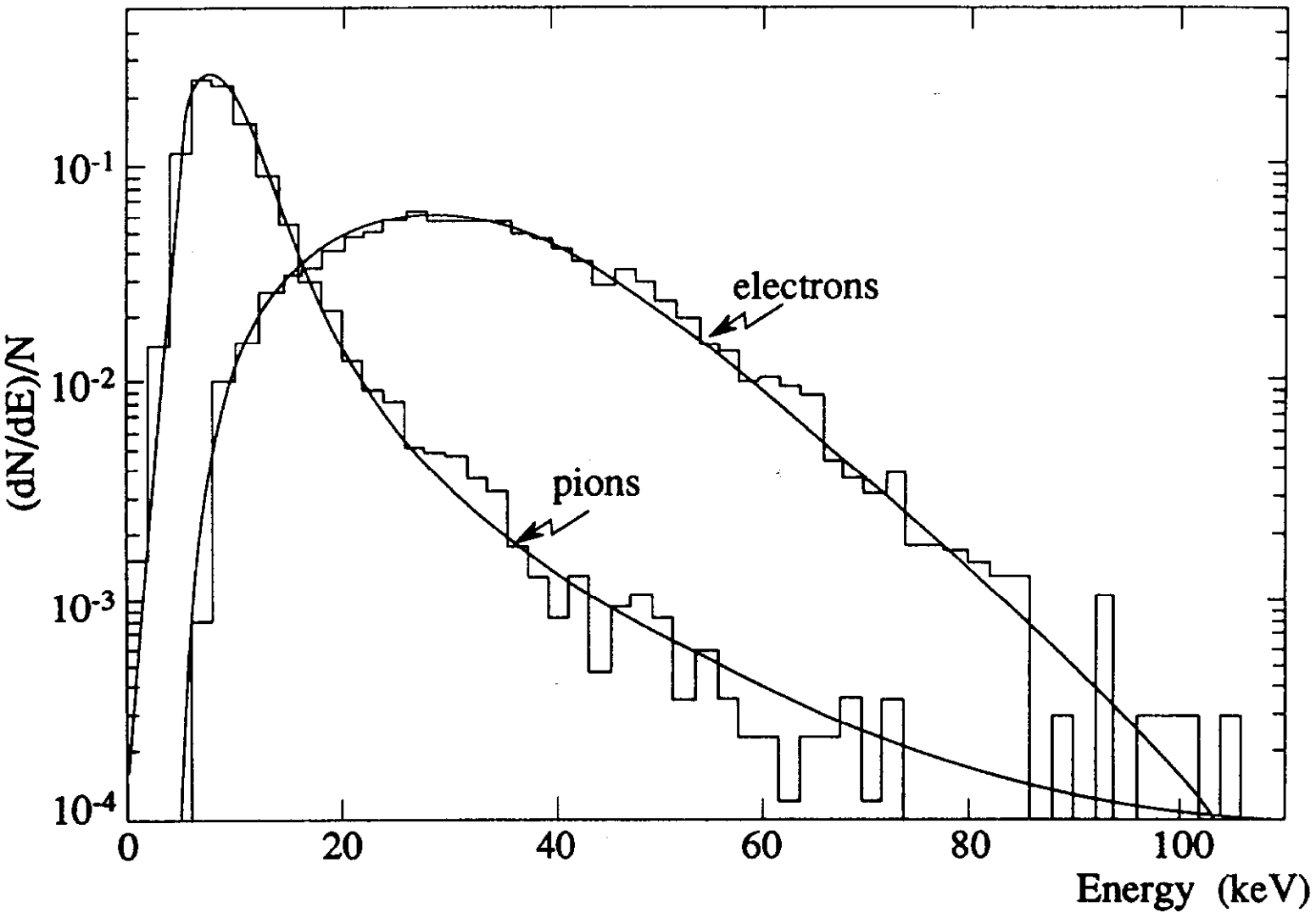
(dN/dE)/N
10^{-1}
10^{-2}
10^{-3}
10^{-4}
0
20
40
60
80
100
Energy (keV)
electrons
pions

Figure 23

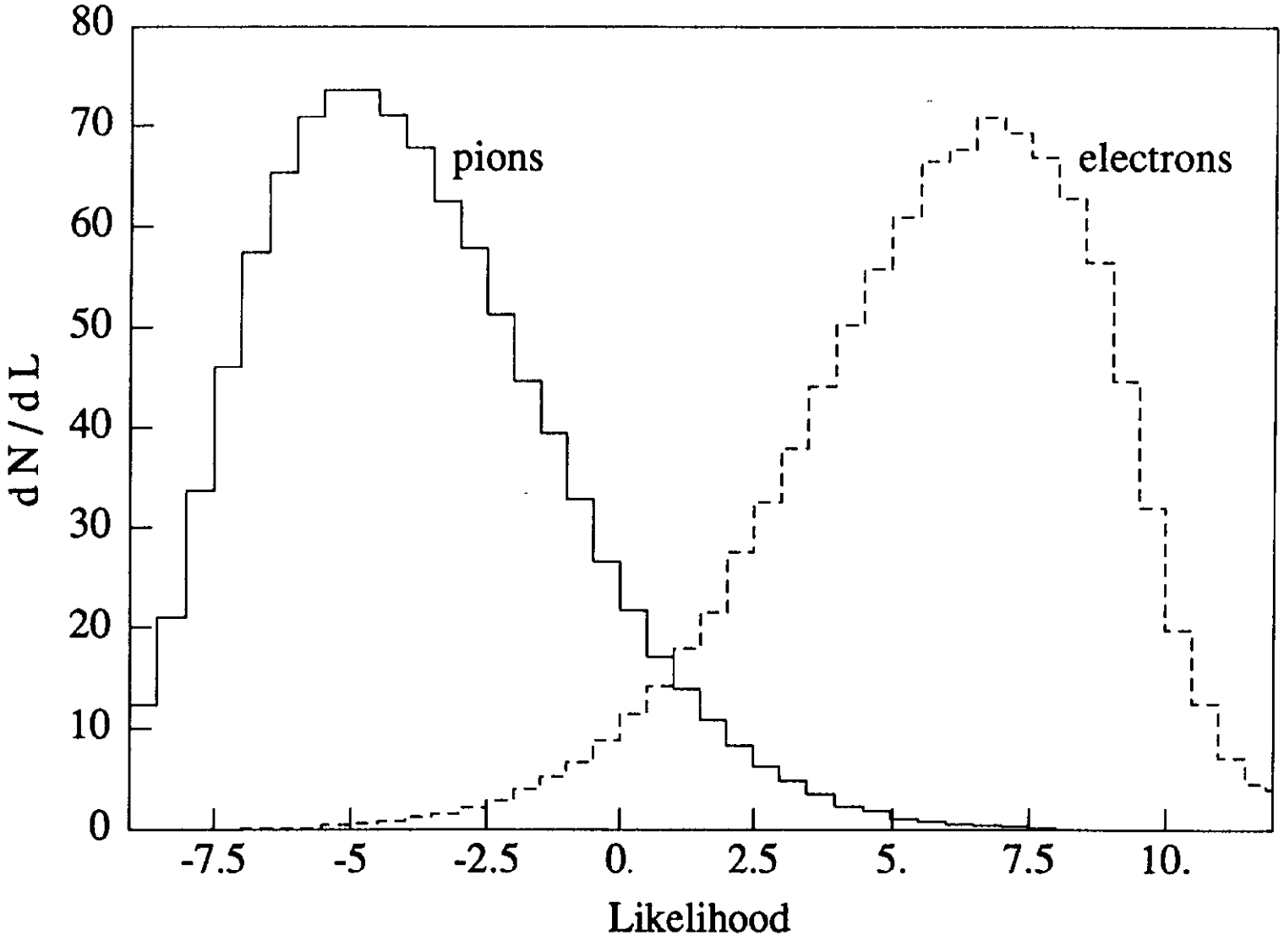
80
70
60
50
40
30
20
10
0
dN/dL
pions
electrons
-7.5
-5
-2.5
0.
2.5
5.
7.5
10.
Likelihood

Figure 24

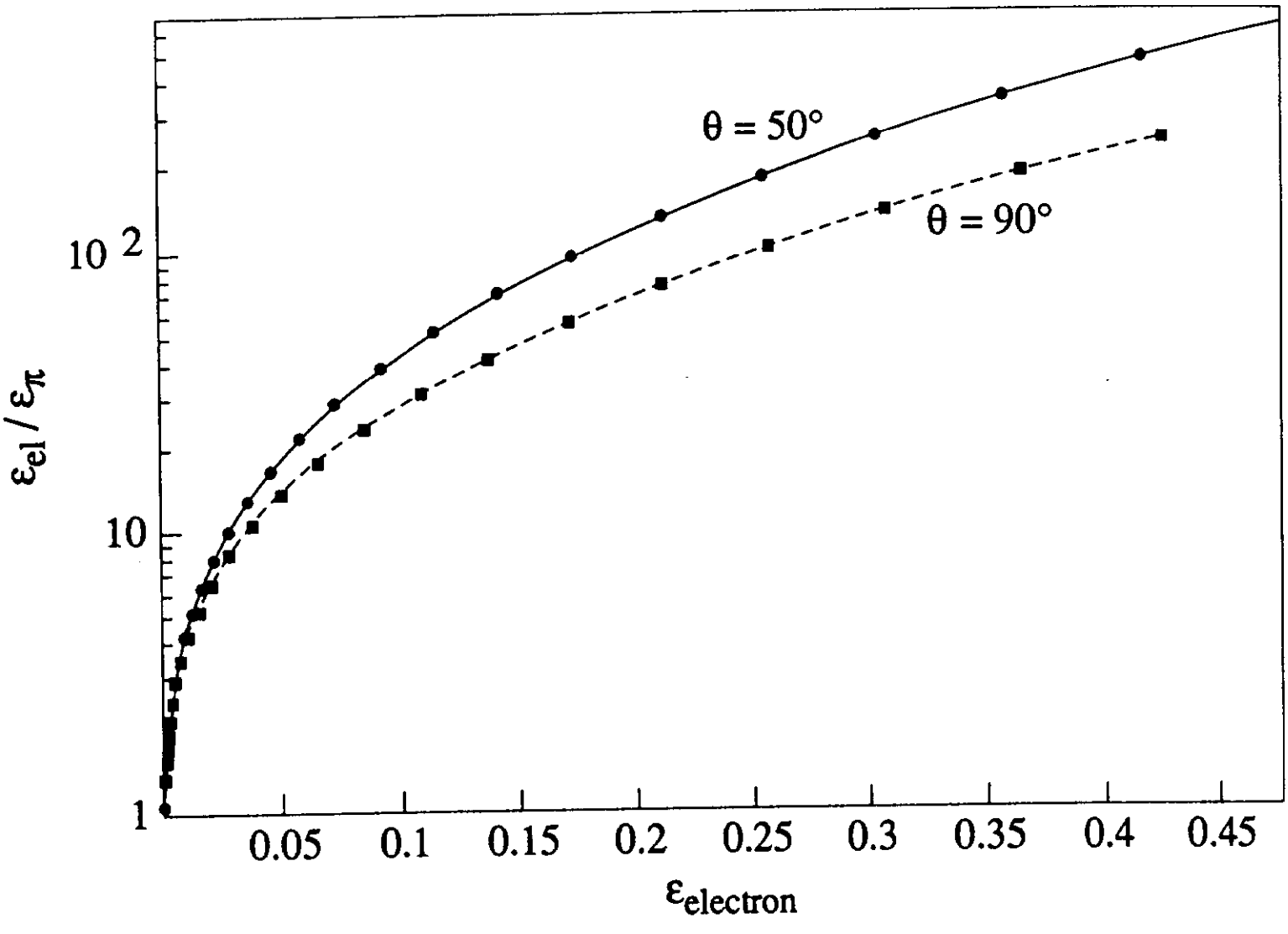
θ = 50°
θ = 90°
10 2
10
1
$\varepsilon_{el} / \varepsilon_{\pi}$
0.05
0.1
0.15
0.2
0.25
0.3
0.35
0.4
0.45
$\varepsilon_{electron}$

Figure 25

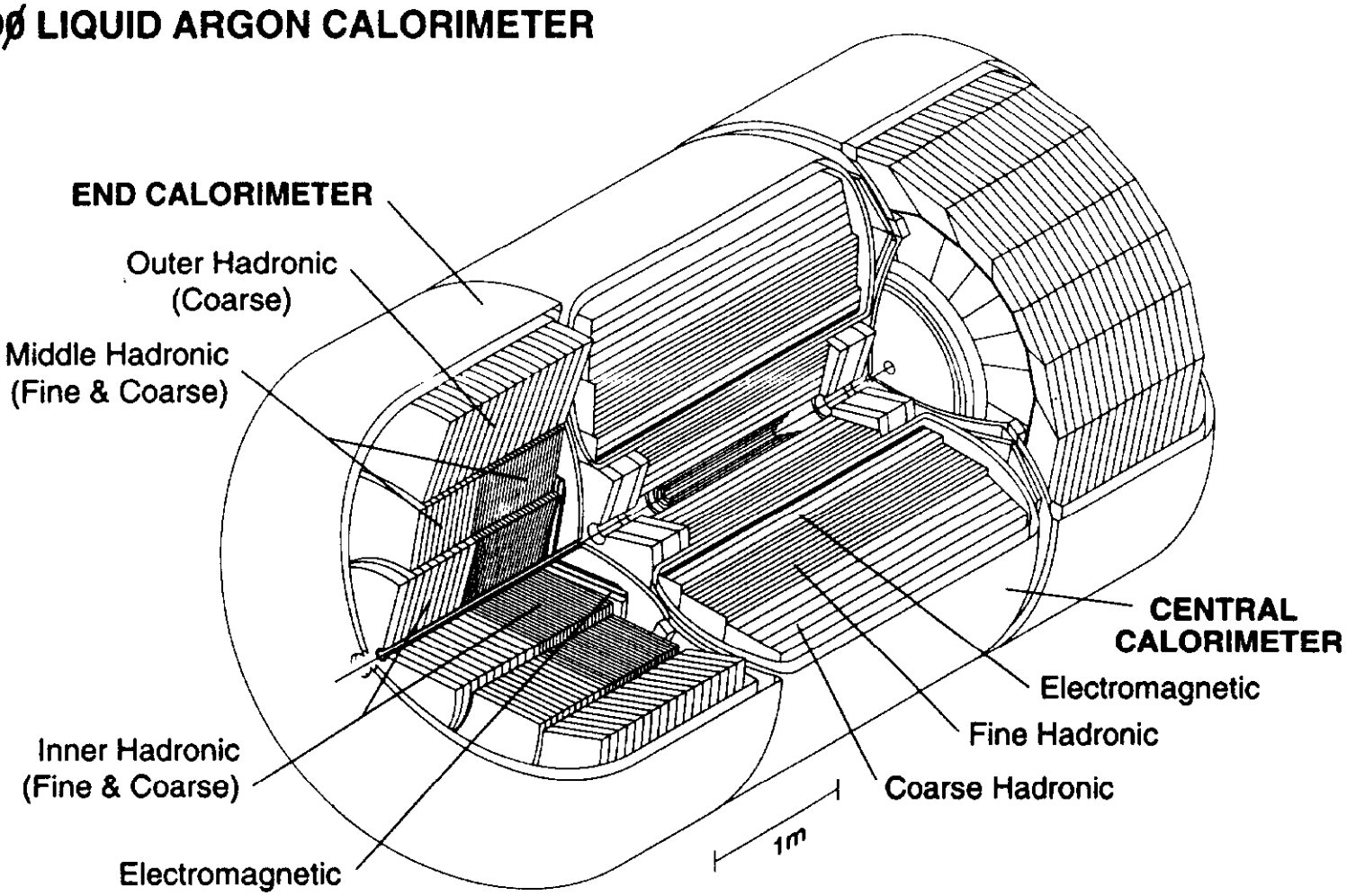
DØ LIQUID ARGON CALORIMETER
END CALORIMETER
Outer Hadronic
(Coarse)
Middle Hadronic
(Fine & Coarse)
CENTRAL
CALORIMETER
Electromagnetic
Fine Hadronic
Coarse Hadronic
Inner Hadronic
(Fine & Coarse)
Electromagnetic
1m

Figure 26

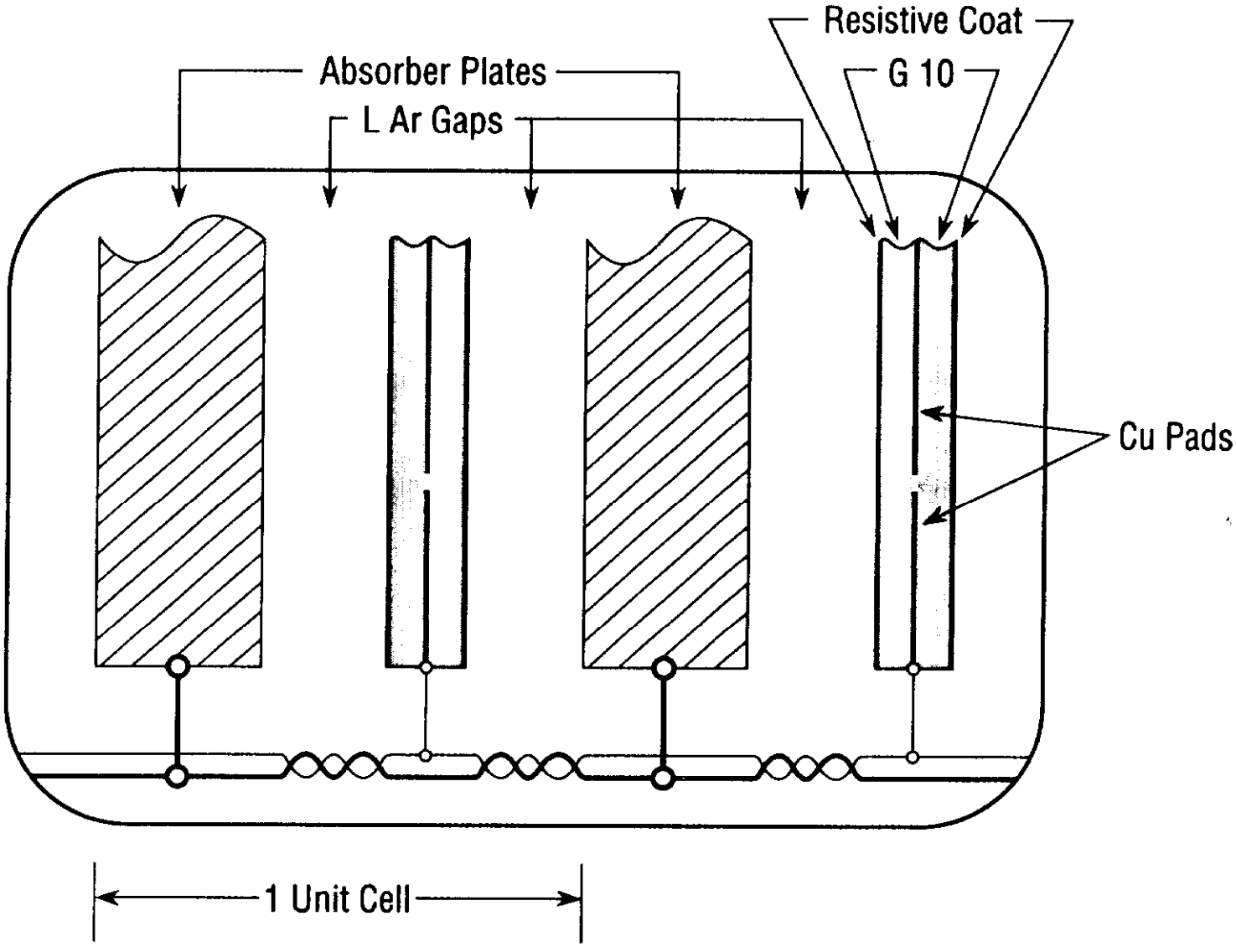
Resistive Coat
G 10
Absorber Plates
L Ar Gaps
Cu Pads
1 Unit Cell

Figure 27

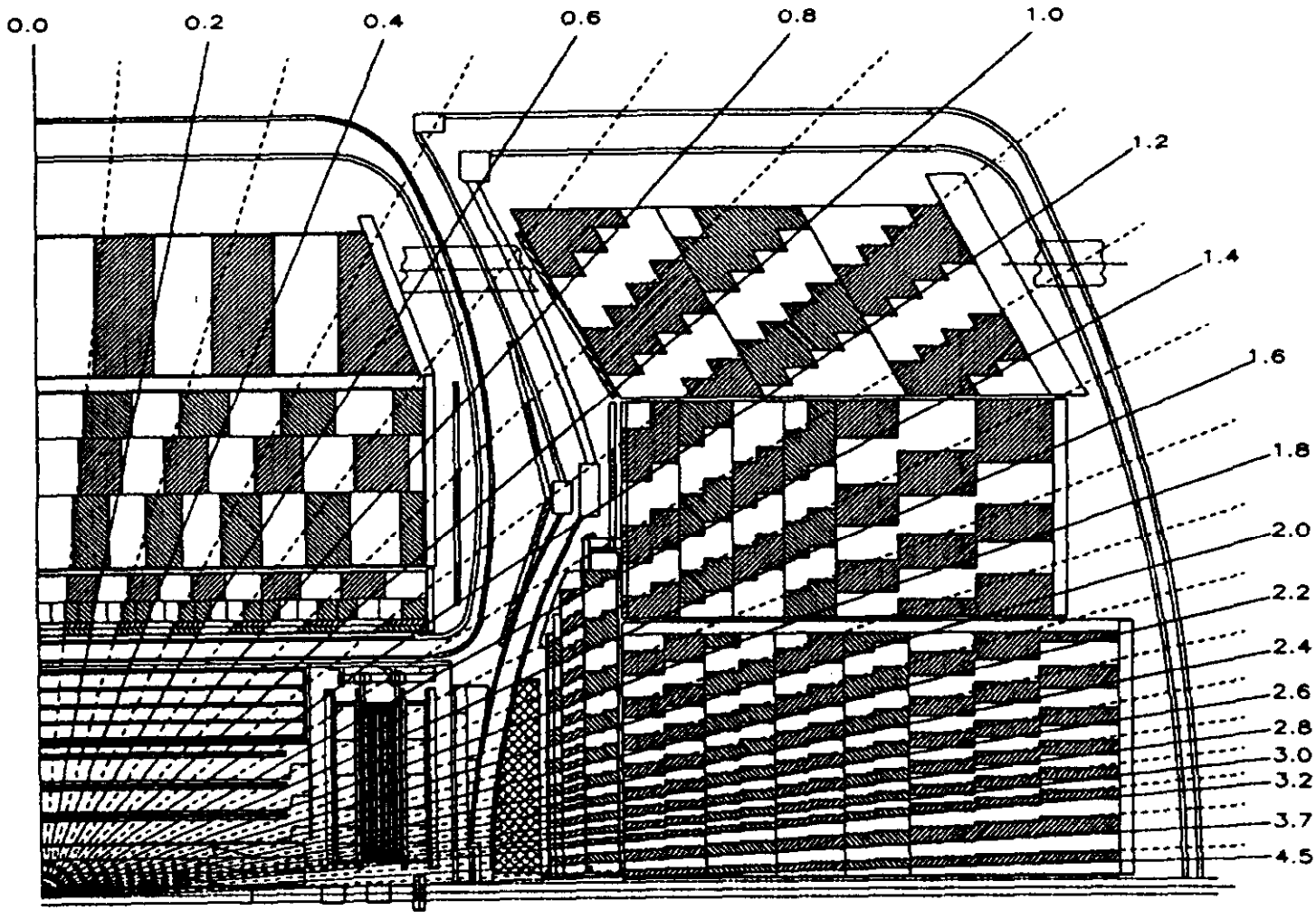

Figure 28

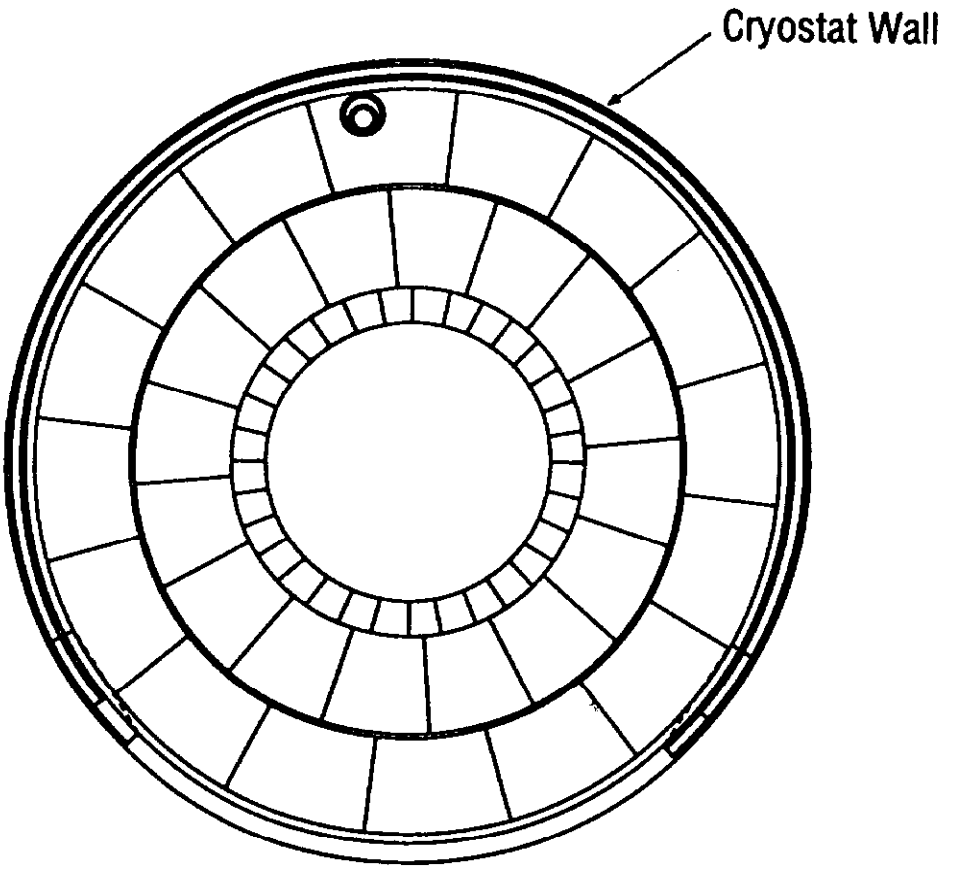

Figure 29 (a)

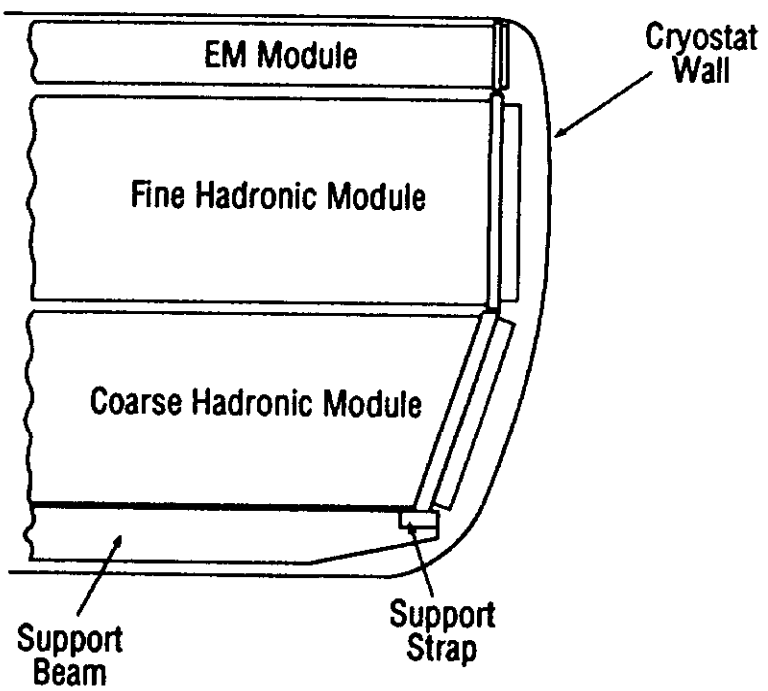

Figure 29 (b)

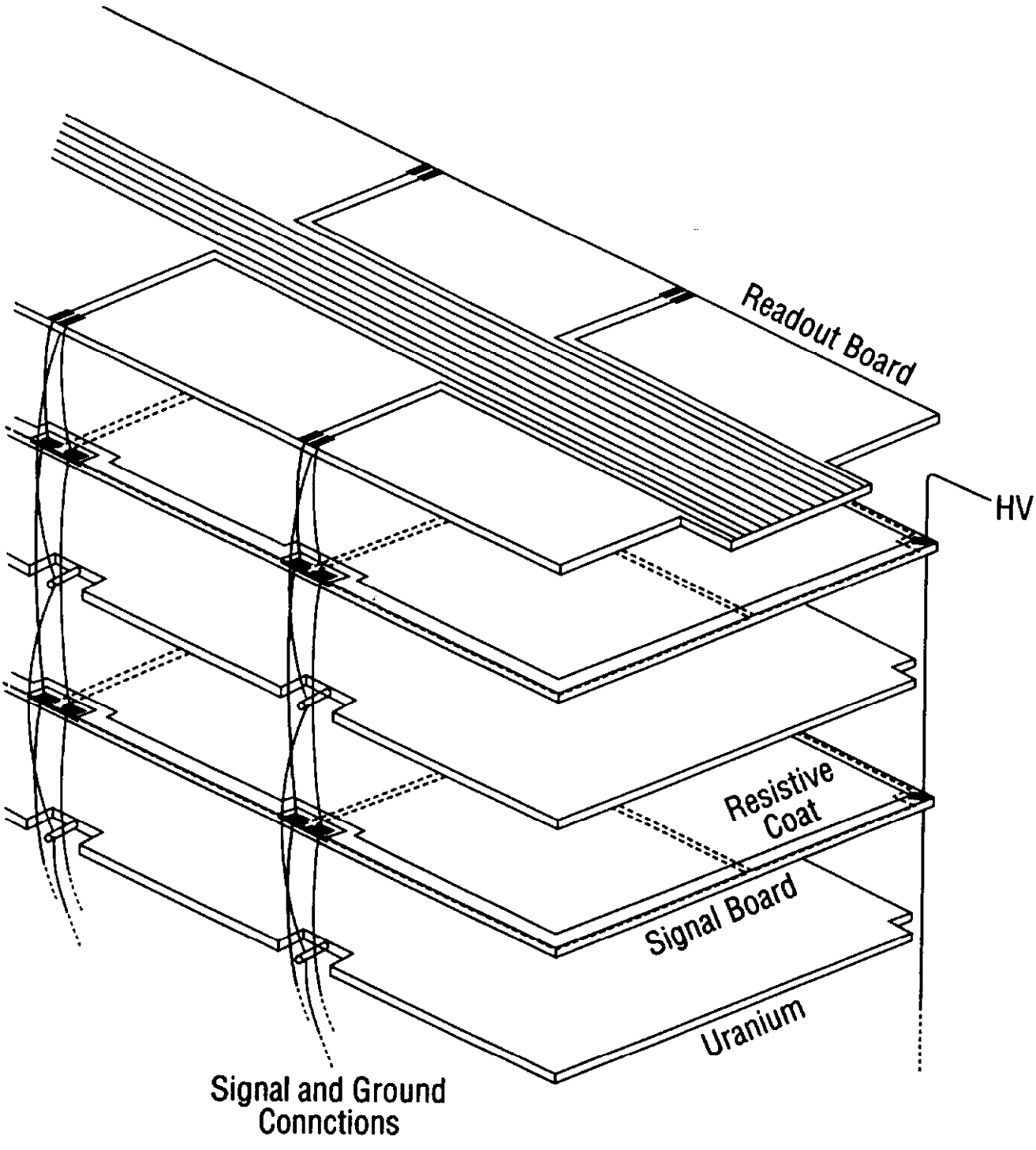
Readout Board
HV
Resistive Coat
Signal Board
Uranium
Signal and Ground Connctions

Figure 30

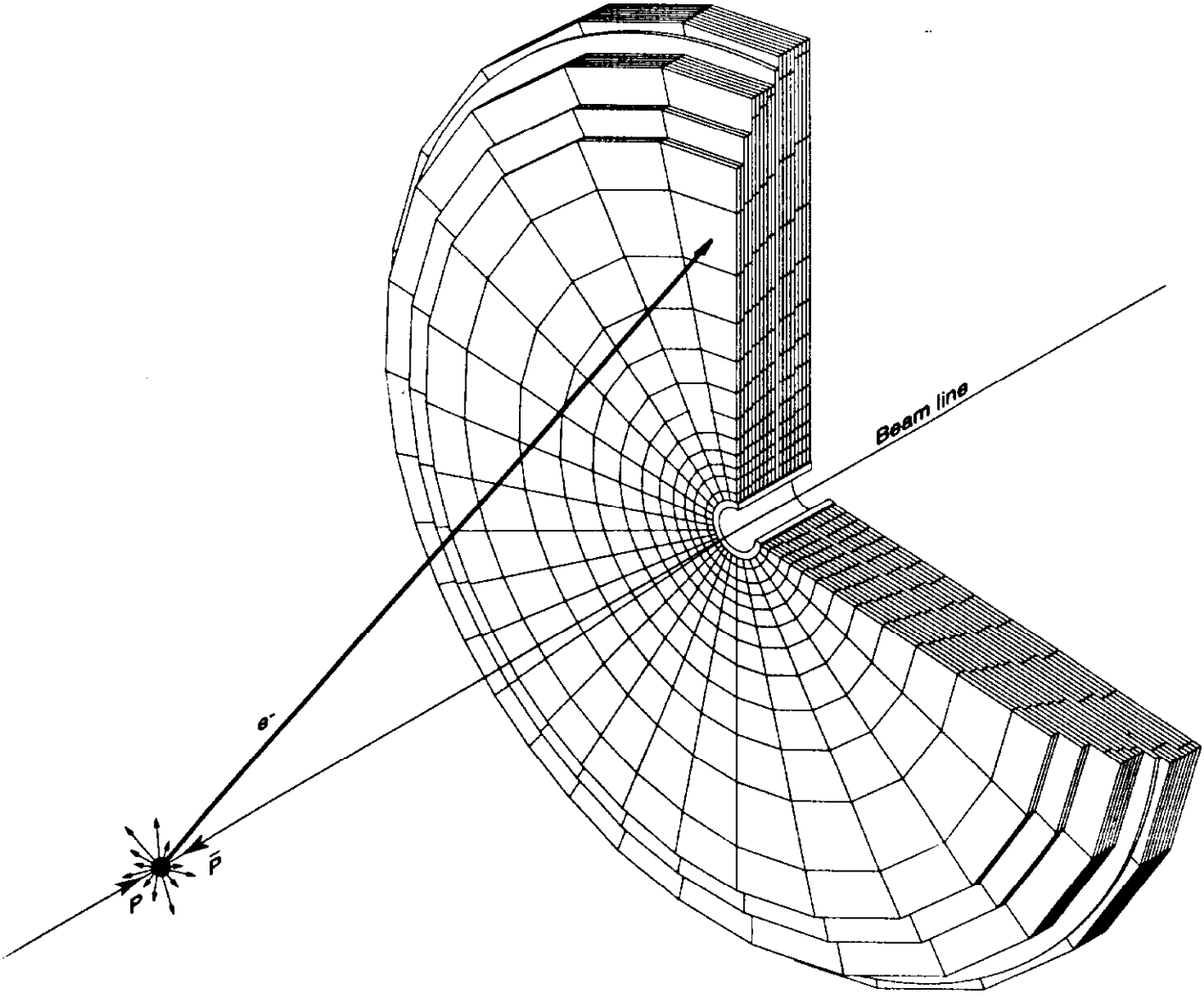

DØ END CALORIMETER ELECTROMAGNETIC MODULE

Figure 31

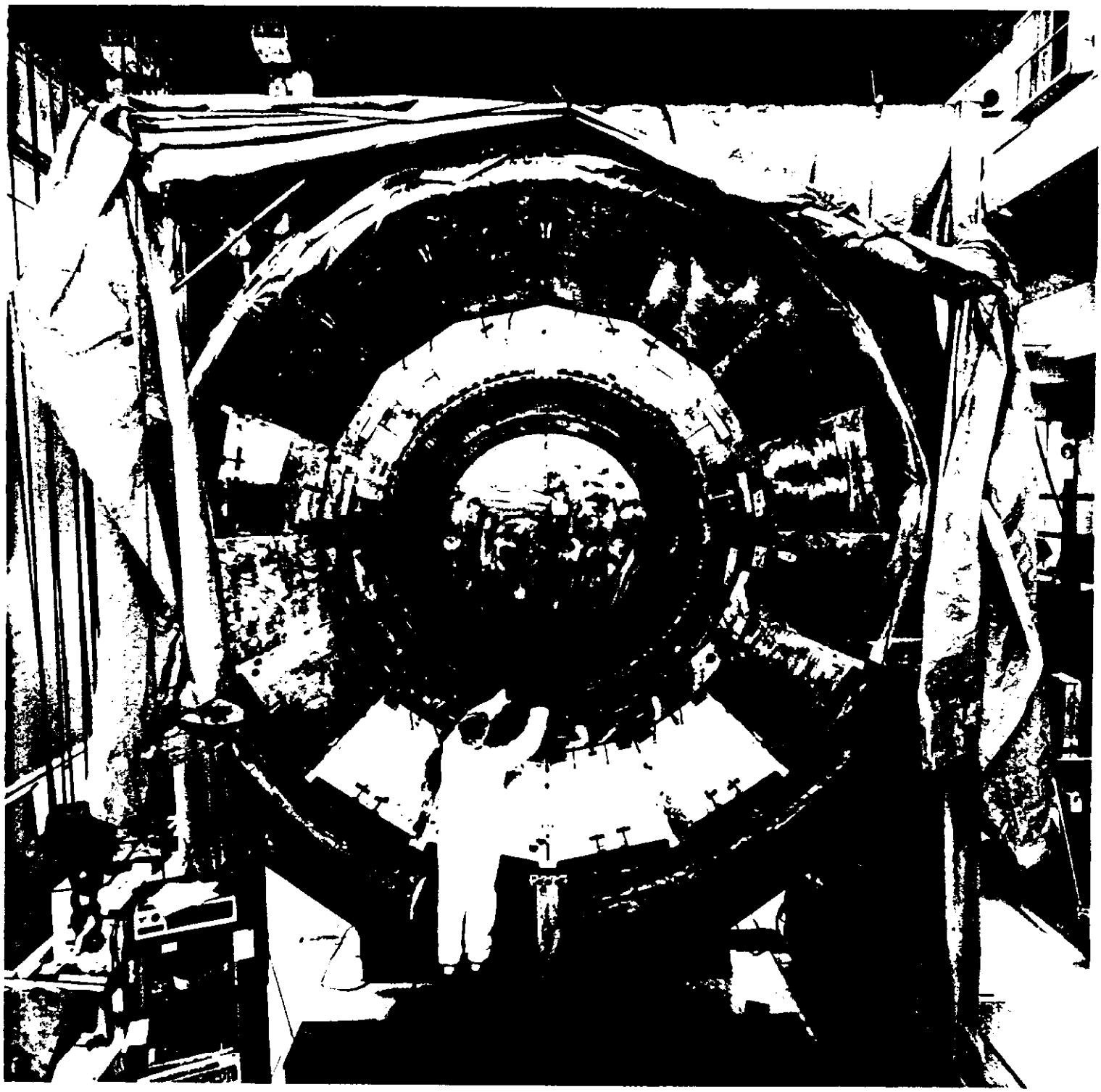

Figure 32

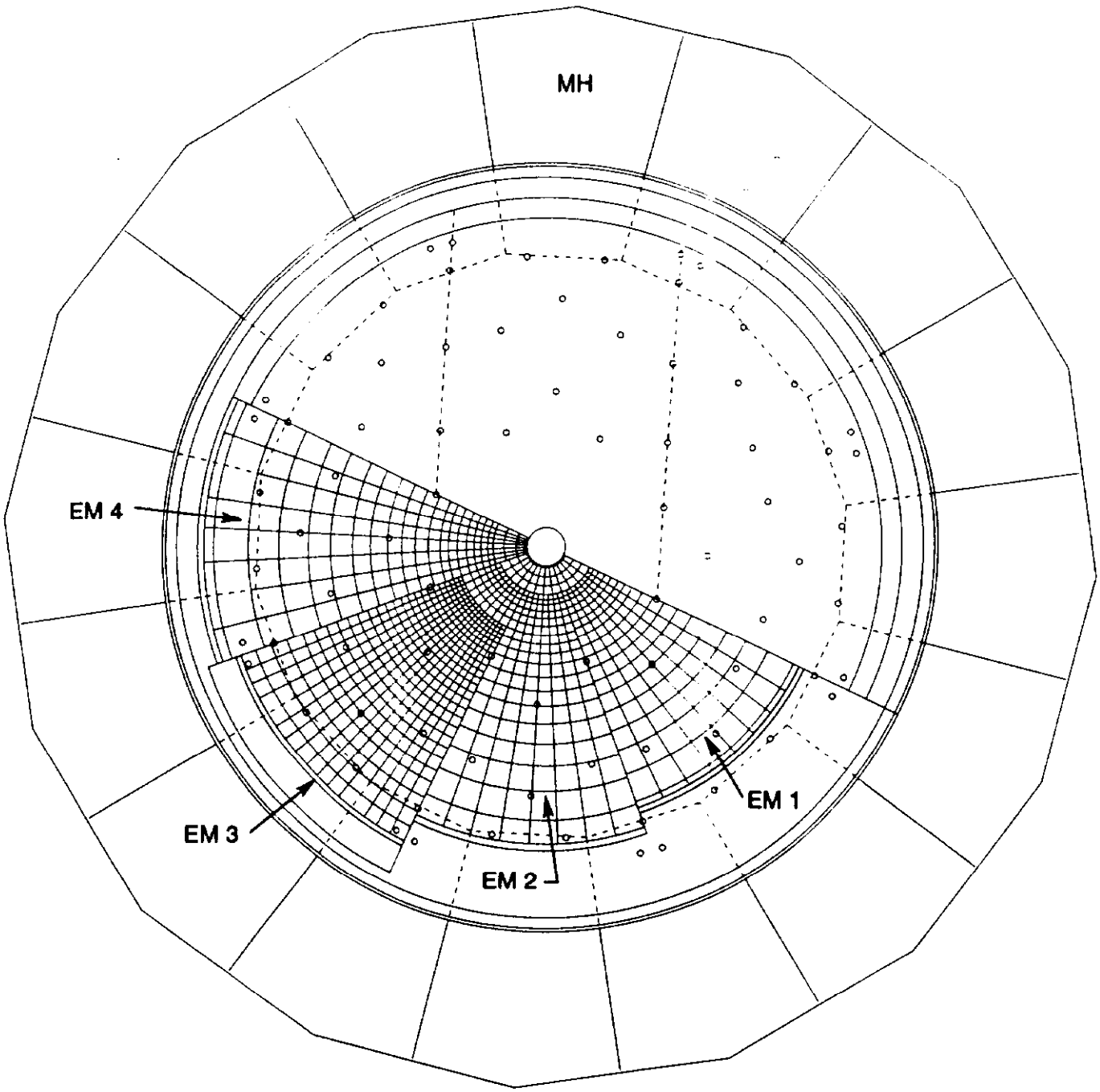

Figure 33

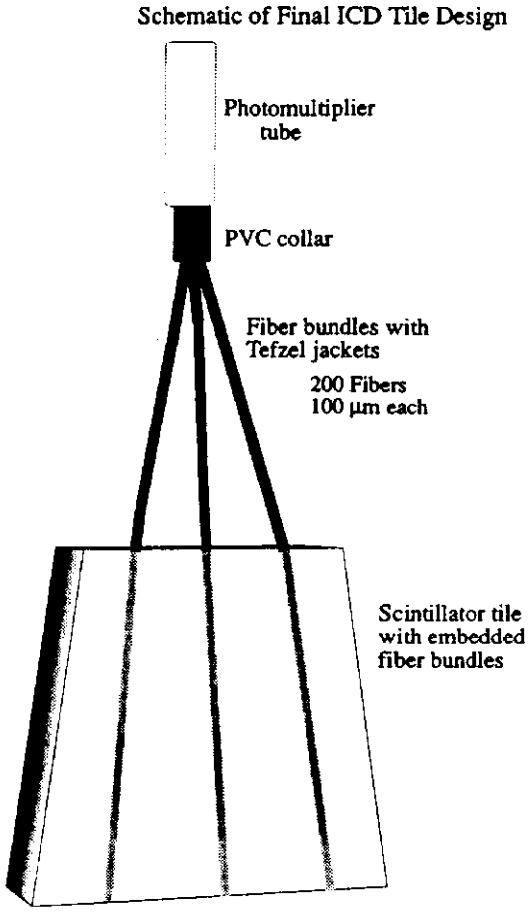

Figure 34 (a)

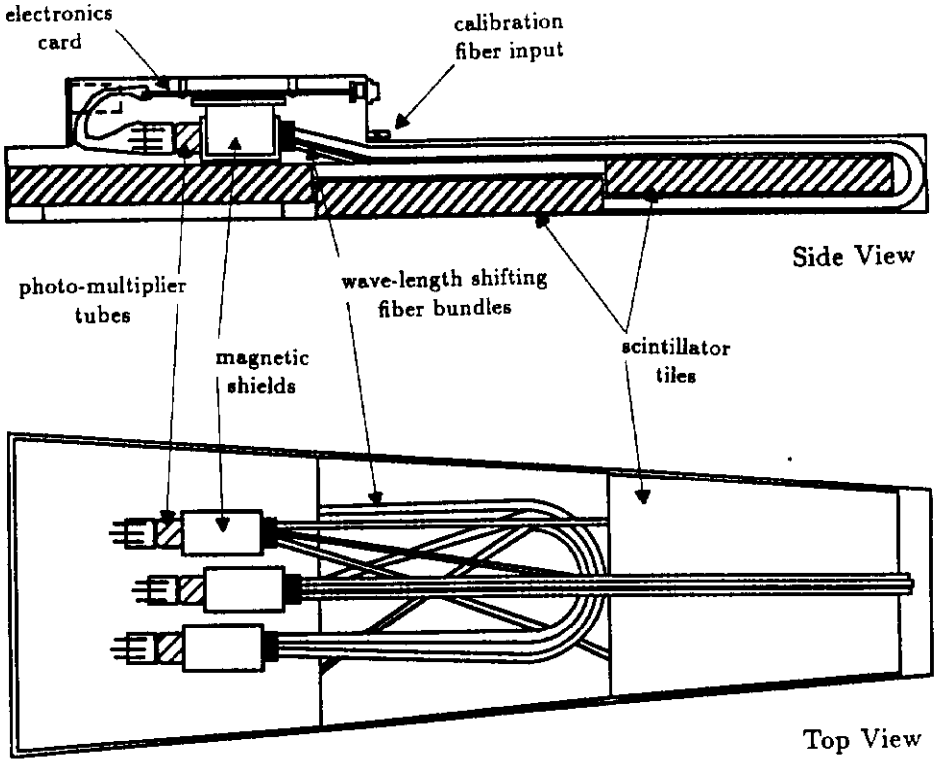

Figure 34 (b)

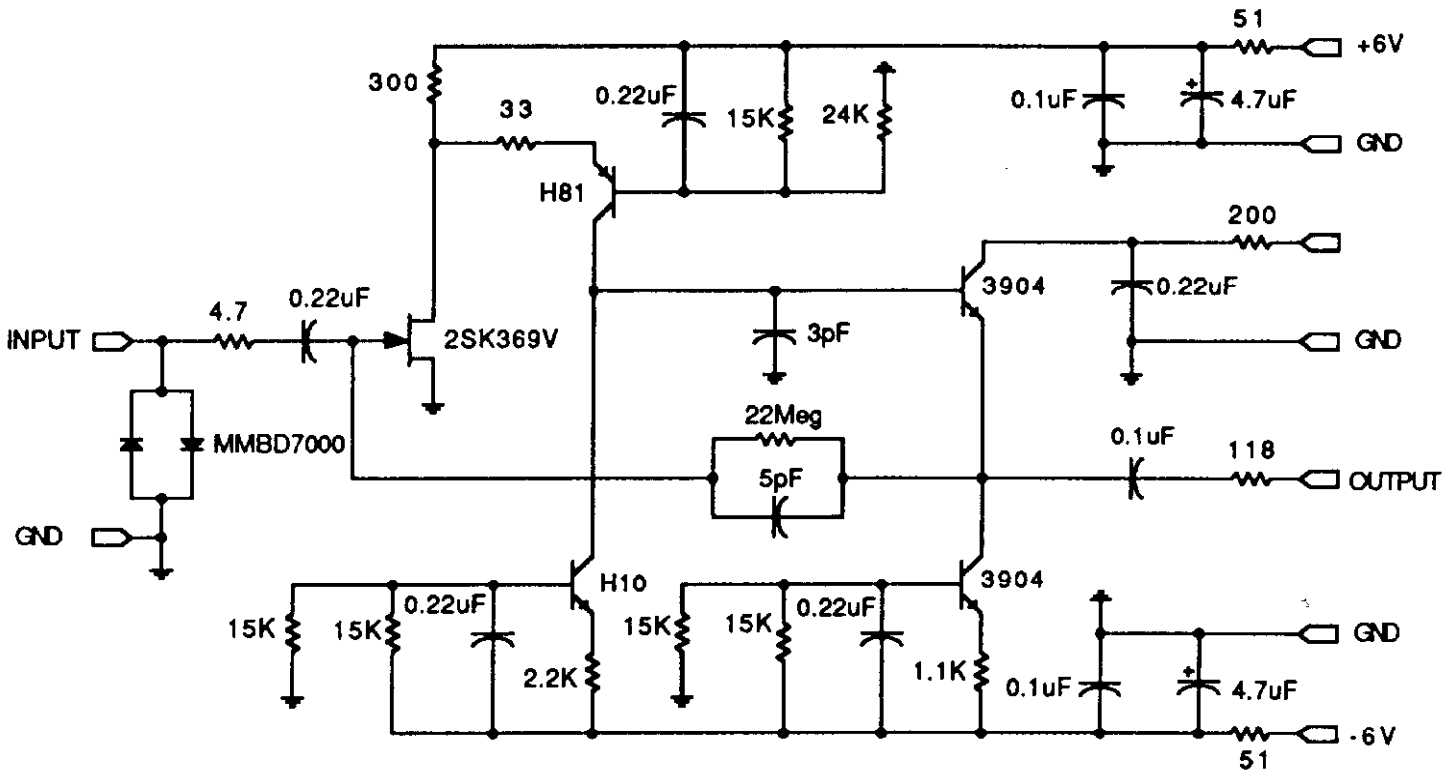
51
+6V
300
33
0.22uF
15K
24K
0.1uF
4.7uF
GND
H81
200
3904
0.22uF
GND
INPUT
4.7
0.22uF
2SK369V
3pF
MMBD7000
22Meg
0.1uF
118
5pF
OUTPUT
GND
H10
3904
15K
15K
0.22uF
15K
15K
0.22uF
GND
2.2K
1.1K
0.1uF
4.7uF
-6V
51

Figure 35

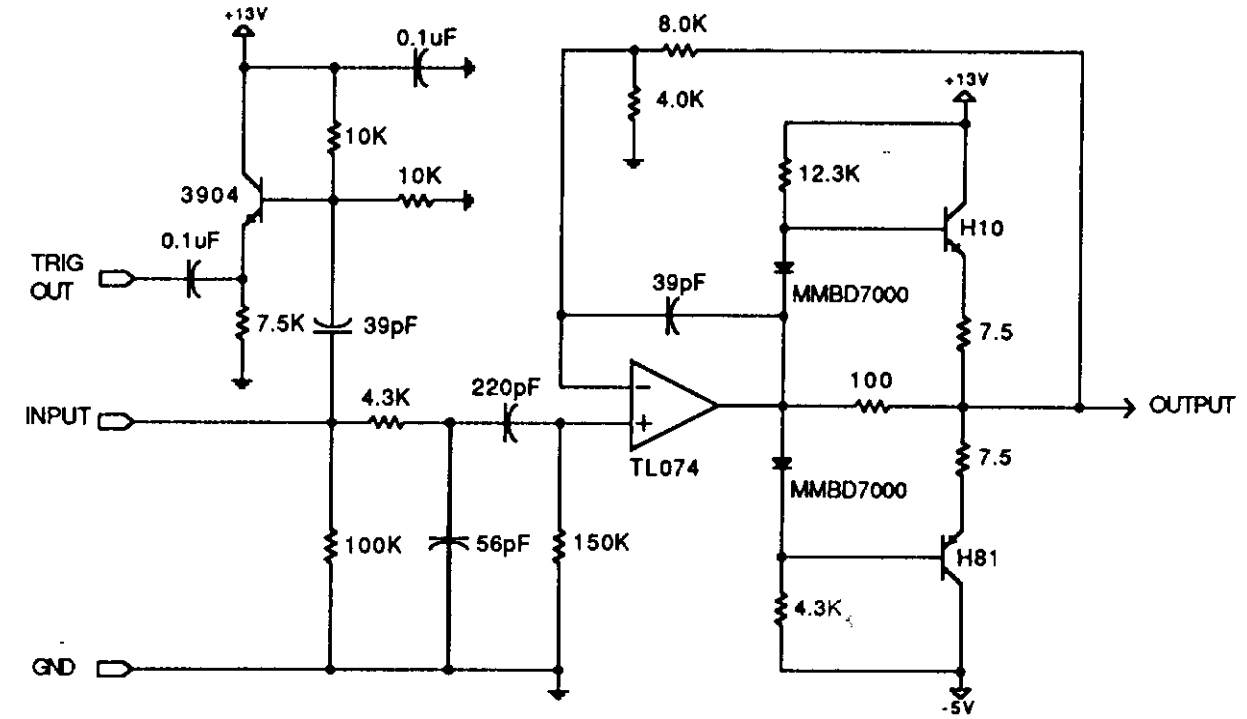
+13V
0.1uF
10K
10K
3904
0.1uF
TRIG
OUT
7.5K
39pF
INPUT
4.3K
220pF
100K
56pF
150K
GND
8.0K
4.0K
+13V
12.3K
H10
39pF
MMBD7000
7.5
100
OUTPUT
TL074
7.5
MMBD7000
H81
4.3K
-5V

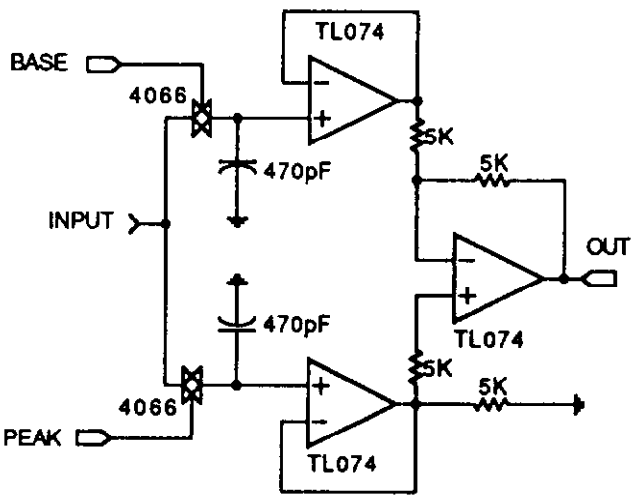
TL074
BASE
4066
5K
5K
470pF
INPUT
OUT
470pF
TL074
5K
4066
5K
PEAK
TL074

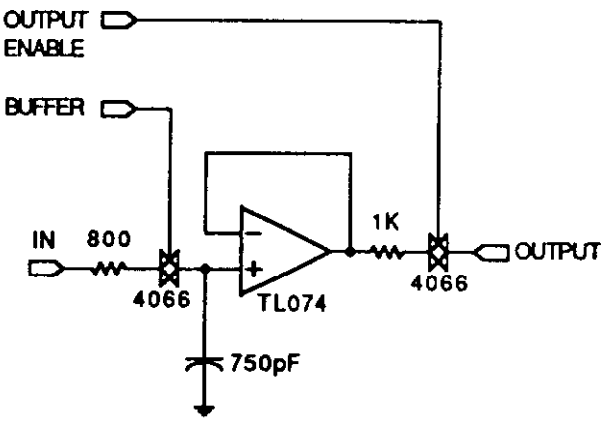
OUTPUT
ENABLE
BUFFER
IN
800
1K
4066
TL074
4066
OUTPUT
750pF

Figure 36

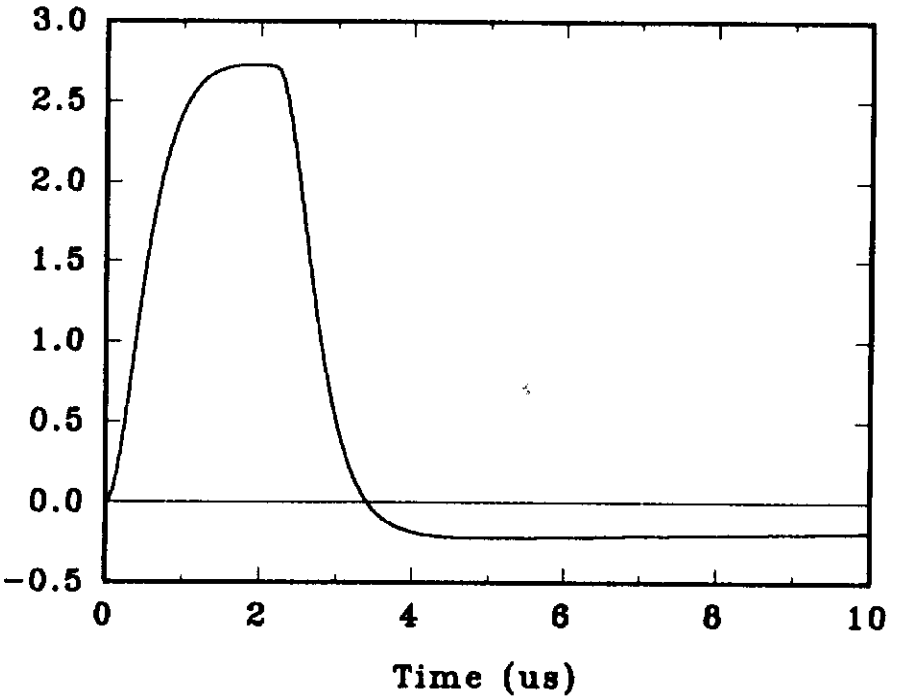

Figure 37

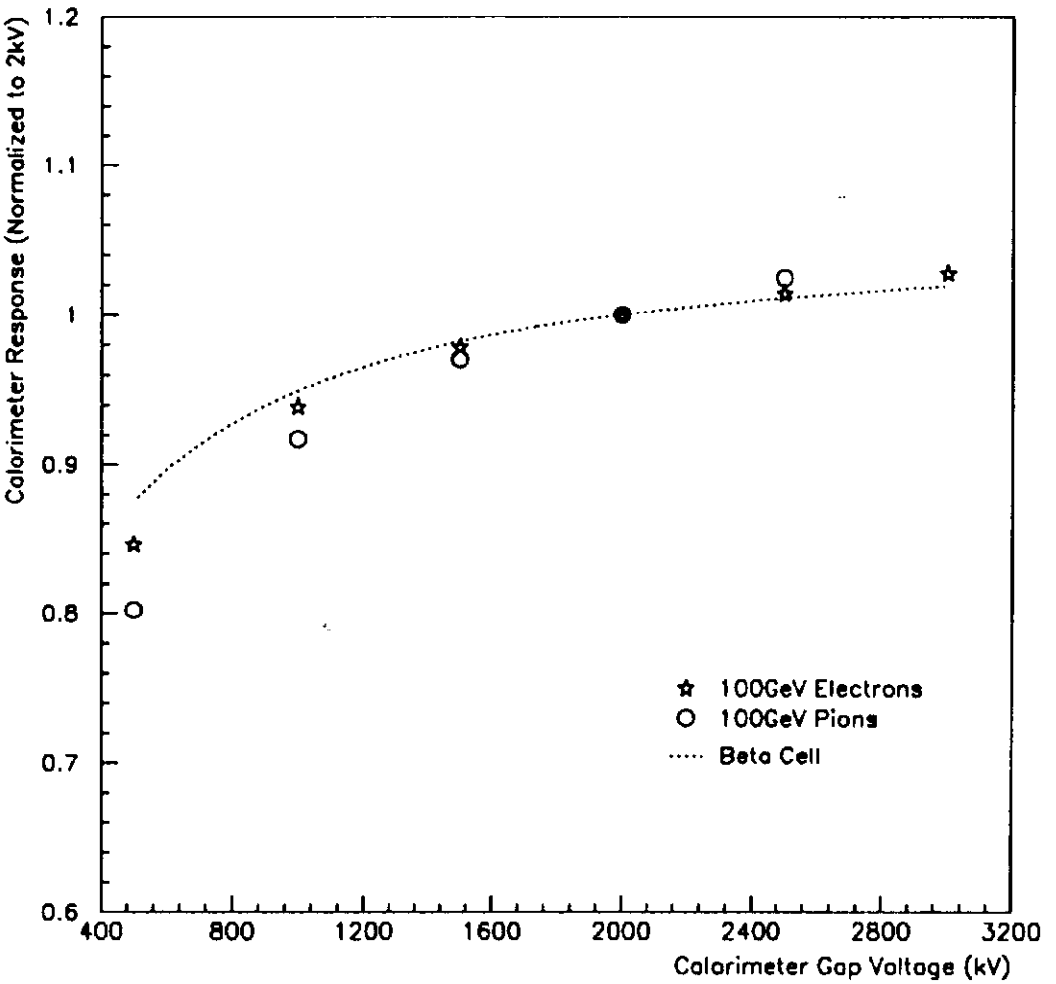
Colorimeter Response (Normalized to 2kV)
1.2
1.1
1
0.9
0.8
0.7
0.6
400
800
1200
1600
2000
2400
2800
3200
Colorimeter Gap Voltage (kV)
100GeV Electrons
100GeV Pions
Beta Cell

Figure 38

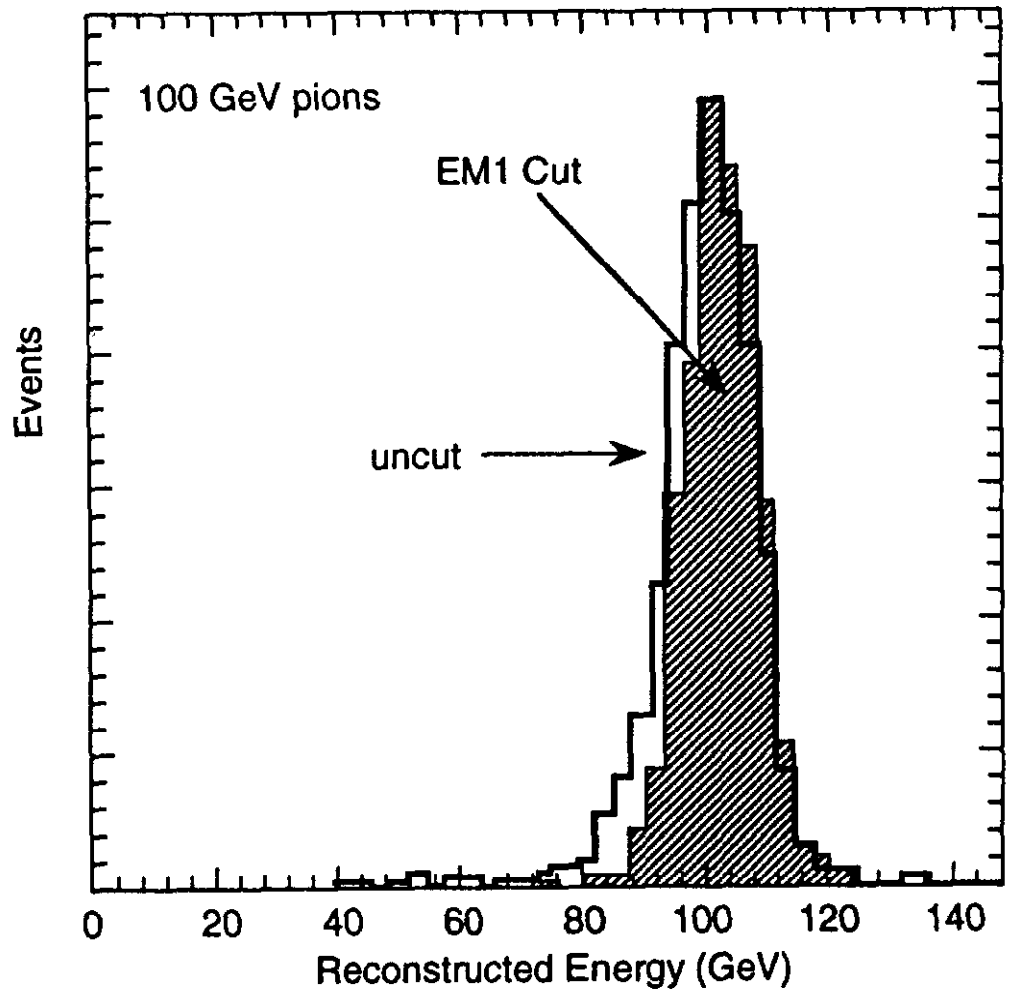
100 GeV pions
EM1 Cut
uncut
Events
0
20
40
60
80
100
120
140
Reconstructed Energy (GeV)

Figure 39

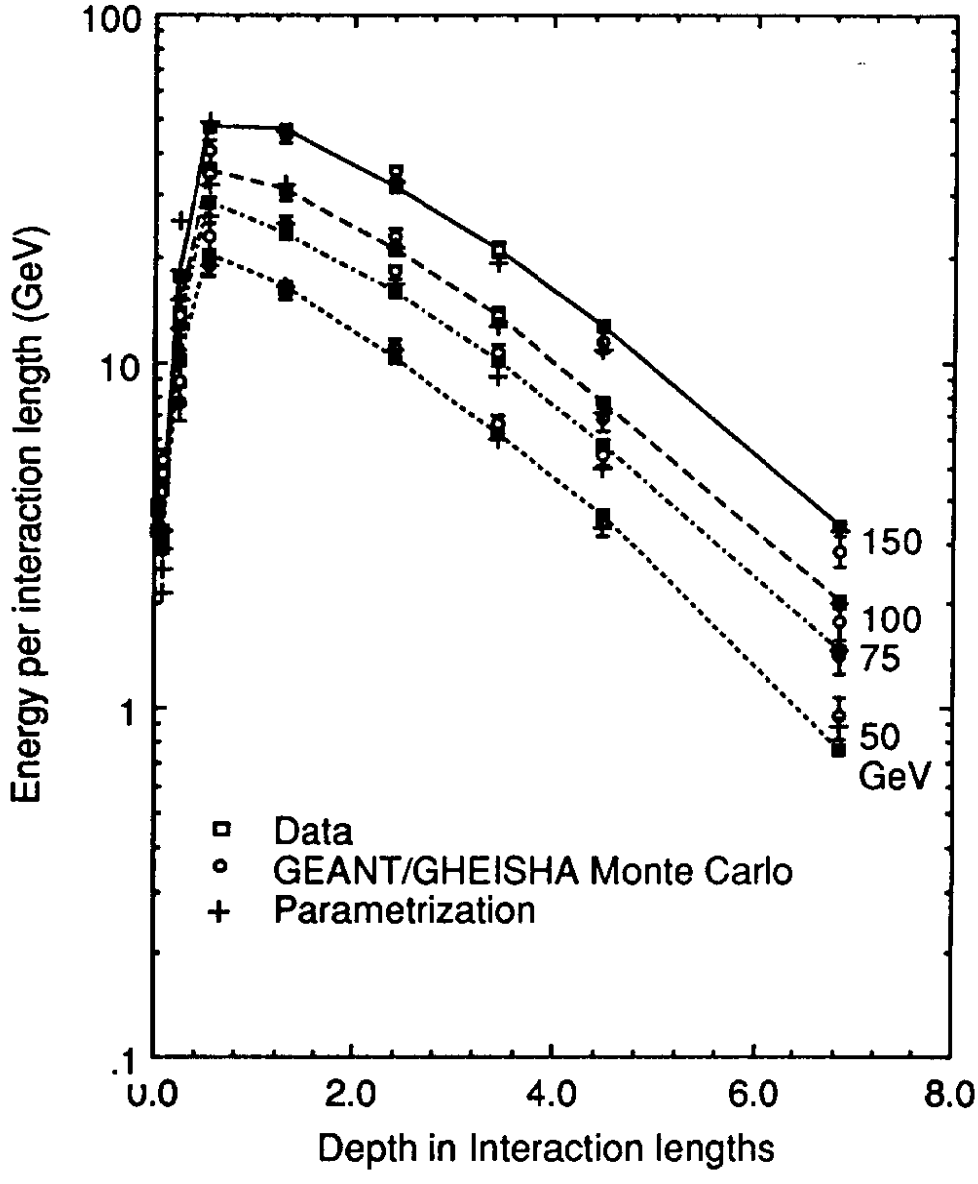
100
10
1
.1
Energy per interaction length (GeV)
0.0
2.0
4.0
6.0
8.0
Depth in Interaction lengths
150
100
75
50
GeV
Data
GEANT/GHEISHA Monte Carlo
Parametrization

Figure 40

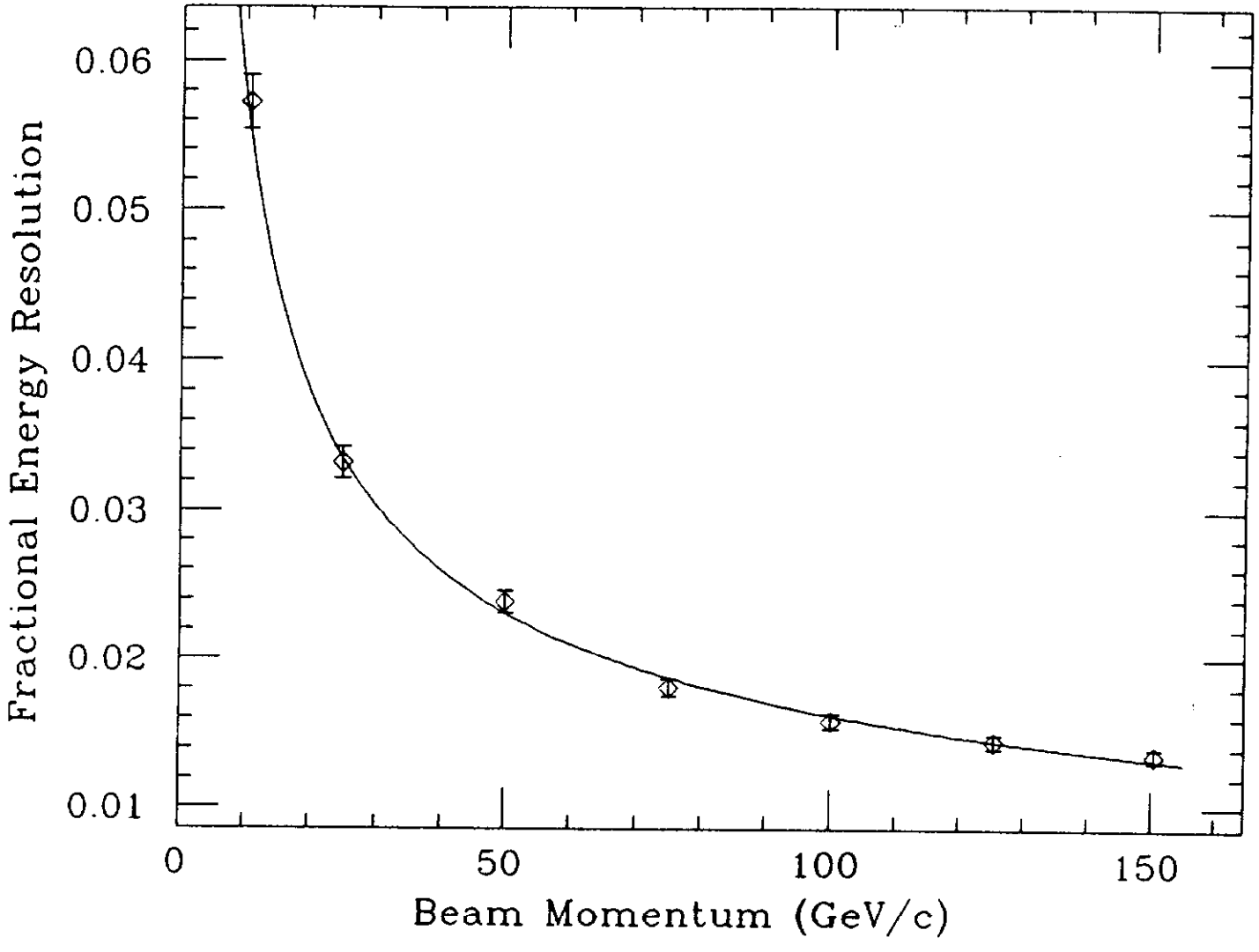
Fractional Energy Resolution
0.06
0.05
0.04
0.03
0.02
0.01
0
50
100
150
Beam Momentum (GeV/c)

Figure 41

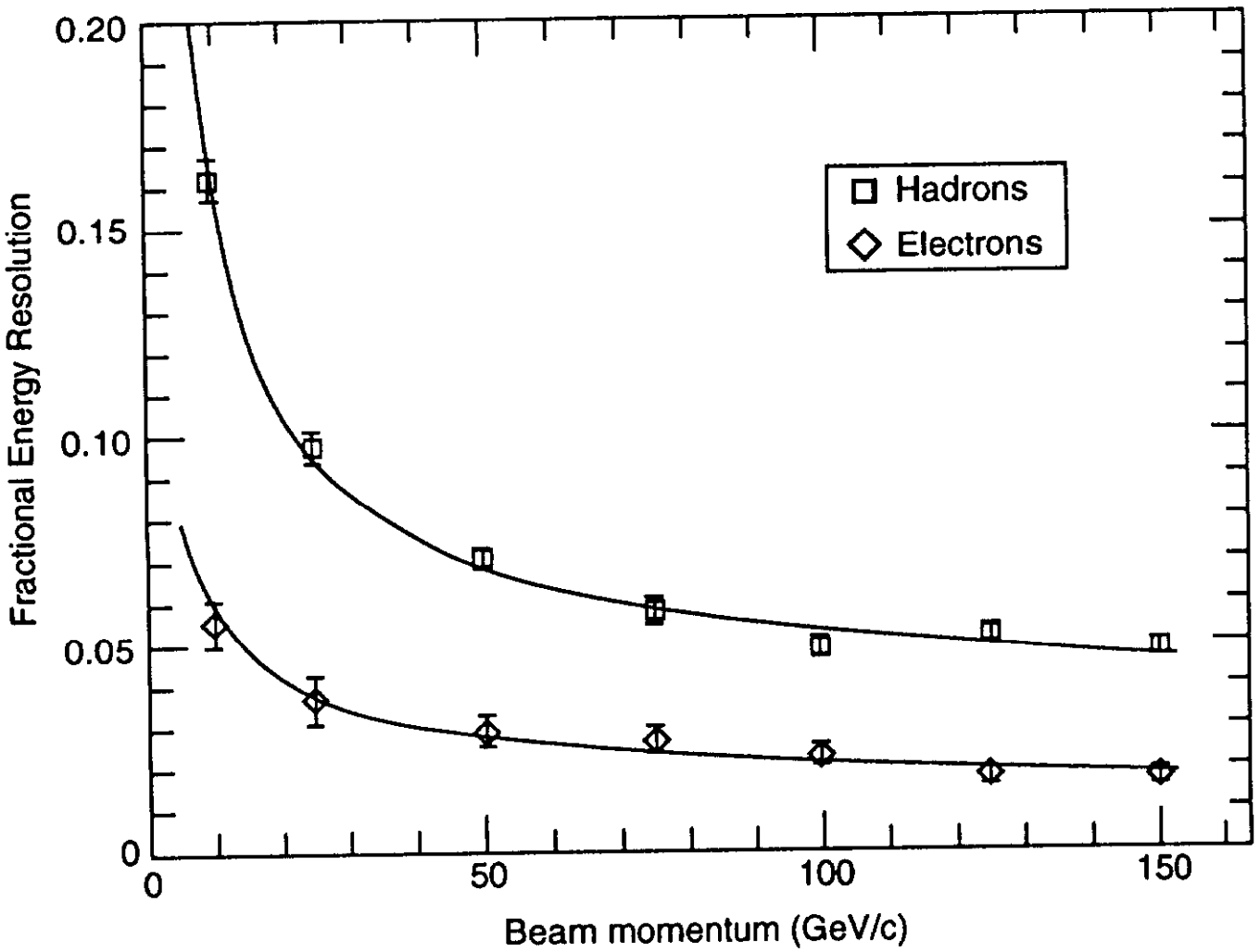
0.20
0.15
0.10
0.05
0
Fractional Energy Resolution
0
50
100
150
Beam momentum (GeV/c)
Hadrons
Electrons

Figure 42

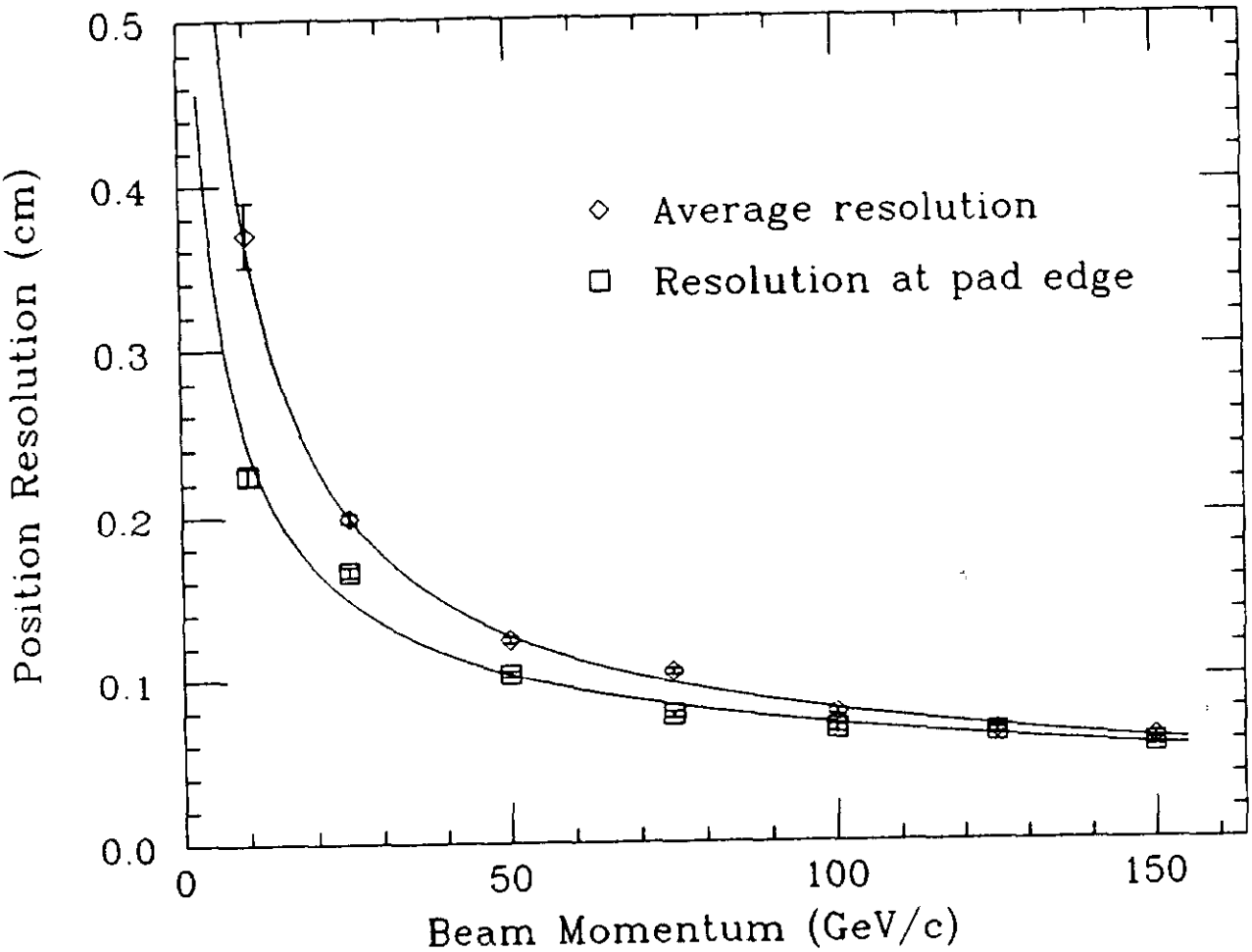
0.5
0.4
0.3
0.2
0.1
0.0
Position Resolution (cm)
Average resolution
Resolution at pad edge
0
50
100
150
Beam Momentum (GeV/c)

Figure 43

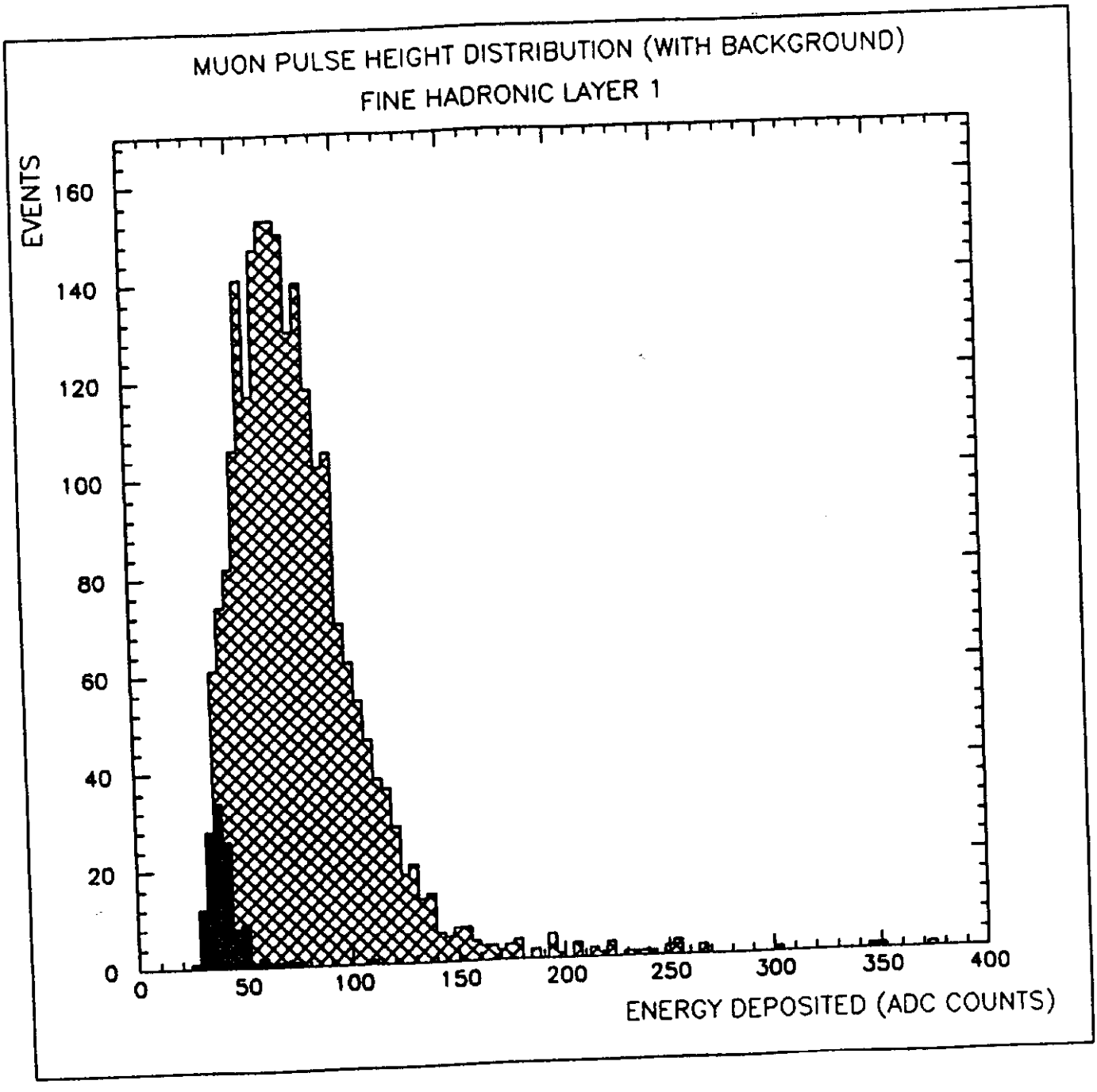
MUON PULSE HEIGHT DISTRIBUTION (WITH BACKGROUND)
FINE HADRONIC LAYER 1
EVENTS
160
140
120
100
80
60
40
20
0
0
50
100
150
200
250
300
350
400
ENERGY DEPOSITED (ADC COUNTS)

Figure 44

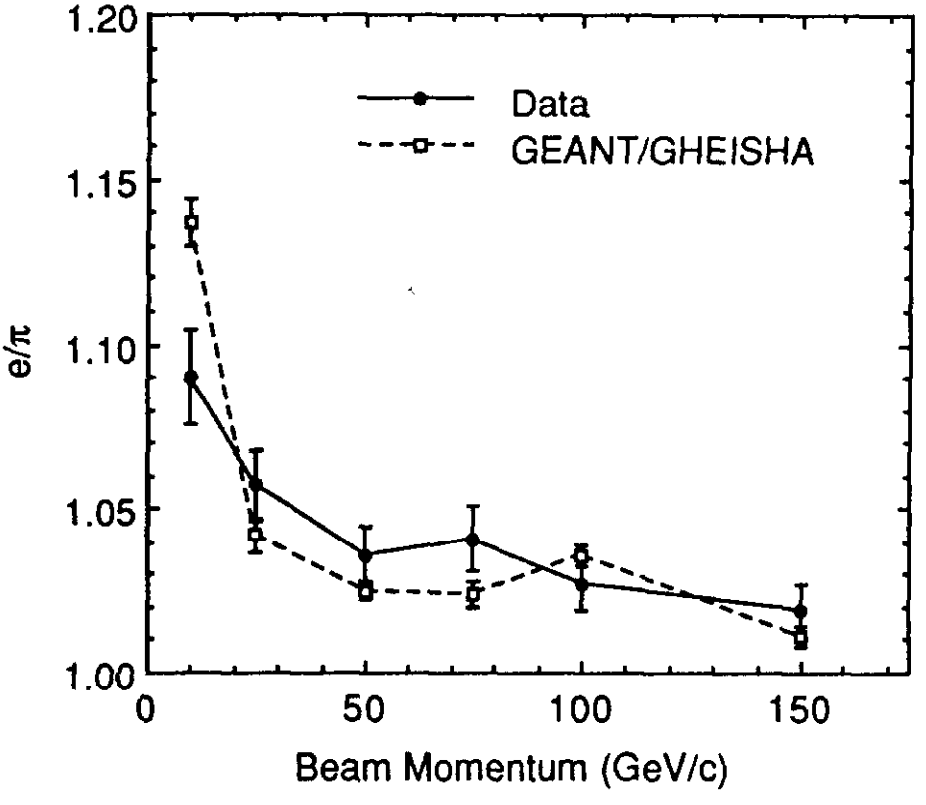
1.20
1.15
1.10
1.05
1.00
e/π
Data
GEANT/GHEISHA
0
50
100
150
Beam Momentum (GeV/c)

Figure 45

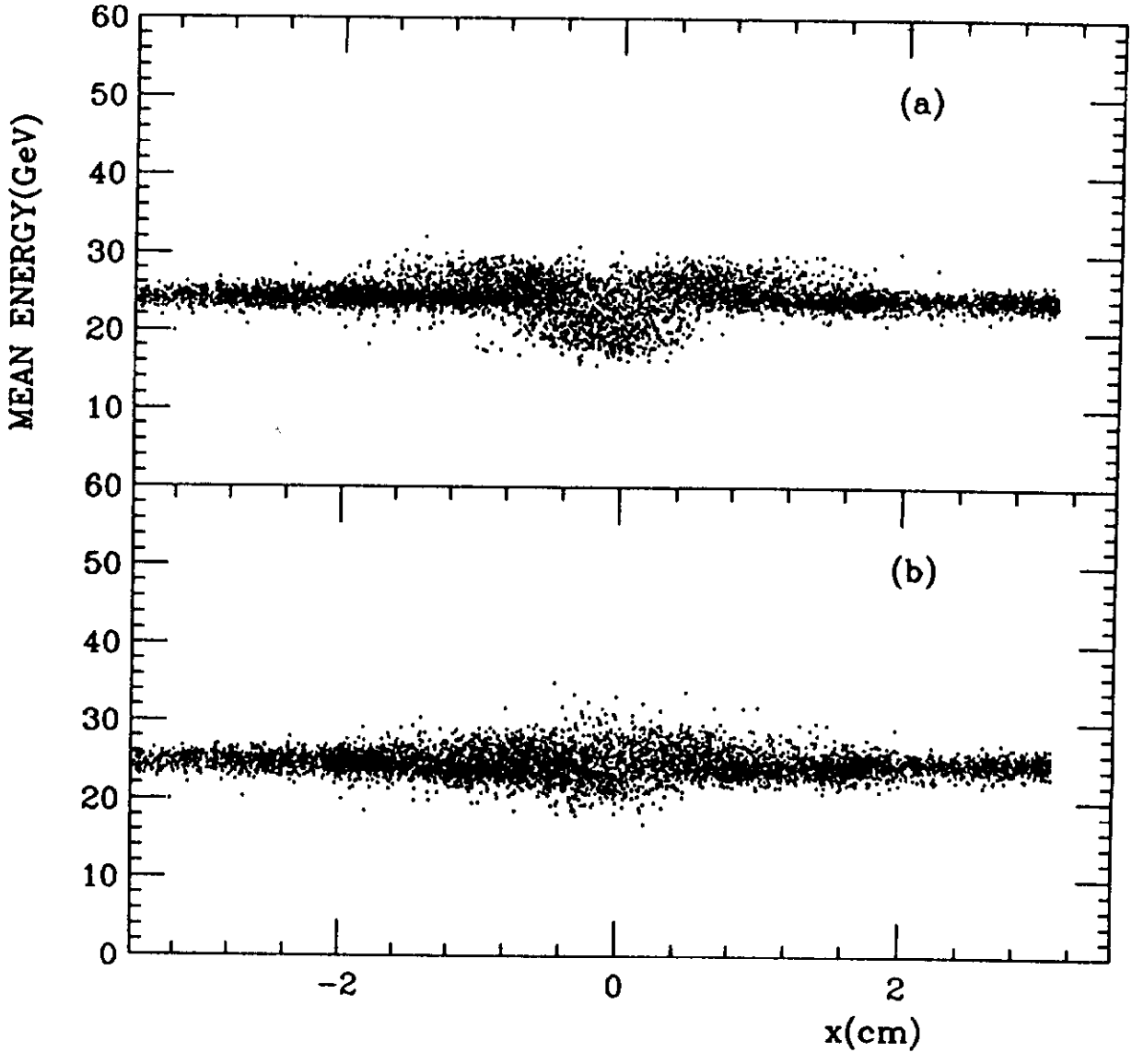

Figure 46

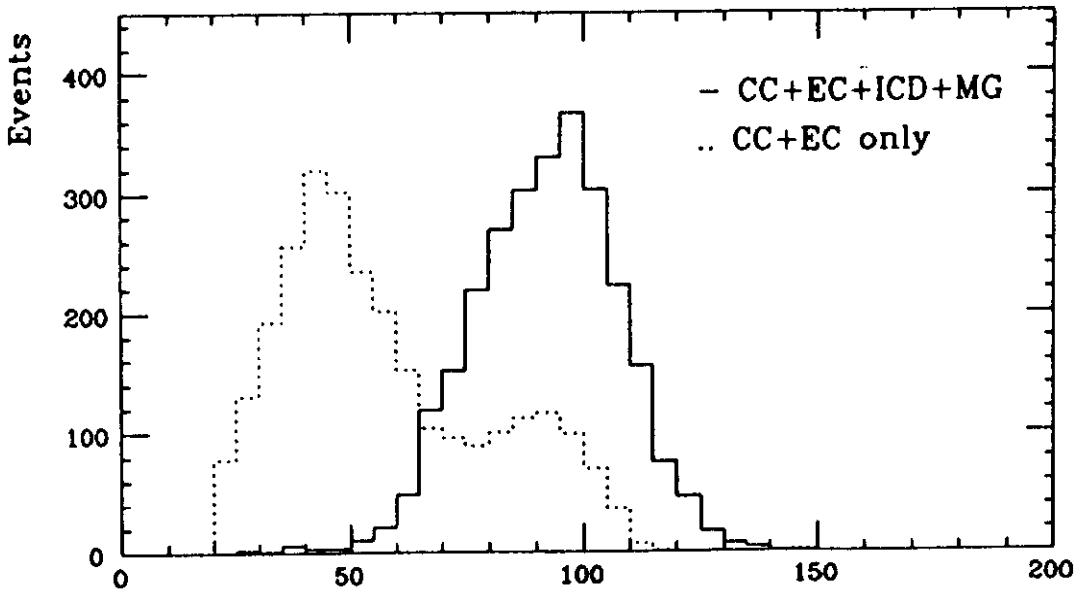

Figure 47 (a)

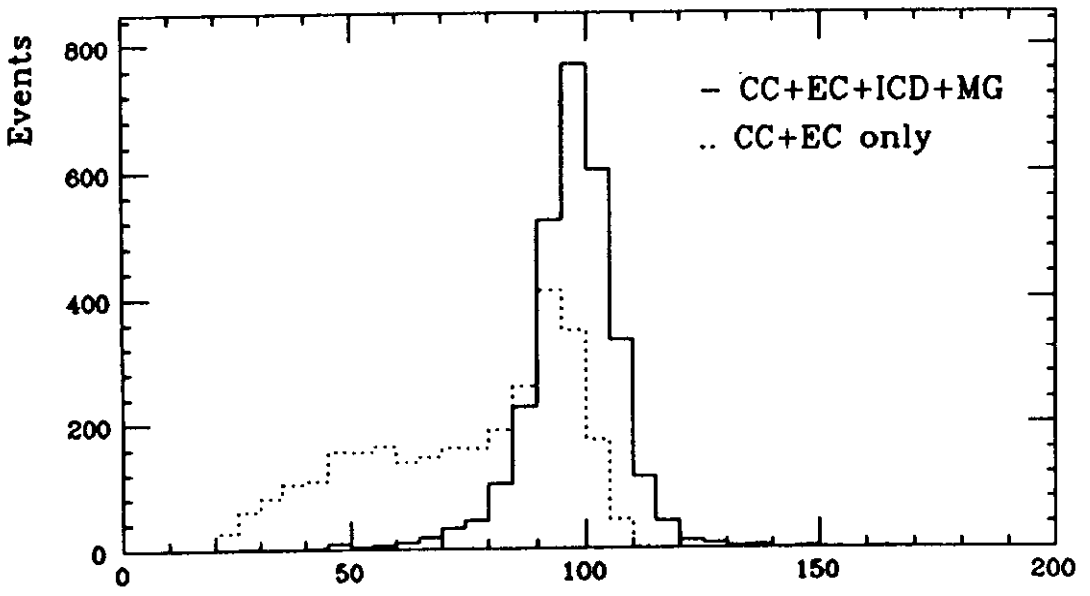

Figure 47 (b)

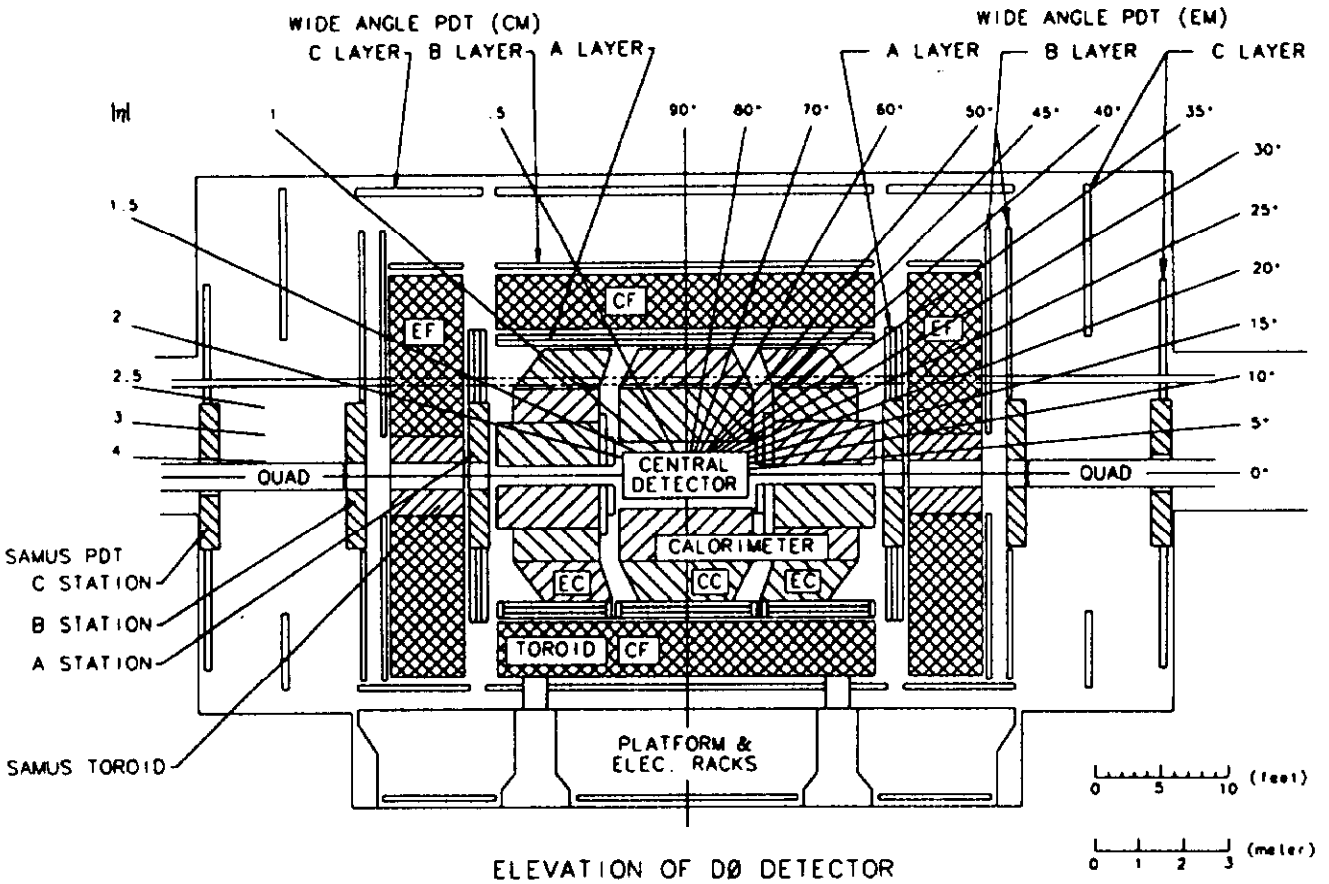

ELEVATION OF DØ DETECTOR

Figure 48

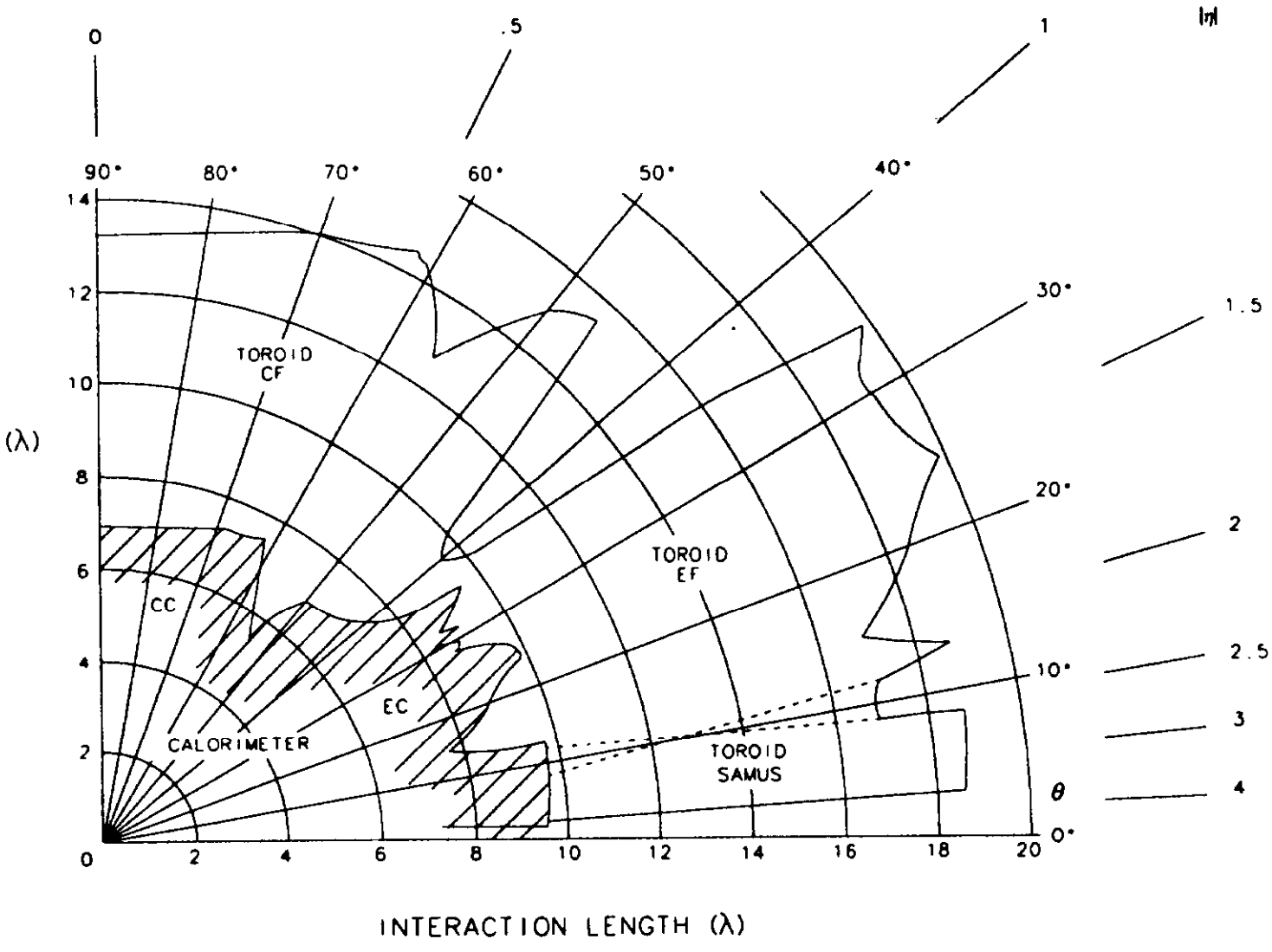
|η|
0
.5
1
90°
80°
70°
60°
50°
40°
30°
20°
10°
θ
0°
1.5
2
2.5
3
4
14
12
10
8
6
4
2
0
(λ)
TOROID
CF
TOROID
EF
CC
EC
CALORIMETER
TOROID
SAMUS
2
4
6
8
10
12
14
16
18
20
INTERACTION LENGTH (λ)

Figure 49

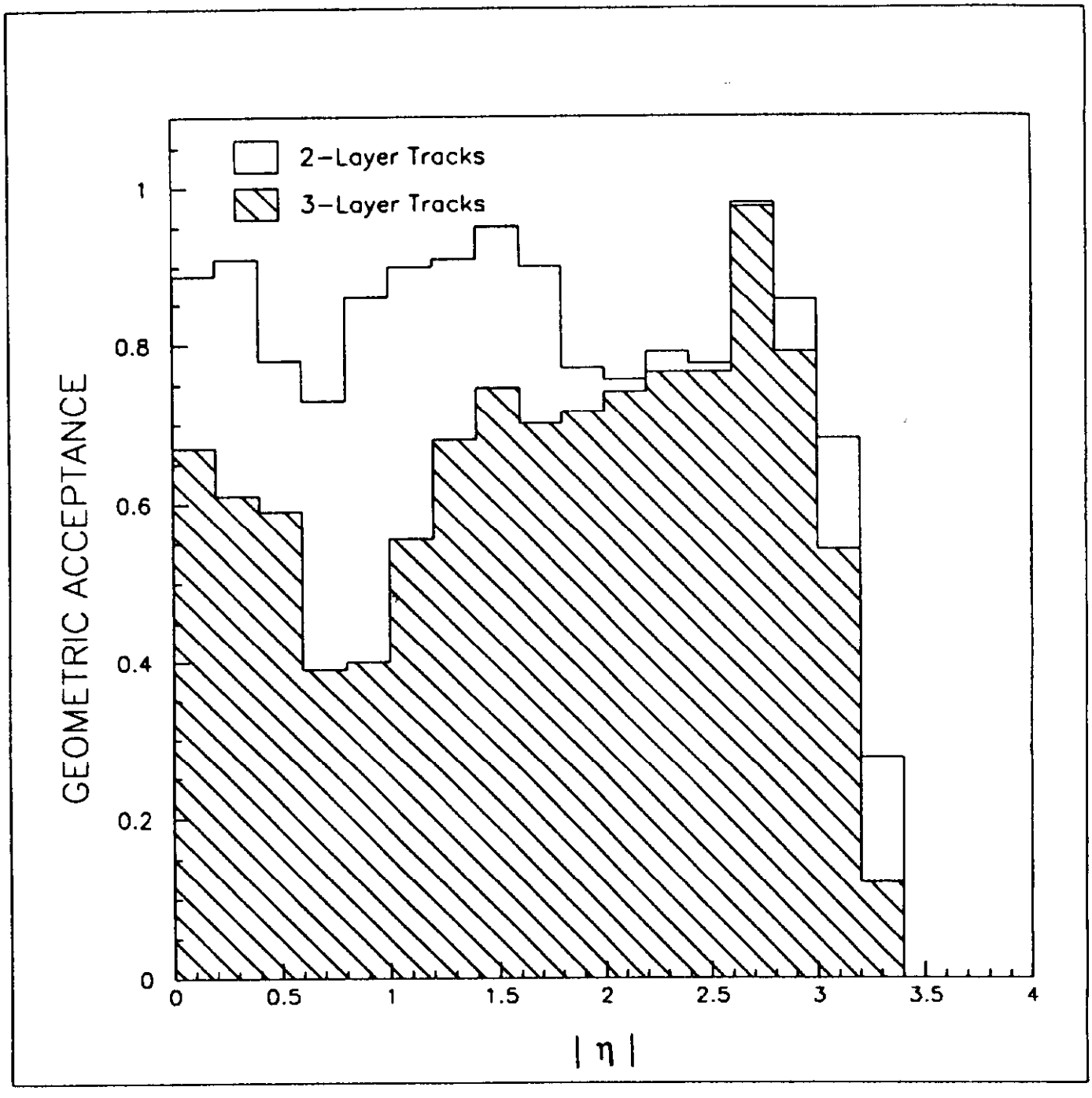
2-Layer Tracks
3-Layer Tracks
GEOMETRIC ACCEPTANCE
0
0.2
0.4
0.6
0.8
1
0
0.5
1
1.5
2
2.5
3
3.5
4
| η |

Figure 50

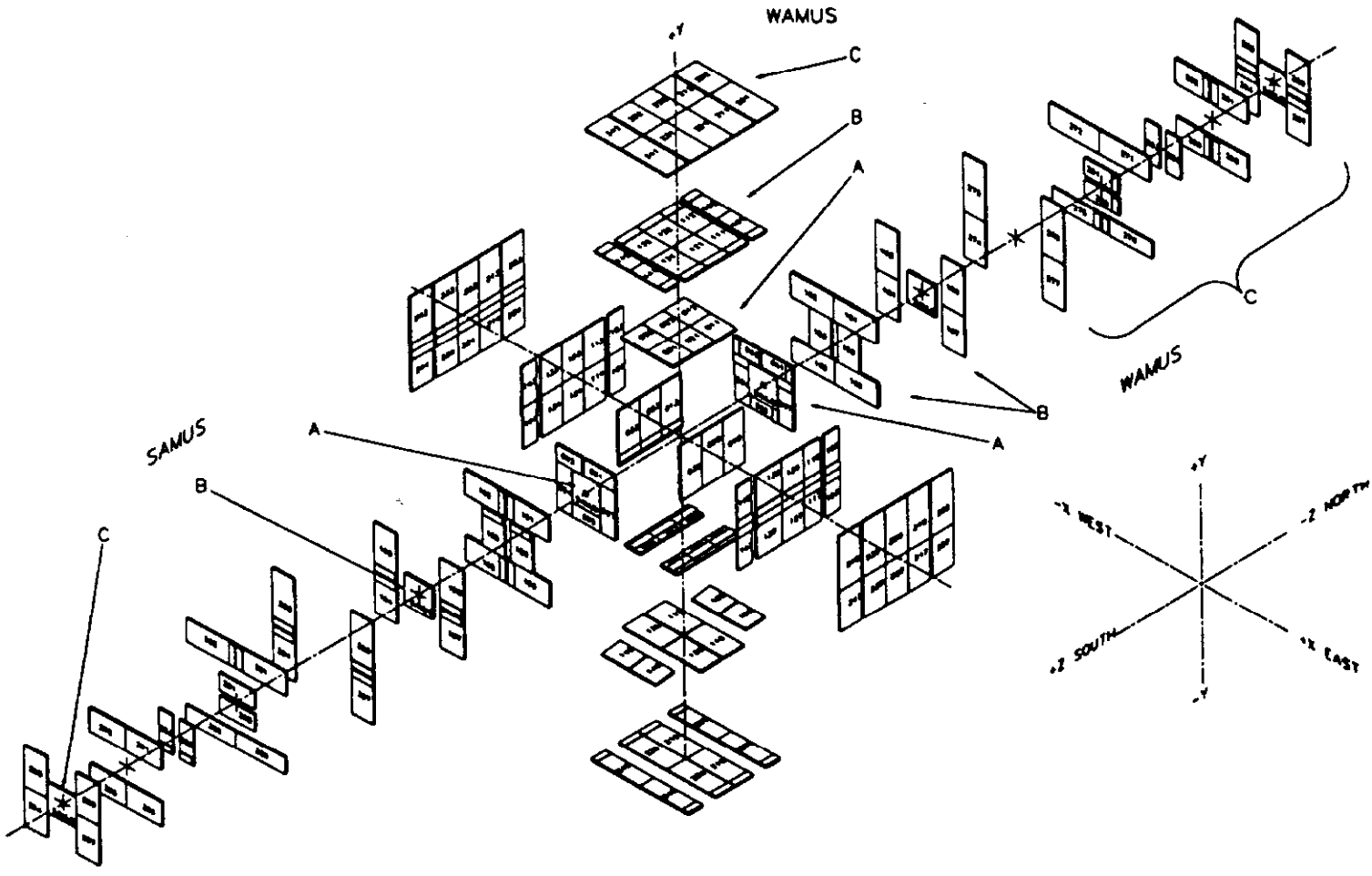

Figure 51

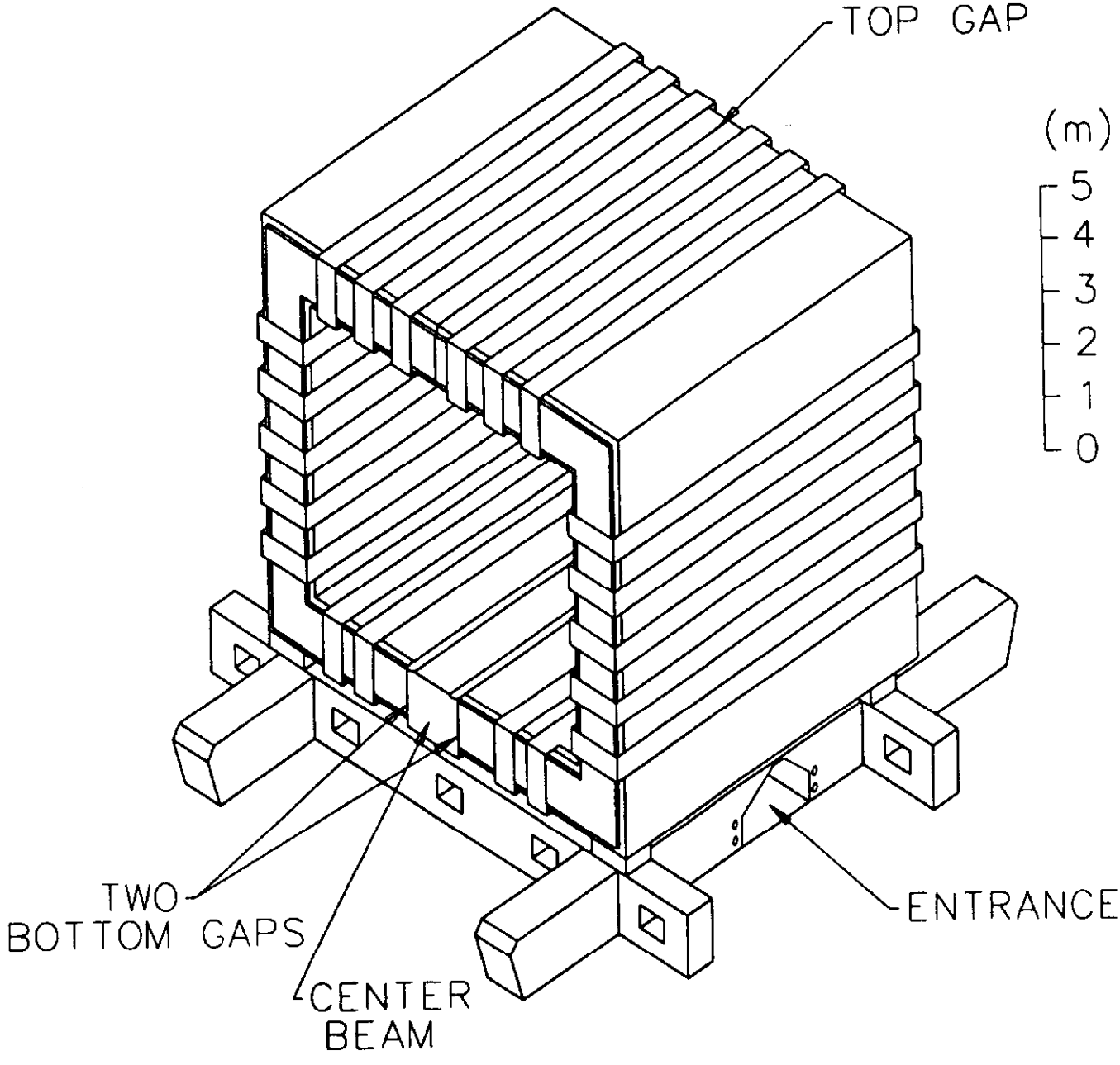

Figure 52

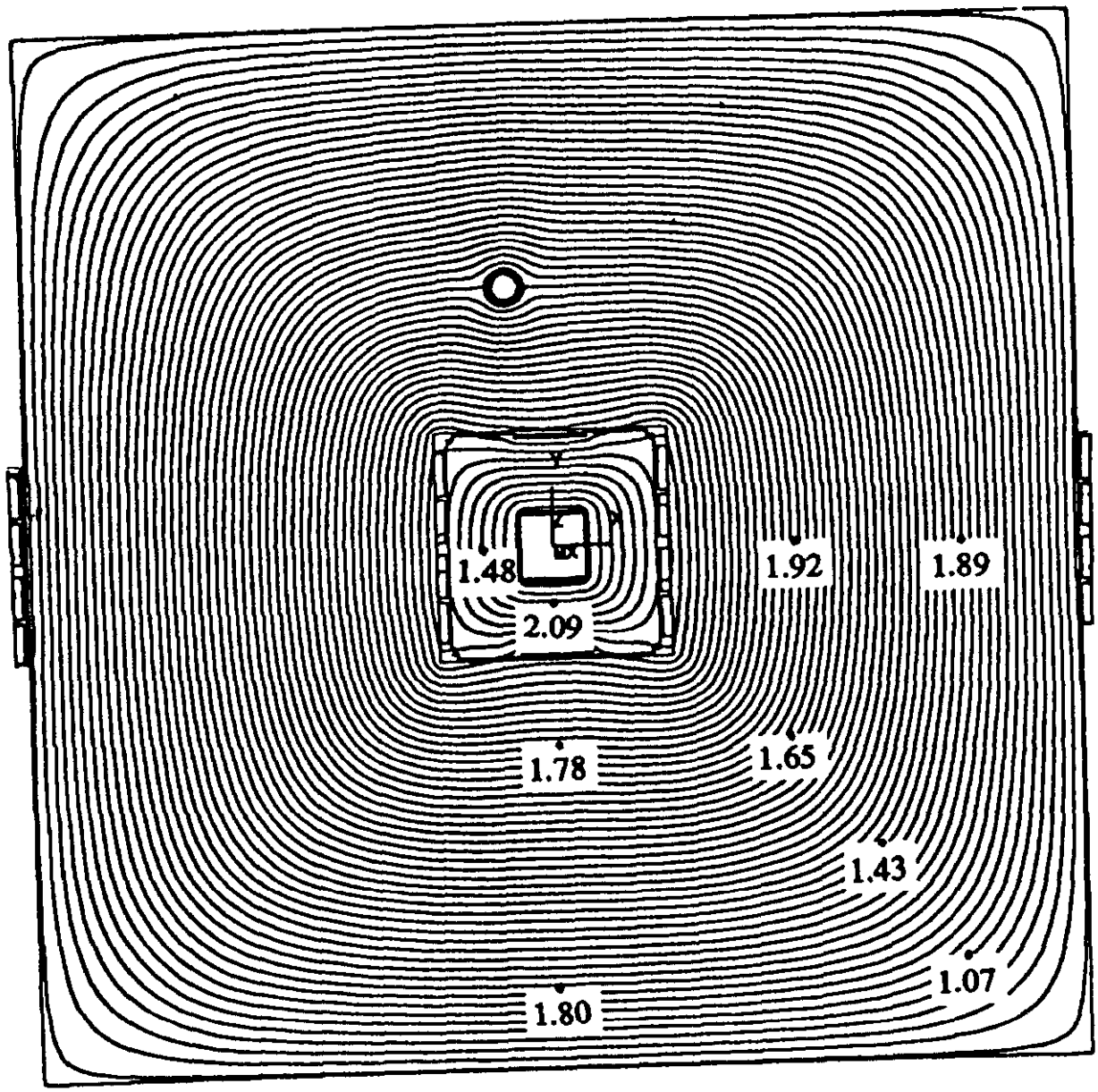

Figure 53

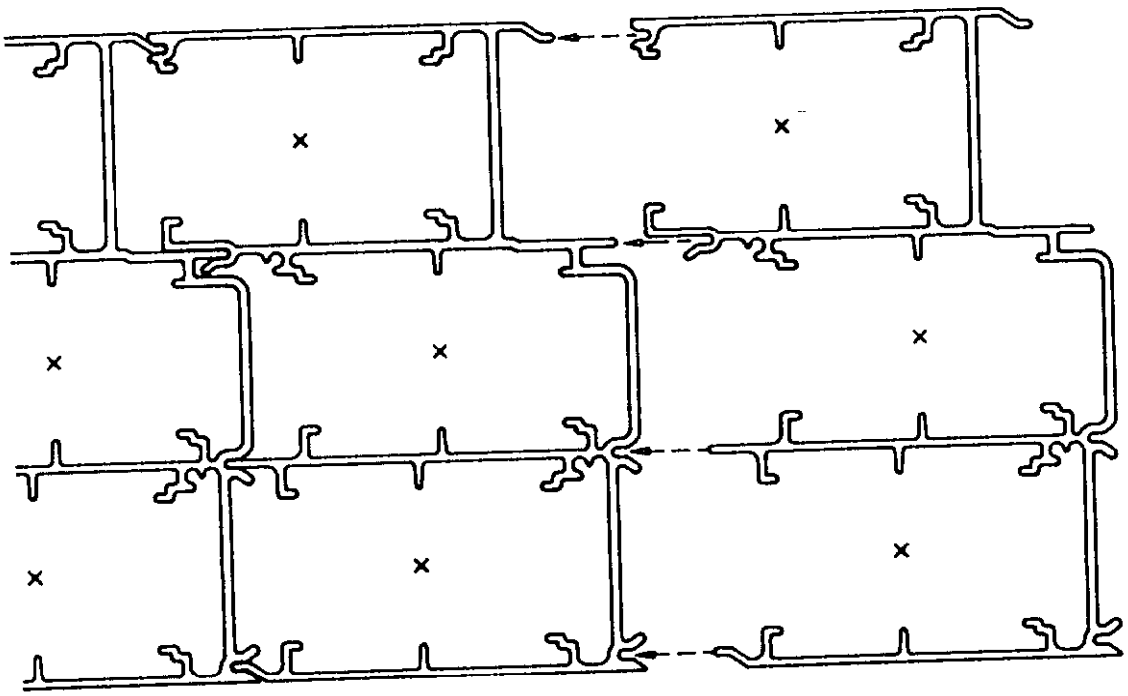

Figure 54

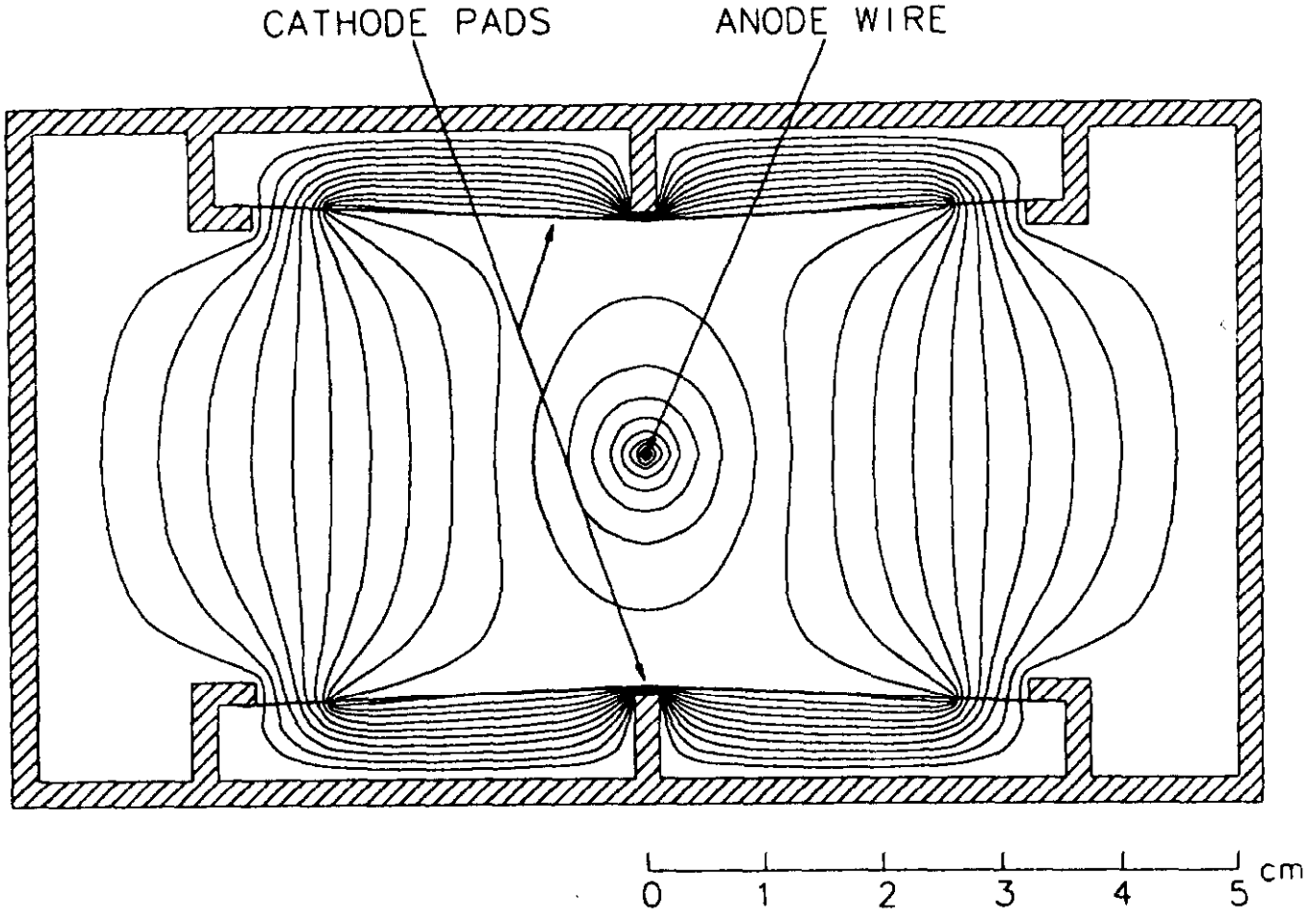

Figure 55

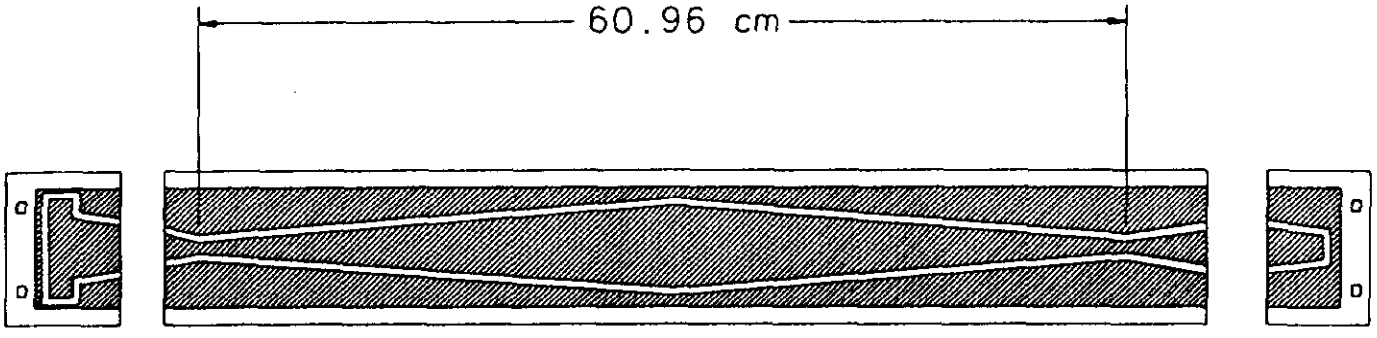

Figure 56

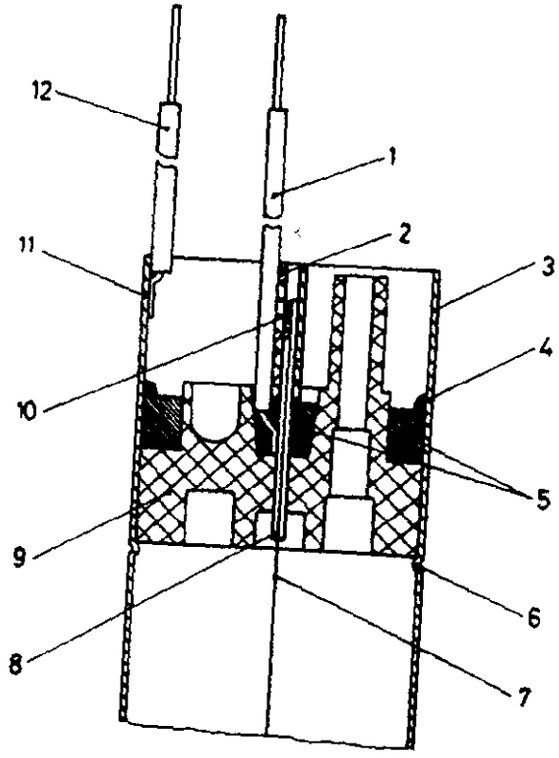

Figure 57

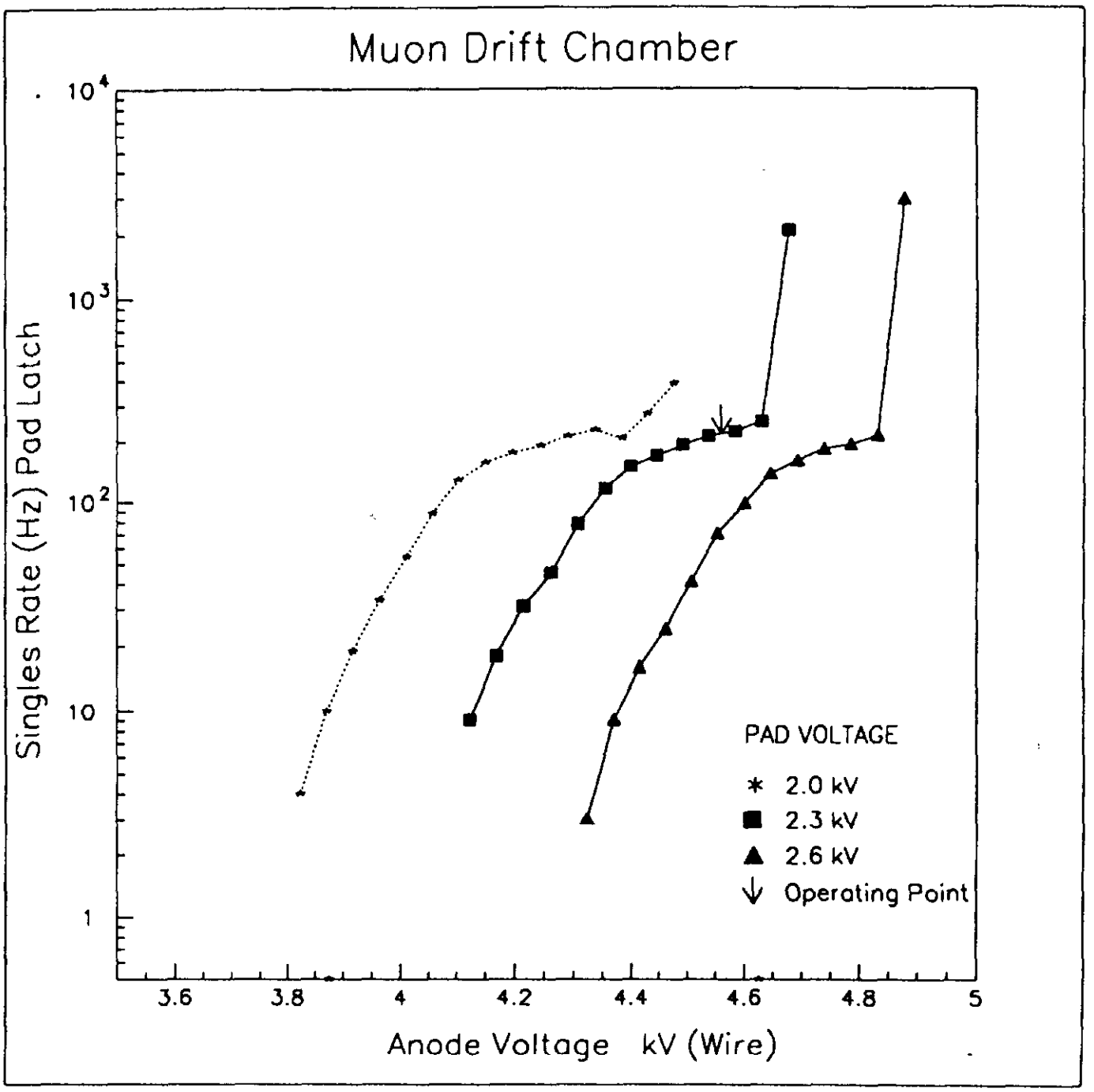
Muon Drift Chamber
Singles Rate (Hz) Pad Latch
10^4
10^3
10^2
10
1
3.6
3.8
4
4.2
4.4
4.6
4.8
5
Anode Voltage kV (Wire)
PAD VOLTAGE
* 2.0 kV
■ 2.3 kV
▲ 2.6 kV
↓ Operating Point

Figure 58

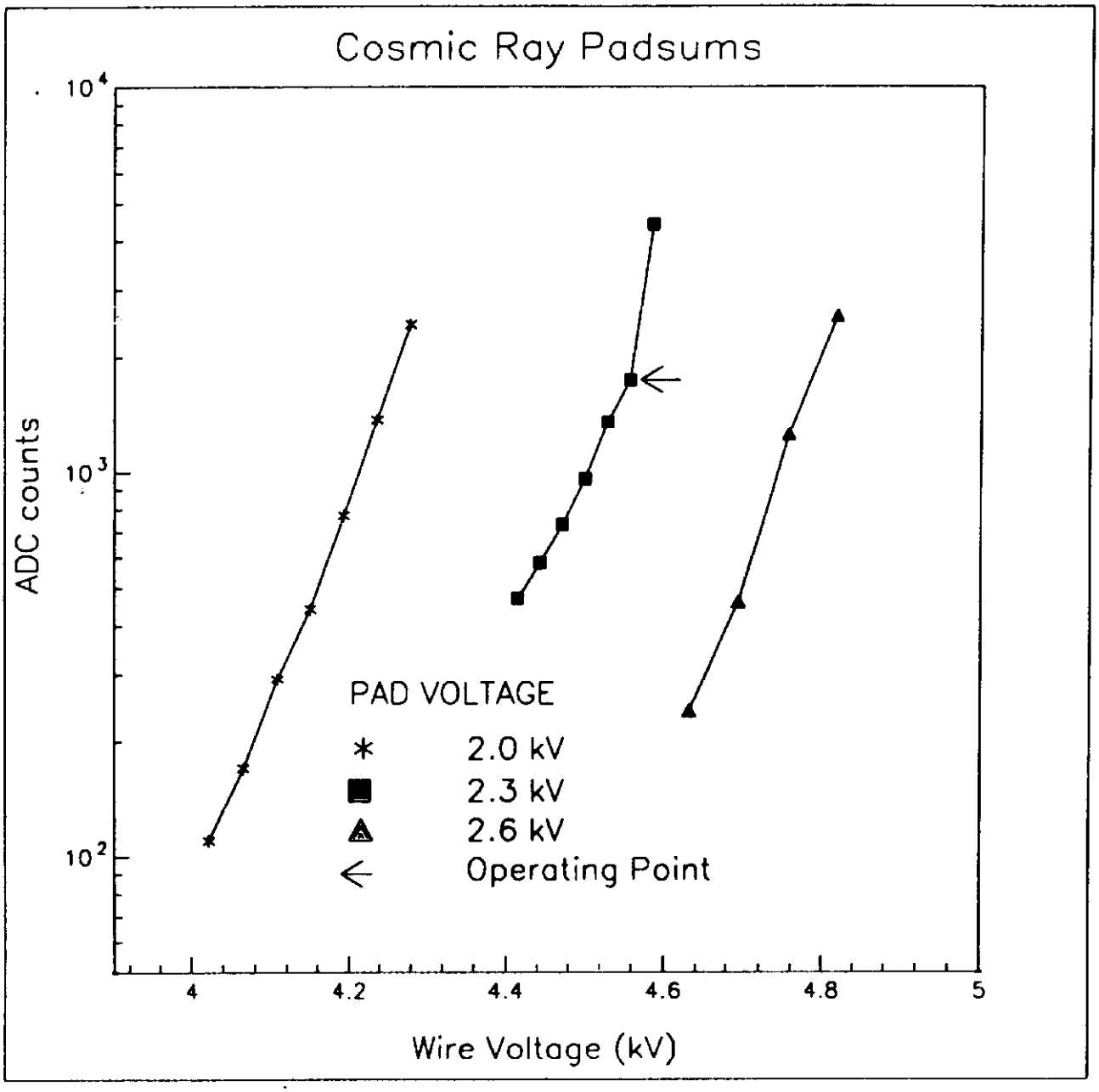
Cosmic Ray Padsums
ADC counts
10^4
10^3
10^2
4
4.2
4.4
4.6
4.8
5
Wire Voltage (kV)
PAD VOLTAGE
2.0 kV
2.3 kV
2.6 kV
Operating Point

Figure 59

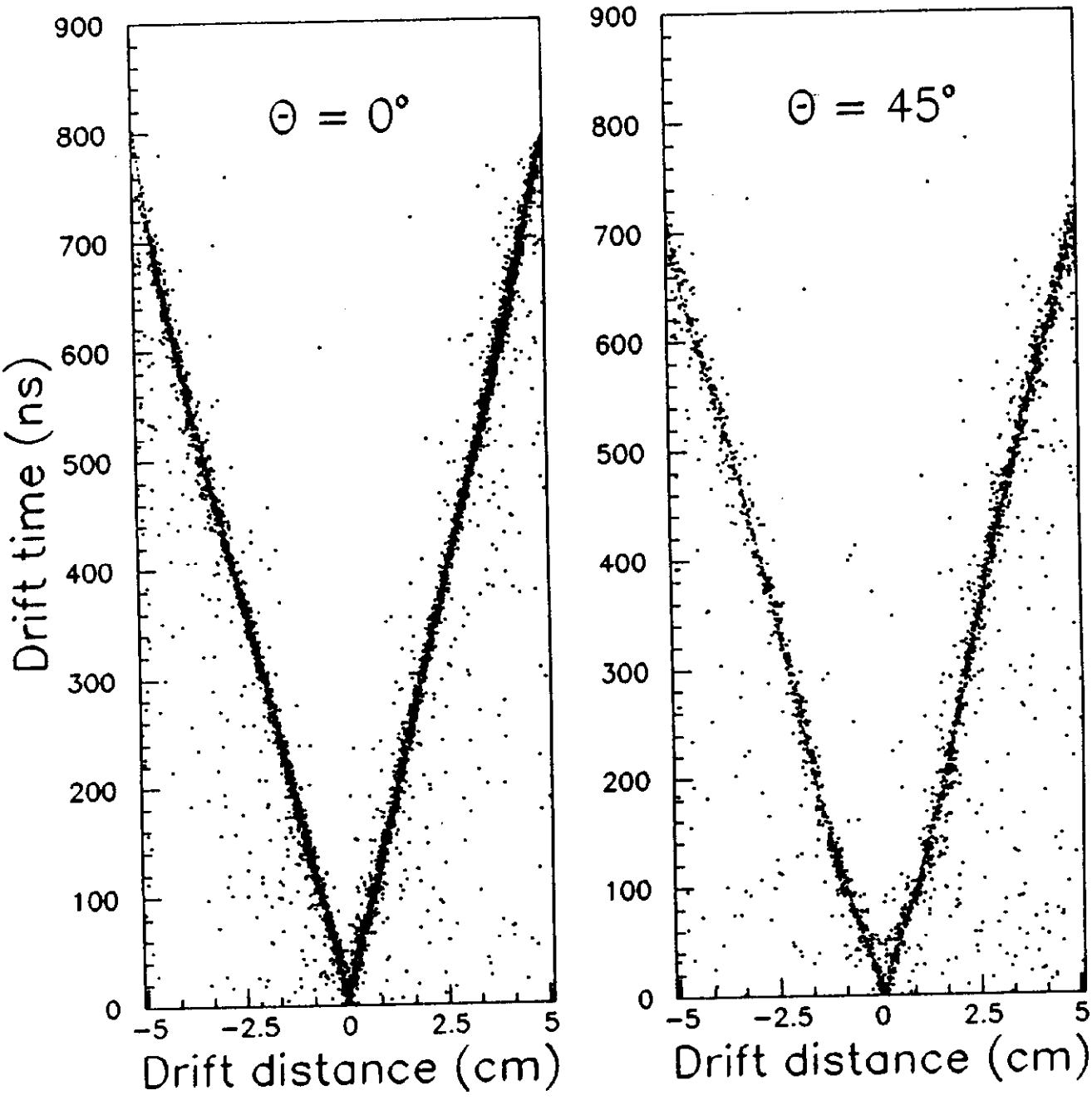
Θ = 0°
Θ = 45°
Drift time (ns)
Drift distance (cm)
Drift distance (cm)
900
800
700
600
500
400
300
200
100
0
−5
−2.5
0
2.5
5

Figure 60

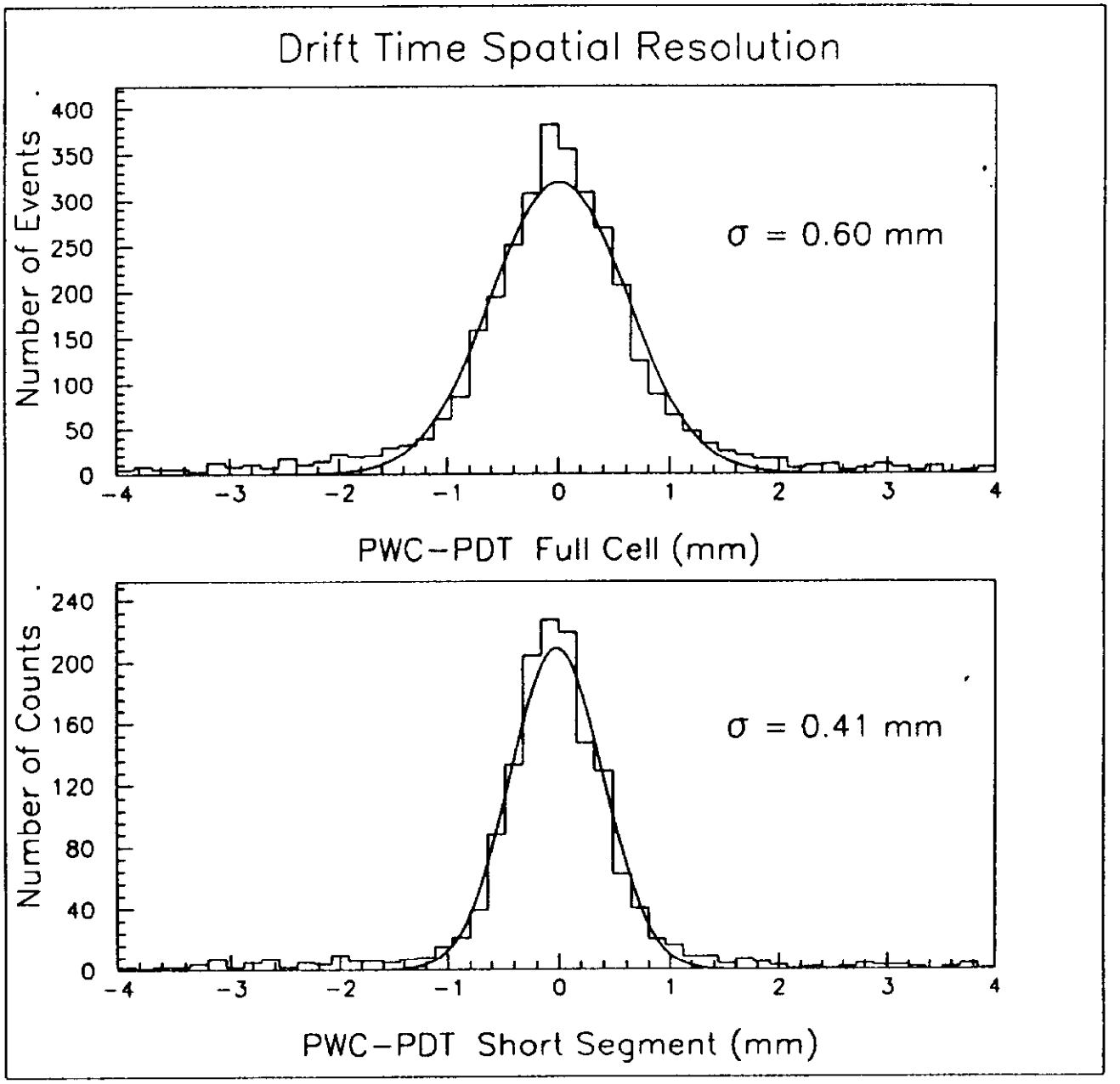
Drift Time Spatial Resolution
Number of Events
400
350
300
250
200
150
100
50
0
σ = 0.60 mm
-4
-3
-2
-1
0
1
2
3
4
PWC−PDT Full Cell (mm)
Number of Counts
240
200
160
120
80
40
0
σ = 0.41 mm
-4
-3
-2
-1
0
1
2
3
4
PWC−PDT Short Segment (mm)

Figure 61

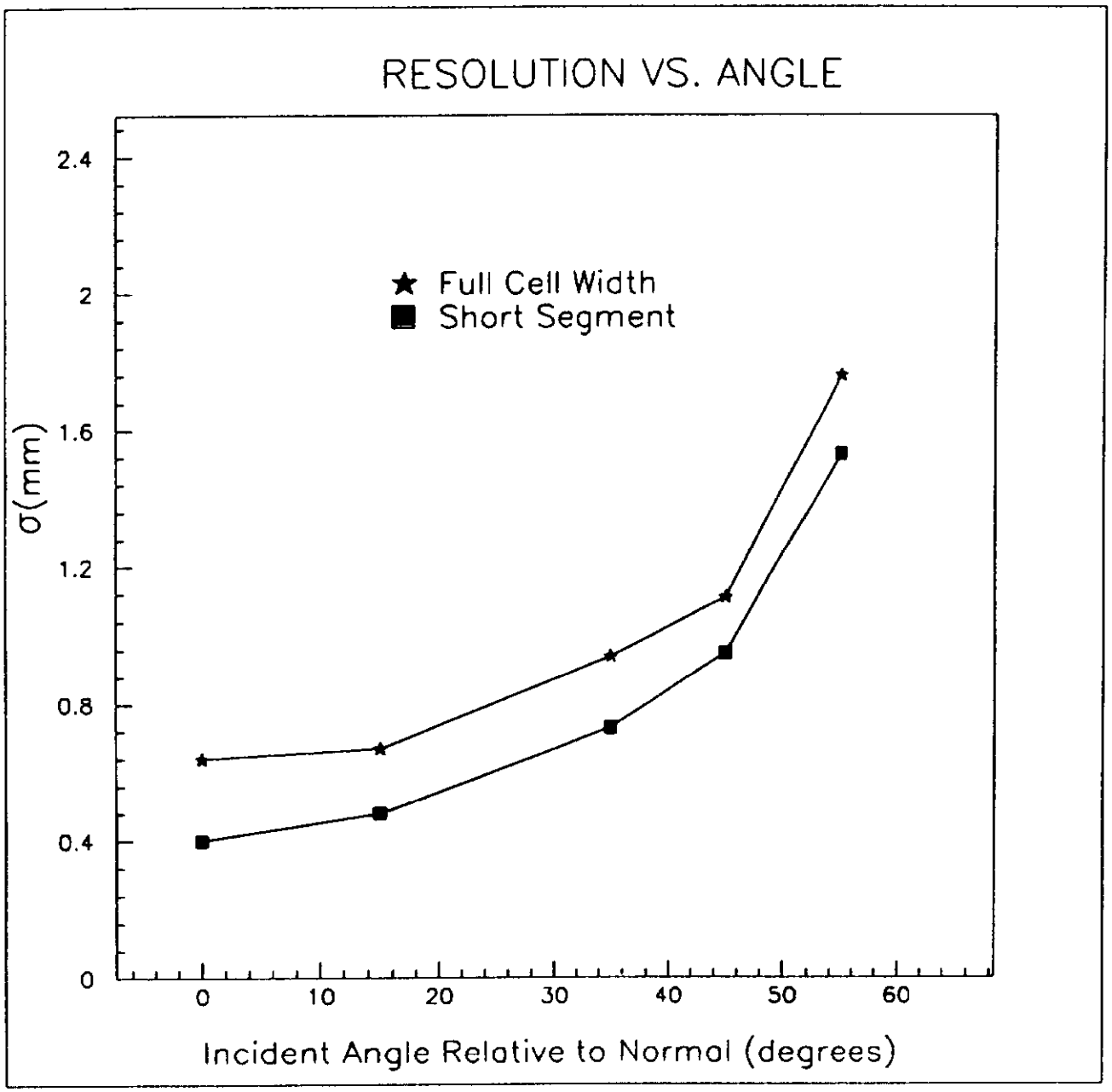
RESOLUTION VS. ANGLE
Full Cell Width
Short Segment
σ(mm)
2.4
2
1.6
1.2
0.8
0.4
0
0
10
20
30
40
50
60
Incident Angle Relative to Normal (degrees)

Figure 62

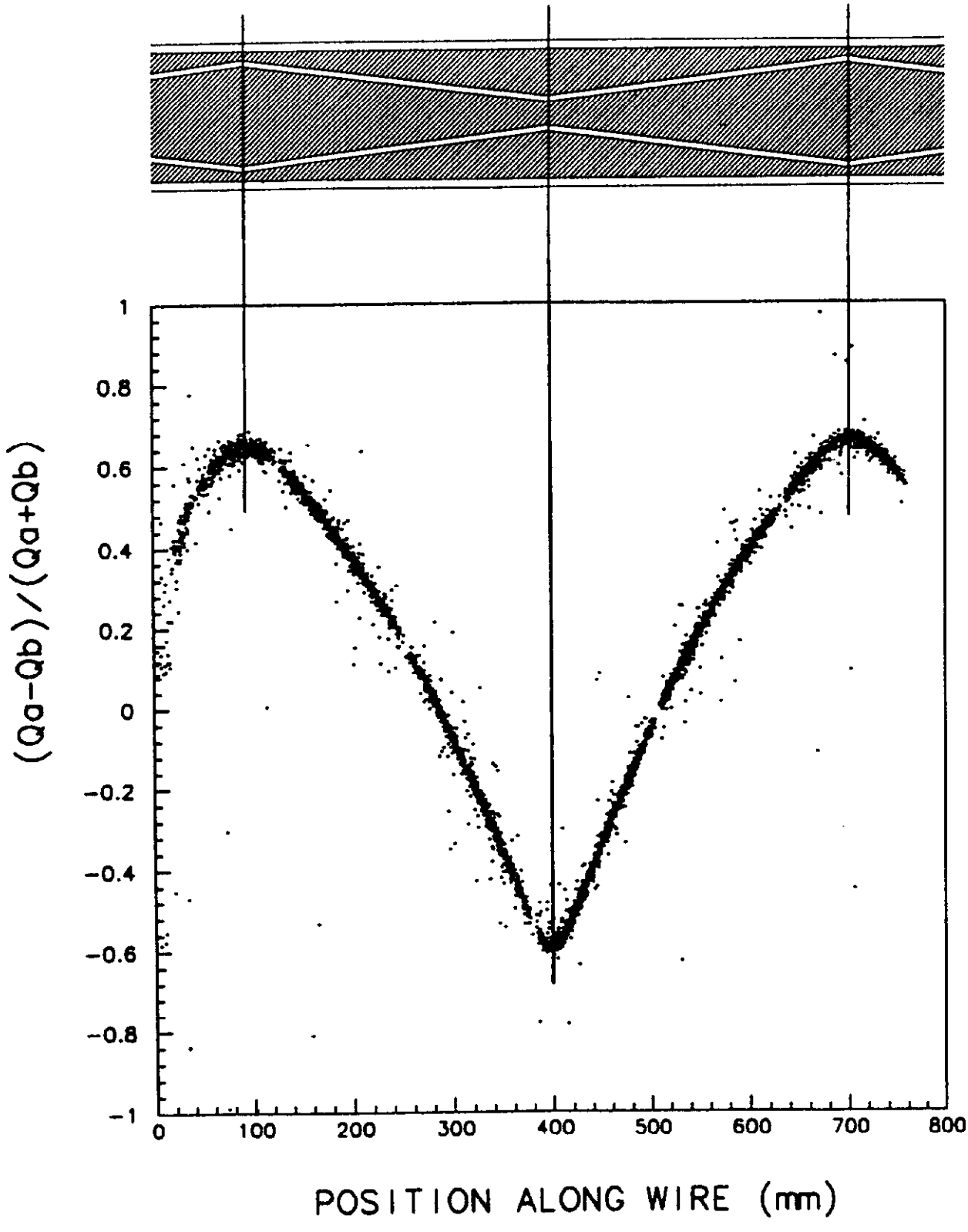
1
0.8
0.6
0.4
0.2
0
-0.2
-0.4
-0.6
-0.8
-1
0
100
200
300
400
500
600
700
800
(Qa-Qb)/(Qa+Qb)
POSITION ALONG WIRE (mm)

Figure 63

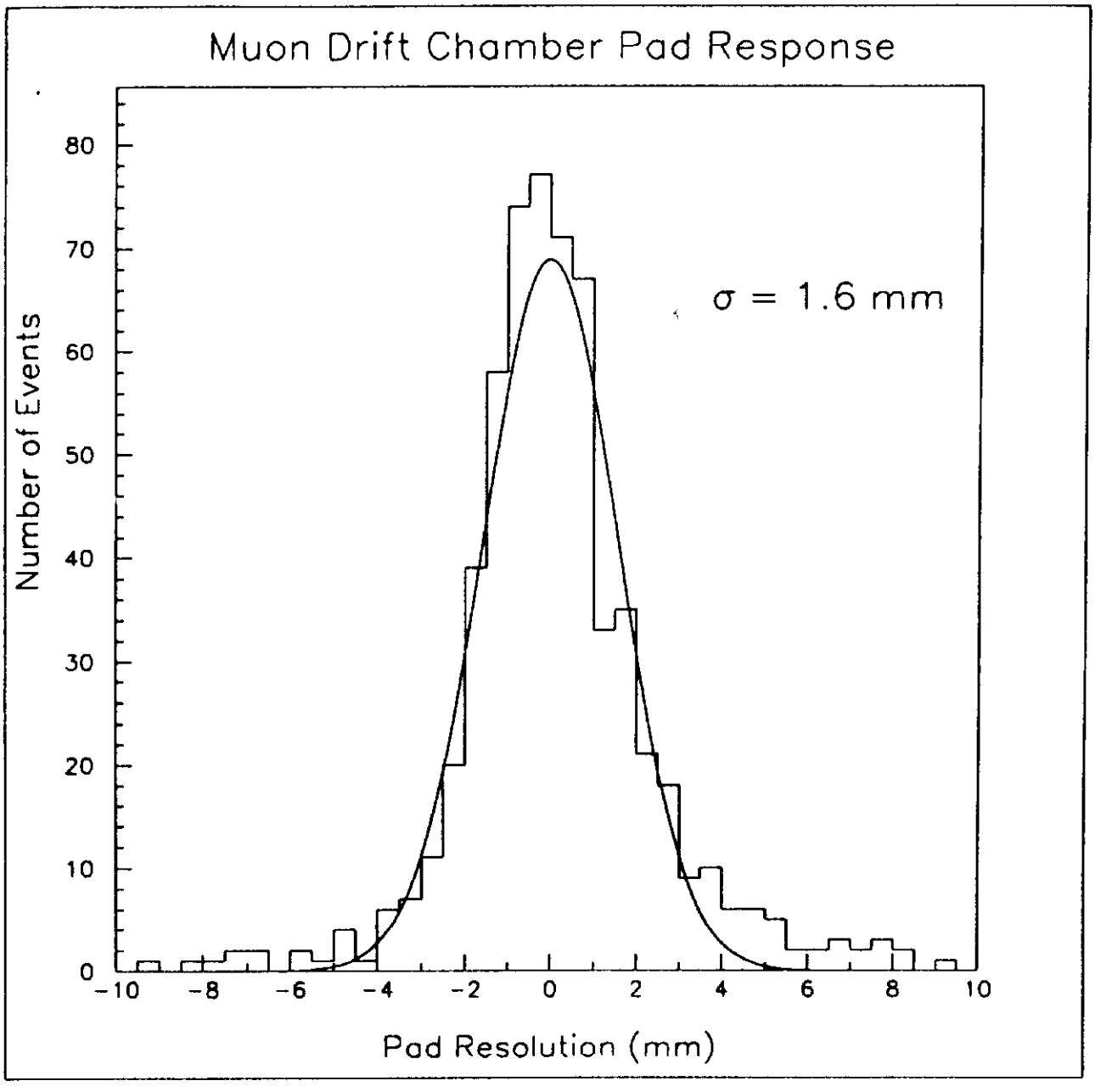
Muon Drift Chamber Pad Response
σ = 1.6 mm
Number of Events
Pad Resolution (mm)
0
10
20
30
40
50
60
70
80
-10
-8
-6
-4
-2
0
2
4
6
8
10

Figure 64

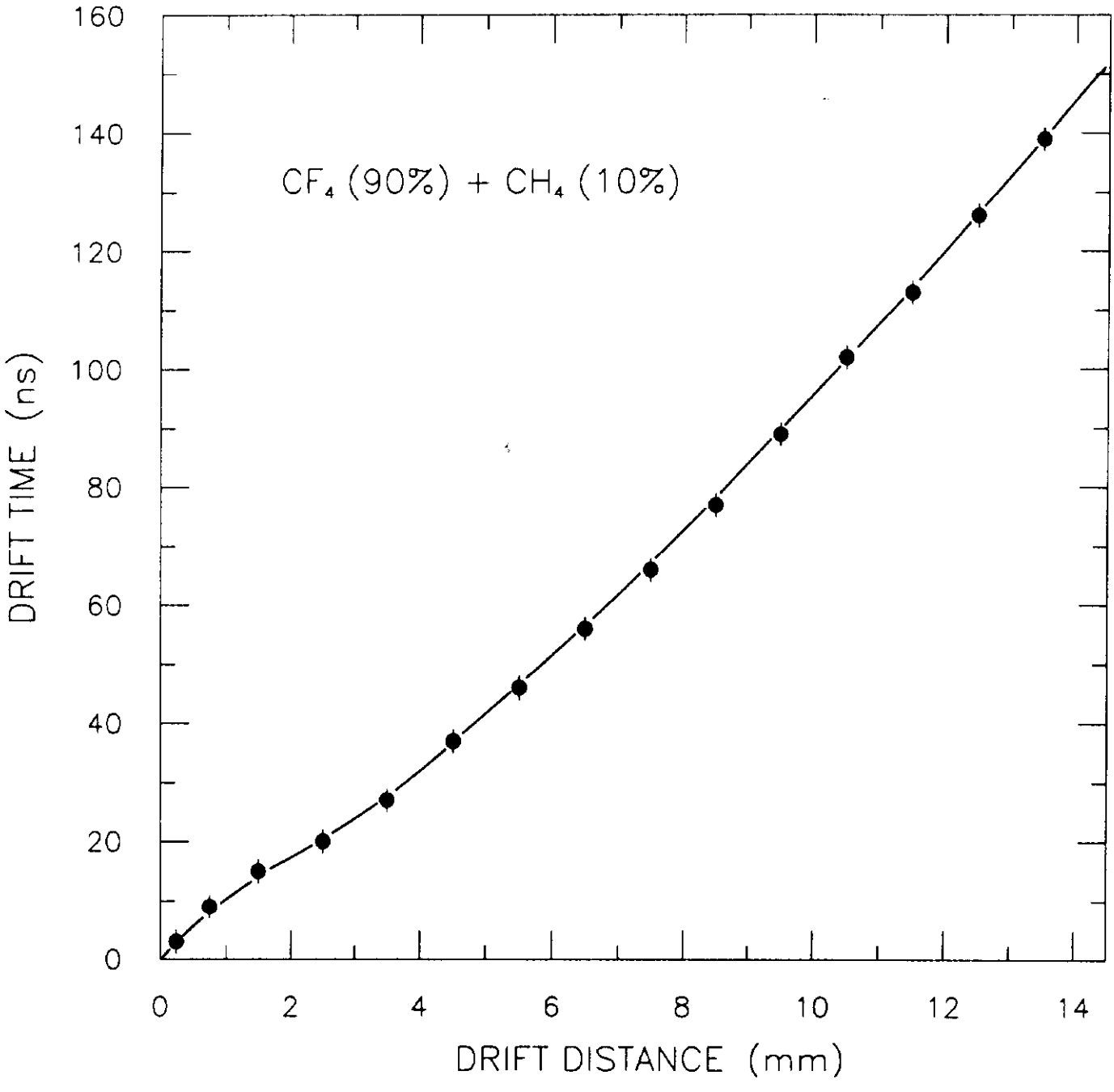
160
140
120
100
80
60
40
20
0
DRIFT TIME (ns)
CF_4 (90%) + CH_4 (10%)
0
2
4
6
8
10
12
14
DRIFT DISTANCE (mm)

Figure 65

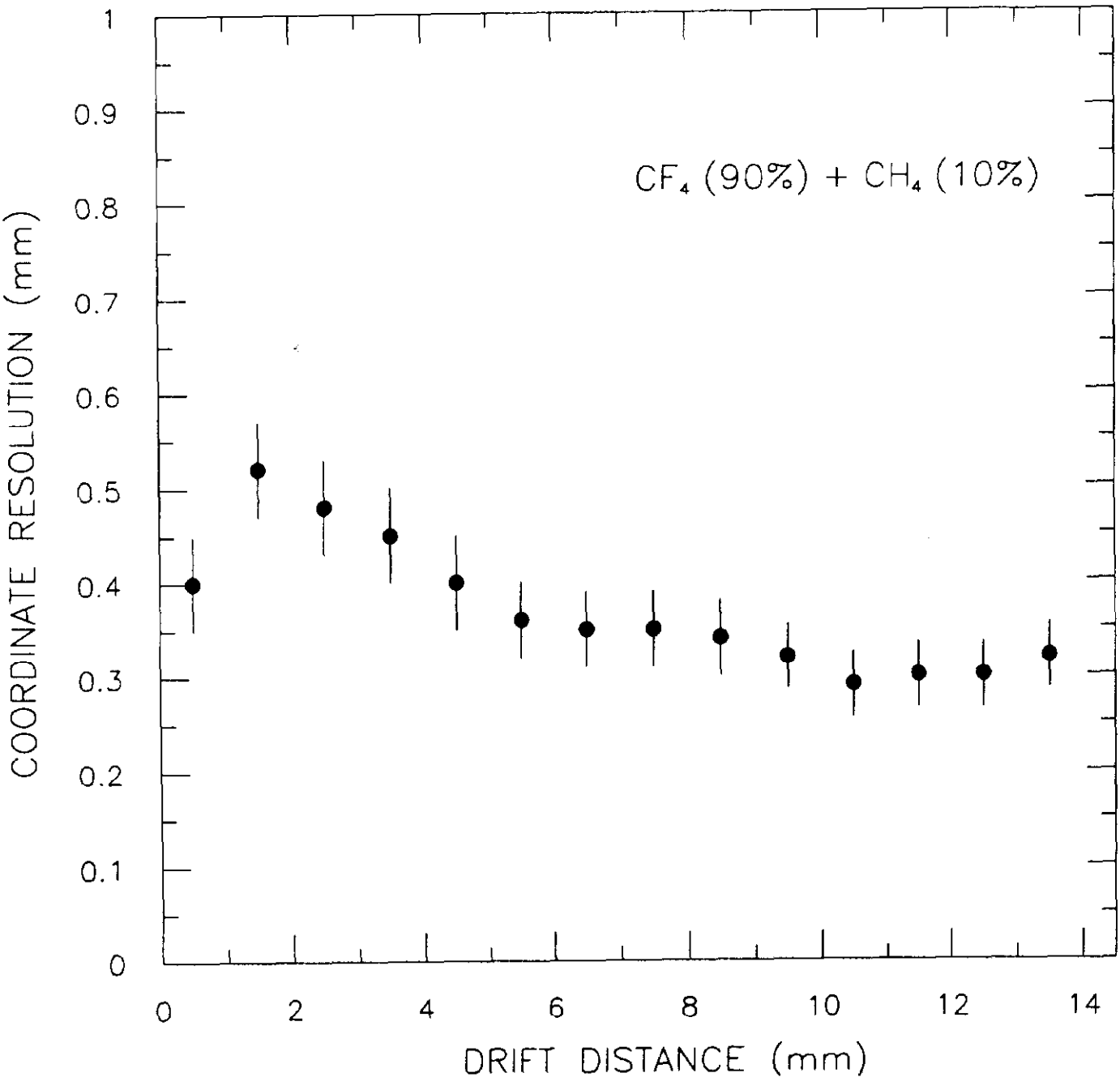
COORDINATE RESOLUTION (mm)
DRIFT DISTANCE (mm)
CF_4 (90%) + CH_4 (10%)
0
0.1
0.2
0.3
0.4
0.5
0.6
0.7
0.8
0.9
1
0
2
4
6
8
10
12
14

Figure 66

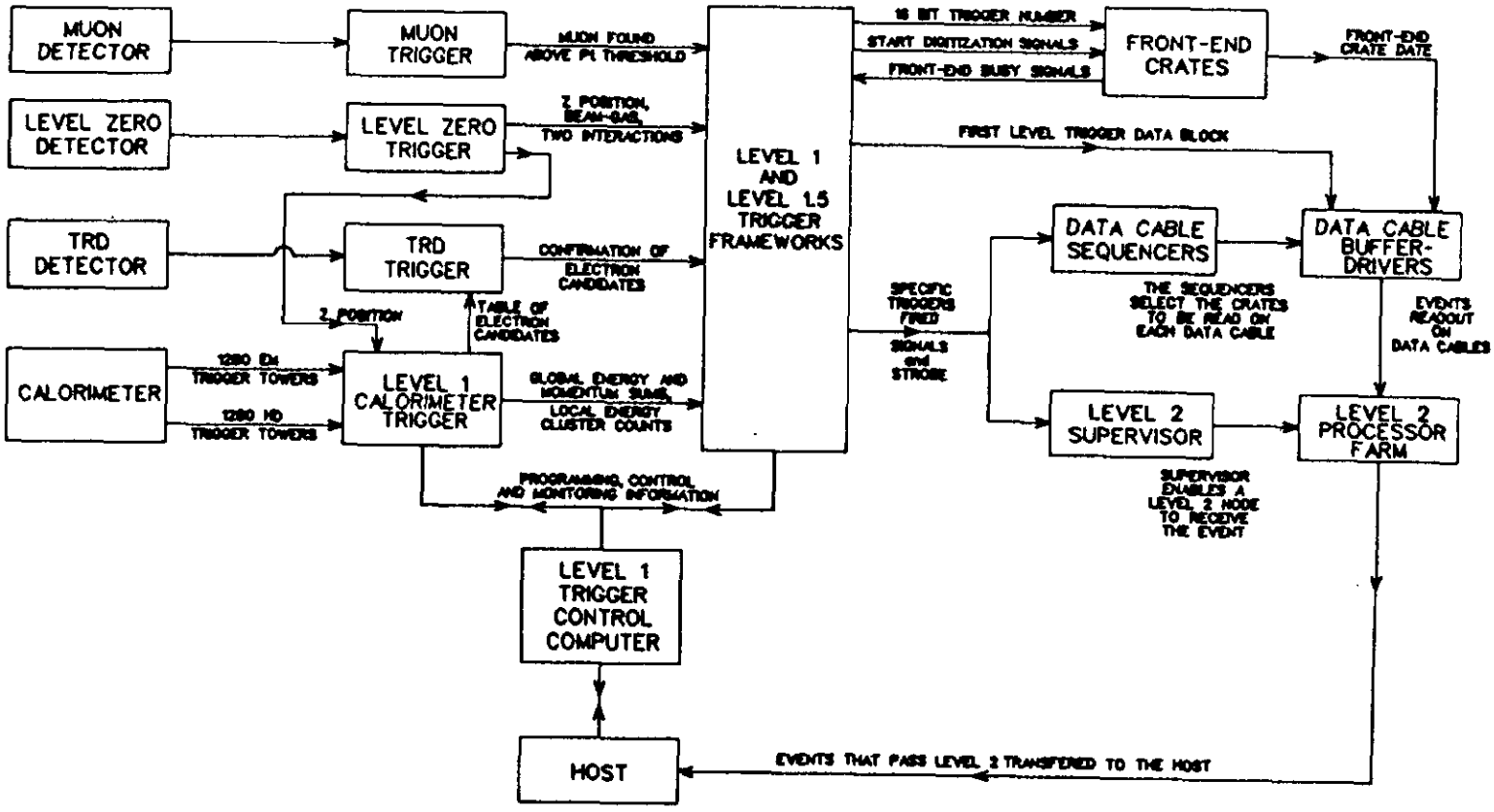
MUON DETECTOR
MUON TRIGGER
MUON FOUND ABOVE PT THRESHOLD
LEVEL ZERO DETECTOR
LEVEL ZERO TRIGGER
Z POSITION, BEAM-GAS, TWO INTERACTIONS
TRD DETECTOR
TRD TRIGGER
CONFIRMATION OF ELECTRON CANDIDATES
Z POSITION
TABLE OF ELECTRON CANDIDATES
CALORIMETER
1280 EM TRIGGER TOWERS
1280 HD TRIGGER TOWERS
LEVEL 1 CALORIMETER TRIGGER
GLOBAL ENERGY AND MOMENTUM SUMS, LOCAL ENERGY CLUSTER COUNTS
LEVEL 1 AND LEVEL 1.5 TRIGGER FRAMEWORKS
16 BIT TRIGGER NUMBER
START DIGITIZATION SIGNALS
FRONT-END BUSY SIGNALS
FRONT-END CRATES
FRONT-END CRATE DATA
FIRST LEVEL TRIGGER DATA BLOCK
SPECIFIC TRIGGERS FIRED SIGNALS and STROBE
DATA CABLE SEQUENCERS
THE SEQUENCERS SELECT THE CRATES TO BE READ ON EACH DATA CABLE
DATA CABLE BUFFER-DRIVERS
EVENTS READOUT ON DATA CABLES
LEVEL 2 SUPERVISOR
SUPERVISOR ENABLES A LEVEL 2 NODE TO RECEIVE THE EVENT
LEVEL 2 PROCESSOR FARM
PROGRAMMING, CONTROL AND MONITORING INFORMATION
LEVEL 1 TRIGGER CONTROL COMPUTER
HOST
EVENTS THAT PASS LEVEL 2 TRANSFERED TO THE HOST

Figure 67

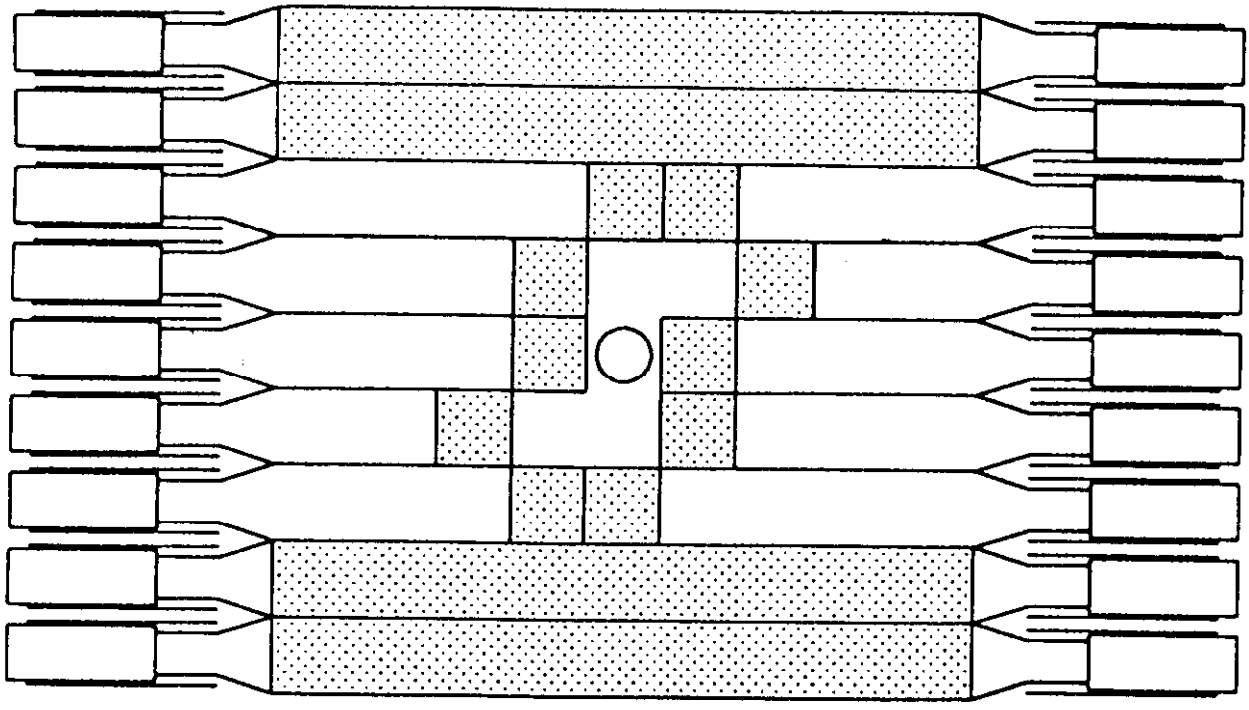

Figure 68 (a)

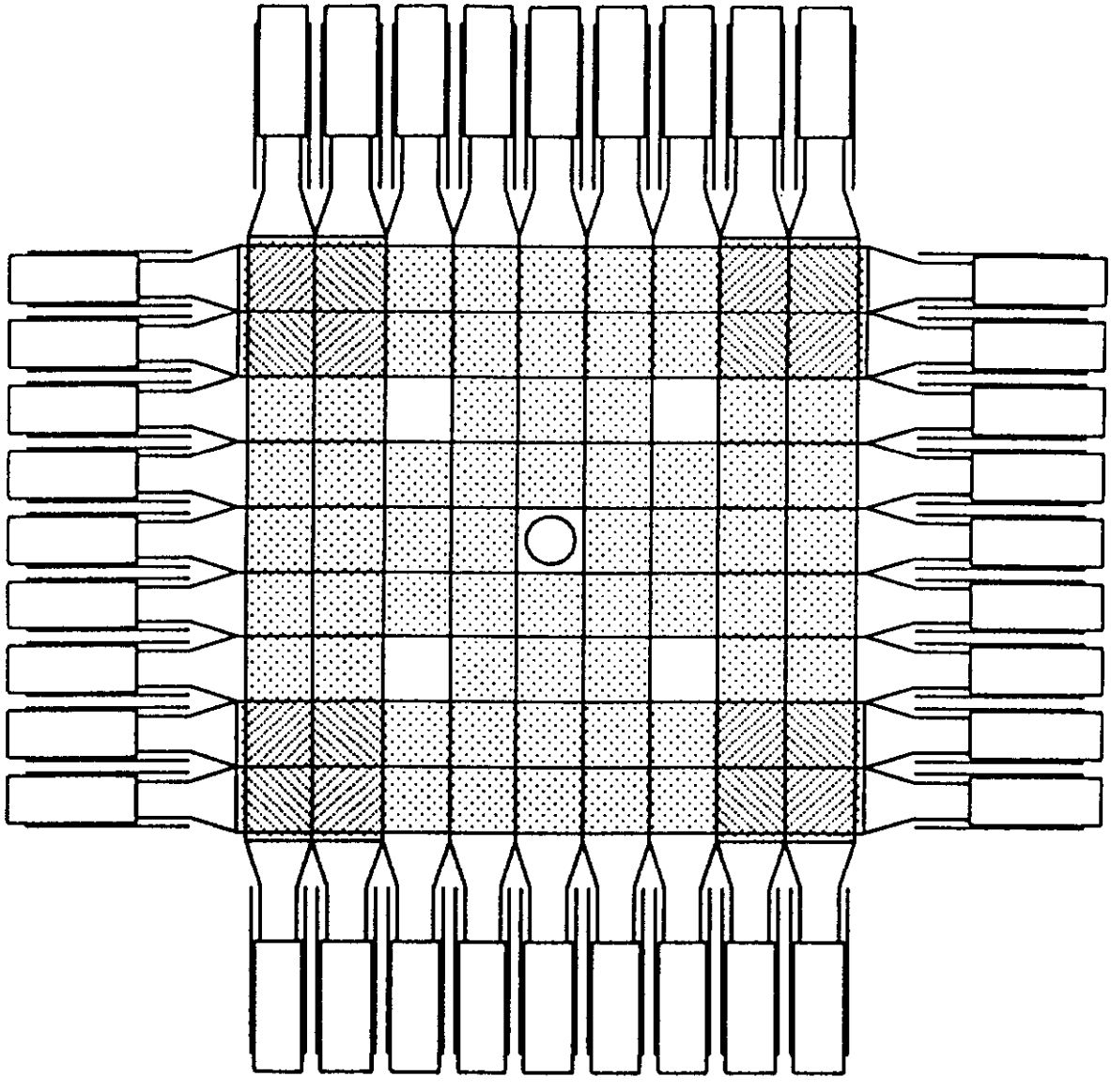

Figure 68 (b)

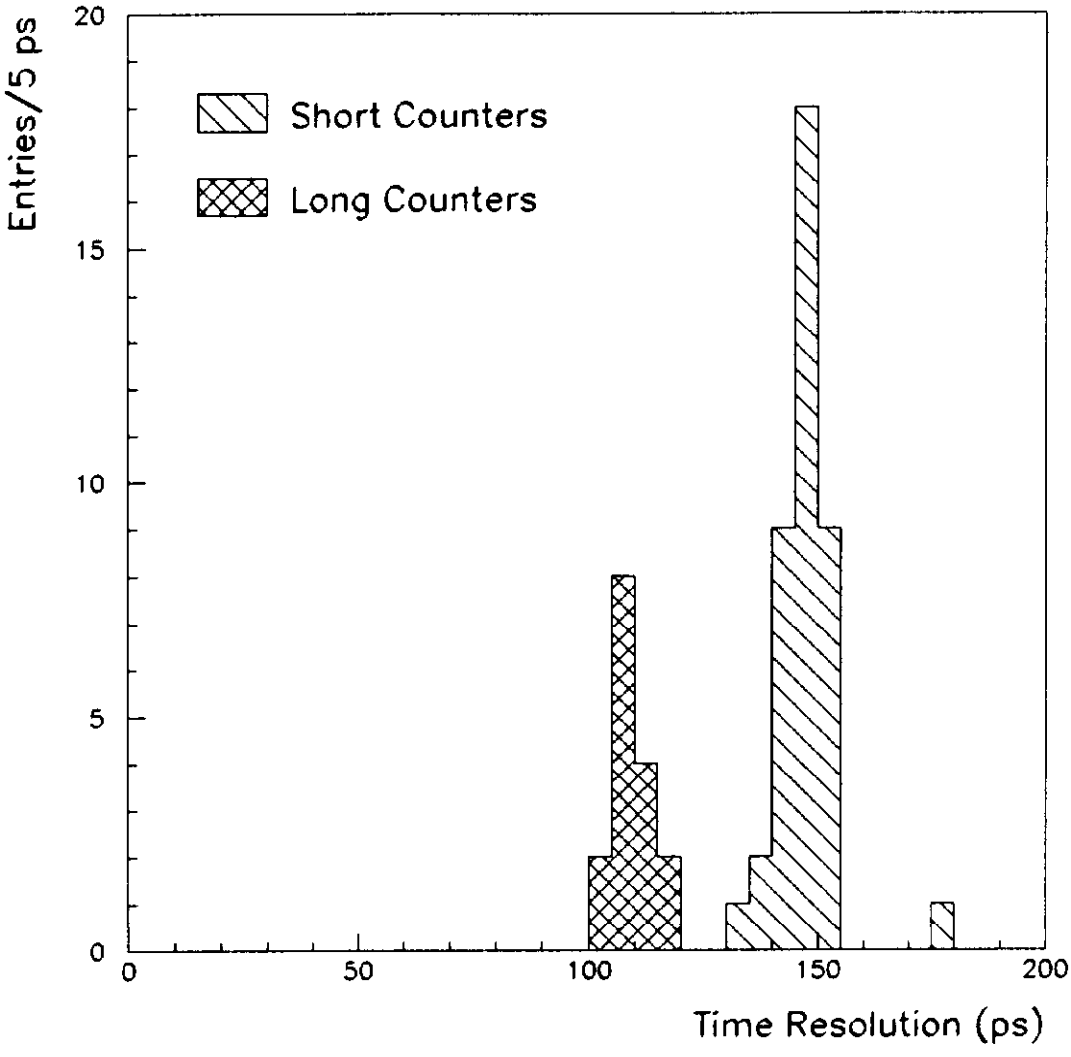
Entries/5 ps
20
15
10
5
0
Short Counters
Long Counters
0
50
100
150
200
Time Resolution (ps)

Figure 69

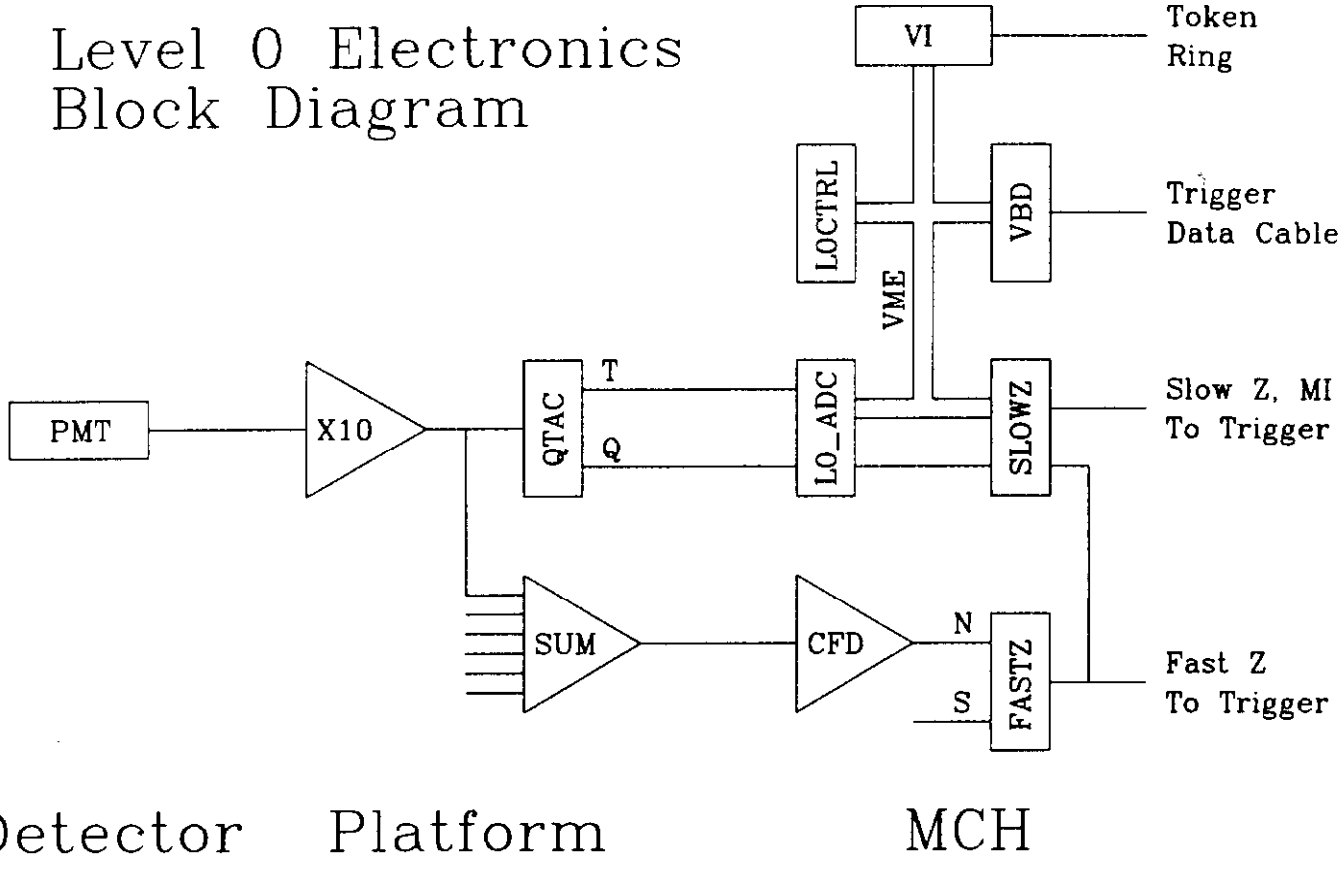
Level 0 Electronics
Block Diagram
VI
Token
Ring
LOCTRL
VBD
Trigger
Data Cable
VME
PMT
X10
QTAC
T
Q
LO_ADC
SLOWZ
Slow Z, MI
To Trigger
SUM
CFD
N
S
FASTZ
Fast Z
To Trigger
Detector Platform
MCH

Figure 70

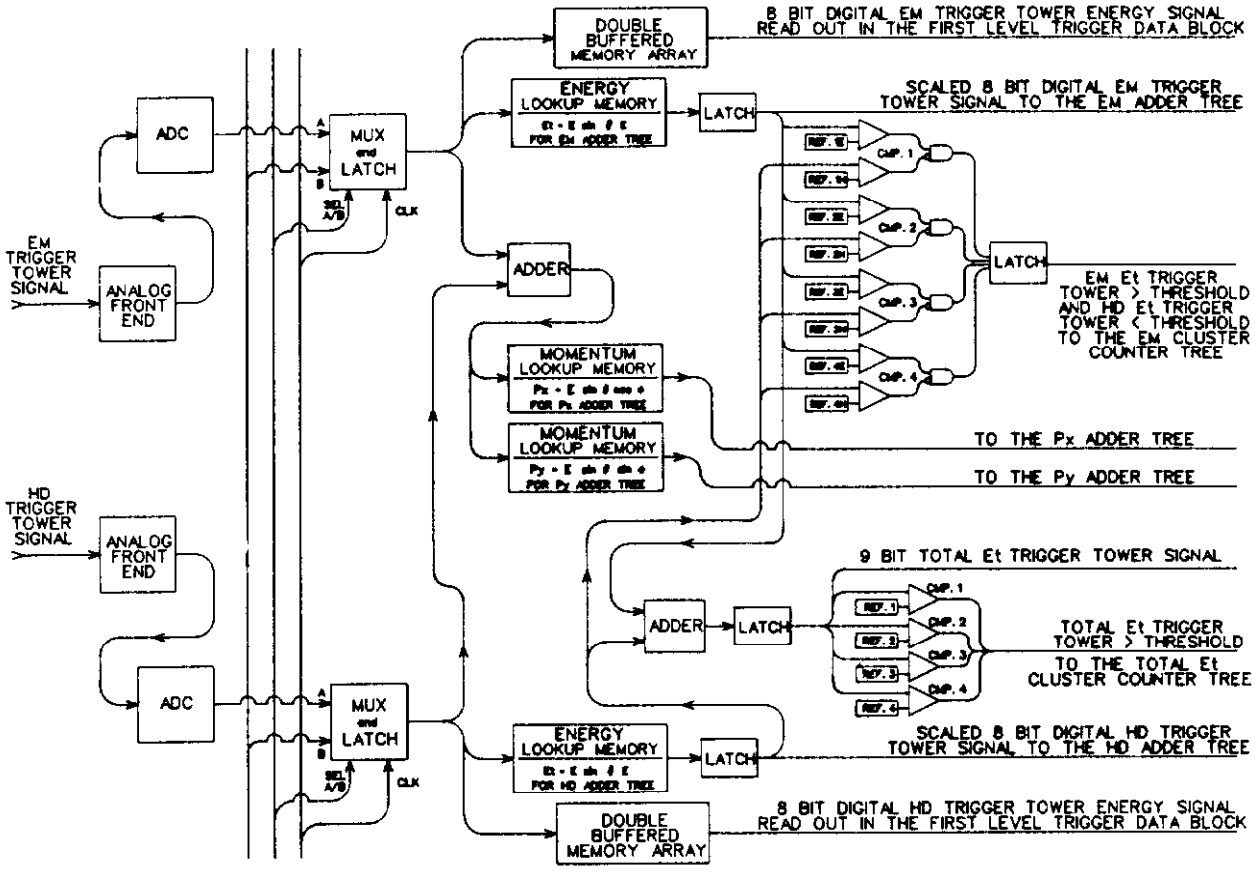

Figure 71a

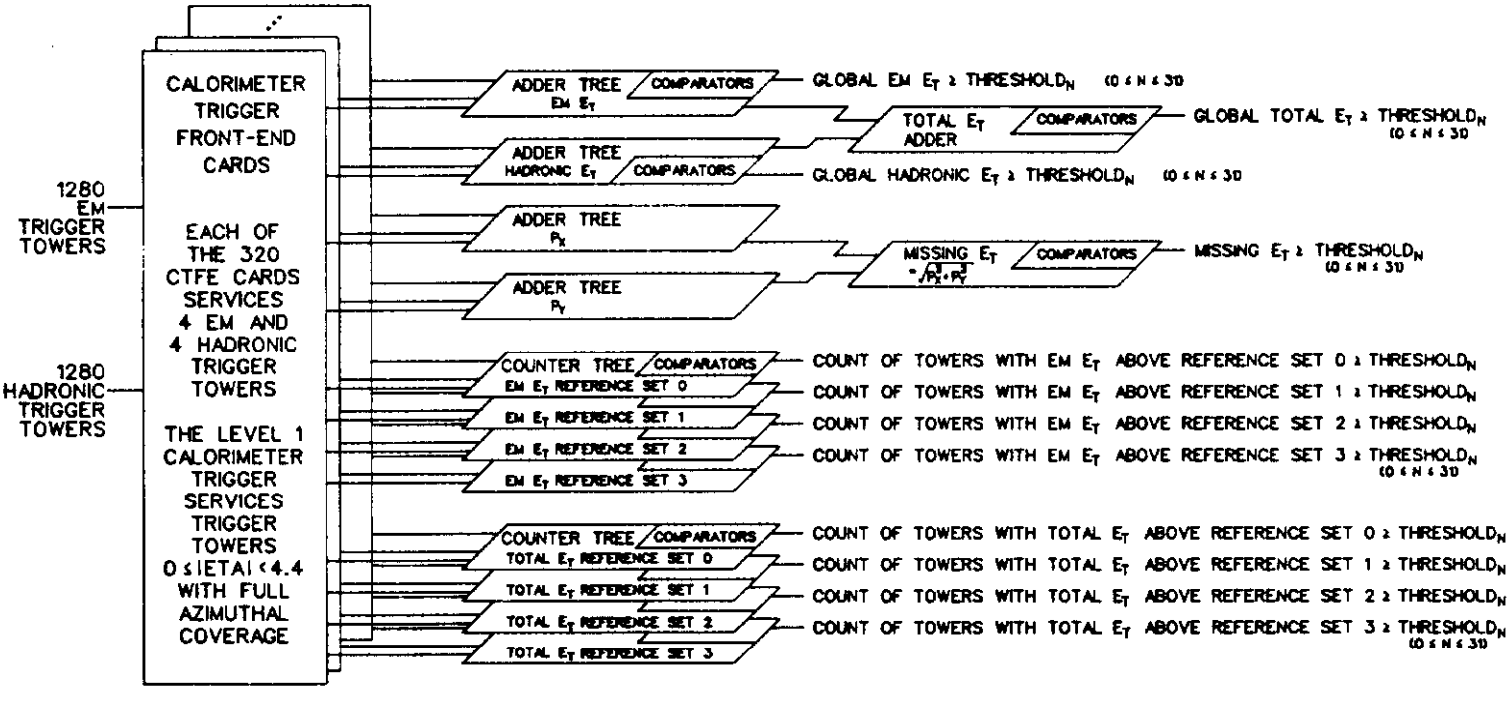

Figure 71b

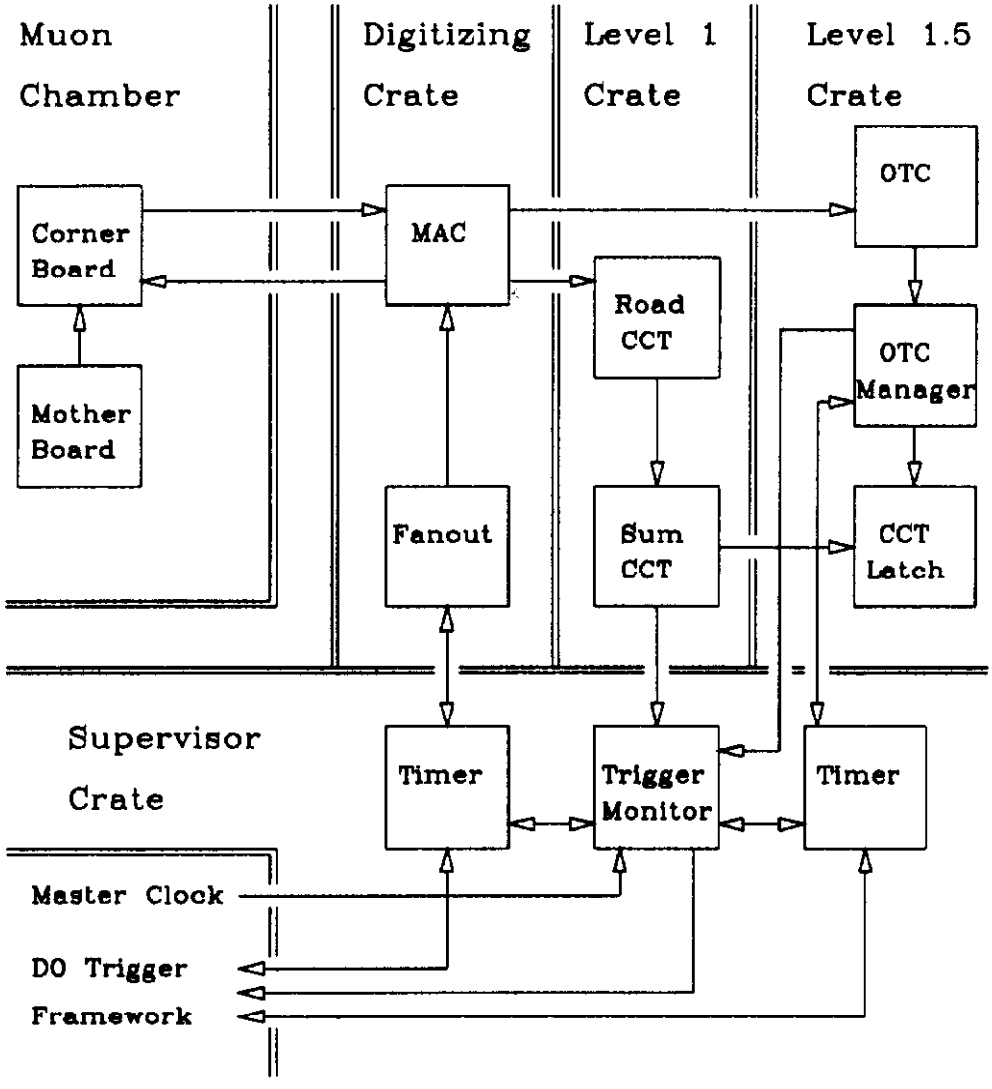
Muon
Chamber
Digitizing
Crate
Level 1
Crate
Level 1.5
Crate
OTC
Corner
Board
MAC
Road
CCT
OTC
Manager
Mother
Board
Fanout
Sum
CCT
CCT
Latch
Supervisor
Crate
Timer
Trigger
Monitor
Timer
Master Clock
DO Trigger
Framework

Figure 72

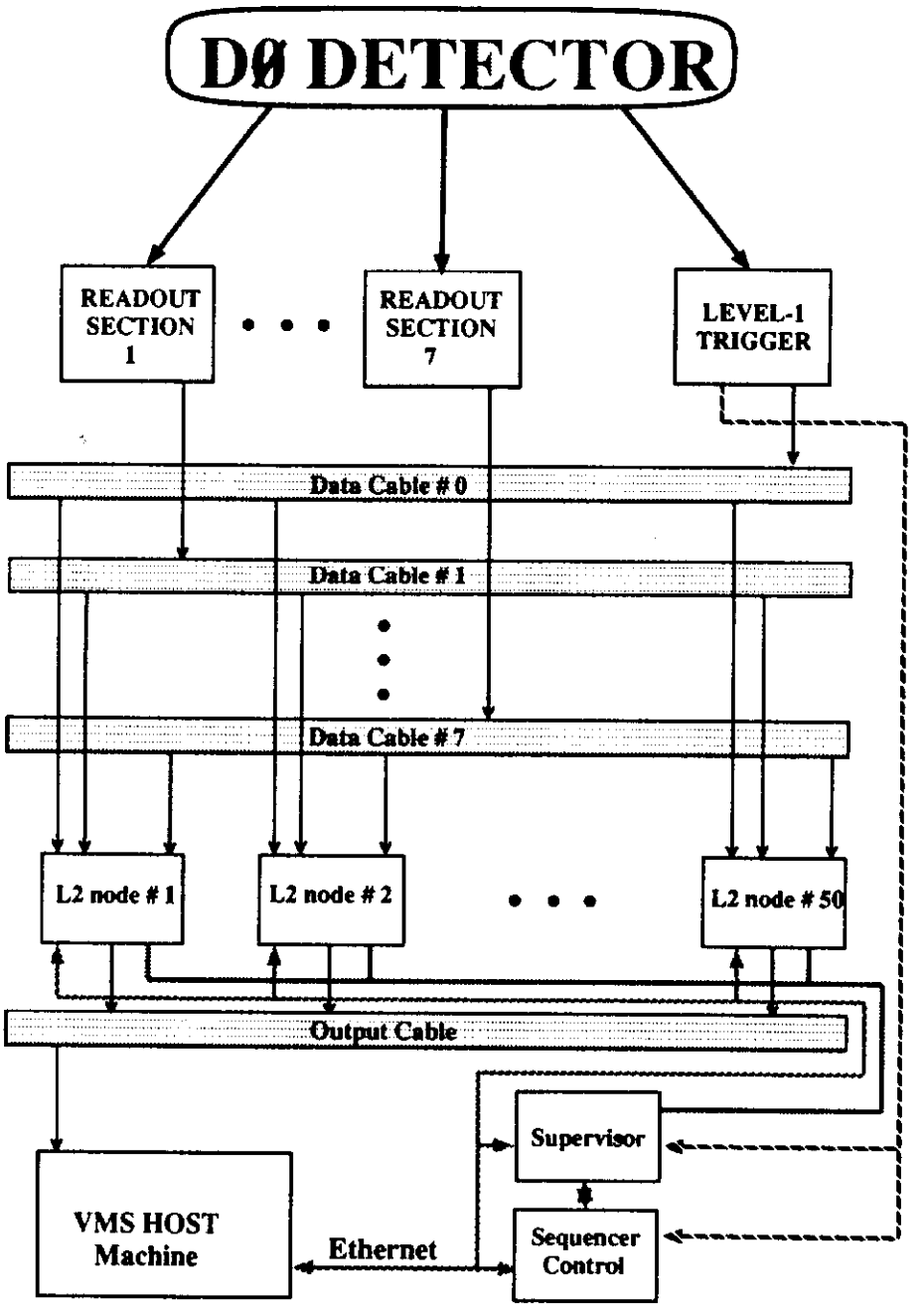
DØ DETECTOR
READOUT SECTION 1
READOUT SECTION 7
LEVEL-1 TRIGGER
Data Cable # 0
Data Cable # 1
Data Cable # 7
L2 node # 1
L2 node # 2
L2 node # 50
Output Cable
Supervisor
VMS HOST Machine
Ethernet
Sequencer Control

Figure 73

Layout of Level-2 Node

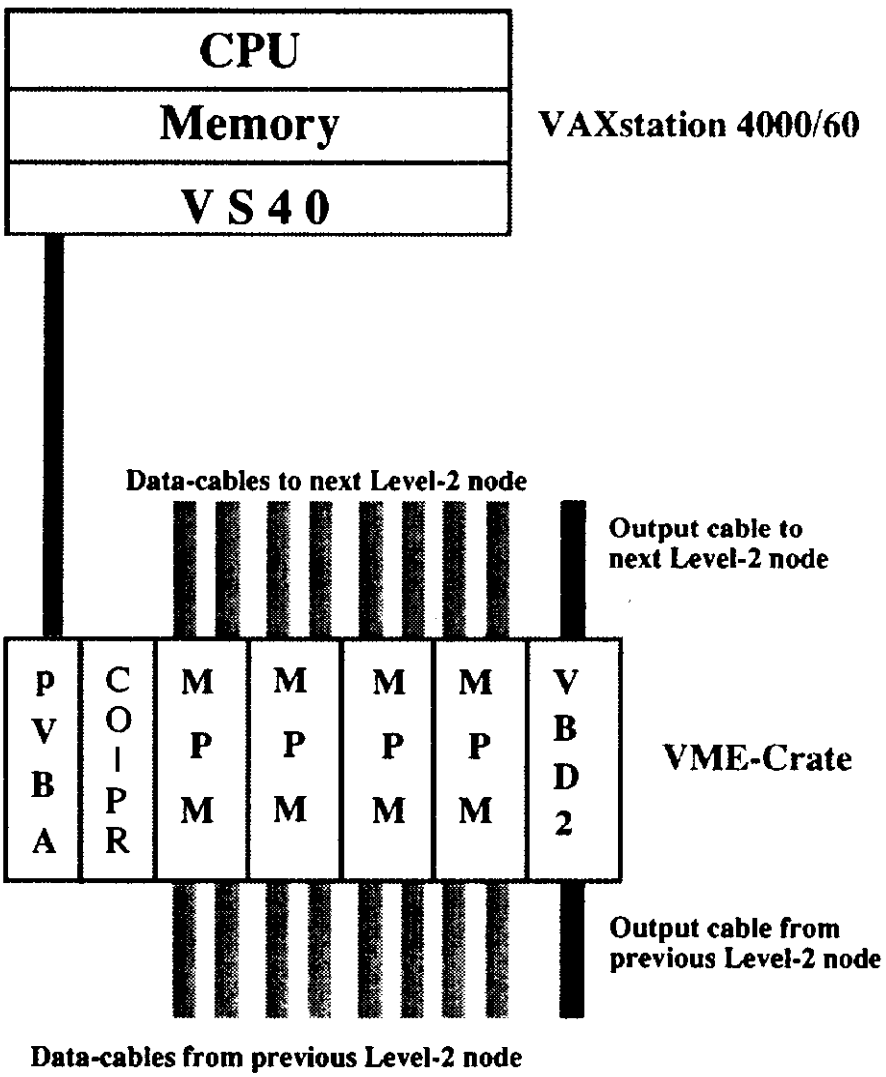

Figure 74

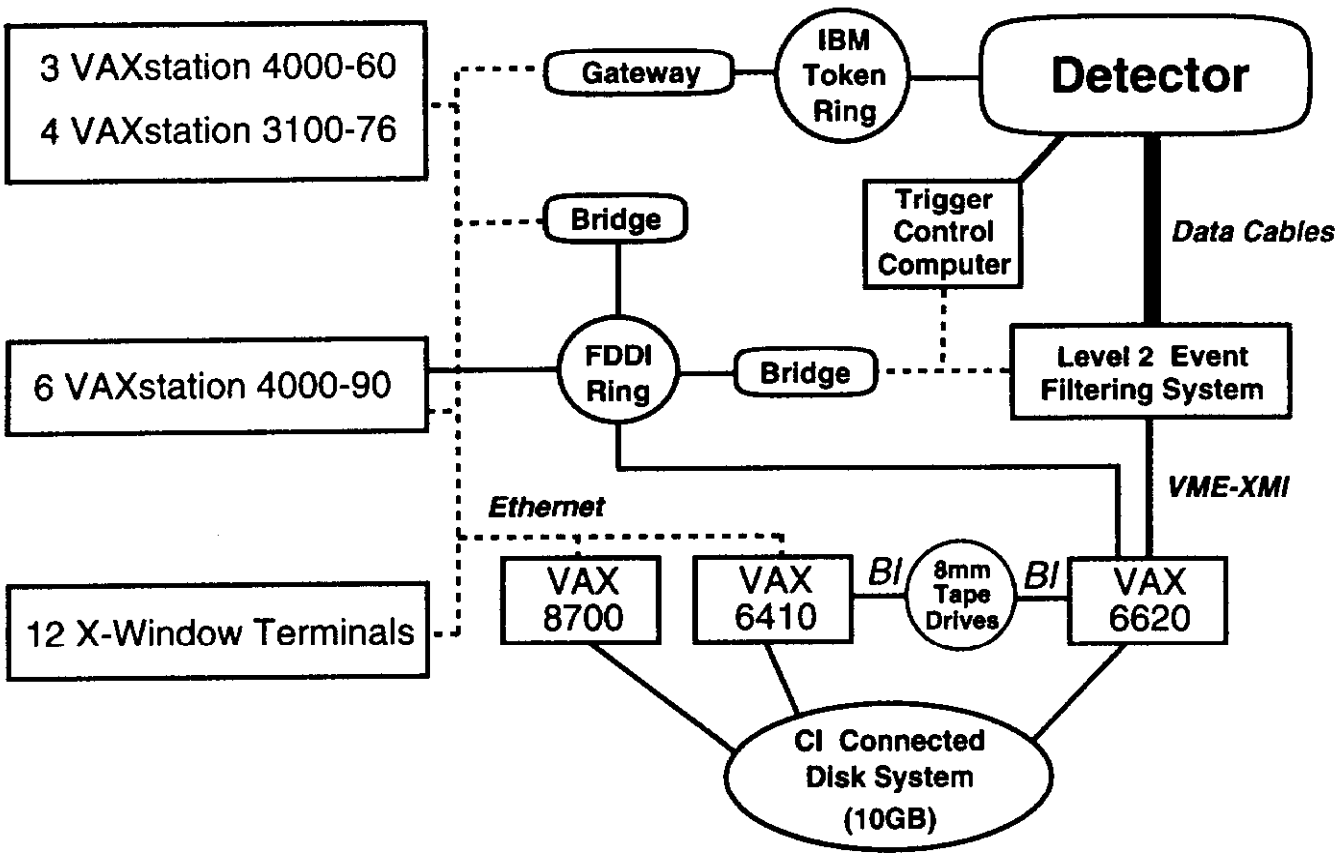
3 VAXstation 4000-60
4 VAXstation 3100-76
Gateway
IBM Token Ring
Detector
Bridge
Trigger Control Computer
Data Cables
6 VAXstation 4000-90
FDDI Ring
Bridge
Level 2 Event Filtering System
VME-XMI
Ethernet
12 X-Window Terminals
VAX 8700
VAX 6410
BI
8mm Tape Drives
BI
VAX 6620
CI Connected Disk System (10GB)

Figure 75

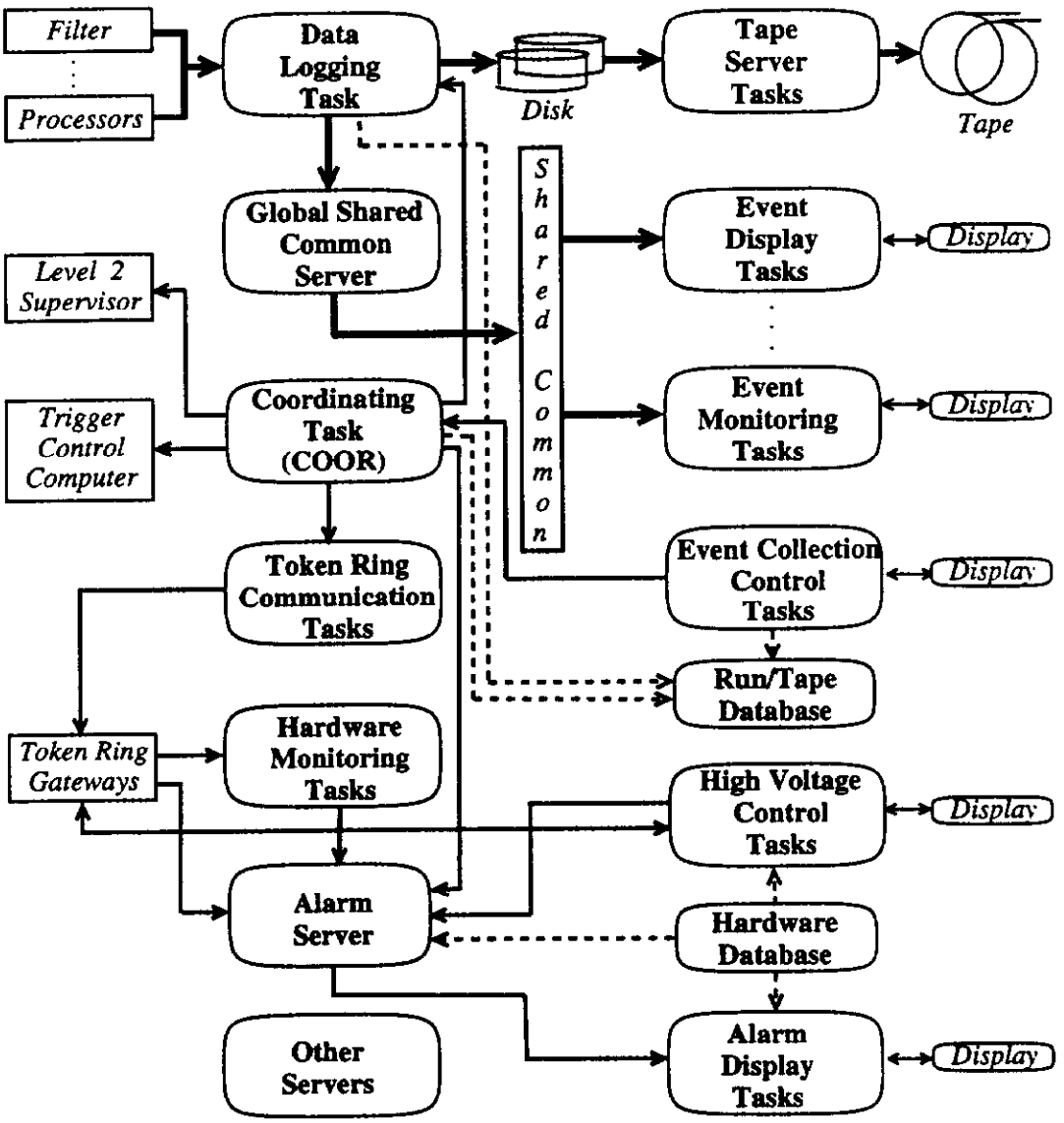
Filter
Processors
Data Logging Task
Disk
Tape Server Tasks
Tape
Global Shared Common Server
Shared Common
Event Display Tasks
Display
Level 2 Supervisor
Coordinating Task (COOR)
Event Monitoring Tasks
Display
Trigger Control Computer
Token Ring Communication Tasks
Event Collection Control Tasks
Display
Run/Tape Database
Token Ring Gateways
Hardware Monitoring Tasks
High Voltage Control Tasks
Display
Alarm Server
Hardware Database
Other Servers
Alarm Display Tasks
Display

Figure 76

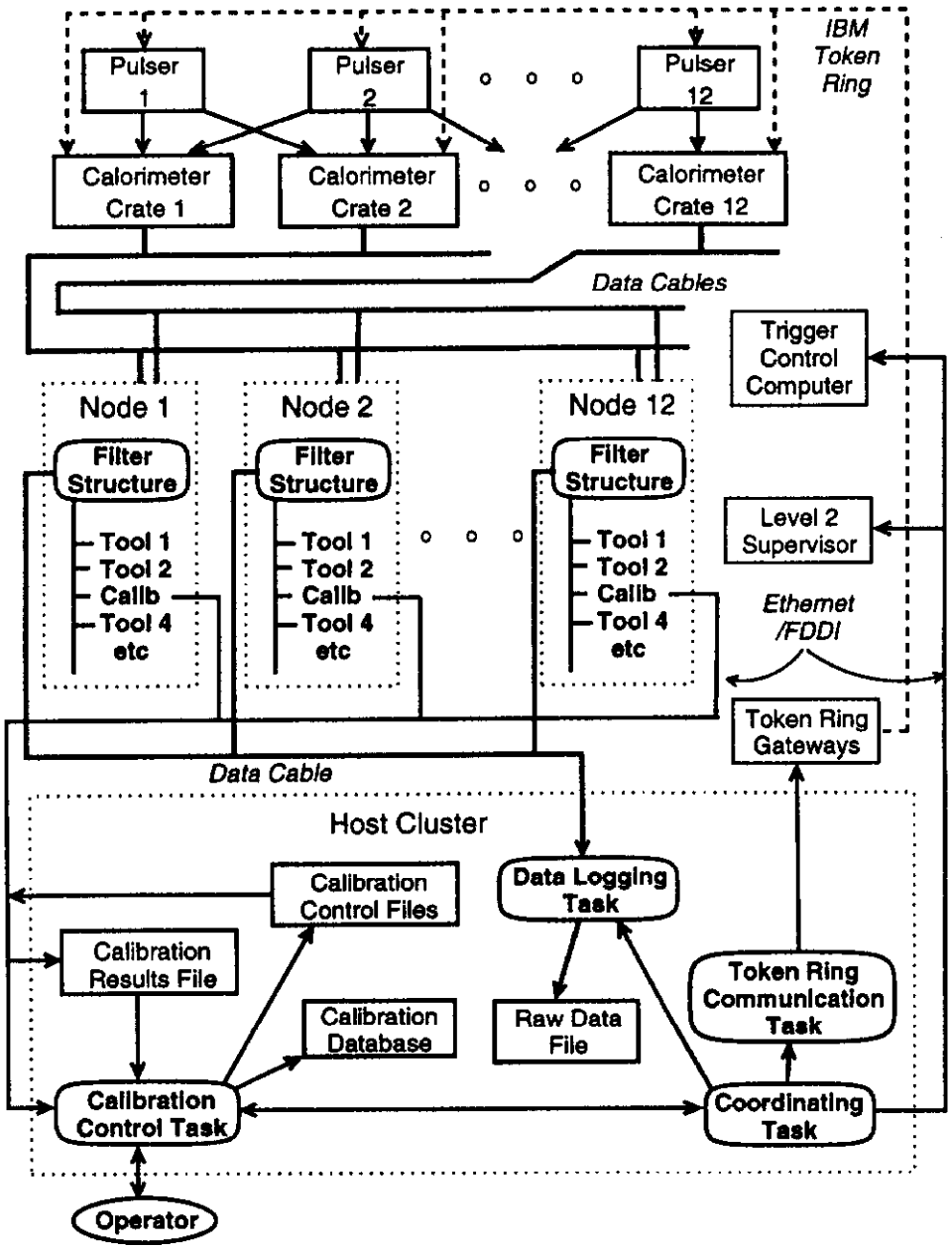
IBM
Token
Ring
Pulser
1
Pulser
2
Pulser
12
Calorimeter
Crate 1
Calorimeter
Crate 2
Calorimeter
Crate 12
Data Cables
Trigger
Control
Computer
Node 1
Node 2
Node 12
Filter
Structure
Tool 1
Tool 2
Calib
Tool 4
etc
Level 2
Supervisor
Ethernet
/FDDI
Token Ring
Gateways
Data Cable
Host Cluster
Calibration
Control Files
Data Logging
Task
Calibration
Results File
Token Ring
Communication
Task
Calibration
Database
Raw Data
File
Calibration
Control Task
Coordinating
Task
Operator

Figure 77

Block Diagram of High Voltage Control Board

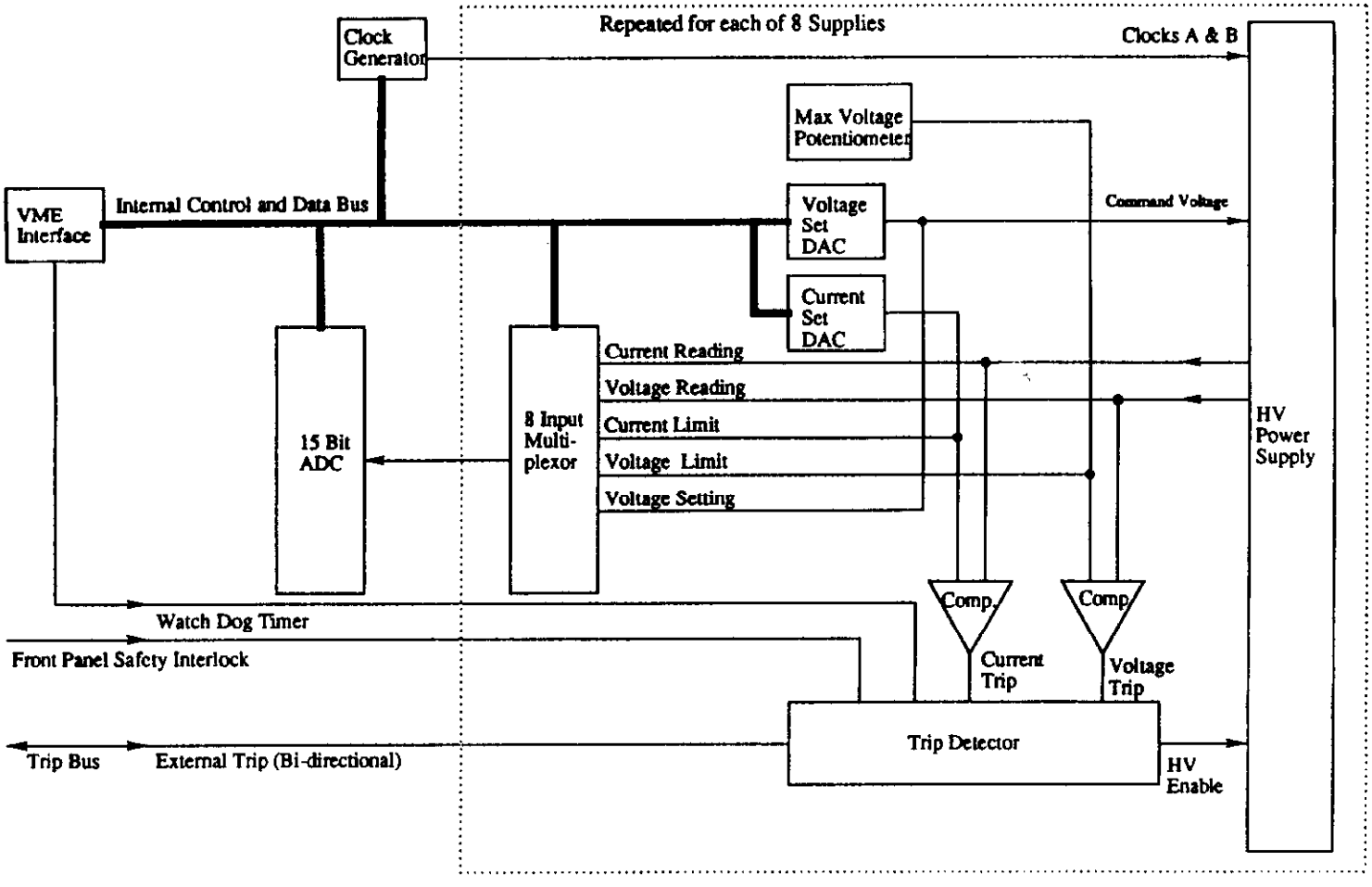

Figure 78

Block Diagram of a High Voltage Power Module

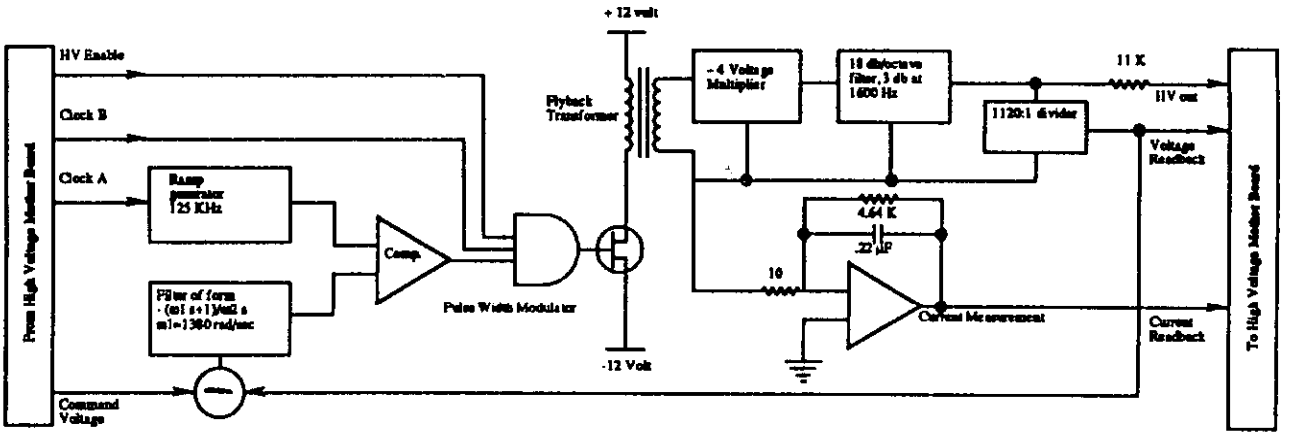

Figure 79

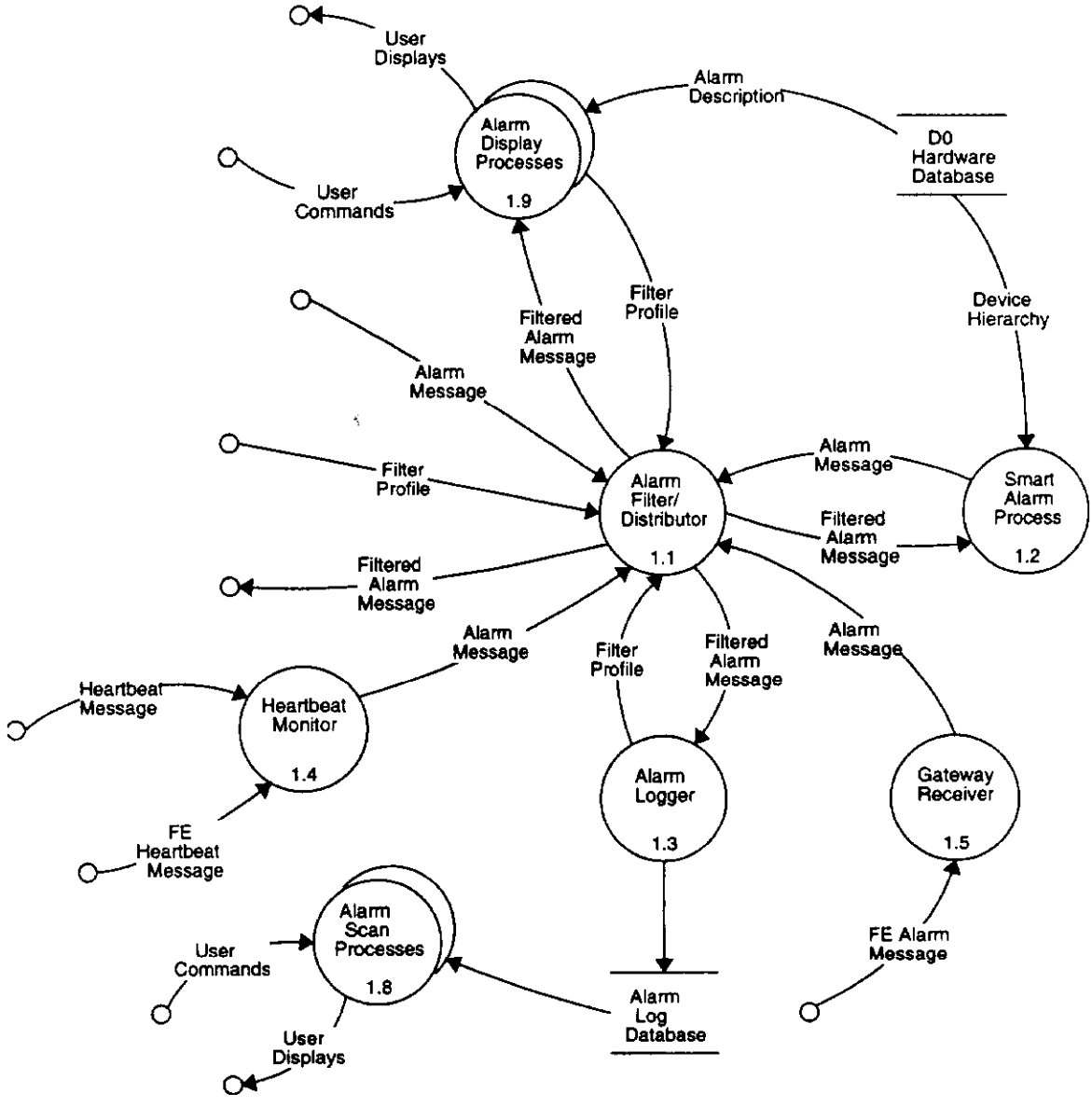

Data Flow Diagram: Alarm Processes

Figure 80

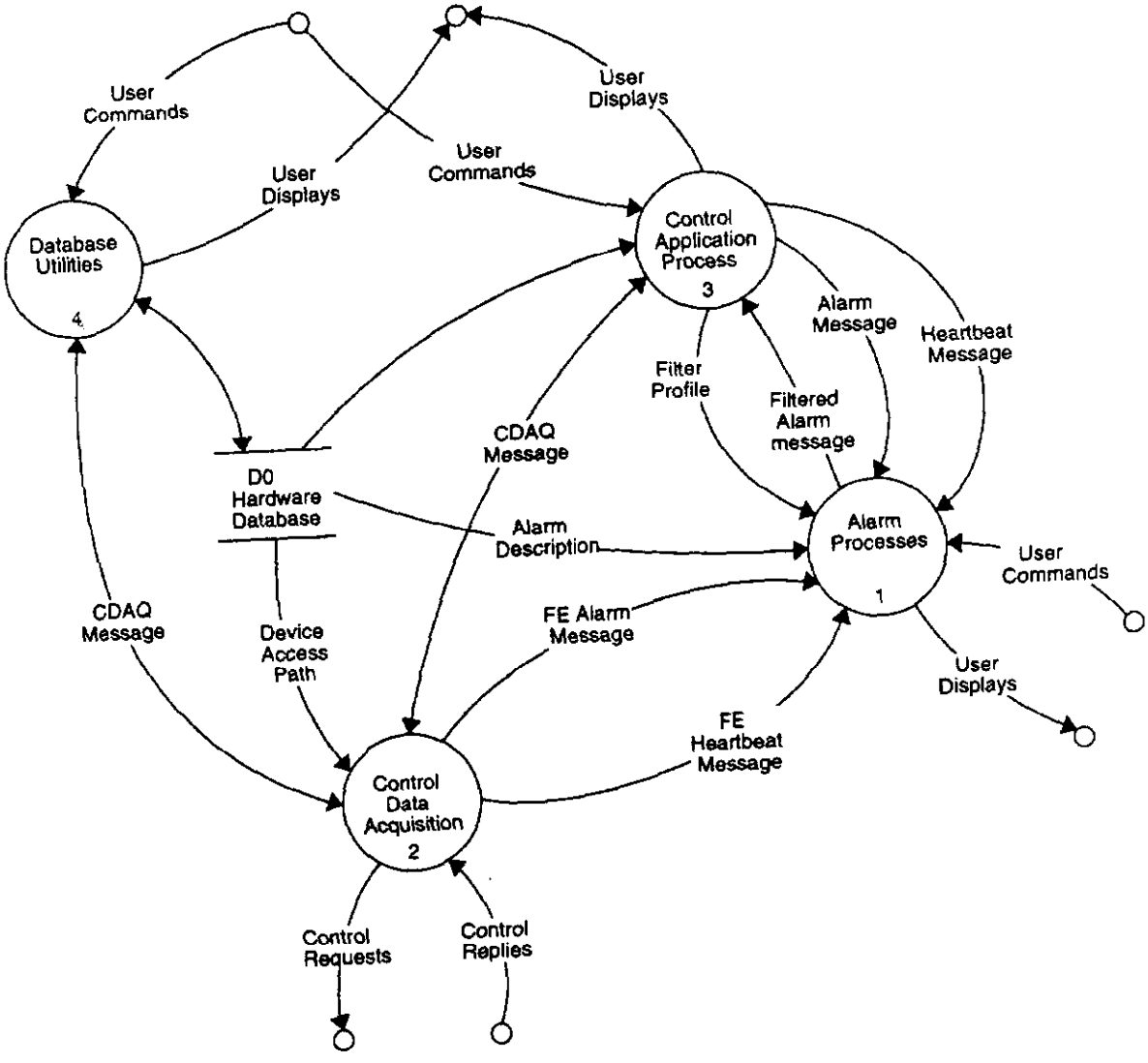
User Commands
User Displays
User Commands
User Displays
Database Utilities
4
Control Application Process
3
Alarm Message
Heartbeat Message
Filter Profile
Filtered Alarm message
CDAQ Message
D0 Hardware Database
Alarm Description
Alarm Processes
1
User Commands
CDAQ Message
Device Access Path
FE Alarm Message
User Displays
FE Heartbeat Message
Control Data Acquisition
2
Control Requests
Control Replies

Figure 81

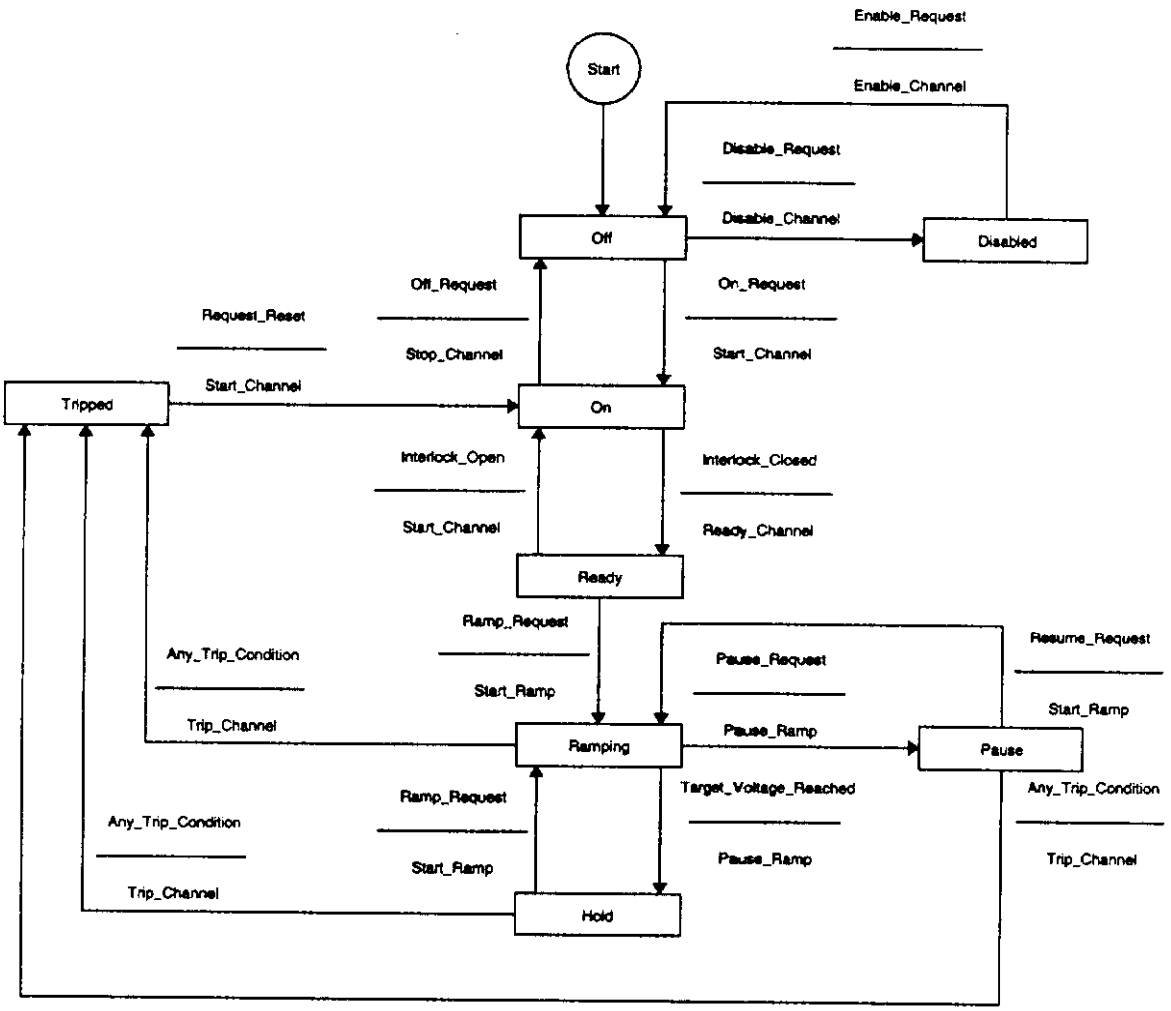
Start
Enable_Request
Enable_Channel
Disable_Request
Disable_Channel
Off
Disabled
Off_Request
Request_Reset
Stop_Channel
On_Request
Start_Channel
Tripped
Start_Channel
On
Interlock_Open
Start_Channel
Interlock_Closed
Ready_Channel
Ready
Ramp_Request
Any_Trip_Condition
Start_Ramp
Pause_Request
Resume_Request
Start_Ramp
Trip_Channel
Ramping
Pause_Ramp
Pause
Ramp_Request
Any_Trip_Condition
Start_Ramp
Target_Voltage_Reached
Pause_Ramp
Any_Trip_Condition
Trip_Channel
Trip_Channel
Hold

Figure 82

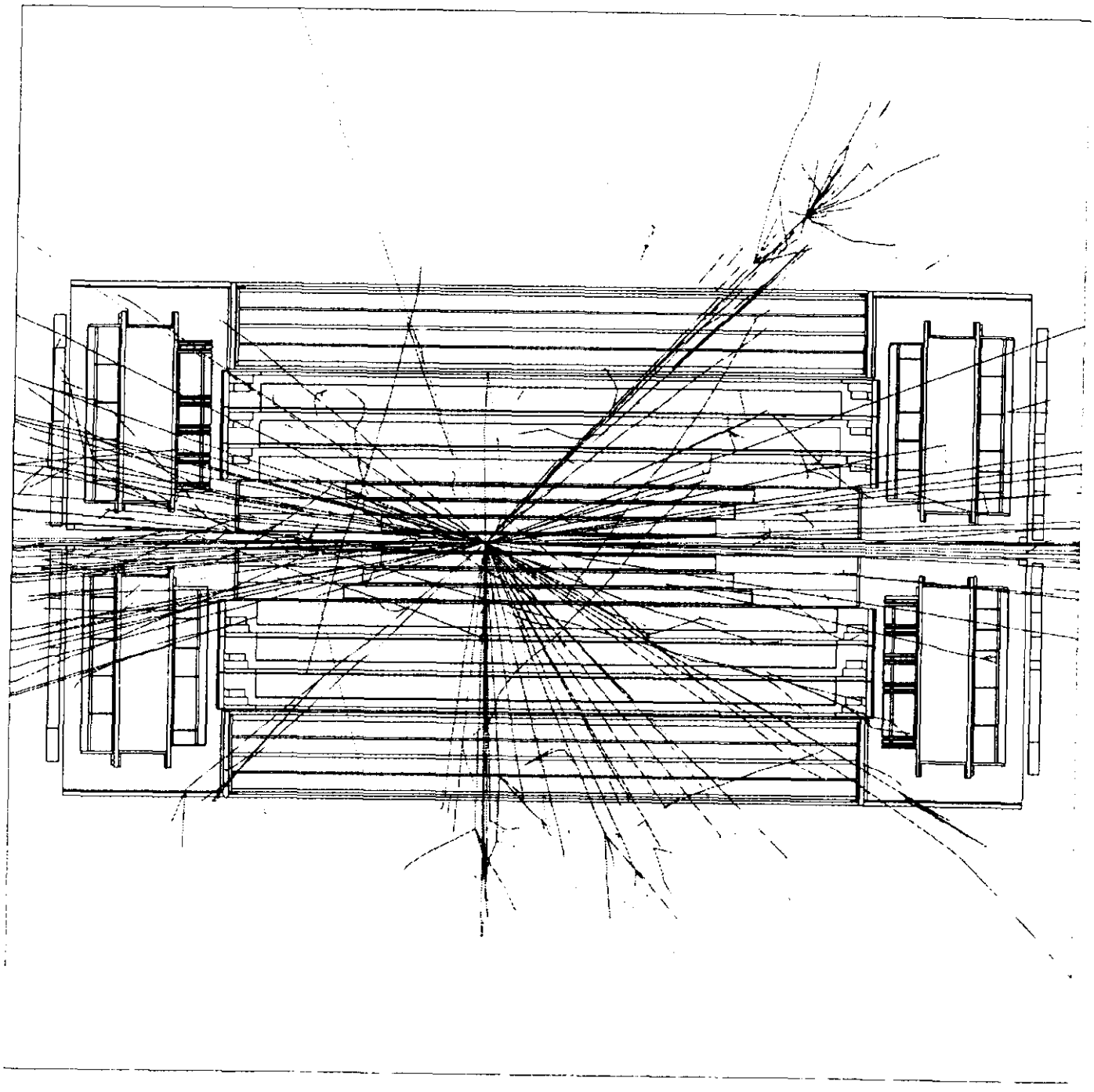

Figure 83

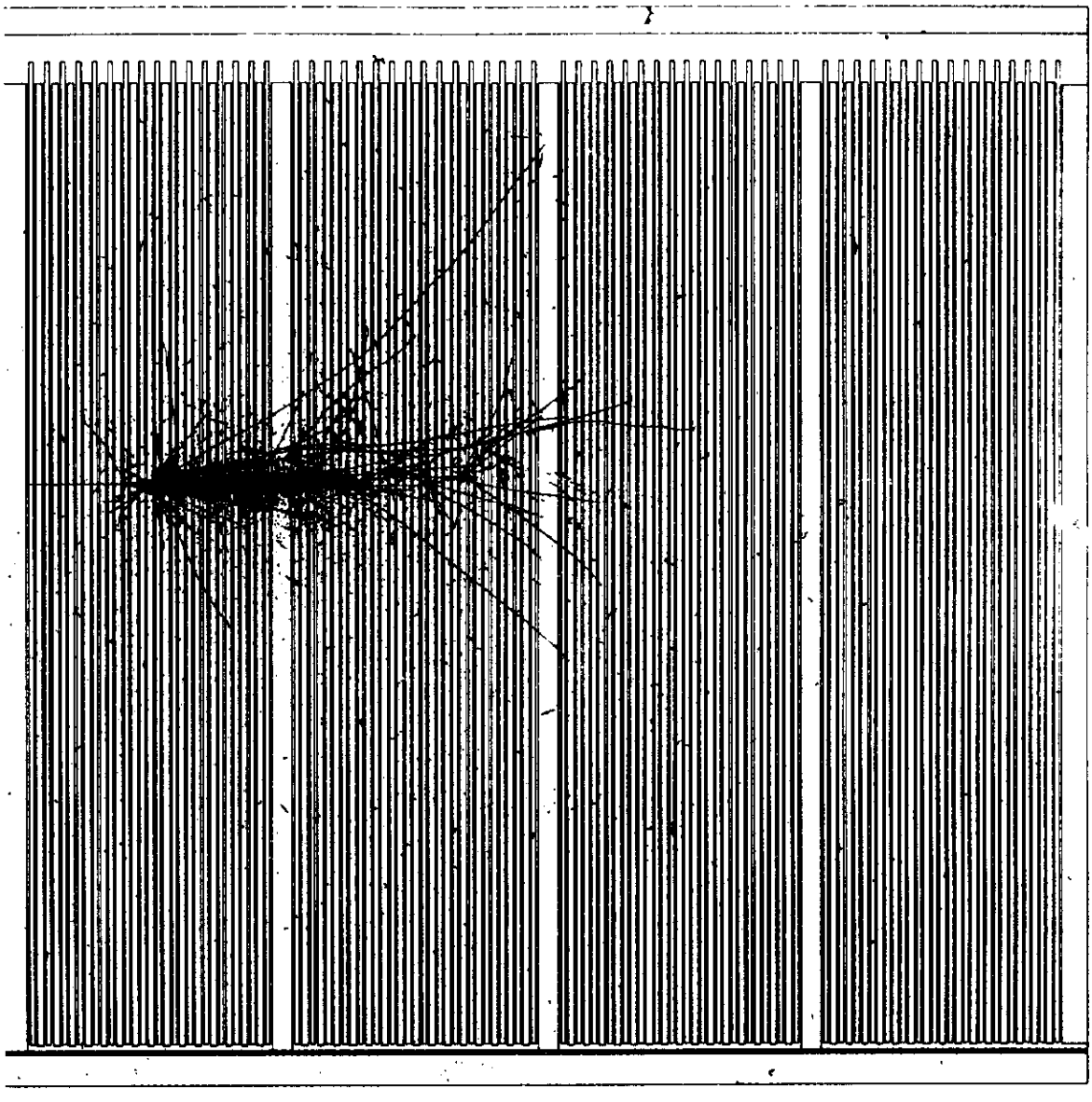

Figure 84

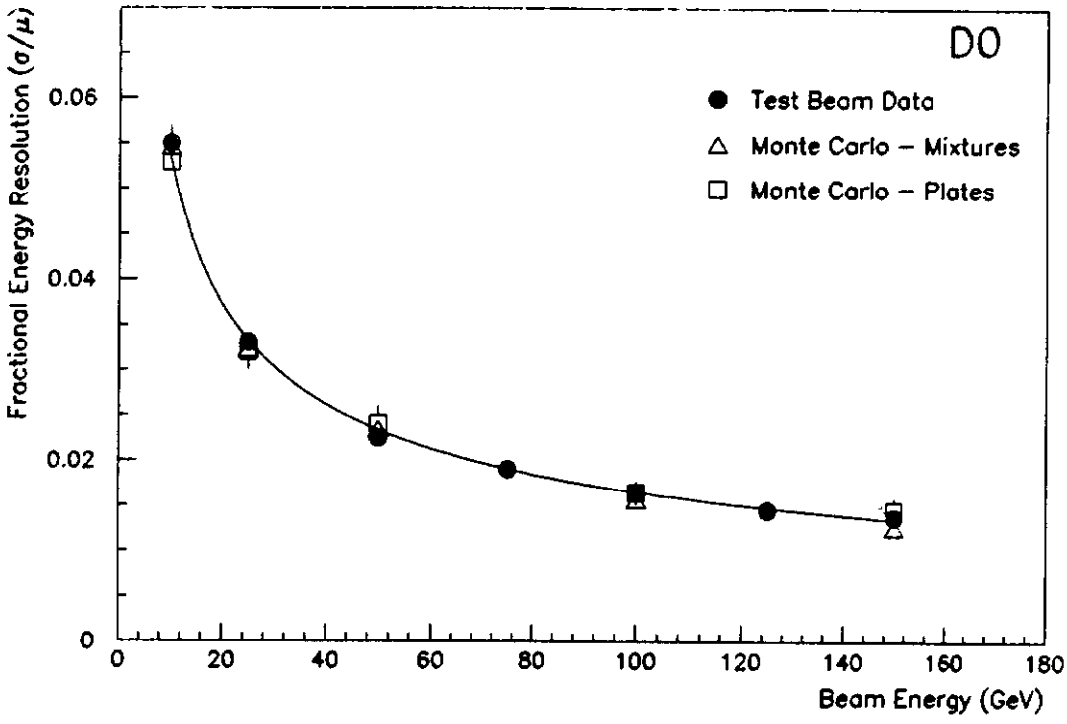

Figure 85a

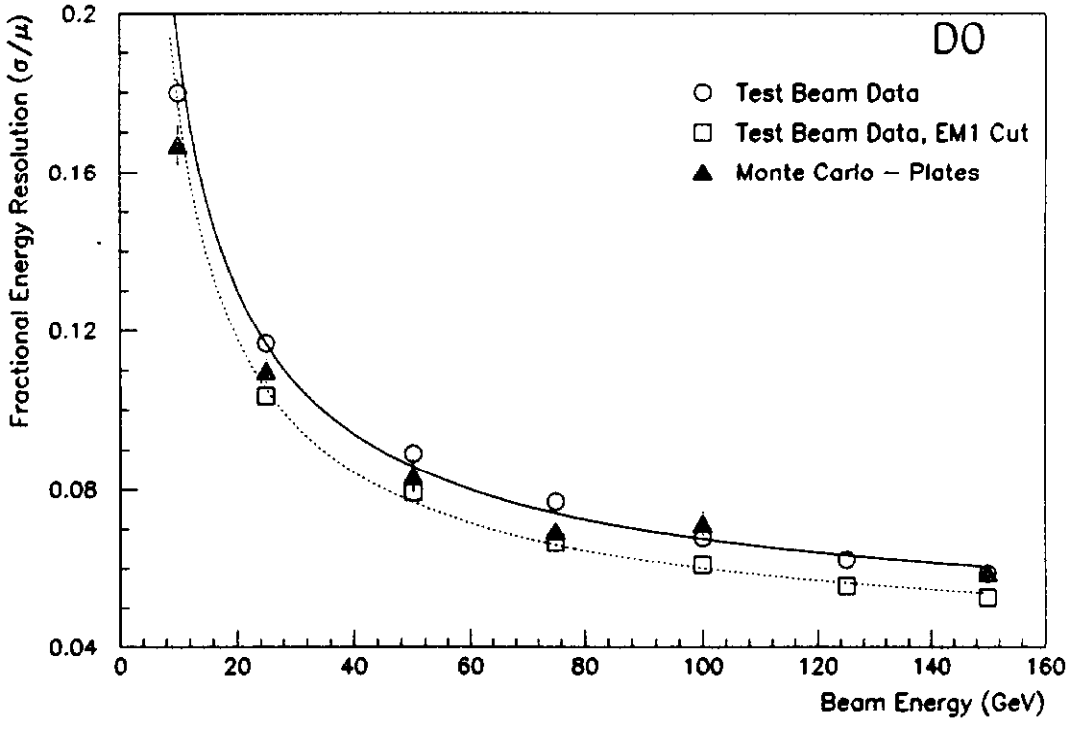

Figure 85b

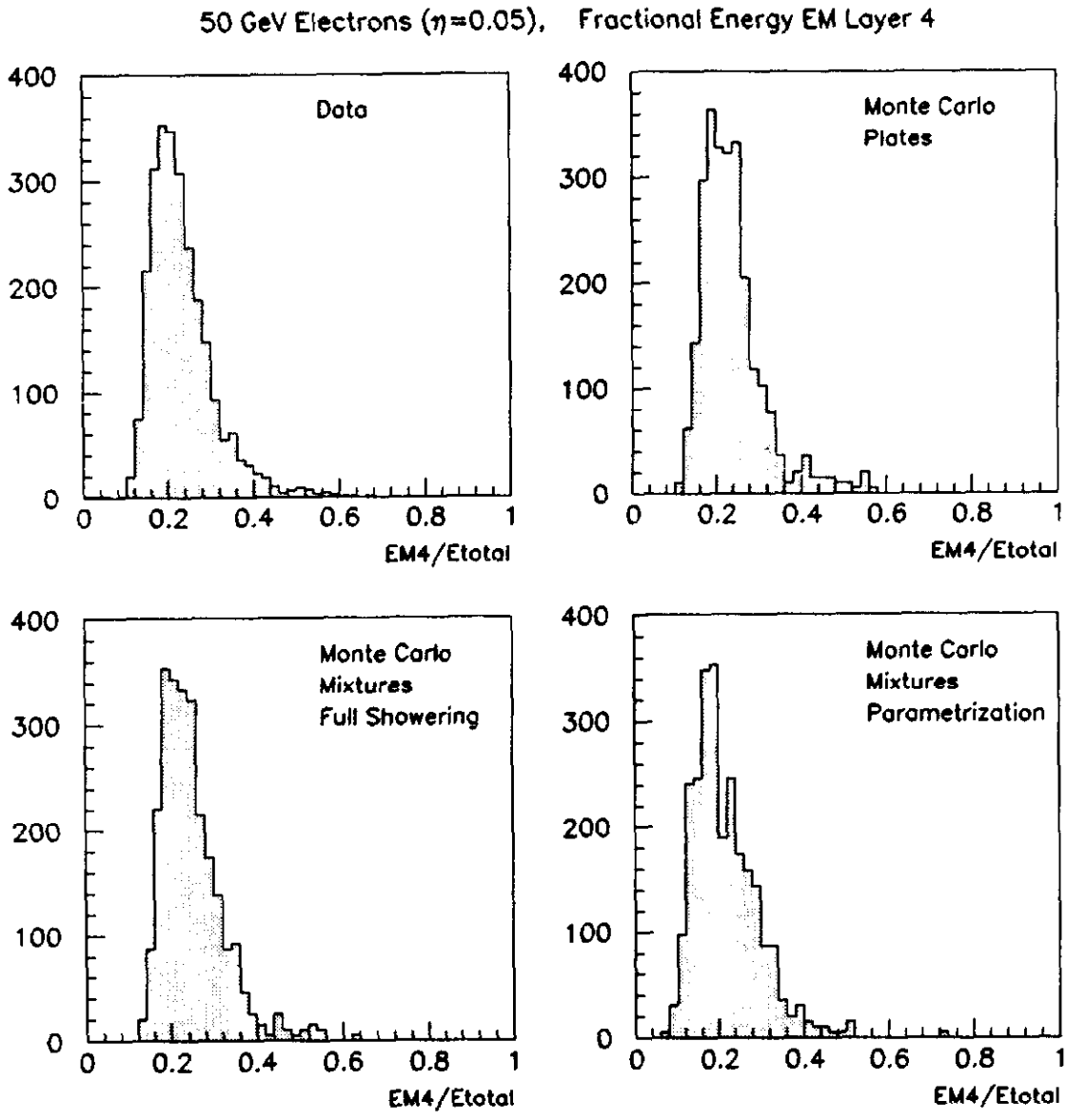
50 GeV Electrons (η=0.05), Fractional Energy EM Layer 4
Data
Monte Carlo
Plates
Monte Carlo
Mixtures
Full Showering
Monte Carlo
Mixtures
Parametrization
EM4/Etotal
0
100
200
300
400
0.2
0.4
0.6
0.8
1

Figure 86

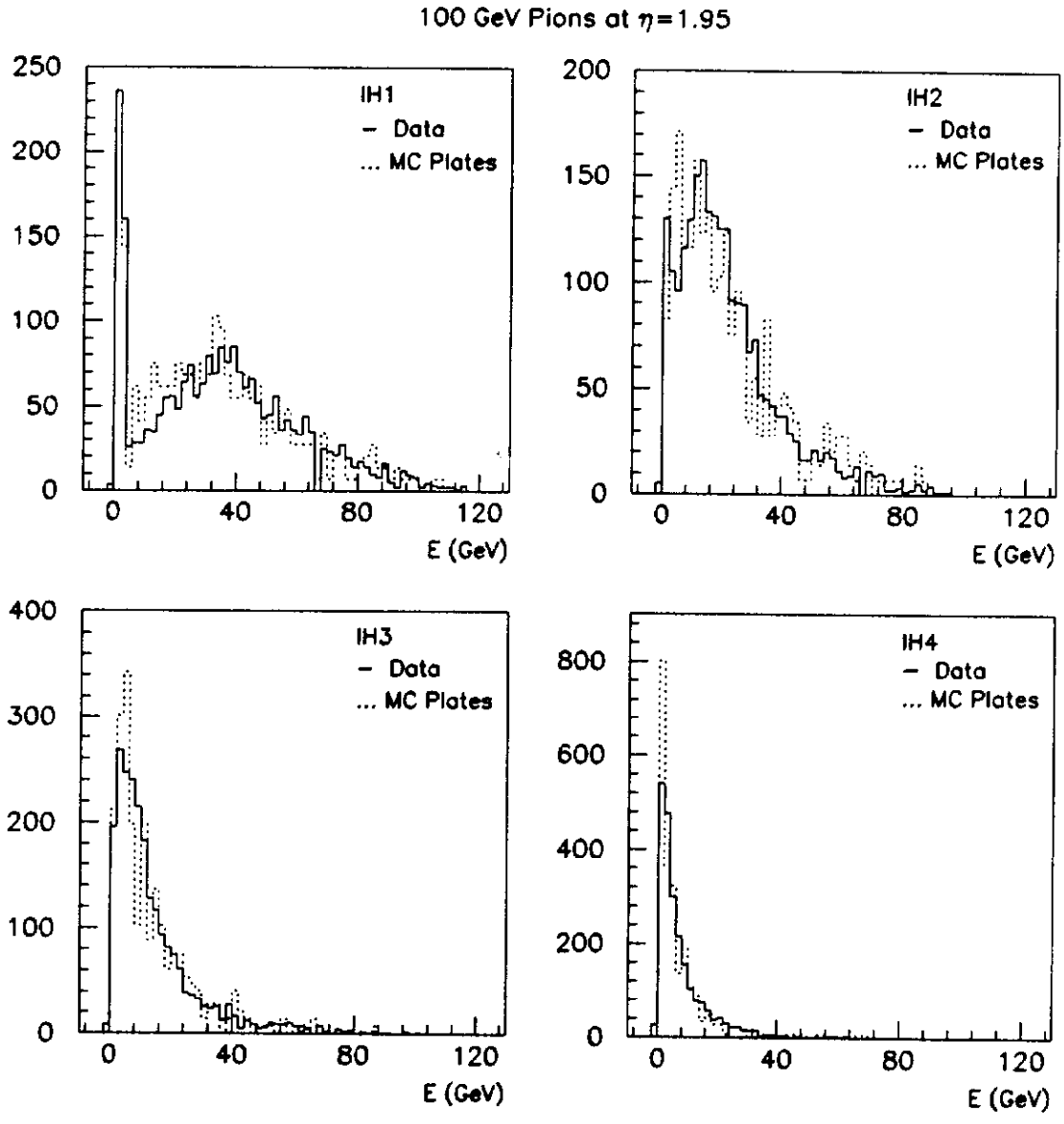
100 GeV Pions at η=1.95
IH1
– Data
... MC Plates
E (GeV)
IH2
– Data
... MC Plates
E (GeV)
IH3
– Data
... MC Plates
E (GeV)
IH4
– Data
... MC Plates
E (GeV)

Figure 87